Stellingen behorende bij het proefschrift

DIRECTIONAL DECOMPOSITION OF ELECTROMAGNETIC AND ACOUSTIC WAVE-FIELDS

Applications in integrated optics, exploration seismics and underwater acoustics

van

Mattheus Jacobus Nicolaas VAN STRALEN

1. De gemodificeerde Crank-Nicolsonmethode voor de vectoriële bundelpropagatiemethode wordt niet, zoals in de literatuur wordt beweerd, geïntroduceerd om een nauwkeuriger numeriek schema te bouwen, maar om schijnbare instabiliteiten te onderdrukken en daarmee dus onnauwkeurigheden te verhullen.

   W.P. Huang, C.-H. Xu, S.K. Chaudhuri, "Application of the finite-difference vector beam propagation method to directional coupler devices", *IEEE Journal of Quantum Electronics*, vol. 28, no. 6, pp. 1527–1532, 1992

2. Een halfgeleiderringlaser met een interne S-golfgeleider als terugkoppelingselement om éénrichtingsresonatie te forceren, is gevoelig voor reflecties vanuit de glasvezel en kan daarom niet onder de categorie *unidirectionele* ringlasers worden geplaatst.

   J.P. Hohimer and G.A. Vawter, "Unidirectional semiconductor ring lasers with racetrack cavities", *Applied Physics Letters*, vol. 63, no. 18, pp. 2457–2459, 1993

3. Het basisprincipe van het documentopmaakprogramma TEX is om de schrijver het kostbaarste deel van een mathematisch getinte tekst ook als zodanig in te laten voeren.

4. Het is bekend dat een golfgeleider een 3D-structuur is die met een 2D-theorie beschreven kan worden. Zo is de 3D-bundelpropagatiemethode in werkelijkheid gebaseerd op een 2D-algoritme.

5. Het opkomende nationalisme in Oost-Europa na het einde van de koude oorlog en de daarmee gepaard gaande verbrokkeling staat haaks op de aldaar levende wens om zich bij de Europese Unie aan te sluiten.

6. Het RTL4-TV-programma "De Vakantieman" voerde herhaaldelijk een onderzoek uit waarin doorsnee-kijkers wordt gevraagd hun vakantieverblijf alsmede Nederland aan te wijzen op de landkaart van Europa. De (vaak) negatieve resultaten lijken aan te geven, dat de meeste kijkers het weerpraatje van de RTL4-weerman niet begrijpen, zodat de weerman net zo goed zelf op vakantie kan gaan.

7. De totale officiële wachttijd van de forensensneltrein op de stations tussen Heemstede-Aerdenhout en Delft neemt lineair toe met het aantal sporen.

8. Bij de analyse van golfgeleiders met verliezende en/of versterkende materialen kunnen de propagerende modi niet altijd éénduidig geclassificeerd worden.

   M.J.N. van Stralen, K.F.I. Haak and H. Blok, "On the classification of discrete modes in lossy planar waveguides: the modal analysis revisited", *Optical and Quantum Electronics*, vol. 29, no. 2, pp. 243-262, 1997
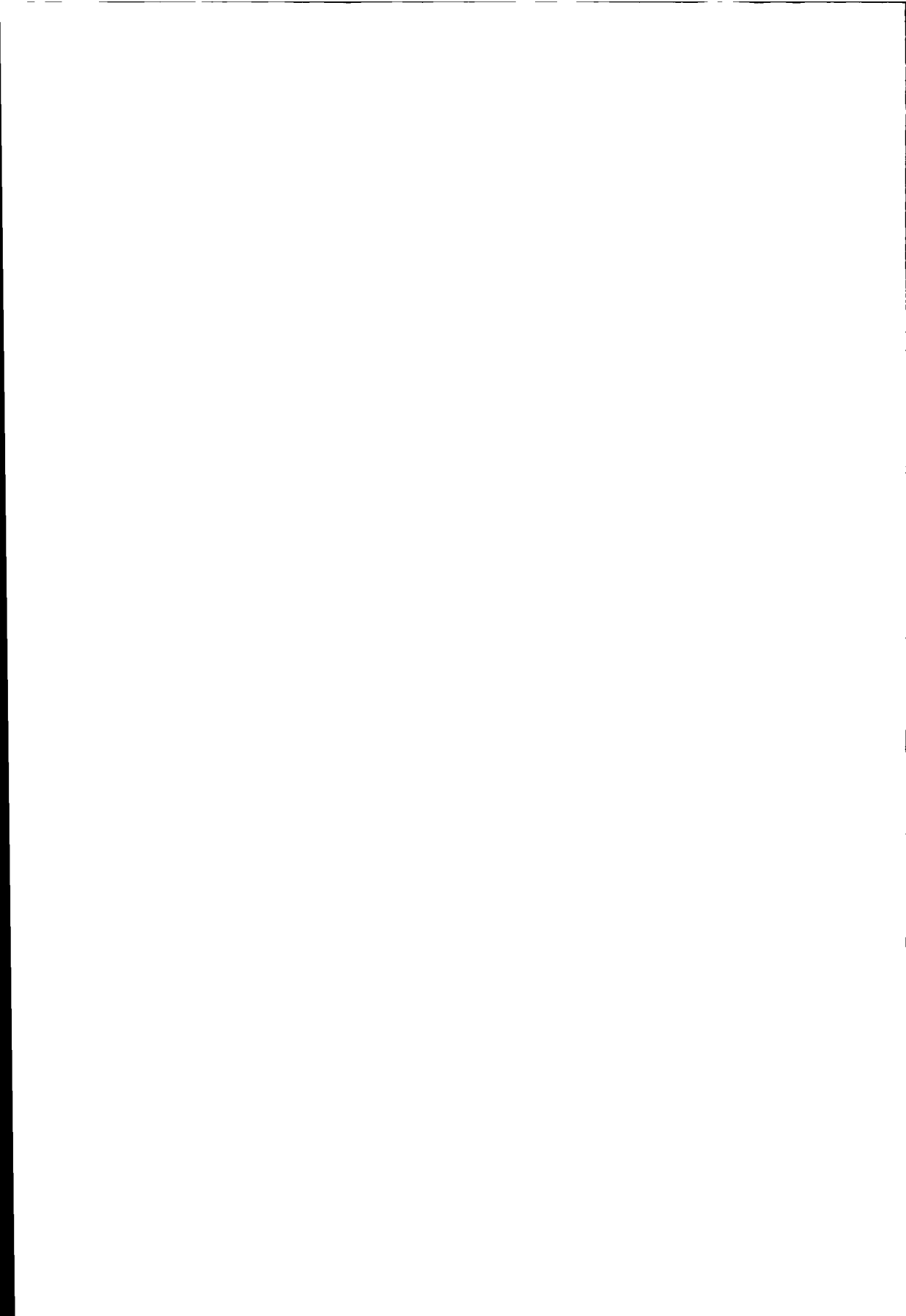
9. In de paraxiale benadering geldt dat $2 \times 27° \simeq 41°$.

10. Dit proefschrift bevat de *mathematiek van stralen*.

DIRECTIONAL DECOMPOSITION
OF ELECTROMAGNETIC AND ACOUSTIC
WAVE-FIELDS

Applications in integrated optics, exploration seismics and underwater acoustics

DIRECTIONAL DECOMPOSITION OF ELECTROMAGNETIC AND ACOUSTIC WAVE-FIELDS

Applications in integrated optics, exploration seismics and underwater acoustics

PROEFSCHRIFT

ter verkrijging van de graad van doctor
aan de Technische Universiteit Delft,
op gezag van de Rector Magnificus Prof. dr. ir. J. Blaauwendraad,
in het openbaar te verdedigen ten overstaan van een commissie,
door het College van Dekanen aangewezen,
op donderdag 1 mei 1997 te 10:30 uur

door

Mattheus Jacobus Nicolaas VAN STRALEN

elektrotechnisch ingenieur
geboren te Haarlem

Dit proefschrift is goedgekeurd door de promotoren:
Prof. dr. ir. H. Blok
Dr. M.V. de Hoop (research professor)

Samenstelling promotiecommissie:

Rector Magnificus,	voorzitter
Prof. dr. ir. H. Blok,	Technische Universiteit Delft, promotor
Dr. M.V. de Hoop (research professor),	Colorado School of Mines, promotor
Prof. dr. ir. P.M. van den Berg,	Technische Universiteit Delft
Prof. dr. ir. J.T. Fokkema,	Technische Universiteit Delft
Prof. dr. B.H. Verbeek,	Philips Optoelectronics Research
Prof. dr. Gy. Veszely,	Budapesti Mûszaki Egyetem
Dr. H.J.W.M. Hoekstra,	Universiteit Twente

Aan mijn ouders

Acknowledgement

Contents

CHAPTER 1

Introduction

In a wide range of nonuniform waveguiding problems, such as in integrated optics, exploration seismics and underwater acoustics, the medium properties along a preferred direction of propagation (longitudinal direction) vary slowly compared to the variation in the plane perpendicular to it (the transverse plane). In such structures, the wave mainly propagates in the preferred, longitudinal direction while being gradually influenced by the transverse inhomogeneities. For the numerical modeling of wave propagation in such structures, we propose a directional decomposition of the wave-field in order to reduce the complexity of the problem and, related to that, the computational time and data storage. This study concentrates on waveguiding problems in the field of integrated optics, but also examples from other fields, in particular exploration seismics and underwater acoustics, are discussed.

The purpose of this thesis is to design and investigate the directional wave-field decomposition method. The method is used to analyze electromagnetic or acoustic wave propagation along a chosen direction of preference and finally to compute or estimate the overall characteristics of a section of a nonuniform waveguiding structure; such as reflection, gain/loss, etc..

This preliminary chapter presents an overview of the thesis. After a brief introduction to the fields of integrated optics, exploration seismics, and underwater acoustics, the basic electromagnetic and acoustic equations and the description of the relevant configuration are discussed. Subsequently, a brief introduction to the directional decomposition technique and an historical overview of various BPM-type (Beam Propagation Method) numerical approaches are elucidated. Finally, the organization of the chapters is explained.

1.1 Applications of the directional wave-field decomposition

One-way wave equation methods, such as the parabolic equation method and the directional wave-field decomposition method, originate from atmospheric wave propagation problems. Such methods became popular tools in underwater acoustics and exploration seismics in the 1970s, and a few years later also in integrated optics. From a mathematical point of view, these methods are also related to the Schrödinger equation in quantum mechanics.

In this section, we introduce the fields of application, which are of interest in this thesis: integrated optics, exploration seismics and underwater acoustics.

1.1.1 Integrated optics

The name *integrated optics* was introduced by Miller[1] and refers to the realization of a number of guided wave optical components on a single substrate to form a more complicated light-wave communication system. If also driver electronics is integrated on the substrate, one normally uses the more encompassing term of *optoelectronics*. Although integrated optics is today finding a way into other fields such as optical storage, sensing and optical computing, light-wave communication (see Figure 1.1, left) has been and still is the driving force for the evolution of integrated optics.

The first experimental light-wave communication systems stem from the 1960s, the decade of the first semiconductor laser (1962)[2] and glass fiber (1966)[3]. The main advantages of glass fiber over alternative communication carriers, like coaxial cables, are the low losses (0.2 dB/km), zero dispersion, high bandwidth and low fabrication costs. The first two decades of the research in integrated optics were dominated by the development of the laser, and glass fiber, and the coupling between them. In more recent years research has been extended to fabrication of more complex components and the integration of various components. As examples, we mention the (de)multiplexers[4,5], ring lasers[6,7], optical receivers[8] and optical amplifiers[9,10]. Fabrication of these components in research laboratories is complicated and expensive, and, therefore, good simulations as part of the design process before product realization are required. This thesis describes such a simulation method.

There are several numerical and (semi-)analytical methods to model optical circuits. They differ, for instance, in the complexity of the configuration, the computational speed, accuracy and dimensionality (1-D, 2-D or 3-D). Well-known examples are mode solvers[11,12] (for analyzing straight and curved waveguides) and the Beam Propagation Method[13] (BPM) (for more general waveguiding and nonwaveguiding structures). Computer Aided Design (CAD) software is today used to integrate various numerical methods. Optical circuit designers use these software packages. At the Delft University of Technology, Leijtens *et al.*[14] adapted a professional microwave design system, Hewlett's Packard's MDS, for the CAD of optical chips. Most CAD software divides large optical circuits into the elementary components (waveguides,
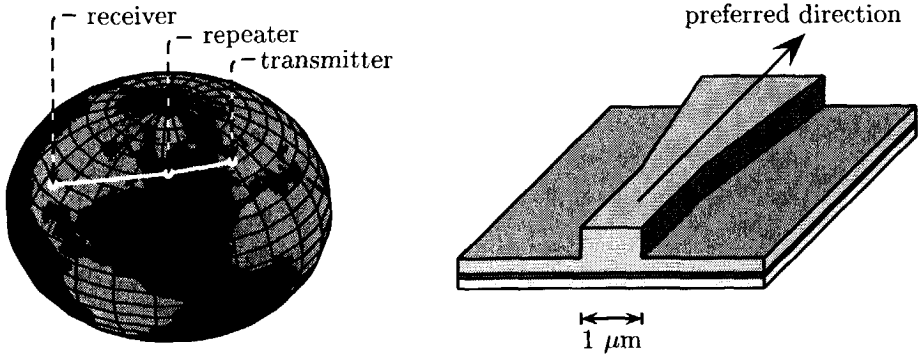
Figure 1.1: *Left: impression of an international optical fiber connection with light-wave telecommunication systems (transmitter, repeater and receiver). Right: example of an integrated optical component: a straight rib waveguide connected to a taper on a substrate.*

tapers, Y-junctions, etc.) or a subset of these components. The method described in this thesis is used to model these elementary components; one individual componentes or a few combined. Integrated optical components are sensitive to the state of polarization of the transmitted light. Thus, often, detailed information of electromagnetic fields in such components is needed in the design. As an example, Figure 1.1 (right) shows a straight waveguide connected to a taper. The light is expected to propagate mainly in one direction: the preferred or longitudinal direction.

1.1.2 Exploration seismics

Exploration seismics is a remote-sensing technique in which the aim is to record as detailed a picture as possible of the subsurface geology. One is, especially, interested in the location of the earth's minerals, among which are the fossil energy resources. The seismic data is acquired using a source and an array of geophones (the detectors or seismometers). The convential seismic source is the explosion of dynamite in a drilled shot hole at a depth of a few meters. In surface seismics (see Figure 1.2, right), the source and detectors are located at the earth's surface, while in cross-well seismics (or tomography, see Figure 1.2, left), the source is located in one bore hole and the detectors are located in at least one other bore hole. The sound waves — generated by the source — are scattered and radiated in the earth and recorded by the geophones. The interpretation of the events which appear on the measured seismic data, consists in identifying them as to their nature (i.e. reflection, refraction, etc.) and in determining the depth and cause of their origin. This helps the geophysicists with their structural mapping of the earth's subsurface.

In exploration seismics one is interested in an inverse problem: the field generated by the source and the measured field at the receiver are known, while the configu-

preferred direction   air
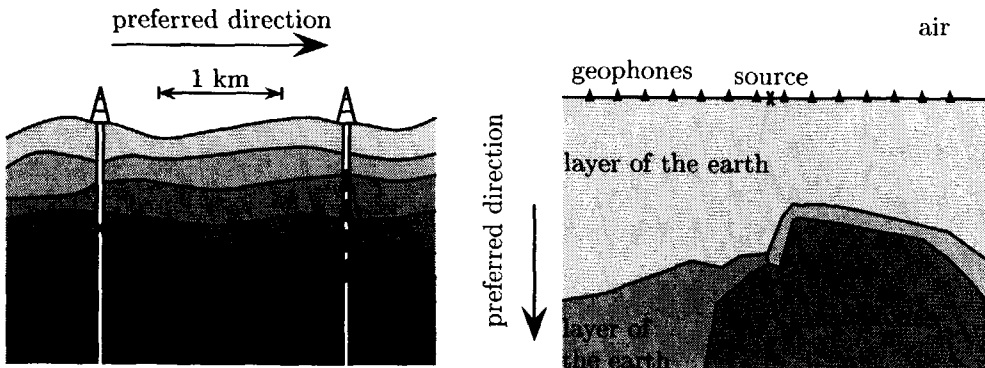
Figure 1.2:   *Left: cross-well seismics between two bore holes. Right: surface seismics above a salt dome.*

ration is unknown. A direct problem is mathematically simpler: the generated field and the configurations are known, but the field at the detectors is unknown. This thesis describes a numerical method for the direct problem. It is based upon separating different physical propagation phenomena, and therefore can be very useful in solving inverse problems.

In cross-well seismics, the preferred direction is along the earth's surface, the horizon. The layers of the earth trap the acoustic wave. However, in exploration seismics, the preferred direction is directed downwards — the vertical. In order to avoid this confusion, we use the more general expressions *longitudinal direction* for the preferred direction, and, the *transverse plane* for the plane perpendicular to the preferred direction. This nomenclature is commonly used in integrated optics.

For a survey on the theory on and methods in seismology, we refer to Aki and Richards[15].

1.1.3   Underwater acoustics

The water of the oceans covers three-quarters of our planet. It controls the earth to a greater degree than any other global system. Although mankind has been interested in the ocean since his early days, the oceans have still not revealed all their mysteries. In the exploration of the oceans, acoustics plays an important role, since low frequency sound has low absorption and acoustical information can propagate over long distances (thousands of kilometers, see Figure 1.3). There are reasons in abundance to explore the oceans are in abudance; for instance to monitor the greenhouse effect, earth's global warming by ocean tomography, to characterize the seabed, and to explore the ocean's resources (mineral, biological and others). Other applications come from the naval industry; detecting submarines is one example.

The ocean environments are described by the speed of sound which depends mainly (but gradually) on the depth in the ocean. As an example, in the North
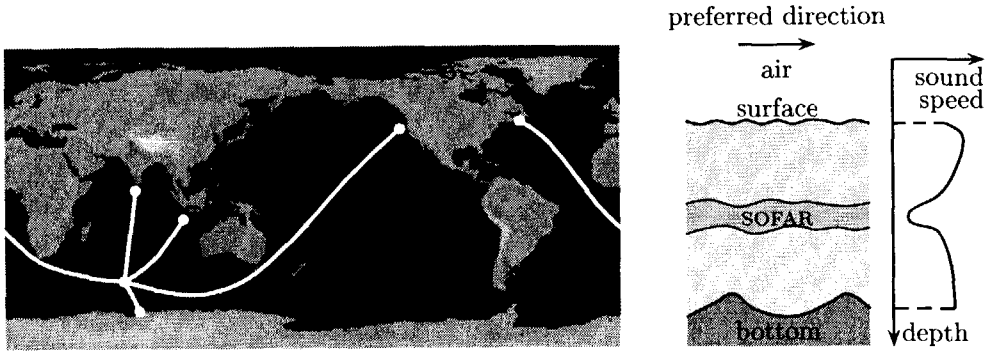
Figure 1.3: *Left: Example of long distance wave propagation in the oceans: the Heard Island experiment. The ray paths from the source to some receivers are indicated. Right: the sound speed dependence on the depth*

Atlantic ocean at equatorial and moderate latitudes, the speed of sound has a minimum at a depth of rather more than 1000 meters. This profile is due to the opposing effects of pressure and temperature. The sound energy can be trapped in this sound channel — in fact it is an acoustical waveguide —, so that very long-range propagation in the ocean is possible. The discoverers, Ewing and Worzel, named it the SOFAR (sound fixing and ranging) channel[16]. Near the surface, a sound channel can also occur, depending on the weather and climate. The surface mainly scatters sound, while the ocean bottom also absorbs sound.

In the ocean acoustics experiments, the main interest is in the wave propagation along the horizon; the direction of preference. Propagation distances are up to a half-round around the earth, and the ocean depths are mostly around four kilometer. Frequencies used for underwater acoustic experiments lie somewhere between 1 Hz and 10 kHz. The lower and upper limits are determined by the ability to generate sound and the absorption, respectively.

In late January 1991, the Heard Island Feasibility test (HIFT) was carried out to examine the use of ocean acoustic tomography to measure the possible warming rates of world's deep oceans. Signals from the 57 Hz acoustic source near Heard Island in the southern Indian Ocean were received at 16 sites worldwide (see Figure 1.3). The results of this experiment were published in a volume of the journal of Acoustical Society of America[17]. We mention this experiment to elucidate the possibilities of underwater acoustics.

Two interesting overviews of underwater acoustics and its techniques are given by Brekhovskikh and Lysanov[18] and by Tolstoy and Clay[19].

Figure 1.4:   *The right-handed Cartesian reference frame and the time.*

1.2   Basic equations and notation

We consider electromagnetic and acoustic waves[20] in matter occupying some sub-domain of the three-dimensional Euclidean background space $\mathbb{R}^3$ and all physical quantities as being functions of space and time. The position of observation is specified by the coordinates $\{x_1, x_2, x_3\}$ in a right-handed Cartesian reference frame with the origin $\{\mathcal{O}\}$ and the three mutually perpendicular base vectors $\{i_1, i_2, i_3\}$ of unit length each (see Figure 1.4). The nomenclature from the field of integrated optics is here used for the directions of these vectors: longitudinal (i_3), transverse (i_1) and also lateral (i_2) directions. The plane spanned by i_1 and i_2 is called the transverse plane. The symbol t represents the time of observation. The vectors and tensors that occur are usually given in subscript notation and the summation convention for repeated subscripts is understood. Unless otherwise specified, lower case Latin subscripts can take the values 1, 2 or 3. In this introductory chapter, the equations are also repeated in the classical vector notation, in which bold-faced symbols denote vectors. In particular, $x = x_1 i_1 + x_2 i_2 + x_3 i_3$ denotes the position vector. Partial differentiation with respect to x_m is denoted by ∂_m. The symbol ∂_t is a reserved symbol for partial differentiation with respect to time. The symmetrical unit tensor of rank 2 (Kronecker tensor) is defined by

$$\delta_{m,n} = \begin{cases} 1, & \text{if } m = n, \\ 0, & \text{if } m \neq n. \end{cases}$$

The completely anti-symmetrical unit tensor of rank 3 (Levi-Civita tensor) is defined by

$$\epsilon_{m,n,p} = \begin{cases} 1, & \text{if } \{m, n, p\} \text{ is an even permutation of } \{1, 2, 3\}, \\ 0, & \text{if not all subscripts are different}, \\ -1, & \text{if } \{m, n, p\} \text{ is an odd permutation of } \{1, 2, 3\}. \end{cases}$$

In our notation, $\epsilon_{m,n,p} A_n B_p$ denotes the outer product of vectors $\mathcal{A}$ and $\mathcal{B}$, while $A_n B_n$ denotes the inner product of $\mathcal{A}$ and $\mathcal{B}$. We employ the International System of Units (SI) for the representation of the electromagnetic and acoustic field quantities.

1.2.1   Maxwell's equations

The description of all electromagnetic problems are based upon Maxwell's two equations in the space-time domain $\{x_1, x_2, x_3, t\}$

$$- \epsilon_{k,m,p} \, \partial_m \mathcal{H}_p + \varepsilon_0 \, \partial_t \mathcal{E}_k \ = -\mathcal{J}_k^{\mathrm{mat}}, \tag{1.1}$$

$$\epsilon_{j,m,r} \, \partial_m \mathcal{E}_r + \mu_0 \, \partial_t \mathcal{H}_j = -\mathcal{K}_j^{\mathrm{mat}}, \tag{1.2}$$

or in vector notation

$$-\boldsymbol{\nabla} \times \boldsymbol{\mathcal{H}} + \varepsilon_0 \, \partial_t \boldsymbol{\mathcal{E}} \ = -\boldsymbol{\mathcal{J}}^{\mathrm{mat}}, \tag{1.1'}$$

$$\boldsymbol{\nabla} \times \boldsymbol{\mathcal{E}} + \mu_0 \, \partial_t \boldsymbol{\mathcal{H}} = -\boldsymbol{\mathcal{K}}^{\mathrm{mat}}, \tag{1.2'}$$

where

$$\mathcal{E}_r = \text{electric field strength (V/m)},$$
$$\mathcal{H}_p = \text{magnetic field strength (A/m)},$$
$$\mathcal{J}_k^{\mathrm{mat}} = \text{volume density of material electric current (A/m}^2),$$
$$\mathcal{K}_j^{\mathrm{mat}} = \text{volume density of material magnetic current (V/m}^2),$$
$$\varepsilon_0 = \mu_0^{-1} c_0^{-2} = \text{permittivity of vacuum (F/m)},$$
$$\mu_0 = \text{permeability of vacuum} = 4\pi \times 10^{-7} \text{ H/m, and,}$$
$$c_0 = \text{speed of light in vacuum } = 299792458 \text{ m/s.}$$

The dependence of the fields ($\mathcal{E}_r$, $\mathcal{H}_p$) and currents ($\mathcal{J}_k$, $\mathcal{K}_j$) on the space-time domain is not explicitly written. These six coupled partial differential equation were found experimentally in vacuum, for which the right-hand sides equal to zero ($\mathcal{J}_k^{\mathrm{mat}} = 0$, $\mathcal{K}_j^{\mathrm{mat}} = 0$). To account for the presence of matter the right-hand sides are split up into two contributions, a induced part and an external part, i.e.

$$\mathcal{J}_k^{\mathrm{mat}} = \mathcal{J}_k^{\mathrm{i}} + \mathcal{J}_k^{\mathrm{e}}, \qquad \boldsymbol{\mathcal{J}}^{\mathrm{mat}} = \boldsymbol{J}^{\mathrm{i}} + \boldsymbol{\mathcal{J}}^{\mathrm{e}}, \tag{1.3}$$

$$\mathcal{K}_j^{\mathrm{mat}} = \mathcal{K}_j^{\mathrm{i}} + \mathcal{K}_j^{\mathrm{e}}, \qquad \boldsymbol{\mathcal{K}}^{\mathrm{mat}} = \boldsymbol{K}^{\mathrm{i}} + \boldsymbol{\mathcal{K}}^{\mathrm{e}}, \tag{1.4}$$

where

$$\mathcal{J}_k^{\mathrm{i}} = \text{induced part of volume density of material electric current (A/m}^2),$$
$$\mathcal{J}_k^{\mathrm{e}} = \text{external part of volume density of material electric current (A/m}^2),$$
$$\mathcal{K}_j^{\mathrm{i}} = \text{induced part of volume density of material magnetic current (V/m}^2),$$

and

$$\mathcal{K}_j^{\mathrm{e}} = \text{external part of volume density of material magnetic current (V/m}^2).$$

The external parts describe the action of sources that generate the field and are assumed to be field independent. Traditionally, the induced parts are written as

$$\mathcal{J}_k^{\text{i}} = \mathcal{J}_k + \partial_t \mathcal{P}_k, \qquad \boldsymbol{\mathcal{J}}^{\text{i}} = \boldsymbol{\mathcal{J}} + \partial_t \boldsymbol{\mathcal{P}}, \qquad (1.5)$$

$$\mathcal{K}_j^{\text{i}} = \mu_0 \, \partial_t \mathcal{M}_j, \qquad \boldsymbol{\mathcal{K}}^{\text{i}} = \mu_0 \, \partial_t \boldsymbol{\mathcal{M}}, \qquad (1.6)$$

where

$$\mathcal{J}_k = \text{volume density of electric conduction current (A/m}^2),$$
$$\mathcal{P}_k = \text{electric polarization (C/m}^2), \text{ and,}$$
$$\mathcal{M}_j = \text{magnetization (A/m).}$$

Further, it is customary to introduce

$$\mathcal{D}_k = \varepsilon_0 \; \mathcal{E}_k + \mathcal{P}_k, \qquad \boldsymbol{\mathcal{D}} = \varepsilon_0 \; \boldsymbol{\mathcal{E}} + \boldsymbol{\mathcal{P}}, \qquad (1.7)$$

$$\mathcal{B}_j = \mu_0(\mathcal{H}_j + \mathcal{M}_j), \qquad \boldsymbol{\mathcal{B}} = \mu_0(\boldsymbol{\mathcal{H}} + \boldsymbol{\mathcal{M}}), \qquad (1.8)$$

where

$$\mathcal{D}_k = \text{electric flux density (C/m}^2), \text{ and,}$$
$$\mathcal{B}_j = \text{magnetic flux density (T).}$$

With the aid of the previous equations, Maxwell's equations, (1.1) and (1.2), can be rewritten as

$$- \epsilon_{k,m,p} \, \partial_m \mathcal{H}_p + \mathcal{J}_k + \partial_t \mathcal{D}_k = - \mathcal{J}_k^{\text{e}}, \qquad (1.9)$$

$$\epsilon_{j,m,r} \, \partial_m \mathcal{E}_r + \qquad \partial_t \mathcal{B}_j = - \mathcal{K}_j^{\text{e}}, \qquad (1.10)$$

or in vector notation

$$- \boldsymbol{\nabla} \times \boldsymbol{\mathcal{H}} + \boldsymbol{\mathcal{J}} + \partial_t \boldsymbol{\mathcal{D}} = - \boldsymbol{\mathcal{J}}^{\text{e}}, \qquad (1.9')$$

$$\boldsymbol{\nabla} \times \boldsymbol{\mathcal{E}} + \qquad \partial_t \boldsymbol{\mathcal{B}} = - \boldsymbol{\mathcal{K}}^{\text{e}}. \qquad (1.10')$$

These six equations contain 15 unknowns, namely the vectors $\mathcal{E}_r$, $\mathcal{H}_p$, $\mathcal{D}_k$, $\mathcal{B}_k$, $\mathcal{J}_j$. In order to be able to solve the electromagnetic problem, we need nine extra relations between the quantities $\mathcal{E}_r$, $\mathcal{H}_p$, $\mathcal{J}_k$, $\mathcal{D}_k$, $\mathcal{B}_j$. These relations contain the macroscopic media properties and are called the constitutive relations.

Constitutive relations

In this thesis, we choose of the standard form for the constitutive relations and write the introduced quantities $\mathcal{J}_k$, $\mathcal{D}_k$, $\mathcal{B}_j$ as functions of the electromagnetic field

quantities $\mathcal{E}_r$, $\mathcal{H}_p$. In almost all known materials, the quantities $\mathcal{J}_k$, $\mathcal{D}_k$, $\mathcal{B}_j$ depend only on one of the two electromagnetic field quantities

$$\mathcal{J}_k = \mathcal{J}_k(\mathcal{E}_r), \qquad \boldsymbol{\mathcal{J}} = \boldsymbol{\mathcal{J}}(\boldsymbol{\mathcal{E}}), \tag{1.11}$$

$$\mathcal{D}_k = \mathcal{D}_k(\mathcal{E}_r), \qquad \boldsymbol{\mathcal{D}} = \boldsymbol{\mathcal{D}}(\boldsymbol{\mathcal{E}}), \tag{1.12}$$

$$\mathcal{B}_j = \mathcal{B}_j(\mathcal{H}_p), \qquad \boldsymbol{\mathcal{B}} = \boldsymbol{\mathcal{B}}(\boldsymbol{\mathcal{H}}). \tag{1.13}$$

From experiments, these functions are determined and generally one makes a classification into different material properties: linear *vs.* nonlinear, time-invariant *vs.* time-variant, instantaneously reacting *vs.* relaxating, locally reacting *vs.* nonlocally reacting, homogeneous *vs.* inhomogeneous and isotropic *vs.* anisotropic.

Here, we assume that all media are **linear, time-invariant** and **locally reacting**. For such media the constitutive relations simplify into

$$\mathcal{J}_k(x_m, t) = \int_0^\infty \kappa_{k,r}^{(\sigma)}(x_m, t') \, \mathcal{E}_r\,(x_m, t - t') \, \mathrm{d}t', \tag{1.14}$$

$$\mathcal{D}_k(x_m, t) = \varepsilon_0 \mathcal{E}_k \; + \varepsilon_0 \int_0^\infty \kappa_{k,r}^{(\varepsilon)}(x_m, t') \, \mathcal{E}_r\,(x_m, t - t') \, \mathrm{d}t', \tag{1.15}$$

$$\mathcal{B}_j(x_m, t) = \mu_0 \mathcal{H}_j + \mu_0 \int_0^\infty \kappa_{j,p}^{(\mu)}(x_m, t') \, \mathcal{H}_p(x_m, t - t') \, \mathrm{d}t', \tag{1.16}$$

where

$$\kappa_{k,r}^{(\sigma)} = \text{conductivity relaxation tensor (S/(sm))},$$

$$\kappa_{k,r}^{(\varepsilon)} = \text{dielectric relaxation tensor (s}^{-1}\text{), and,}$$

$$\kappa_{j,p}^{(\mu)} = \text{magnetic relaxation tensor (s}^{-1}\text{)}.$$

If all media are also **instantaneously reacting**, the relaxation tensors become delta distributions with respect to time and the constitutive relations can be written as

$$\mathcal{J}_k(x_m) = \sigma_{k,r}(x_m) \, \mathcal{E}_r(x_m), \tag{1.17}$$

$$\mathcal{D}_k(x_m) = \varepsilon_{k,r}(x_m) \, \mathcal{E}_r(x_m), \tag{1.18}$$

$$\mathcal{B}_j(x_m) = \mu_{j,p}(x_m) \, \mathcal{H}_p(x_m), \tag{1.19}$$

where

$$\sigma_{k,r} = \text{conductivity tensor (S/m)},$$

$$\varepsilon_{k,r} = \text{permittivity tensor (F/m), and,}$$

$$\mu_{j,p} = \text{permeability tensor (H/m)},$$

are functions of the space coordinates only. If all media are also **isotropic**, the tensorial character of the conductivity, permittivity and permeability tensors vanishes

and the constitutive relations simplify to

$$\mathcal{J}_k(x_m) = \sigma(x_m)\,\mathcal{E}_k(x_m), \qquad \mathcal{J}(x) = \sigma(x)\,\mathcal{E}(x), \qquad (1.20)$$

$$\mathcal{D}_k(x_m) = \varepsilon(x_m)\,\mathcal{E}_k(x_m), \qquad \mathcal{D}(x) = \varepsilon(x)\,\mathcal{E}(x), \qquad (1.21)$$

$$\mathcal{B}_j(x_m) = \mu(x_m)\,\mathcal{H}_j(x_m), \qquad \mathcal{B}(x) = \mu(x)\,\mathcal{H}(x), \qquad (1.22)$$

where

$$\sigma = \text{conductivity (S/m)},$$
$$\varepsilon = \text{permittivity (F/m), and,}$$
$$\mu = \text{permeability (H/m).}$$

Boundary conditions

The boundary conditions interrelate the electromagnetic fields on both sides of an interface. The boundary conditions state that the tangential components of both the electric and magnetic field strength are continuous across an interface.

Time-Laplace transformation

All sources that generate the electromagnetic field are assumed to be switched on at an instant $t = t_0$. The causality condition requires all field quantities to be equal to zero in the time interval previous to $t = t_0$, and the time interval

$$T = \{t \in \mathbb{R} \,|\, t_0 < t < \infty\}, \qquad (1.23)$$

is the interval of primary interest.

The time-Laplace domain (or s-domain) representation $\hat{A}(x_1, x_2, x_3, s)$ of a time-varying field quantity $\mathcal{A}(x_1, x_2, x_3, t)$ is defined through the time-Laplace transformation

$$\hat{A}(x_1, x_2, x_3, s) = \int_{t_0}^{\infty} e^{-st} \mathcal{A}(x_1, x_2, x_3, t)\, dt, \qquad s \in \mathbb{C}. \qquad (1.24)$$

For physical (bounded) quantities, the integral is convergent for $\text{Re}(s) > 0$. In the s-domain, the time coordinate is eliminated from Maxwell's equations. As differentiation with respect to t has been replaced by multiplication by s (assuming zero-initial state), a field problem in space results, in which the transformation variable s occurs as a parameter. Causality of the field is taken into account by taking $\text{Re}(s) > 0$, and requiring that all field quantities are analytic functions of s in the right half of the complex s plane, $0 < \text{Re}(s) < \infty$. The inverse Laplace transformation is defined as

$$\mathcal{A}(x_1, x_2, x_3, t) = \frac{1}{2\pi j} \int_{-j\infty}^{j\infty} e^{st}\, \hat{A}(x_1, x_2, x_3, s)\, ds, \qquad (1.25)$$

in which j is the imaginary unit.

Maxwell's equations in the time-Laplace domain $\{x_1, x_2, x_3, s\}$ are

$$- \epsilon_{k,m,p} \, \partial_m \hat{H}_p + \hat{\eta}_{k,r} \hat{E}_r = -\hat{J}_k^e, \qquad (1.26)$$

$$\epsilon_{j,m,r} \, \partial_m \hat{E}_r + \hat{\zeta}_{j,p} \hat{H}_p = -\hat{K}_j^e, \qquad (1.27)$$

where

$\hat{\eta}_{k,r}(s) =$ transverse admittance per length (S/m)

$$= \begin{cases} s\varepsilon_0 \, \delta_{k,r} + s\varepsilon_0 \hat{\kappa}_{k,r}^{(\varepsilon)}(s) + \hat{\kappa}_{k,r}^{(\sigma)}(s), & \text{for general media,} \\ s\varepsilon_{k,r} + \sigma_{k,r}, & \text{for instantaneously reacting media,} \\ (s\varepsilon + \sigma) \, \delta_{k,r}, & \text{for isotropic instantaneously reacting media,} \end{cases}$$

$\hat{\zeta}_{j,p}(s) =$ longitudinal impedance per length (Ω/m)

$$= \begin{cases} s\mu_0 \, \delta_{j,p} + s\mu_0 \hat{\kappa}_{j,p}^{(\mu)}(s), & \text{for general media,} \\ s\mu_{j,p}, & \text{for instantaneously reacting media,} \\ s\mu \, \delta_{j,p}, & \text{for isotropic instantaneously reacting media,} \end{cases}$$

in which only the s-dependence is written explicitly. The transverse admittance and the longitudinal impedance are introduced to simplify the formulas.

At the imaginary s-axis in the s plane, the real and imaginary parts of the causal functions $\hat{\kappa}^{(\sigma, \varepsilon, \mu)}$ (and thus also $\hat{\sigma}_{k,r}$, $\hat{\varepsilon}_{k,r}$, $\hat{\mu}_{j,p}$ and $\hat{\sigma}$, $\hat{\varepsilon}$, $\hat{\mu}$) are interrelated by the Kramers-Kronig relations.

Steady-state analysis

In the steady-state analysis, all field quantities are assumed to depend harmonically on time with a common real angular frequency ω. Then, every real quantity $\mathcal{A}(x_1, x_2, x_3, t)$ is associated with the complex representation $\hat{A}(x_1, x_2, x_3, j\omega)$ through

$$\mathcal{A}(x_1, x_2, x_3, t) = \text{Re} \left[\hat{A}(x_1, x_2, x_3, j\omega) \, e^{j\omega t} \right]. \qquad (1.28)$$

Substitution of the complex quantities of the type $\hat{A}(x_1, x_2, x_3, j\omega) \, e^{j\omega t}$ in Maxwell's equations in the space-time domain yields, except for the common time factor $\exp(j\omega t)$, a set of equations identical to those in the Laplace domain with $s = j\omega$. Hence, we interpret the steady-state analysis as the limiting case

$$s = \lim_{\delta \downarrow 0} (j\omega + \delta). \qquad (1.29)$$

Thus, the fulfillment of the causality condition is assured. Since $\hat{A}(x_m, -j\omega) = \hat{A}^*(x_m, j\omega)$ (* denotes complex conjugation), we restrict our analysis in the thesis to positives values of ω.

Maxwell's equations in the space-frequency domain $\{x_1, x_2, x_3, j\omega\}$ read

$$- \epsilon_{k,m,p} \, \partial_m \hat{H}_p + \hat{\eta}_{k,r} \, \hat{E}_r = - \hat{J}_k^e, \tag{1.30}$$

$$\epsilon_{j,m,r} \, \partial_m \hat{E}_r + \hat{\zeta}_{j,p} \, \hat{H}_p = - \hat{K}_j^e. \tag{1.31}$$

We now discuss some properties of the transverse admittance $\hat{\eta}_{k,r}(j\omega)$ and the longitudinal impedance $\hat{\zeta}_{j,p}(j\omega)$ of isotropic and anisotropic dielectric media in more detail. Dielectrics are materials in which the permeability tensor is reduced to the scalar constant μ_0. The wavelength in vacuum equals $\lambda_0 = 2\pi c_0/\omega$.

Isotropic dielectrics

The transverse admittance is related to the complex permittivity $\hat{\varepsilon}$ as

$$\hat{\eta}(j\omega) = j\omega \, \hat{\varepsilon}(j\omega). \tag{1.32}$$

We now consider two kinds of isotropic dielectrics: relaxating without conduction and instantaneously reacting. The complex permittivity for relaxating dielectrics without conduction equals

$$\hat{\varepsilon}(j\omega) = \varepsilon_0 + \varepsilon_0 \, \hat{\kappa}^{(\varepsilon)}(j\omega), \tag{1.33}$$

while the complex permittivity for instantaneously reacting dielectrics is given by

$$\hat{\varepsilon}(j\omega) = \varepsilon + \frac{\sigma}{j\omega}. \tag{1.34}$$

In isotropic dielectrics, it is convenient to introduce the dimensionless relative permittivity as

$$\hat{\varepsilon}_r \overset{\text{def}}{=} \varepsilon_0^{-1} \hat{\varepsilon}, \tag{1.35}$$

and the dimensionless complex plane-wave index of refraction as

$$\hat{n} = n' - jn'' \overset{\text{def}}{=} \left(\frac{\hat{\varepsilon}}{\varepsilon_0} \right)^{1/2} = (\hat{\varepsilon}_r)^{1/2}. \tag{1.36}$$

From energy considerations we have

$$n'' \geq 0, \qquad \text{for passive media,}$$
$$n'' > 0, \qquad \text{for lossy media,}$$
$$n'' = 0, \qquad \text{for lossless media, and,}$$
$$n'' < 0, \qquad \text{for active media.}$$

The complex wave speed $\hat{c}$ in the medium equals

$$\hat{c} = c_0/\hat{n}. \tag{1.37}$$

The wave speed in lossless media equals

$$c = c_0/n'. \tag{1.38}$$
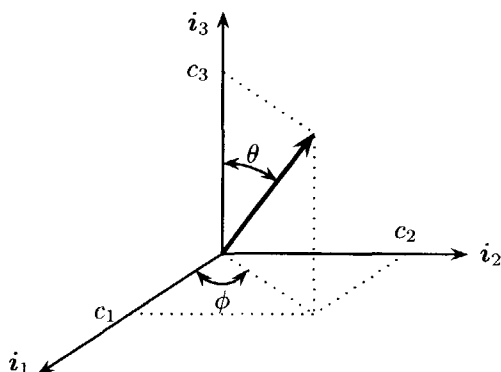
Figure 1.5: *The orientation of the optic axis within the Cartesian reference frame.*

Anisotropic media

The properties of anisotropic media are characterized by the principal values of the three material tensors: $\sigma_{k,r}$, $\varepsilon_{k,r}$ and $\mu_{j,p}$. We now assume that only the permittivity shows anisotropy and that no losses occur. In that case, $\varepsilon_{k,r}$ is a real and symmetric tensor, while the conductivity equals $\sigma_{k,r} = 0$ and the permeability equals $\mu_{j,p} = \mu_0 \delta_{j,p}$. The media under investigation are thus lossless anisotropic dielectrics. An important theorem of linear algebra states that any symmetric matrix can be diagonalized through a proper choice of basis vectors (principal directions). This diagonal matrix contains the three principal permittivities ($\varepsilon^{(1)}$, $\varepsilon^{(2)}$, $\varepsilon^{(3)}$). Based upon this, a classification of anisotropy can be made: biaxial, uniaxial and anaxial (isotropic). The corresponding crystal system are orthorhombic, monoclinic, triclinic (biaxial), tetragonal, trigonal, hexagonal (uniaxial), and cubic (anaxial), see Nye[21].

The second class of anisotropic media in optics, the uniaxial lossless dielectrics, are of special interest in this thesis, because of the later-introduced equivalent medium theory. The (uniaxial) permittivity is defined through

$$\varepsilon_{k,r} = \varepsilon^{(o)} \delta_{k,r} + (\varepsilon^{(e)} - \varepsilon^{(o)}) c_k c_r, \tag{1.39}$$

where

$$\varepsilon^{(o)} = \text{ordinary permittivity (F/m), and,}$$

$$\varepsilon^{(e)} = \text{extraordinary permittivity (F/m).}$$

It can be verified that the inverse $(\varepsilon^{-1})_{k,r}$ is given by

$$(\varepsilon^{-1})_{k,r} = \frac{1}{\varepsilon^{(o)}} \delta_{k,r} + \left(\frac{1}{\varepsilon^{(e)}} - \frac{1}{\varepsilon^{(o)}} \right) c_k c_r. \tag{1.40}$$

In (1.39), the optic or c-axis is chosen along the principal $(\varepsilon^{(e)})$ permittivity axis of the uniaxial dielectric medium, see Figure 1.5. The unit vector c_k along this c-axis has the components

$$
\begin{aligned}
c_1 &= \sin(\theta)\cos(\phi), \\
c_2 &= \sin(\theta)\sin(\phi), \\
c_3 &= \cos(\theta),
\end{aligned}
\tag{1.41}
$$

with $0 \le \theta < 2\pi$, $0 \le \phi < 2\pi$ and $c_k c_k = 1$. If the c-axis is along one of the Cartesian base vectors, the permittivity tensor simplifies into a diagonal tensor. If the c-axis is in the x_1, x_2 plane, we have equatorial uniaxial anisotropy. Its permittivity is found by taking $\theta = \pi/2$ ($c_1 = \cos(\phi)$, $c_2 = \sin(\phi)$ and $c_3 = 0$)

$$
\varepsilon = \begin{pmatrix}
\varepsilon^{(e)}\cos^2(\phi) + \varepsilon^{(o)}\sin^2(\phi) & (\varepsilon^{(e)} - \varepsilon^{(o)})\sin(\phi)\cos(\phi) & 0 \\
(\varepsilon^{(e)} - \varepsilon^{(o)})\sin(\phi)\cos(\phi) & \varepsilon^{(e)}\sin^2(\phi) + \varepsilon^{(o)}\cos^2(\phi) & 0 \\
0 & 0 & \varepsilon^{(o)}
\end{pmatrix}.
\tag{1.42}
$$

In equatorial anisotropic media, wave propagation with respect to the x_3 direction is reciprocal. In general, this type of reciprocal anisotropic media is obtained when $\hat{\eta}_{13}, \hat{\eta}_{23}, \hat{\eta}_{31}, \hat{\eta}_{32}, \hat{\zeta}_{13}, \hat{\zeta}_{23}, \hat{\zeta}_{31}, \hat{\zeta}_{32} = 0$.

Similar to isotropic dielectrics, the relative permittivity tensor is introduced as

$$
\varepsilon_{\mathrm{r};k,r} \stackrel{\mathrm{def}}{=} \varepsilon_0^{-1}\varepsilon_{k,r},
\tag{1.43}
$$

and the tensorial plane-wave index of refraction is defined through

$$
n_{k,r} \stackrel{\mathrm{def}}{=} \left(\frac{\varepsilon}{\varepsilon_0}\right)^{1/2}_{k,r}.
\tag{1.44}
$$

In the numerical implementation, we assume that only the permittivity shows anisotropy. If losses occur, this effect is taken into account by introducing a complex permittivity, as was done for isotropic media, see Equation (1.34).

Poynting vector

The transfer of electromagnetic power is governed by the Poynting vector $\mathcal{S}_m\,(\mathrm{W/m^2})$

$$
\mathcal{S}_m = \epsilon_{m,r,p}\mathcal{E}_r\mathcal{H}_p, \qquad \boldsymbol{\mathcal{S}} = \boldsymbol{\mathcal{E}} \times \boldsymbol{\mathcal{H}}.
\tag{1.45}
$$

The Poynting vector quantifies the amount of electromagnetic power flow per unit area. In the steady-state analysis, we define the time-averaged Poynting vector $\langle \mathcal{S}_m \rangle_T$ as the quantity $\mathcal{S}_m(x_m, t)$ averaged over a period T

$$
\langle \mathcal{S}_m \rangle_T = \frac{1}{T}\int_{t=t'}^{t'+T} \epsilon_{m,r,p}\mathcal{E}_r\mathcal{H}_p \,\mathrm{d}t, \qquad \langle \boldsymbol{\mathcal{S}} \rangle_T = \frac{1}{T}\int_{t=t'}^{t'+T} \boldsymbol{\mathcal{E}} \times \boldsymbol{\mathcal{H}} \,\mathrm{d}t.
\tag{1.46}
$$

Using the complex representation of the type of Equation (1.28), it follows that

$$\langle \mathcal{S}_m \rangle_T = \tfrac{1}{2} \text{Re} \left(\epsilon_{m,r,p} \hat{E}_r \hat{H}_p^* \right), \qquad \langle \boldsymbol{\mathcal{S}} \rangle_T = \tfrac{1}{2} \text{Re} \left(\hat{\boldsymbol{E}} \times \hat{\boldsymbol{H}}^* \right). \tag{1.47}$$

The vector $\hat{S}_m \stackrel{\text{def}}{=} \epsilon_{m,r,p} \hat{E}_r \hat{H}_p^*$ is known as the complex Poynting vector.

Integrating the x_3 component of the time-averaged Poynting vector, $\hat{S}_3$, over the $x_1 x_2$ plane yields the time-averaged power transferred through the $x_1 x_2$ plane at x_3 in one period T (*guided power along x_3*)

$$\langle P \rangle_T (x_3) = \tfrac{1}{2} \text{Re} \left[\int_{x_1 = -\infty}^{\infty} \int_{x_2 = -\infty}^{\infty} \hat{S}_3(x_1, x_2, x_3) \, \mathrm{d}x_1 \mathrm{d}x_2 \right]. \tag{1.48}$$

Polarized fields

In 2-D configurations (x_1 and x_3; invariance in x_2), Maxwell's equations decompose into two independent sets of equations, namely one for transverse electric fields (TE: $\{\hat{E}_2, \hat{H}_1, \hat{H}_3\} \neq 0$) and one for transverse magnetic fields (TM: $\{\hat{H}_2, \hat{E}_1, \hat{E}_3\} \neq 0$). It is common practice to make a comparable distinction for fields in 3-D configurations. Because Maxwell's equations cannot be decomposed into two independent sets — except in some special situations —, the fields have a hybrid character. These fields are classified according to their longitudinal components: quasi-TE polarized fields ($\hat{E}_3 \simeq 0$) and quasi-TM polarized fields ($\hat{H}_3 \simeq 0$).

1.2.2 Acoustic wave equations

The description of acoustic waves are based upon the equation of motion[20, 22]

$$\partial_k p + \dot{\Phi}_k = f_k, \tag{1.49}$$

and the deformation equation

$$\partial_k v_k - \dot{\Theta}^{\mathrm{i}} = q. \tag{1.50}$$

In these equations

$$p = \text{acoustic pressure (Pa)},$$
$$\dot{\Phi}_k = \text{mass-flow density rate (kg/m}^2\text{s}^2\text{)},$$
$$f_k = \text{volume source density of volume force (N/m}^3\text{)},$$
$$v_k = \text{particle velocity (m/s)},$$
$$\dot{\Theta}^{\mathrm{i}} = \text{induced part of the cubic dilatation rate (s}^{-1}\text{), and,}$$
$$q = \text{volume source density of injection rate (s}^{-1}\text{)}.$$

Acoustic constitutive relations

Here, we choose for the standard form for the constitutive relations and write the introduced quantities $\dot{\Phi}_k$ and $\dot{\Theta}^i$ as functions of the acoustic quantities v_k and p. These relations are established by a physical experiment. In this report we assume that all media are linear, time-invariant, instantaneously reacting, locally reacting and isotropic and inhomogeneous in their acoustic behavior. We then have

$$\dot{\Phi}_k(x_m, t) = \rho(x_m)\, D_t\, v_k(x_m, t), \tag{1.51}$$

and

$$\dot{\Theta}^i = -\kappa(x_m)\, D_t\, p(x_m, t), \tag{1.52}$$

where

$$\rho = \text{volume density of mass (kg/m}^3), \text{ and,}$$
$$\kappa = \text{compressibility (Pa}^{-1}),$$

are the constitutive coefficients and

$$D_t = \partial_t + v_k \partial_k, \tag{1.53}$$

is the time derivative that an observer experiences when co-moving with the fluid (with speed v_k). In a domain where the constitutive coefficients introduced here change with position, the fluid is inhomogeneous; in a domain where they are constant, the fluid is homogeneous.

Linearized basic acoustic wave equation

The system of equations that consists of the equation of motion, the deformation equation and the constitutive relations discussed in the previous subsection, is nonlinear in the particle velocity, due to the occurrence of the latter in the operator D_t of Equation (1.53). Fortunately, in seismic practice, the quantities associated with the acoustic wave-field are small-amplitude variations on the equilibrium state of the earth. Then, the results of sufficient accuracy are obtained by solving the linearized equations. Therefore, we shall employ Equations (1.51)-(1.52) in their low-velocity approximation, i.e., we replace D_t as defined by Equation (1.53) by

$$D_t = \partial_t. \tag{1.54}$$

The basic linearized acoustic wave equations are then given by

$$\partial_k p + \rho\, \partial_t v_k = f_k, \tag{1.55}$$

$$\partial_k v_k + \kappa\, \partial_t p = q. \tag{1.56}$$

Steady-state analysis

Analogous to the electromagnetic waves, a steady-state analysis is done for the acoustice wave equations. In this steady-state analysis, Equations (1.55) and (1.56) transform into

$$\partial_k \hat{p} + j\omega\rho\hat{v}_k = \hat{f}_k, \tag{1.57}$$

$$\partial_k \hat{v}_k + j\omega\kappa\hat{p} = \hat{q}. \tag{1.58}$$

Note that acoustic quantities κ and ρ are real valued, while the electromagnetic quantity $\hat{\varepsilon}_r$ can be complex valued.

Acoustic Poynting vector

The transfer of acoustic power is governed by the acoustic Poynting vector S_m (W/m^2)

$$S_m = p\,v_m. \tag{1.59}$$

In the steady-state analysis, we define the time averaged Poynting vector $\langle S_m \rangle_T$

$$\langle S_m \rangle_T = \frac{1}{T} \int_{t=t'}^{t'+T} p\,v_m \, \mathrm{d}t. \tag{1.60}$$

Using the complex representation of the type of Equation (1.28), it follows that

$$\langle S_m \rangle_T = \tfrac{1}{2}\mathrm{Re}\,(\hat{p}\,\hat{v}_m^*). \tag{1.61}$$

The vector $\hat{S}_m \stackrel{\text{def}}{=} \hat{p}\hat{v}_m^*$ is known as the complex acoustic Poynting vector.

1.3 Description of the configuration

The configurations under investigation are in principle arbitrary. Some restrictions, however, are dictated by the accuracy of the numerical implementation and the assumptions made in the mathematical analysis. In general, it is assumed that the wave propagates mainly in the preferred, longitudinal direction and that the area of interest is the paraxial region around the longitudinal axis. At this stage, however, we will not go in more detail about the validity and accuracy of various numerical approaches, which will be introduced later. In this section, the description of the configuration is explained by using an example from integrated optics.

In order to elucidate the description of the configuration under investigation, we consider the Y-junction in an integrated optics configuration as given in Figure 1.6. This Y-junction contains three main parts: ① the input waveguide $-\infty < x_3 < x_3^{(1)}$, ② the two branching waveguides $x_3^{(1)} < x_3 < x_3^{(\text{exit})}$ and ③ two exit waveguides
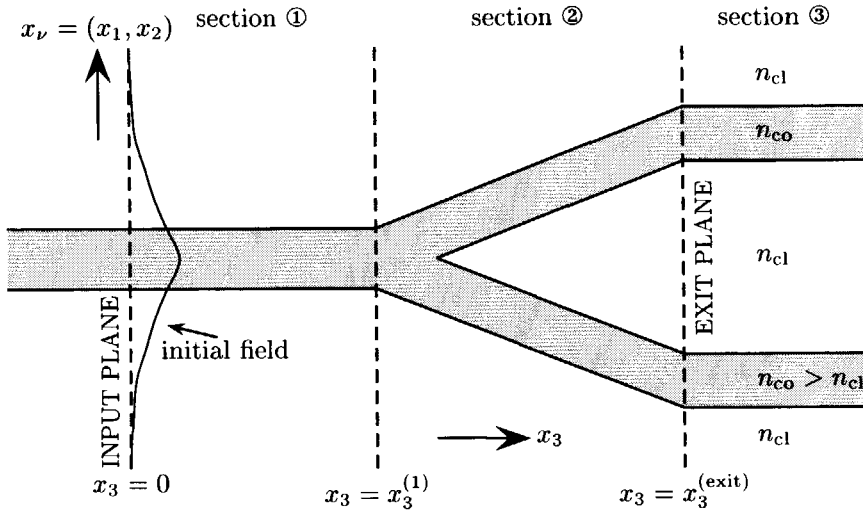
Figure 1.6: *A Y-junction as an example to elucidate the description of the configuration. The is given in the plane $x_3 = 0$.*

$x_3^{\text{exit}} < x_3 < \infty$. The core of the waveguide has a higher refractive index than the cladding ($n_{\text{co}} > n_{\text{cl}}$). It is clear that, in the first part, the preferred direction of the waves in the waveguide coincides with the waveguide orientation. The purpose of the second part is to split the light into two equal parts, each into one branching waveguide. In this part, the longitudinal direction cannot coincide with the orientation of both branches. The interest goes primarily to the light leaving the two branches at the output plane $x_3 = x_3^{(\text{exit})}$, but also to the light reflected backward towards the input plane $x_3 = 0$, and the light radiated away from the junction.

At first, a direction of preference is chosen based upon the configuration. This direction is chosen to coincide with the longitudinal direction. The orientation of the configuration is chosen such that this longitudinal direction coincides with the x_3-axis. In the case of the Y-junction, the preferred direction coincides with the input waveguide orientation. We assume that both on the left ($x_3 < 0$) and on the right ($x_3 > x_3^{(\text{exit})}$) side of the configuration under investigation, no reflection occurs and that the field vanishes at infinity. In the initial plane $x_3 = 0$, a field distribution belonging to the initial wave propagating to the right is prescribed.

For convenience in the mathematical analysis, we make a classification into three different classes of configurations based upon the properties of the configuration and well in order of increasing difficulty (for electromagnetic waves)

- isotropic dielectrics with invariance in the two transverse directions (1-D),

- isotropic dielectrics with invariance in one transverse direction only (x_2) (2-D),

- isotropic and anisotropic dielectrics (3-D).

Each class is treated in separate chapters: Chapter 2, Chapters 3-5, and Chapters 6-7, respectively. The mathematics for acoustic wave propagation in 1-D and 2-D configurations is equivalent to the electromagnetic counterpart, while in 3-D configurations it can be seen as a mathematical simplification of the 3-D electromagnetic wave propagation.

1.4 Overview of the directional wave-field decomposition

In this thesis, the directional wave-field decomposition, based upon the complete electromagnetic and acoustic field equations is introduced. The approach is linked with ideas in seismics and underwater acoustics. In this method, we assume that a direction of preference in the configuration can be chosen. In generalized waveguiding structures — such as in integrated optics, underwater acoustics and cross-well seismics — and transversely layered structures — such as in surface seismics — this can be the case. Figure 1.7 shows an example of a section of an arbitrarily nonuniform waveguiding structure, the origin of which can vary from the submicron scale, like parts of optoelectronic circuits, to the large scale of the earth's layer. In this figure, we show the three main steps of the procedure described here. First, the initial field at some reference plane is mathematically decomposed into waves traveling forward and backward with respect to the preferred direction. The interaction between the forward- and backward-propagating waves due to inhomogeneities in the (preferred) direction of propagation is then described by a generalized Bremmer coupling series: the first term (or *zeroth order* term) describes the forward-propagating wave, the second term describes the once-reflected wave, the third term describes the twice-reflected wave, and so forth. If the reflections can be neglected, only the first term corresponding to the direct wave needs to be determined and the scheme changes into a simple and fast initial-value problem, in which the longitudinal axis plays mathematically the role of a time axis. In general, a few terms of the generalized Bremmer coupling series must be taken into account. Finally, the forward- and backward-traveling waves are recomposed in the field at the desired positions. In the general case of a transverse inhomogeneous medium, this decomposition procedure involves the calculus of pseudo-differential operators (ΨDO) and Fourier integral operators (FIO)[23-29].

For a brief historical overview of the directional wave-field decomposition, we mention the early paper of Leontovich and Fock[30] (1946), who investigated electromagnetic wave propagation along the earth's surface. Their ideas on transforming the boundary value problem resulted in the parabolic approximation of the wave equation, which is a forward-directed scheme and is only valid for paraxial waves,

transverse directions
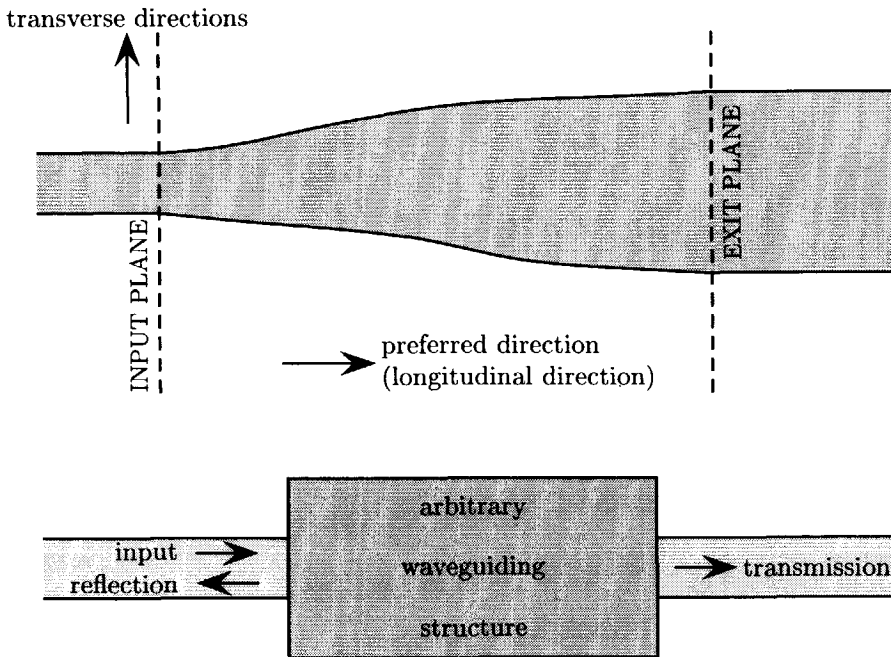
Figure 1.7:   *Section of a nonuniform waveguiding structure (upper). The purpose of the directional wave-field decomposition is to evaluate the electromagnetic field propagation in the direction of preference, and finally compute or estimate the transmission and reflection of the nonuniform waveguiding section (lower).*

i.e. waves propagating at a small angle with respect to the preferred direction. Their approximations resulted in a simple and also computationally fast algorithm.

In 1970, Claerbout[31] introduced the parabolic equation in seismics for both scalar and elastic wave propagation, and a few years later Hardin and Tappert[32] reported on the parabolic equation in underwater acoustics.

In the late 1970s, Feit and Fleck[33-35] developed their method which is also based upon the parabolic approximation, which they named the *Propagating Beam Method* (PBM). This method was first applied for the propagation of high energy laser beams through the atmosphere[36] and was later on introduced in integrated optics. The same method, but only renamed by the now more commonly used name *Beam Propagation Method* (BPM), was studied by van Roey[37,38], van der Donk[38-40], Lagasse[38,41,42] and Baets[41,42] in the early 1980s. Since then, the number of research

groups working on the BPM and related methods has increased enormously. In Section 1.5, more details about BPM-type methods are given.

Simultaneously and almost independently, directional wave-field decomposition methods were studied and developed by groups in the field of underwater acoustics and exploration geophysics. Our ideas stem from the Fishman and McCoy's papers[23, 24, 43–47] and de Hoop's thesis[48, 49]; They developed general methods based upon the directional wave-field decomposition, which include the interaction between the forward- and backward-propagating waves. In their schemes, the pseudo-differential operator calculus plays an important role. As a starting point, Fishman and McCoy split the Helmholtz equation into two one-way wave equations: one for forward- and one for backward-propagating waves. With the use of approximations in the Weyl symbol calculus for pseudo-differential operators[27, 28], they introduced the extended parabolic marching algorithms in terms of path integrals. In their more recent papers, they added the interaction between the counter-propagating waves and reported numerical results. In 1992, Brent and Fishman[50] derived a scheme based upon Maxwell's equations. More recent developments are the uniform expansion of the ΨDO, see Fishman, Gautesen and Sun[51], and the two-way wave marching algorithms based upon the Dirichlet-to-Neumann map[52], which can be seen as an alternative of the Bremmer series to include two-way wave propagation. De Hoop[48, 49] generalized the Bremmer series for transversely heterogeneous configurations. The Bremmer series is also discussed in this thesis. Haines and de Hoop[53] describe an invariant imbedding technique in which they carried out a factorization with respect to the direction of average power flow.

Another important area which, from a mathematical point of view, is related to directional wave-field decomposition is used in quantum mechanics. This is because of the formal similarity between the time-dependent Schrödinger equation and the parabolic wave equation or between the Klein-Gordon equation and the generalized one-way wave equation, see Kragl[54] and Lämmerzahl[55]. Other applications of the parabolic wave theory can be found in e.g. X-ray diffraction optics (see Kopylov et al.[56]).

1.5 Overview of the Beam Propagation Method

In designing optical communication network devices, powerful and flexible computational methods are needed to model general waveguiding structures. Such computational methods are directional decomposition methods. A well-known example is the Beam Propagation Method (BPM), which was introduced by Fleck, Morris and Feit[36] in 1976. At present, various numerical methods are built as computer-aided-design tools for optical system designers. The validity and accuracy of these tools, however, are limited and not always clear.

In this section, we discuss first the classical BPM for scalar fields. Subsequently, we discuss an extended scheme. With this in mind, an overview of the BPM and related methods is given.

Classical scalar (FFT-)BPM

The first Beam Propagation Methods were based upon the *parabolic* or *Fresnel*
approximation of the 2-D or 3-D *Helmholtz* equations. In order to elucidate this
method and the original idea of the BPM, we present a short, tutorial derivation
for scalar fields. These fields satisfy the scalar 2-D Helmholtz equation

$$\partial_3^2 \hat{\Psi} + \partial_1^2 \hat{\Psi} + \omega^2 c^{-2} \hat{\Psi} = 0. \tag{1.62}$$

This equation is derived from the Maxwell equations and holds, e.g., for TE-fields
($\hat{\Psi} = \hat{E}_2$, $\hat{H}_1$ or $\hat{H}_3$) in isotropic dielectric media with invariance in the x_2 direction.
Since the orientation of the waveguiding structure is mainly along the longitudinal
axis, the Helmholtz equation can be simplified. The classical BPM of Feit, Fleck
and Morris[33-36] contains two main steps

- construction of the Fresnel equation, and,

- application of the split-step algorithm.

For the construction of the Fresnel equation, the idea is to eliminate the *fast varying
phase* (or *axial phase*) term. The electromagnetic field is then split into a slowly
varying part, $\hat{\psi}$, and a fast varying part with respect to the x_3 direction

$$\hat{\Psi}(x_1, x_3) = \hat{\psi}(x_1, x_3) \ \exp(-j\omega c_{\text{ref}}^{-1} x_3), \tag{1.63}$$

in which c_{ref} is some reference value of the wave speed of the medium: $\hat{\psi}$ is the field
in a co-moving reference frame with speed c_{ref}. Substitution of this relation in the
Helmholtz equation and rearrangement result in

$$j\frac{c_{\text{ref}}}{2\omega}\partial_3^2\hat{\psi} + \partial_3\hat{\psi} = -j\omega\left(\frac{c^{-2} - c_{\text{ref}}^{-2}}{2c_{\text{ref}}^{-1}} + \frac{\partial_1^2}{2c_{\text{ref}}^{-1}\omega^2}\right)\hat{\psi}. \tag{1.64}$$

In the *slowly varying envelope approximation* (SVEA), it is then assumed that

$$\left\|j\frac{c_{\text{ref}}}{2\omega}\partial_3^2\hat{\psi}\right\| \ll \|\partial_3\hat{\psi}\| \tag{1.65}$$

This approximation is valid for wave propagation near the longitudinal axis in the
paraxial region. Neglecting the second derivative, changes the Helmholtz equation
into a parabolic equation, which is known as the *paraxial* or *Fresnel* equation

$$\partial_3\hat{\psi} \simeq -j\omega\left(\frac{c^{-2} - c_{\text{ref}}^{-2}}{2c_{\text{ref}}^{-1}} + \frac{\partial_1^2}{2c_{\text{ref}}^{-1}\omega^2}\right)\hat{\psi}$$

$$\overset{\text{def}}{=} -j\omega\left(\hat{\Gamma}_{\text{par}} - c_{\text{ref}}^{-1}\right)\hat{\psi}, \tag{1.66}$$

where we have introduced the operator $\hat{\Gamma}_{\text{par}}$. Returning to the original fast varying
quantity $\hat{\Psi}$, the Fresnel equation becomes

$$\partial_3\hat{\Psi} = -j\omega\hat{\Gamma}_{\text{par}} \ \hat{\Psi}. \tag{1.67}$$

The operator $\hat{\Gamma}_{\text{par}}$ contains three terms: first, the *phase correction* term (or *lens correction*), which does not involve the derivative ∂_1,

$$\hat{\Gamma}_{\text{par}}^{(1)}(x_1, x_3) = \frac{c^{-2}(x_1, x_3) - c_{\text{ref}}^{-2}}{2c_{\text{ref}}^{-1}}, \tag{1.68}$$

second, the *propagation* term, which is independent on the coordinates x_1 and x_3,

$$\hat{\Gamma}_{\text{par}}^{(2)}(\partial_1) = \frac{\partial_1^2}{2c_{\text{ref}}^{-1}\omega^2}, \tag{1.69}$$

and also c_{ref}^{-1}. Thus we have

$$\hat{\Gamma}_{\text{par}} = \hat{\Gamma}_{\text{par}}^{(1)} + \hat{\Gamma}_{\text{par}}^{(2)} + c_{\text{ref}}^{-1}. \tag{1.70}$$

Equation (1.66) contains only one first-order derivative with respect to the x_3 direction. Thus in Equation (1.66), x_3 plays physically the role of a time axis. In an x_3-invariant section, the forward propagation reads

$$\hat{\Psi}(x_1, x_3 + \Delta x_3) = \exp(-\text{j}\omega \Delta x_3 \hat{\Gamma}_{\text{par}}) \, \hat{\Psi}(x_1, x_3). \tag{1.71}$$

The exponent is called the propagator: *it propagates the field from x_3 to $x_3 + \Delta x_3$.* The operators $\hat{\Gamma}_{\text{par}}^{(1)}$ and $\hat{\Gamma}_{\text{par}}^{(2)}$, however, do not generally commute. This means

$$\exp(\hat{\Gamma}_{\text{par}}^{(1)} + \hat{\Gamma}_{\text{par}}^{(2)}) \neq \exp(\hat{\Gamma}_{\text{par}}^{(1)}) \exp(\hat{\Gamma}_{\text{par}}^{(2)}). \tag{1.72}$$

In the classical BPM, a higher approximate solution is then constructed by approximating this exponent with a symmetrized split-step, i.e.,

$$\hat{\psi}(x_1, x_3 + \Delta x_3) \approx \exp(-\tfrac{1}{2}\text{j}\omega \Delta x_3 \hat{\Gamma}_{\text{par}}^{(2)}) \exp(-\text{j}\omega \Delta x_3 \hat{\Gamma}_{\text{par}}^{(1)})$$
$$\exp(-\tfrac{1}{2}\text{j}\omega \Delta x_3 \hat{\Gamma}_{\text{par}}^{(2)}) \, \hat{\psi}(x_1, x_3), \quad (1.73)$$

which is recursively solved by marching through the configuration. The spatial operator $\exp(-\tfrac{1}{2}\text{j}\omega \Delta x_3 \hat{\Gamma}_{\text{par}}^{(2)})$ is numerically evaluated in the transverse Fourier domain with a fast Fourier transform (FFT). The operator $\exp(-\text{j}\omega \Delta x_3 \hat{\Gamma}_{\text{par}}^{(1)})$, which is called the lens correction, can be directly calculated and is evaluated half-way along the propagation step in order to improve the numerical accuracy. Due to the FFT routine, the solution becomes periodic in the transverse direction. Adjustable absorbing boundary conditions must prevent the light from traveling numerically from one window size to another. Bamberger, Coron and Ghidaglia[57] have mathematically analyzed this classical BPM.

Extended scalar BPM's

The forward-directed BPM scheme can be simply extended to wider angle schemes. To achieve this, we split the scalar Helmholtz equation into two one-way wave equations (the influence of the invariance in the x_3 direction is neglected) and write

$$(\partial_3 + j\omega\hat{\Gamma})\,\hat{\Psi}^{(+)} = 0, \tag{1.74}$$

$$(\partial_3 - j\omega\hat{\Gamma})\,\hat{\Psi}^{(-)} = 0, \tag{1.75}$$

which corresponds to the fields traveling forward ($\hat{\Psi}^{(+)}$) and backward ($\hat{\Psi}^{(-)}$). The operator $\hat{\Gamma}$ is given by $\hat{\Gamma} = (c^{-2} + \omega^{-2}\partial_1^2)^{1/2}$. The general recursive solution scheme for forward wave-fields, $\hat{\Psi}^{(+)}$, is found formally as

$$\hat{\Psi}^{(+)}(x_1, x_3 + \Delta x_3) = \exp(-j\omega\Delta x_3\hat{\Gamma})\,\hat{\Psi}^{(+)}(x_1, x_3). \tag{1.76}$$

The main problem of the extended scalar BPM in equation (1.76) is the way to tackle the *evolution operator* or propagator $\exp(-j\omega\Delta x_3\hat{\Gamma})$. This operator contains the *pseudo-differential operator* $\hat{\Gamma}$. Note that a first-order Taylor approximation of $\hat{\Gamma}$ with respect to c_{ref} and subsequent application of the split-step numerical solution method result in the classical (FFT-)BPM of Fleck, Morris and Feit.

Overview of the BPM and related methods

Besides Feit and Fleck, much pioneer work has been done by van Roey[37, 38], van der Donk[38–40], Lagasse[38, 41, 42] and Baets[41, 42]. In the early 1980s, the research was concentrated on the 2-D split-step algorithms, e.g., Thylèn[58, 59] and Yevick[59] introduced anisotropy in the scheme, Saijonmaa and Yevick[60] and Baets and Lagasse[41] applied the BPM to curved waveguides. In the second half of the 1980s, extensions to the split-step solution were sought: ① higher approximations of the operator $\hat{\Gamma}$ were applied (e.g. the extended Fresnel approximation of Feit and Fleck[33, 61]), ② the propagation steps were executed with a finite-difference (FD) or finite-element (FE) algorithm (see Yevick and Hermansson[62–64]) or ③ higher split-step algorithms were used (see Glassner, Yevick and Hermansson[65, 66]). However, despite of these extensions, great variations in the refractive index could not be tackled numerically accurately enough, except for very dense discretizations (in the order of 1000 points per wavelength). The resulting errors appear as numerical power leakage and are caused by the fact that the operators $\hat{\Gamma}_{\mathrm{par}}^{(1)}$ and $\hat{\Gamma}_{\mathrm{par}}^{(2)}$ are noncommuting.

A big breakthrough in numerical speed and the possibility to take into account the greater variation of the refractive index without numerical leakage came with the introduction of the Crank-Nicolson scheme (see Accornero *et al.*[67], Chung and Dagli[68], Scarmozzino and Osgood[69], Kim and Ramaswamy[70], Clauberg and von Allmen[71]). This finite-difference (FD) approximation was based upon the (1,1)

Padé approximation of the paraxial evolution operator after discretization, i.e.,

$$\hat{\psi}(x_1, x_3 + \Delta x_3) = (1 - j\omega \Delta x_3 \hat{\Gamma}_{\text{par}})^{-1}(1 + j\omega \Delta x_3 \hat{\Gamma}_{\text{par}}) \; \hat{\psi}(x_1, x_3).$$

(1.77)

This equation results in a tridiagonal system of linear equations for which the numerical implementation is simple and fast. Hadley[72,73] developed special transparent boundary conditions for this FD-BPM. This caused an increase in the popularity of the BPM among optical component designers. The validity of this FD-BPM, however, is still restricted to the paraxial region.

In recent years, various strategies have been developed in order

- to broaden the angle of validity (nonparaxiality),

- to include the vectorial nature of electromagnetic fields,

- to increase the numerical efficiency,

- to include reflections at plane interfaces and general continuous reflections,

- to compute modal properties of waveguides, and,

- to investigate curved waveguides.

The *angle of validity* can be increased by computing the evolution operator more accurately. The rigorous way is to find the local eigenvalues and eigenvectors of $\hat{\Gamma}$. There are several methods for the computation of the longitudinal spectrum of $\hat{\Gamma}$; all of them are very time consuming, especially when all the discrete modes and a great number of continuous modes are taken into account. In 2-D structures, this latter BPM-type approach is known under the name of Mode Expansion Method (MEM), see Willems, Haes and Baets[74,75] and Haes[76], Sztefka and Nolting[77]. Many BPM-type methods in optics are based upon rewriting the evolution operator such that a faster numerical scheme is possible. In general, a discretization in the form of a set basis functions is introduced. Thus, the operator $\hat{\Gamma}$ transforms into a matrix, the square of which is easily determined. We call this square the transverse Helmholtz operator (notation in this thesis: $\hat{A}$). The evolution operator can be calculated by first computing the eigenpairs of the transverse Helmholtz operator. If the basis functions are (some of) the local eigenmodes, the matrix representation of the transverse Helmholtz operator is diagonal. As a second example, the collocation method, which was introduced by Sharma, Bannerjee and Tanaje[78-82] in 2-D structures, uses the Hermite-Gauss basis functions. The matrix representation of the transverse Helmholtz operator is then small in size, but could be dense. Thylèn and Lee[83] proposed a method in which Fourier components (or plane waves) serve as the basis functions. The matrix representation of the transverse Helmholtz operator, however, is dense for high contrasts and the diagonalization procedure is time consuming. Another efficient and probably most used choice is when, for the basis

functions, triangular-type functions are used. This leads to a Crank-Nicolson finite difference approximation[67-71] or a Douglas finite difference approximation of $\hat{A}$ (see Sun and Yip[84]). In this way the transverse Helmholtz operator is a tridiagonal matrix. The evolution operator can be calculated by diagonalizing the transverse Helmholtz operator, as, e.g., in the methods of Lines (MoL), which is developed by Pregla, Gerdes, Kornatz, Ahlers, Rogge, Lunitz and Benish[85-89]. This is, however, a time-consuming task. In most situations, only a few eigenpairs are necessary. In the Lanczos method, as proposed by Ratowsky, Fleck and Fleck[90-92], Hermansson, Yevick, Bardyszewski and Glasner[93,94], and Liu and Li[95,96], only the most relevant eigenpairs are calculated approximately. Higher Padé approximations or other rational approximations of the evolution operator yield wider-angle propagation methods (see Hadley[97,98], Hoekstra, Krijnen and Lambeck[99-101], and Lee, Schulz, Voges and Glingener[102-104]). Splett, Majd and Petermann[105], Gonthier, Hénault and Lacroix[106] and Feit and Fleck[107] proposed a Taylor series expansion for the paraxial evolution operator in order to take higher contrasts into account. The validity of the Padé and Taylor expansion is restricted to the propagating waves; the evanescent waves cannot be correctly taken into account.

In principle, the *extension to (semi-)vectorial* BPM-type methods is straightforward. Vectorial BPM-type methods have been studied by many researchers, like Clauberg and von Allmen[71], Huang, Xu, Chaudhuri, Chu and Chrostowski[108-110], Li and Gomelsky[111], Yip and Noutsios[112], Li, van Brug and Frankena[113], and Rivera[114]. The main drawbacks of vectorial BPM-type methods are data storage and that they become very time consuming. Therefore, *numerically more efficient* methods are needed. Schmidt[115] proposed an adaptive approach to the scalar Fresnel's wave equation. Kunz, Zimulinda and Heinlein[116] use a split-step solution which reduces the problem to simple equations with tridiagonal matrices, which can be solved fast.

To date, most BPM-type methods are only forwardly directed. In many applications, the influence of *reflections*, however, is important. Recently, it has been shown that reflections in standard devices today, such as MMIs, may play an important role, see Pennings et al.[117]. In addition, the Fabry-Perot laser operates by virtue of the reflection (approximately 30%) at the laser facets. It is therefore a surprise that only a few numerical methods have been developed to include backward-traveling waves and the interaction between the counterpropagating waves. We mention Kaczmarski, Lagasse[118], Lin and Korpel[119] and Yevick, Bardyszewski, Hermansson and Glasner[120]. And we would also like to mention the bidirectional Mode Expansion Method, see Haes[76], Sztefka and Nolting[77]. Smartt, Benson and Kendall[121] analyzed waveguide discontinuities along the longitudinal direction, e.g., junctions and laser facets.

In order to include the interaction between the counter-propagating waves, alternative methods have been developed. These methods are not based upon a directional wave-field decomposition, although they are used for typical waveguiding structures. We mention Martin, Dereux and Girard's method[122]; they used an iterative scheme for determining the Green's function of configuration, and Hadley[123],

who applied a finite difference scheme directely to the Helmholtz equation.

Several techniques, which have been based upon the BPM, are developed to analyze the *modal properties* of waveguides. Feit and Fleck[35] used a spectral method to extract the modal propagation constants and the modal eigenfunctions. Hawkins introduced the imaginary distance BPM. Wijnands *et al.* used the same method[124] and extended it to waveguides with nonlinear materials[125, 126]. There are two slightly different versions: the Inverse Iteration Method and the Power Method. These methods are powerful and useful because of the transparant boundary conditions.

One of the key components on integrated optical chips are *waveguiding bends*. These curved waveguides can also be analyzed with the BPM. Recently, Rivera[114] developed a vectorial BPM for general curving waveguides, such as S-bends. He formulated the BPM in a local coordinate system. In Figure 1.8, we show a numerical example of the BPM for curved waveguides.

Some BPM-type methods have also been extended to time-domain and nonlinear problems. We mention Schulz, Glingener, Nöker, Voges[127], Huang, Xu and Chaudhuri[128], Gomelsky and Liu[129] and Wijnands, Hoekstra, Krijnen and de Ridder[125] and Krijnen[130].

In the last decade, hundreds of papers were published about the BPM. In this overview we refer only to a few important papers.

In the present thesis, we describe a directional wave-field decomposition, which can be seen as a bidirectional and wide-angle extension of the BPM-type methods discussed above. In the general frame of directional wave-field decomposition, all above BPM-type methods can be placed. It gives us a better understanding of such methods. We use a Bremmer series to include the interaction between the counter-propagating waves. We discuss pseudo-differential operators to give a new insight in wave-field propagation. We build a numerical Bremmer scheme based upon rational approximations.

1.6   Organization of the thesis

In addition this introductory chapter, the thesis contains seven other chapters. The thesis discusses the directional wave-field decomposition in a 1-D, 2-D and 3-D electromagnetic and acoustic configuration.

Chapter 2 is devoted to the 1-D configuration. It introduces the description of the scattering problem along the longitudinal (preferred) direction. For this purpose, we use the Bremmer series. A new fast numerical implementation is introduced. The implementation is the same for higher dimensions and can thus easily be extended.

Chapter 3 extends the theory to two dimensions. For the scattering problem along the longitudinal direction the Bremmer series is employed. The numerical implementation is analogeous to the 1-D case. The scattering problem in the transverse direction is described by the slowness operator.

This operator is a square root operator and is of the class of pseudo-differential operators. In **Chapter 4**, the theory of pseudo-differential operators is summarized
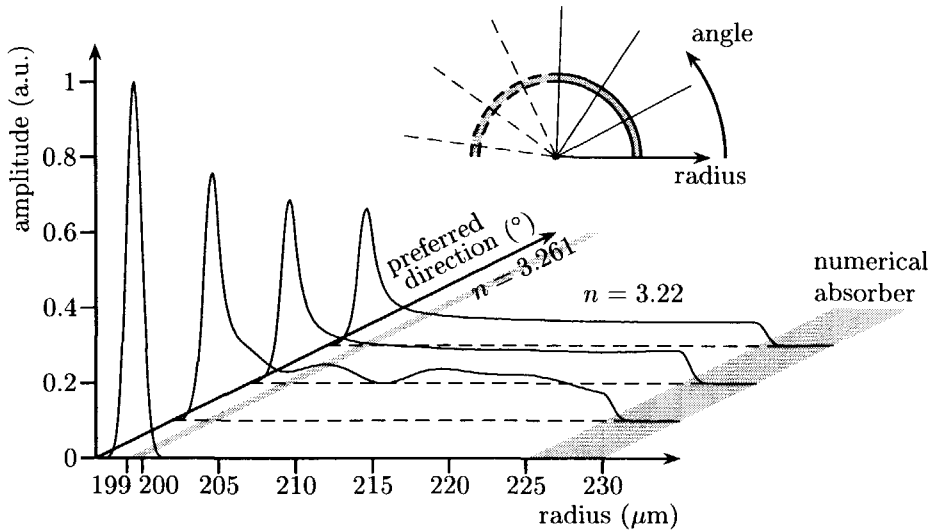
Figure 1.8: *Evaluation of a Gaussian beam propagating through a bent wave-guide. Computations were done with a 2-D Lanczos-BPM in polar coordinates. The wavelength in vacuo is 1.3 μm. The refractive indices are 3.261 (inside) and 3.22 (outside). The outer radius is 200 μm, the waveguide width is 1 μm. At the outer region (between 225 μm and 230 μm), a numerical absorber was positioned. The step size is 0.01 radian. The plots are made after 50 steps (28.6°). Prof. Dr. Gy. Veszely is acknowledged for the computations.*

and discussed. It, basicly, extends the Fourier analysis for longitudinal invariant structures to longitudinal variant structures. Special attention is paid to the relation between the theory on pseudo-differential operators and the modal analysis of slab waveguides. Subsequently, we go into more detail about the pseudo-differential operators for two special configurations: the quadratic profile waveguide and the symmetric step-index slab waveguide. These configurations are intended to elucidate the calculus of pseudo-differential operators.

Chapter 5 discusses the numerical implementation of the Bremmer series using rational approximations for the square root operator (longitudinal slowness), the propagator and the transverse derivatives. Using an optimization procedure, a higher degree of accuracy for wide-angle one-way wave propagation is reached. Numerical results are presented.

Chapter 6 extends the theory of Chapters 2 and 3 to a 3-D configuration with anisotropic media. In this chapter, special attention is paid to stabilizing the numerical scheme.

Chapter 7 extends the numerical implementation given in Chapter 5 to a 3-D configuration. The numerical implementation is based upon rational approximations. The transverse plane is discretized on a hexagonal grid in order to minimize

the transverse artificial anisotropy. Using optimization procedures similar in Chapter 5, a higher degree of accuracy is obtained for wide-angle one-way wave propagation. Some different approaches are followed and argued in the text. Numerical results are presented.

The last chapter, **Chapter 8**, is devoted to the conclusions and discussion.

All chapters are self-contained and can be read separately. Cross-links are used to elucidate the extension from 1-D to 2-D and 3-D, and from 2-D to 3-D. Some chapters go into more detail on one subject than other chapters. We advise the reader who has no experience with the concept of directional wave-field decomposition to start with Chapter 2.

CHAPTER 2

Directional Wave-Field Decomposition in a One-dimensional, Isotropic, Dielectric Configuration

In directional wave-field decomposition, a solution is constructed by separately treating the problem along the preferred direction and in the directions perpendicular to it. By doing so, the problem along the preferred direction becomes relatively simple. However, one has to take the scattering problem in the transverse plane into account. Before discussing this, we use this chapter to explain the longitudinal scattering problem in a *one-dimensional* isotropic configuration, in which the scattering problem in the transverse plane is not present. We choose to solve the longitudinal scattering problem with the Bremmer series. This chapter deals with the electromagnetic quantities. The acoustic equivalent is found by a simple substitution.

The chapter is organized as follows. After describing the configuration in Section 2.1, we rewrite the Maxwell equations into a differential equation for the field matrix (Section 2.2). Application of the directional decomposition introduces the wave matrix. Its differential equation (Section 2.3) are transformed into an integral equation (Section 2.4). Some special attention is given to the reflection properties at a single interface. Subsequently, the numerical aspects (Section 2.5) and some numerical results are discussed (Section 2.6). Finally, the results are discussed in Section 2.7.
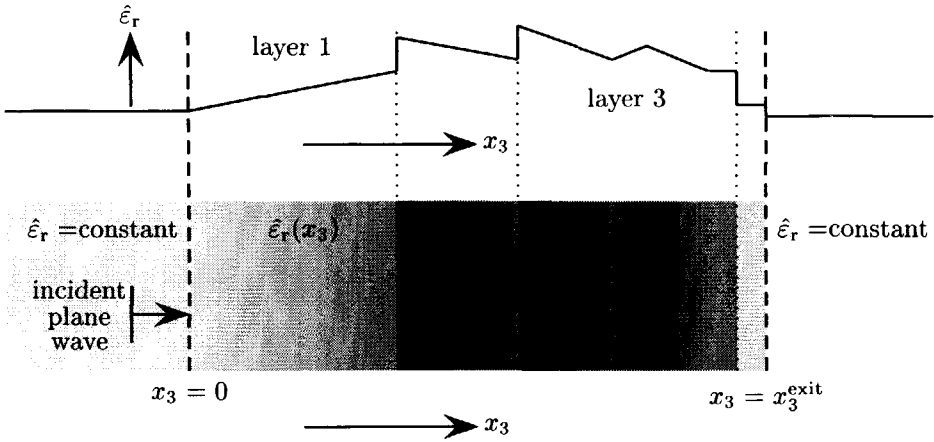
Figure 2.1: *An example of a one-dimensional configuration under investigation.*

2.1 Description of the configuration

A typical example of the configurations under investigation is illustrated in Figure 2.1. This configuration is used only to demonstrate the scattering problem in the preferred x_3 direction. Therefore, the configuration is assumed to be isotropic, source free and invariant in the transverse x_1, x_2 plane. This invariance means that the configuration under investigation is a planarily layered medium. These layers might be inhomogeneous with respect to the preferred direction. We assume that these layers are sandwiched between two homogeneous half-spaces, one at $x_3 \leq 0$ and one at $x_3 \geq x_3^{\text{exit}}$. Thus, no reflections occur outside the region of interest, $0 < x_3 < x_3^{\text{exit}}$.

The purpose of our method is to find the field at the exit plane $x_3 = x_3^{\text{exit}}$ and at the incident plane $x_3 = 0$, while the field corresponding to an incident plane wave at $x_3 = 0$ is given. This plane wave propagates in the preferred direction. Besides, one is interested in the field inside the configuration in order to facilitate the design of optical components.

2.2 Differential equation for the field matrix

In this section, Maxwell's equations are rewritten into a form suitable for the directional wave-field decomposition. Subsequently, we list the corresponding quantities for acoustic wave propagation. Finally, we compare the longitudinal slowness and the wave number.

In a source-free isotropic configuration with invariance in the transverse plane $(\partial_1, \partial_2 \equiv 0)$, the Maxwell's equations in the frequency domain, (1.30) and (1.31),

simplify into

$$\partial_3 \hat{E}_2 - j\omega\mu_0 \hat{H}_1 = 0, \tag{2.1}$$

$$\partial_3 \hat{H}_1 - j\omega\hat{\varepsilon}\hat{E}_2 = 0, \tag{2.2}$$

for transverse electric (TE) fields and an equivalent set of equations for the components $\{\hat{H}_2, \hat{E}_1\}$ for transverse magnetic (TM) fields. Here, we discuss the case of TE fields in order to link up in notation with the next chapter. The resulting equations contain only the field components which are perpendicular to the preferred direction. The complex Poynting vector has only a component in that direction, $\hat{S}_3 = -\hat{E}_2 \hat{H}_1^*$. The propagation is thus along the preferred axis. The field components are organized in the field matrix $\hat{F}_I$ as

$$\hat{F} = \begin{pmatrix} \hat{E}_2 \\ -\hat{H}_1 \end{pmatrix}. \tag{2.3}$$

Due to this choice, the complex Poynting vector component along the preferred direction equals $\hat{S}_3 = \hat{F}_1 \hat{F}_2^*$. The resulting differential equation for the field matrix is written as

$$\partial_3 \hat{F}_I + j\omega \hat{A}_{I,J} \hat{F}_J = 0, \tag{2.4}$$

in which the electromagnetic system matrix $A_{I,J}$ is given by

$$\hat{A}_{1,1}(x_3) = 0,$$
$$\hat{A}_{1,2}(x_3) = \mu_0,$$
$$\hat{A}_{2,1}(x_3) = \hat{\varepsilon}(x_3),$$
$$\hat{A}_{2,2}(x_3) = 0.$$

This equation is often referred to as a two-way wave equation. Since matrix $\hat{A}_{I,J}$ depends on x_3, we cannot construct a simple analytic solution. For further computations it is more convenient to introduce the wave matrix.

Acoustic field matrix and system matrix

When starting with the complex acoustic wave equations, one introduces the field matrix $\hat{F}_I$ as

$$\hat{F} = \begin{pmatrix} \hat{p} \\ \hat{v}_3 \end{pmatrix}. \tag{2.5}$$

Now, the acoustic Poynting vector $\hat{S}_m$ also has only one component along the positive x_3 direction: $\hat{S}_3 = \hat{F}_1 \hat{F}_2^* = \hat{p}\hat{v}_3^*$, while $\hat{S}_1 = \hat{S}_2 = 0$. The nonzero elements of the system matrix $\hat{A}_{I,J}$ are

$$\hat{A}_{1,2}(x_3) = \rho(x_3),$$
$$\hat{A}_{2,1}(x_3) = \kappa(x_3).$$

Relation between the longitudinal slowness and the wave number

It is customary in exploration seismics to extract $s = j\omega$ from the system matrix. The square root of $\hat{A}_{2,1}\hat{A}_{1,2} = \mu_0\hat{\varepsilon}$ can be interpreted as a longitudinal slowness[20] $\hat{\gamma}$

$$\hat{\gamma}(x_3) \overset{\text{def}}{=} (\hat{A}_{2,1}\hat{A}_{1,2})^{1/2}(x_3) = [\mu_0\hat{\varepsilon}(x_3)]^{1/2}\,, \tag{2.6}$$

and is the reciprocal of the complex wave speed $\hat{c} = (\mu_0\varepsilon)^{-1/2}$ of the medium

$$\hat{\gamma}(x_3) = \hat{c}^{-1}(x_3). \tag{2.7}$$

In the field of integrated optics the (longitudinal) wave number (k_3) is also often used

$$k_3 = k_0\hat{n} = k_0\hat{\varepsilon}_r^{1/2}. \tag{2.8}$$

Here $k_0 = \omega\sqrt{\varepsilon_0\mu_0}$ is the wave number in vacuum and is the reciprocal of the free-space wavelength $\lambda_0 = 2\pi/k_0$. It is customary to normalize the longitudinal wave number as k_3/k_0, which equals the refractive index $\hat{n}$. The relation between the longitudinal wave number and the longitudinal slowness is (taking $\omega > 0$)

$$k_3 = \omega\hat{\gamma}. \tag{2.9}$$

Note that the quantities $\hat{\gamma}$ and $\hat{c}$ have the physical meaning of slowness and wave speed, respectively, only when dealing with lossless media.

2.3   Differential equation for the wave matrix

In this section, the field is decomposed into forward- and backward-traveling waves with respect to the preferred direction x_3.

The two-way wave equation can be transformed into a one-way wave equation by diagonalizing the matrix $\hat{A}_{I,J}$

$$\hat{A}_{I,J}\hat{L}_{J,M} = \hat{L}_{I,J}\hat{\Lambda}_{J,M}. \tag{2.10}$$

Thus, the elements of the diagonal matrix $\hat{\Lambda}_{J,M}$ are the longitudinal slownesses $\pm\hat{\gamma}$

$$\hat{\Lambda} = \begin{pmatrix} \hat{\gamma} & 0 \\ 0 & -\hat{\gamma} \end{pmatrix}. \tag{2.11}$$

The matrix $\hat{L}_{J,M}$ is called the composition matrix, while its inverse is called the decomposition matrix.

This diagonalization is the fundamental step in the directional wave-field decomposition. By applying it, the field is decomposed into a wave $\hat{W}_1 = \hat{W}^{(+)}(x_3)$ physically traveling in the positive x_3 direction and a wave $\hat{W}_2 = \hat{W}^{(-)}(x_3)$ physically traveling in the negative x_3 direction (see Figure 2.2). These waves are gathered
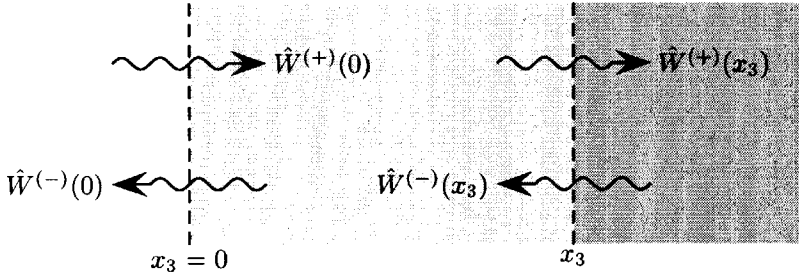
Figure 2.2:   Wave $\hat{W}^{(+)}$ propagates in the positive x_3-direction, while wave $\hat{W}^{(-)}$ propagates in the negative x_3-direction.

in the wave matrix, which is defined through

$$\hat{W}_I = (\hat{L}^{-1})_{I,J}\hat{F}_J. \tag{2.12}$$

The resulting differential equation for the wave matrix is given by

$$\partial_3\hat{W}_I + j\omega\hat{\Lambda}_{I,M}\hat{W}_M = -(\hat{L}^{-1})_{I,J}(\partial_3\hat{L}_{J,M})\hat{W}_M. \tag{2.13}$$

This equation is often called coupled set of two one-way wave equations. The coupling matrix $-(\hat{L}^{-1})_{I,J}(\partial_3\hat{L}_{J,M})$ has the general form

$$-\hat{L}^{-1}(\partial_3\hat{L}) = \begin{pmatrix} \hat{T} & \hat{R} \\ \hat{R} & \hat{T} \end{pmatrix}, \tag{2.14}$$

in which $\hat{T}$ and $\hat{R}$ represent a transmission[a] and reflection coefficient, respectively. The coefficients $\hat{T}$ and $\hat{R}$ vanish in homogeneous layers. This demonstrates that the two wave matrix components represent forward and backward waves, independently propagating in a homogeneous layer[23]. The following subsection contains more detailed discussion on these reflection and transmission coefficients.

The columns of the composition equation can be constructed, noting that the normalization of the wave matrix is still a degree of freedom. In this chapter, we made the following choice

$$\hat{L} = \begin{pmatrix} 1 & 1 \\ \hat{y} & -\hat{y} \end{pmatrix}, \qquad \hat{L}^{-1} = \frac{1}{2}\begin{pmatrix} 1 & \hat{y}^{-1} \\ 1 & -\hat{y}^{-1} \end{pmatrix}, \tag{2.15}$$

where $\hat{y}$ is the admittance

$$\hat{y} = \hat{A}_{1,2}^{-1}\hat{\gamma}. \tag{2.16}$$

---

[a]Note that within this definition of the transmission coefficient, $\hat{T} = 0$ if the medium is constant.

The above choice is called the *electric-field strength normalization*[b] (EFN), because we find that the electric field $\hat{F}_1$ is the sum of the two wave matrices

$$\hat{F}_1 = \left(\hat{W}^{(+)} + \hat{W}^{(-)}\right),$$ (2.17)

while the magnetic field $\hat{F}_2$ depends on the local admittance $\hat{y}$

$$\hat{F}_2 = \hat{y}\left(\hat{W}^{(+)} - \hat{W}^{(-)}\right).$$ (2.18)

Note that two elements of the composition matrix depend on x_3. The final results are independent of the chosen normalization. Some more discussion about the normalization will be held for the 2D and 3D configurations. With our choice for the normalization we have for the wave matrix

$$\hat{W}^{(+)} = \tfrac{1}{2}\left(\hat{F}_1 + \hat{y}^{-1}\hat{F}_2\right),$$ (2.19)

$$\hat{W}^{(-)} = \tfrac{1}{2}\left(\hat{F}_1 - \hat{y}^{-1}\hat{F}_2\right),$$ (2.20)

while the transmission and reflection coefficients are found as

$$\hat{T} = -\hat{R} = -\tfrac{1}{2}\hat{y}^{-1}\partial_3\hat{y} = -\tfrac{1}{2}\hat{\gamma}^{-1}\partial_3\hat{\gamma} = -\tfrac{1}{2}\hat{n}^{-1}\partial_3\hat{n}.$$ (2.21)

The wave matrix differential equation is a coupled set of two one-way wave equations (compare with (2.13))

$$\partial_3\hat{W}^{(+)} + j\omega\,\hat{\gamma}\hat{W}^{(+)} = \hat{T}\hat{W}^{(+)} + \hat{R}\hat{W}^{(-)},$$ (2.22)

$$\partial_3\hat{W}^{(-)} - j\omega\,\hat{\gamma}\hat{W}^{(-)} = \hat{R}\hat{W}^{(+)} + \hat{T}\hat{W}^{(-)}.$$ (2.23)

Reflection and transmission coefficients at an interface

Some special attention must be given to media with discontinuities in their medium properties. Let us consider a single interface, as depicted in Figure 2.3. We denote the waves on the left-hand side of the interface as $\hat{W}_{\text{left}}^{(\pm)}$ and on the right-hand side as $\hat{W}_{\text{right}}^{(\pm)}$. In a similar way we define n_{left} and n_{right} as the refractive indices on the left-hand side and on right-hand side of the interface, respectively. At the interface we have in the sense of generalized functions

$$\hat{W}_{\text{interface}}^{(\pm)} = \tfrac{1}{2}\left(\hat{W}_{\text{left}}^{(\pm)} + \hat{W}_{\text{right}}^{(\pm)}\right),$$ (2.24)

$$\hat{n}_{\text{interface}} = \tfrac{1}{2}\left(\hat{n}_{\text{left}} + \hat{n}_{\text{right}}\right),$$ (2.25)

$$\hat{T} = -\hat{R} = \frac{\hat{n}_{\text{left}} - \hat{n}_{\text{right}}}{\hat{n}_{\text{left}} + \hat{n}_{\text{right}}}\,\delta(x_3) = T'\delta(x_3).$$ (2.26)

---

[b]For acoustic waves, it is called the acoustic-pressure normalization.
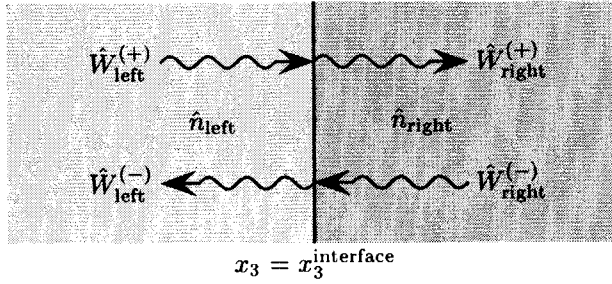
$$x_3 = x_3^{\text{interface}}$$

Figure 2.3: *Interface between two media. The notation used in the text is indicated.*

Here $\hat{T}'$ is introduced as

$$\hat{T}' = -\hat{R}' = \frac{\hat{n}_{\text{left}} - \hat{n}_{\text{right}}}{\hat{n}_{\text{left}} + \hat{n}_{\text{right}}}. \tag{2.27}$$

Integrating the wave matrix differential equation (2.22) and (2.23) over the interval $x_3^{\text{interface}} - \epsilon$ to $x_3^{\text{interface}} + \epsilon$ and taking the limit $\epsilon \downarrow 0$ yields

$$\hat{W}_{\text{right}}^{(+)} - \hat{W}_{\text{left}}^{(+)} = \tfrac{1}{2}\hat{T}'\hat{W}_{\text{left}}^{(+)} + \tfrac{1}{2}\hat{T}'\hat{W}_{\text{right}}^{(+)} + \tfrac{1}{2}\hat{R}'\hat{W}_{\text{left}}^{(-)} + \tfrac{1}{2}\hat{R}'\hat{W}_{\text{right}}^{(-)}, \tag{2.28}$$

$$\hat{W}_{\text{right}}^{(-)} - \hat{W}_{\text{left}}^{(-)} = \tfrac{1}{2}\hat{R}'\hat{W}_{\text{left}}^{(+)} + \tfrac{1}{2}\hat{R}'\hat{W}_{\text{right}}^{(+)} + \tfrac{1}{2}\hat{T}'\hat{W}_{\text{left}}^{(-)} + \tfrac{1}{2}\hat{T}'\hat{W}_{\text{right}}^{(-)}. \tag{2.29}$$

This equation can now be written into a more suitable form for making a physical interpretation. From the boundary conditions (see Page 10)

$$\hat{E}_2, \hat{H}_1 \text{ continuous across the interface,} \tag{2.30}$$

we find

$$\hat{W}_{\text{left}}^{(+)} + \hat{W}_{\text{left}}^{(-)} - \hat{W}_{\text{right}}^{(+)} - \hat{W}_{\text{right}}^{(-)} = 0. \tag{2.31}$$

Multiplying this by $\tfrac{1}{2}\hat{T}'$ and adding the result at the left-hand side to the right-hand side of the Equations (2.28) and (2.29), result in

$$\hat{W}_{\text{right}}^{(+)} - \hat{W}_{\text{left}}^{(+)} = \hat{T}'\hat{W}_{\text{left}}^{(+)} + \hat{R}'\hat{W}_{\text{right}}^{(-)}, \tag{2.32}$$

$$\hat{W}_{\text{right}}^{(-)} - \hat{W}_{\text{left}}^{(-)} = \hat{R}'\hat{W}_{\text{left}}^{(+)} + \hat{T}'\hat{W}_{\text{right}}^{(-)}. \tag{2.33}$$
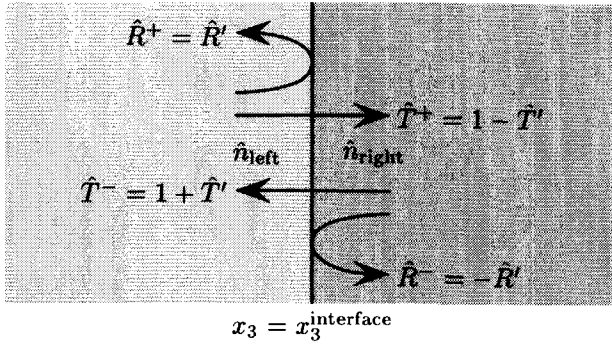
$$x_3 = x_3^{\text{interface}}$$

Figure 2.4:   *Interface between two media. The arrows symbolize the physical
interpretation of the transmission and reflection coefficients.*

These equations can be rewritten into a more suitable form (of the interface)

$$\begin{pmatrix} \hat{W}_{\text{right}}^{(+)} \\ \hat{W}_{\text{left}}^{(-)} \end{pmatrix} = \begin{pmatrix} \hat{T}^{(+)} & \hat{R}^{(-)} \\ \hat{R}^{(+)} & \hat{T}^{(-)} \end{pmatrix} \begin{pmatrix} \hat{W}_{\text{left}}^{(+)} \\ \hat{W}_{\text{right}}^{(-)} \end{pmatrix}. \tag{2.34}$$

Here

$$\hat{R}^{(+)} = \frac{\hat{n}_{\text{left}} - \hat{n}_{\text{right}}}{\hat{n}_{\text{left}} + \hat{n}_{\text{right}}} = \hat{R}', \tag{2.35}$$

$$\hat{R}^{(-)} = \frac{\hat{n}_{\text{right}} - \hat{n}_{\text{left}}}{\hat{n}_{\text{left}} + \hat{n}_{\text{right}}} = -\hat{R}^{(+)}, \tag{2.36}$$

$$\hat{T}^{(+)} = 2\frac{\hat{n}_{\text{left}}}{\hat{n}_{\text{left}} + \hat{n}_{\text{right}}} = 1 + \hat{R}^{(+)}, \tag{2.37}$$

$$\hat{T}^{(-)} = 2\frac{\hat{n}_{\text{right}}}{\hat{n}_{\text{left}} + \hat{n}_{\text{right}}} = 1 - \hat{R}^{(+)}, \tag{2.38}$$

are the transmission and reflection coefficients at an interface. Their physical inter-
pretation and the relation with the previous introduced transmission and reflection
coefficient, T' and R', are indicated in Figure 2.4. Equation (2.34) represents the
scattering-matrix relation for the interface between two media.

2.4   Integral equation for the wave matrix

The solution of the set of two coupled one-way wave equations, (2.22) and (2.23),
derived above is constructed by first transforming these equations into corresponding
integral equations. In this approach, the behavior of the left-hand sides of these

equations is required. The Green functions corresponding to the left-hand sides of (2.22) and (2.23) satisfy

$$\partial_3 \hat{\mathcal{G}}^{(+)}(x_3; x_3') + \mathrm{j}\omega\, \hat{\gamma}(x_3)\, \hat{\mathcal{G}}^{(+)}(x_3; x_3') = \delta(x_3 - x_3'), \qquad (2.39)$$

$$\partial_3 \hat{\mathcal{G}}^{(-)}(x_3; x_3') - \mathrm{j}\omega\, \hat{\gamma}(x_3)\, \hat{\mathcal{G}}^{(-)}(x_3; x_3') = \delta(x_3 - x_3'). \qquad (2.40)$$

With a simple substitution and using the causality conditions

$$\hat{\mathcal{G}}^{(+)}(x_3; x_3') = 0, \qquad \text{for } x_3 < x_3', \qquad (2.41)$$

$$\hat{\mathcal{G}}^{(-)}(x_3; x_3') = 0, \qquad \text{for } x_3 > x_3', \qquad (2.42)$$

it is found that the Green functions are given by

$$\hat{\mathcal{G}}^{(+)}(x_3; x_3') = \quad H(x_3 - x_3')\, \exp\left[-\mathrm{j}\omega \int_{z=x_3'}^{x_3} \hat{\gamma}(z)\,\mathrm{d}z \right], \qquad (2.43)$$

$$\hat{\mathcal{G}}^{(-)}(x_3; x_3') = -H(x_3' - x_3)\, \exp\left[\mathrm{j}\omega \int_{z=x_3'}^{x_3} \hat{\gamma}(z)\,\mathrm{d}z \right] \qquad (2.44)$$

$$= -\hat{\mathcal{G}}^{(+)}(x_3'; x_3),$$

where $H(x_3)$ denotes the Heaviside unit step function

$$H(x_3) = \begin{cases} 0, & \text{if } x_3 < 0, \\ \frac{1}{2}, & \text{if } x_3 = 0, \\ 1, & \text{if } x_3 > 0. \end{cases} \qquad (2.45)$$

Using these Green functions, we can transform the differential equation for the wave matrix into corresponding integral equations. Multiplication of Equation (2.22) by $\hat{\mathcal{G}}^{(-)}(x_3; x_3')$ and of Equation (2.40) by $\hat{W}^{(+)}(x_3)$ and adding the results yield

$$\hat{\mathcal{G}}^{(-)}\partial_3 \hat{W}^{(+)} + \hat{W}^{(+)}\partial_3 \hat{\mathcal{G}}^{(-)} = \hat{\mathcal{G}}^{(-)}\hat{T}\hat{W}^{(+)} + \hat{\mathcal{G}}^{(-)}\hat{R}\hat{W}^{(-)} + \hat{W}^{(+)}\delta(x_3 - x_3'). \qquad (2.46)$$

Integration of the left-hand side over the interval $0 < x_3 < x_3^{\text{exit}}$ results in

$$\int_{x_3=0}^{x_3^{\text{exit}}} \left[\hat{\mathcal{G}}^{(-)}(x_3; x_3')\, \partial_3 \hat{W}^{(+)}(x_3) + \hat{W}^{(+)}(x_3)\, \partial_3 \hat{\mathcal{G}}^{(-)}(x_3; x_3') \right] \mathrm{d}x_3$$

$$= \int_{x_3=0}^{x_3^{\text{exit}}} \partial_3 \left[\hat{\mathcal{G}}^{(-)}(x_3; x_3')\hat{W}^{(+)}(x_3) \right] \mathrm{d}x_3 = -\hat{\mathcal{G}}^{(-)}(0; x_3')\, \hat{W}^{(+)}(0), \quad (2.47)$$

where we have substituted

$$\hat{G}^{(-)}(x_3^{\text{exit}}, x_3') = 0, \qquad (x_3' < x_3^{\text{exit}}). \qquad (2.48)$$

Integration of Equation (2.46) over the interval $0 < x_3 < x_3^{\text{exit}}$ and using (2.44) yield

$$\hat{\mathcal{G}}^{(+)}(x_3'; 0)\hat{W}^{(+)}(0) = \hat{W}^{(+)}(x_3')$$
$$- \int_{x_3=0}^{x_3^{\text{exit}}} \hat{\mathcal{G}}^{(+)}(x_3'; x_3) \left[\hat{T}(x_3)\hat{W}^{(+)}(x_3) + \hat{R}(x_3)\hat{W}^{(-)}(x_3)\right] dx_3. \quad (2.49)$$

In a similar way, we find

$$0 = \hat{W}^{(-)}(x_3')$$
$$- \int_{x_3=0}^{x_3^{\text{exit}}} \hat{\mathcal{G}}^{(-)}(x_3'; x_3) \left[\hat{R}(x_3)\hat{W}^{(+)}(x_3) + \hat{T}(x_3)\hat{W}^{(-)}(x_3)\right] dx_3. \quad (2.50)$$

Knowing the Green functions $\hat{\mathcal{G}}^{(+)}$ and $\hat{\mathcal{G}}^{(-)}$ (as given in (2.39) and (2.40)), we can also use the superposition principle to obtain the above relations directly from Equations (2.22) and (2.23). In a compact operator form, the integral equations for the wave matrix read

$$\left[\delta_{I,J} - \hat{K}_{I,J}(x_3)\right]\hat{W}_J(x_3) = \hat{W}_J^{(0)}(x_3), \quad (2.51)$$

where, for $0 < x_3 < x_3^{\text{exit}}$,

$$\hat{W}_1^{(0)}(x_3) = \exp\left[-j\omega \int_{z=0}^{x_3} \hat{\gamma}(z)\,dz\right]\hat{W}^{(+)}(0), \quad (2.52)$$

$$\hat{W}_2^{(0)}(x_3) = 0, \quad (2.53)$$

are the transmitted forward waves and

$$(\hat{K}_{1,1}\hat{W}^{(+)})(x_3) = \int_{\zeta=0}^{x_3} \exp\left[-j\omega \int_{z=\zeta}^{x_3} \hat{\gamma}(z)\,dz\right] \hat{T}(\zeta)\hat{W}^{(+)}(\zeta)\,d\zeta, \quad (2.54)$$

$$(\hat{K}_{1,2}\hat{W}^{(-)})(x_3) = \int_{\zeta=0}^{x_3} \exp\left[-j\omega \int_{z=\zeta}^{x_3} \hat{\gamma}(z)\,dz\right] \hat{R}(\zeta)\hat{W}^{(-)}(\zeta)\,d\zeta, \quad (2.55)$$

$$(\hat{K}_{2,1}\hat{W}^{(+)})(x_3) = -\int_{\zeta=x_3}^{x_3^{\text{exit}}} \exp\left[-j\omega \int_{z=x_3}^{\zeta} \hat{\gamma}(z)\,dz\right] \hat{R}(\zeta)\hat{W}^{(+)}(\zeta)\,d\zeta, \quad (2.56)$$

$$(\hat{K}_{2,2}\hat{W}^{(-)})(x_3) = -\int_{\zeta=x_3}^{x_3^{\text{exit}}} \exp\left[-j\omega \int_{z=x_3}^{\zeta} \hat{\gamma}(z)\,dz\right] \hat{T}(\zeta)\hat{W}^{(-)}(\zeta)\,d\zeta, \quad (2.57)$$

describe the interaction between the counter-propagating waves. Observe that (2.54) and (2.55) can be combined into one integral because $\hat{T} = -\hat{R}$. For the same reason, Equations (2.56) and (2.57) can be combined.

2.5 Numerical aspects of the Bremmer coupling series

The directional wave-field decomposition method contains three main steps:

① directional decomposition of the field of the given incident plane wave (compare with (2.17))

$$\hat{W}^{(+)}(0) = \hat{E}_2^{\text{incident}}(0), \tag{2.58}$$

when the electric field is predescribed, or

$$\hat{W}^{(+)}(0) = -\hat{y}\,\hat{H}_1^{\text{incident}}(0), \tag{2.59}$$

when the magnetic field is predescribed.

② computation of the counter-propagating waves inside the configuration by solving the integral equations (2.51), and,

③ composition of the counter-propagating waves into the electromagnetic fields at the positions of interest (Equations (2.17) and (2.18)).

The numerical implementation of the second step deserves some more attention. In this section we discuss two methods to tackle this: a forward scheme (BPM-type approach) and the Bremmer coupling series.

2.5.1 BPM-type approach

The classical Beam Propagation Method (BPM) and many related methods assume that the medium properties vary slowly in the longitudinal direction. In such configurations, the influence of operator $\hat{K}_{I,J}$ can be neglected. The forward-directed transmitted wave is then dominant

$$\hat{W}^{(+)}(x_3) \simeq \hat{W}_1^{(0)}(x_3), \tag{2.60}$$

$$\hat{W}^{(-)}(x_3) \simeq 0. \tag{2.61}$$

In the classical BPM-type methods only the forward-directed waves are calculated from Equation (2.52) while it is assumed that in (2.54)-(2.57), $\partial_3 \hat{n} \simeq 0$. Hence $\hat{K}_{I,J}(x_3) \simeq 0$. This calculation is then performed with a recurrent scheme. In the current scheme, the forward-directed wave at a particular position $x_3 = m\Delta x_3$ is related to the forward-directed wave at the *previous* position $(m-1)\Delta x_3$, see Figure 2.5. The configuration is then divided into M points and the forward-directed waves are only calculated at the positions $x_3 = 0, \Delta x_3, \cdots, m\Delta x_3, \cdots, M\Delta x_3$ ($\Delta x_3 = x_3^{\text{exit}}/M$). The recurrent scheme then follows from rewriting Equation (2.52)

$$\hat{W}_1^{(0)}(0) = \hat{W}^{(+)}(0), \tag{2.62}$$

$$\hat{W}_1^{(0)}(m\Delta x_3) = \hat{P}(m)\hat{W}_1^{(0)}[(m-1)\Delta x_3], \qquad m \geq 1, \tag{2.63}$$
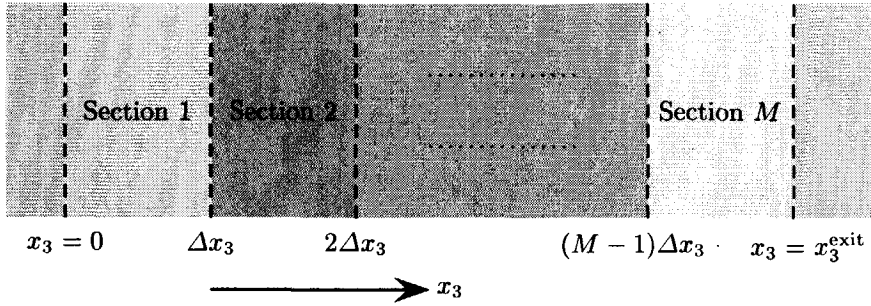
Figure 2.5:   *In the BPM-type approach, the field is recursively calculated at a finite number of x_3-positions.*

where

$$\hat{P}(m) = \exp\left[-\mathrm{j}\omega \int_{z=(m-1)\Delta x_3}^{m\Delta x_3} \hat{\gamma}(z)\, \mathrm{d}z\right].\tag{2.64}$$

The (positive) distance Δx_3 is often called the propagation step. In the numerical implementation, we can approximate $\hat{P}(m)$ by its value half-way

$$\hat{P}(m) \simeq \exp\left\{-\mathrm{j}\omega\hat{\gamma}\left[(m-\tfrac{1}{2})\Delta x_3\right]\Delta x_3\right\} + \mathcal{O}(\Delta x_3),\tag{2.65}$$

where the error is of order Δx_3. The application of the trapezoidal rule to the integral in (2.64), however, results in a more accurate scheme (error of order $(\Delta x_3)^2$)

$$\hat{P}(m) \simeq \exp\left\{-\mathrm{j}\omega\tfrac{1}{2}\hat{\gamma}[(m-1)\Delta x_3]\Delta x_3\right\} \exp\left[-\mathrm{j}\omega\tfrac{1}{2}\hat{\gamma}(m\Delta x_3)\Delta x_3\right] + \mathcal{O}(\Delta x_3^2).\tag{2.66}$$

We refer to this numerical scheme as the one-dimensional forward BPM-type scheme.

2.5.2   Bremmer coupling series

In many applications, the interaction between the counter-propagating waves is weak. In such a case we may assume that the norm of the operator $\hat{K}_{I,J}$ is less than 1, so that the Neumann expansion can be applied to the inverse of $(\delta_{I,J} - \hat{K}_{I,J})$ in Equation (2.51). This leads to the Bremmer coupling series[49, 131]

$$\hat{W}_I = \sum_{j=0}^{\infty} (\hat{K}^j)_{I,J}\hat{W}_J^{(0)} = \hat{W}_I^{(0)} + \hat{K}_{I,J}\hat{W}_J^{(0)} + (\hat{K}^2)_{I,J}\hat{W}_J^{(0)} + \cdots.\tag{2.67}$$

It is convenient to write

$$\hat{W}_I = \sum_{j=0}^{\infty} \hat{W}_I^{(j)},\tag{2.68}$$
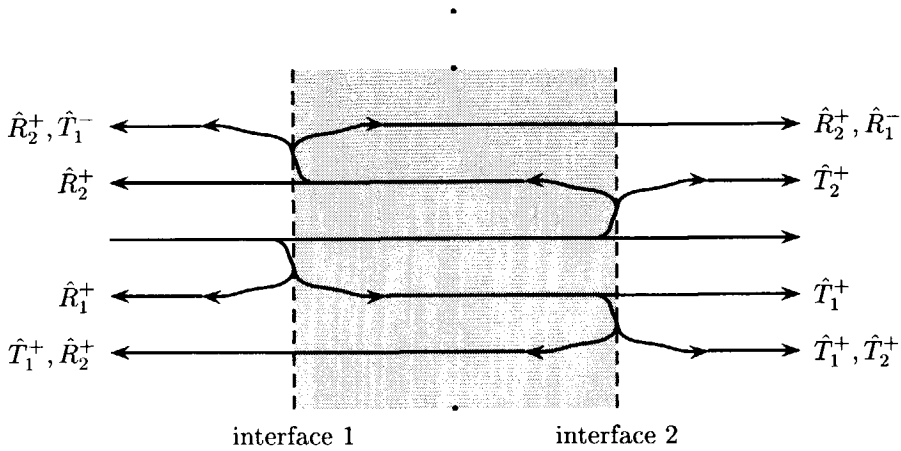
Figure 2.6: *An impression of the Bremmer coupling series. The subscripts of the reflection and transmission coefficients denote the corresponding interface.*

in which

$$\hat{W}_I^{(j)} = \hat{K}_{I,J}\hat{W}_J^{(j-1)}, \qquad (j \geq 1), \tag{2.69}$$

can be interpreted as the j-times reflected/transmitted wave, see Figure 2.6. This equation shows that the solution is found by solving an iterative scheme. The separate terms are subsequently determined in a similar way. The total number of computed terms, J, is limited. Often $J = 0$, 1 or 2. The BPM corresponds to $J = 0$. The conditions for convergence of the 1-D Bremmer coupling series are discussed by Atkinson[132] in detail.

To show the numerical implementation of each term of the Bremmer coupling series, we first consider one element on the right-hand side of (2.69), e.g., $\hat{K}_{1,1}\hat{W}_1^{(j-1)}$. For convenience we introduce the shorthand notation

$$\hat{Q}_I^{(j)}(\zeta) \stackrel{\text{def}}{=} \hat{T}(\zeta)\hat{W}_I^{(j-1)}(\zeta), \tag{2.70}$$

$$\hat{I}_{I,1}^{(j)}(m) \stackrel{\text{def}}{=} (\hat{K}_{I,1}\hat{W}_1^{(j-1)})(m\Delta x_3), \tag{2.71}$$

and

$$\hat{I}_{I,2}^{(j)}(m) \stackrel{\text{def}}{=} (\hat{K}_{I,2}\hat{W}_2^{(j-1)})(m\Delta x_3). \tag{2.72}$$

In a way similar to that of the case of the forward BPM-type scheme, a recursive scheme for $\hat{I}_{1,1}^{(j)}(m)$ is constructed

$$\hat{I}_{1,1}^{(j)}(m) = \int_{\zeta=0}^{m\Delta x_3} \exp\left[-j\omega \int_{z=\zeta}^{m\Delta x_3} \hat{\gamma}(z)\, dz\right] \hat{Q}_1^{(j)}(\zeta)\, d\zeta$$

$$= \exp\left[-j\omega \int_{z=(m-1)\Delta x_3}^{m\Delta x_3} \hat{\gamma}(z)\, dz\right]$$

$$\int_{\zeta=0}^{(m-1)\Delta x_3} \exp\left[-j\omega \int_{z=\zeta}^{(m-1)\Delta x_3} \hat{\gamma}(z)\, dz\right] \hat{Q}_1^{(j)}(\zeta)\, d\zeta$$

$$+ \int_{\zeta=(m-1)\Delta x_3}^{m\Delta x_3} \exp\left[-j\omega \int_{z=\zeta}^{m\Delta x_3} \hat{\gamma}(z)\, dz\right] \hat{Q}_1^{(j)}(\zeta) d\zeta$$

$$= \hat{P}(m)\hat{I}_{1,1}^{(j)}(m-1) + \hat{q}_{1,1}^{(j)}(m), \tag{2.73}$$

where $\hat{P}(m)$ is given in (2.64) and

$$\hat{I}_{1,1}^{(j)}(0) = 0, \tag{2.74}$$

$$\hat{q}_{1,1}^{(j)}(m) = \int_{\zeta=(m-1)\Delta x_3}^{m\Delta x_3} \exp\left[-j\omega \int_{z=\zeta}^{m\Delta x_3} \hat{\gamma}(z)\, dz\right] \hat{Q}_1^{(j)}(\zeta)\, d\zeta. \tag{2.75}$$

In the numerically implementation we apply the trapezoidal rule to $\hat{q}_{1,1}^{(j)}(m)$

$$\hat{q}_{1,1}^{(j)}(m) \simeq \tfrac{1}{2}\Delta x_3 \left\{ \hat{Q}_1^{(j)}(m\Delta x_3) + \hat{P}(m)\hat{Q}_1^{(j)}[(m-1)\Delta x_3] \right\} + \mathcal{O}(\Delta x_3^2), \tag{2.76}$$

which has an error of the order $(\Delta x_3)^2$, and we apply a finite difference approximation to $\hat{R} = -\hat{T} = \tfrac{1}{2}\hat{y}^{-1}\partial_3\hat{y} = \tfrac{1}{2}\hat{n}^{-1}\partial_3\hat{n}$

$$\hat{R}(m\Delta x_3) \simeq \frac{\hat{n}\left[(m+\tfrac{1}{2})\Delta x_3\right] - \hat{n}\left[(m-\tfrac{1}{2})\Delta x_3\right]}{\left\{\hat{n}[(m+\tfrac{1}{2})\Delta x_3] + \hat{n}[(m-\tfrac{1}{2})\Delta x_3]\right\}\Delta x_3} + \mathcal{O}(\Delta x_3^2). \tag{2.77}$$

The error is of the order of $(\Delta x_3)^2$.

We are now in a position to show the equivalence between this numerical discretized scheme applied to a configuration with one interface and the analytical result obtained in Subsection 2.3. In Figure 2.7, each term on the right-hand side of Equation (2.28) is symbolized by an arrow. These terms corresponds to the constituents of the forward-propagating field in our numerical scheme. As an example, on the left-hand side of the interface (section m), only the first term of $\hat{q}_{11}^{(j)}$ in Equation (2.76) is nonzero. This term is generated near the interface on the right-hand side of section m and is subsequently propagated (multiplied by $P(m+1)$) to the position $x_3 = (m+1)\Delta x_3$. On the right-hand side of the interface (section $m+1$), only the second term of $\hat{q}_{11}^{(j)}$ in Equation (2.76) is nonzero. This term is generated near the interface on the left-hand side of section $m+1$. Both contributions are equal and are indicated in the Figure 2.7. A similar analysis can be done for $\hat{q}_{12}^{(j)}$.
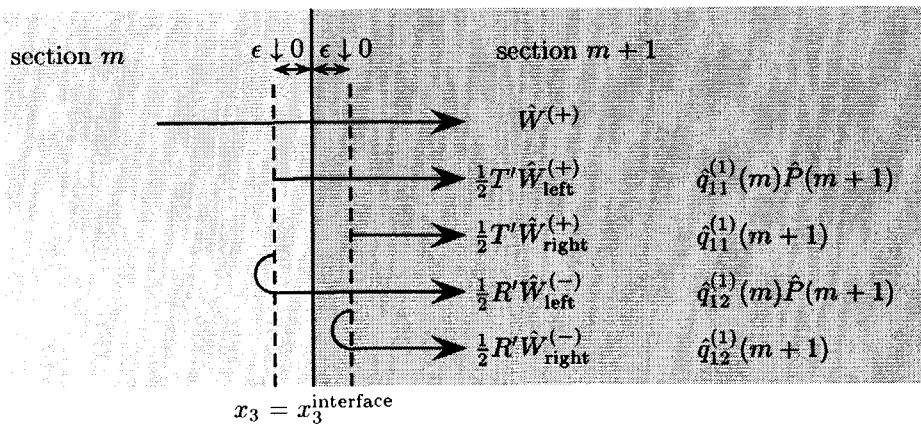
Figure 2.7: *Interface between two media. The contributions to the forward-propagating wave are indicated in the figure. A comparison between the analytic quantities and quantities of the numerical scheme is made.*

Similarly, the other terms on the right-hand side of (2.69) can be determined. Our numerical scheme for the j-times reflected wave reads

$$\hat{W}_1^{(j)}(m\Delta x_3) = \hat{I}_{1,1}^{(j)}(m) - \hat{I}_{1,2}^{(j)}(m), \tag{2.78}$$

$$\hat{W}_2^{(j)}(m\Delta x_3) = -\hat{I}_{2,1}^{(j)}(m) + \hat{I}_{2,2}^{(j)}(m), \tag{2.79}$$

$(j, m = 0, 1, 2, \cdots)$ with

$$\hat{I}_{1,J}^{(j)}(m) = \hat{P}(m) \quad \hat{I}_{1,J}^{(j)}(m-1) + \hat{q}_{1,J}^{(j)}(m), \quad m \geq 1, \tag{2.80}$$

$$\hat{I}_{2,J}^{(j)}(m) = \hat{P}(m+1)\hat{I}_{2,J}^{(j)}(m+1) + \hat{q}_{2,J}^{(j)}(m), \quad m \leq M-1, \tag{2.81}$$

in which

$$\hat{q}_{1,J}^{(j)}(m) = \int_{\zeta=(m-1)\Delta x_3}^{m\Delta x_3} \exp\left[-j\omega\int_{z=\zeta}^{m\Delta x_3} \hat{\gamma}(z)\,dz\right]\hat{Q}_J^{(j)}(\zeta)\,d\zeta$$

$$\simeq \quad \tfrac{1}{2}\Delta x_3\left\{\hat{Q}_J^{(j)}(m\Delta x_3) + \hat{P}(m)\hat{Q}_J^{(j)}[(m-1)\Delta x_3]\right\}, \tag{2.82}$$

$$\hat{q}_{2,J}^{(j)}(m) = \int_{\zeta=(m+1)\Delta x_3}^{m\Delta x_3} \exp\left[\quad j\omega\int_{z=\zeta}^{m\Delta x_3} \hat{\gamma}(z)\,dz\right]\hat{Q}_J^{(j)}(\zeta)\,d\zeta$$

$$\simeq -\tfrac{1}{2}\Delta x_3\left\{\hat{Q}_J^{(j)}(m\Delta x_3) + \hat{P}(m+1)\hat{Q}_J^{(j)}[(m+1)\Delta x_3]\right\}, \tag{2.83}$$

where

$$\hat{Q}_J^{(j)}(m\Delta x_3) = \hat{T}(m\Delta x_3)\hat{W}_J^{(j-1)}(m\Delta x_3), \qquad\qquad j > 1, \qquad\qquad (2.84)$$

and with the initial values

$$\hat{I}_{1,J}^{(0)}(0) \quad\quad = \hat{W}^{(+)}(0), \qquad\qquad\qquad\qquad (2.85)$$

$$\hat{I}_{1,J}^{(j)}(0) \quad\quad = 0, \qquad\qquad\qquad\qquad\qquad (2.86)$$

$$\hat{I}_{2,J}^{(j)}(M) \quad = 0, \qquad\qquad\qquad\qquad\qquad (2.87)$$

$$\hat{Q}_J^{(0)}(m\Delta x_3) = 0. \qquad\qquad\qquad\qquad\qquad (2.88)$$

The whole numerical scheme is given in a flow chart, see Figure 2.8. Observe that $\hat{I}_{1,1}^{(j)}$ and $\hat{I}_{1,2}^{(j)}$ in (2.80) (and also $\hat{I}_{21}^{(j)}$ and $\hat{I}_{2,2}^{(j)}$ in (2.81)) can be computed simultaneously.

The computer capacity for data storing might be too small, because in every term j of the Bremmer coupling series, the reflected and transmitted field $\hat{Q}_J^{(j+1)}(m\Delta x_3)$ must be calculated and stored. In an x_3-invariant region, however, $\hat{Q}_J^{(j+1)}(m\Delta x_3)$ equals 0. In a very slowly varying region, the transmitted and reflected fields are small and can be neglected. An energy criterion for detecting these neglectable fields can be introduced through which the amount of data to be stored is reduced. Time-domain results are obtained using a time-Fourier transform and its inverse.

2.6   Numerical simulations

We have implemented the Bremmer coupling series and have tested its convergence. We have not seen divergence of the method for any tested configuration, not even for high contrasts and periodic structures. Two numerical experiments demonstrate the possibilities and accuracy of the method. General convergence has not been proved.

Dielectric barrier

We have compared our results to those of Martin, Dereux and Girard[122], who have presented another independent method, based upon a solution of the domain-integral equation method. In Figure 2.9, a plane-wave is incident on a barrier with different permittivities. The calculated total field is illustrated and agrees very well with the results from Martin et al.[122].

An analytic solution can be easily obtained[122]. To examine the accuracy, we introduce the global root mean-square error ERR as

$$\text{ERR} = \sqrt{\frac{\int_{0\mu m}^{2\mu m}|\hat{E}_2^{\text{exact}} - \hat{E}_2^{\text{num}}|^2\,\mathrm{d}x_3}{\int_{0\mu m}^{2\mu m}|\hat{E}_2^{\text{exact}}|^2\,\mathrm{d}x_3}}. \qquad\qquad (2.89)$$

$\mathcal{E}_2^{\text{incident}}(0,t)$
Fourier transformation $\longrightarrow \hat{E}_2^{\text{incident}}(0,\omega)$

For every ω

decomposition: $\hat{W}_1(0) = \hat{E}_2^{\text{incident}}(0)$

For every term j of Bremmer Coupling Series $(j = 0, 1, 2, \cdots)$

$\hat{I}_{1,J}^{(j)}(0) = 0,\ \hat{I}_{1,J}^{(0)}(0) = \hat{W}^{(+)}(0)$

For every forward propagation step m $(m = 1, 2, 3, \cdots, M)$

$\hat{I}_{1,J}^{(j)}(m) = \hat{P}(m)\hat{I}_{1,J}^{(j)}(m-1) + \hat{q}_{1,J}^{(j)}(m)$
$\hat{W}_1^{(j)}(m\Delta x_3) = \hat{I}_{1,1}^{(j)}(m) - \hat{I}_{1,2}^{(j)}(m)$
Calculate $\hat{Q}_1^{(j+1)}(m\Delta x_3)$ + storage
composition $\longrightarrow \hat{F}_1^{(j)}$ and $\hat{F}_2^{(j)}$
adding to previous fields + storage

$\hat{I}_{2,J}^{(j)}(M) = 0$

For every backward propagation step m $(m = M - 1, \cdots, 0)$

$\hat{I}_{2,J}^{(j)}(m) = \hat{P}(m+1)\hat{I}_{2,J}^{(j)}(m+1) + \hat{q}_{2,J}^{(j)}(m)$
$\hat{W}_2^{(j)}(m\Delta x_3) = -\hat{I}_{2,1}^{(j)}(m) + \hat{I}_{2,2}^{(j)}(m)$
Calculate $\hat{Q}_2^{(j+1)}(m\Delta x_3)$ + storage
composition $\longrightarrow \hat{F}_1^{(j)}$ and $\hat{F}_2^{(j)}$
adding to previous fields + storage

Inverse Fourier transform $\longrightarrow \mathcal{E}_2(x_3,t)$ and $\mathcal{H}_1(x_3,t)$ at the positions of interest

Figure 2.8: *Flow chart of the numerical implementation of the one-dimensional Bremmer coupling series.*
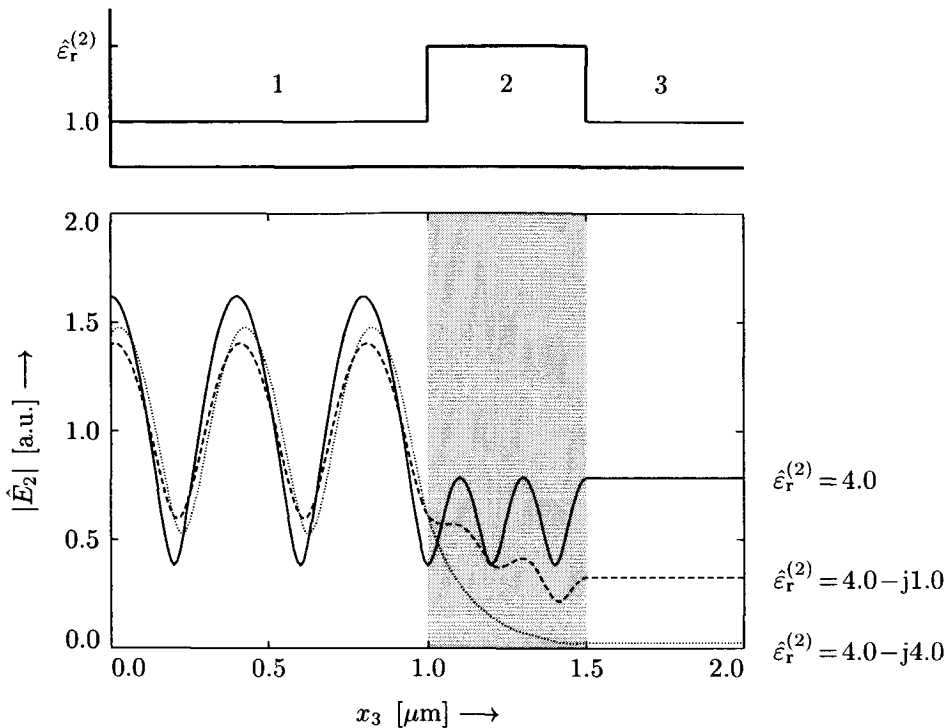
Figure 2.9: Amplitude of the computed field in a geometry consisting of a di-
electric barrier sandwiched between two half-spaces. Three dielec-
tric barriers with different absorption values are investigated. The
wavelength of the incoming wave is $\lambda_0 = 0.8$ μm. The mesh size
for the calculation was $\Delta x_3 = 0.01$ μm. The results correspond to
those in the literature[122].

Note that ERR ≥ 0 and that ERR $= 0$ if and only if $\hat{E}_2^{\mathrm{num}} = \hat{E}_2^{\mathrm{exact}}$. The error is
normalized such that ERR $= 1$ if $\hat{E}_2^{\mathrm{num}} = 0$. Using the same configuration as above
(no losses), we have determined the convergence of the Bremmer coupling series,
see Figure 2.10. After five terms, the error is already less than 10^{-5}. This suggests
that only a few terms of the Bremmer coupling series have to be taken into account
to obtain accurate results.

Due to the discretization, the exact location of the interface is lost: it is some-
where between two grid points. If the interface is at a grid point, the numerical
scheme converges to the exact solution. If not, an error remains. This error is indi-
cated in Figure 2.11. In the following chapters, the permittivity will be numerically
smoothed. The error for a numerically smoothed configuration is indicated in the
same figure. This error is more or less constant over the interval and is lower for
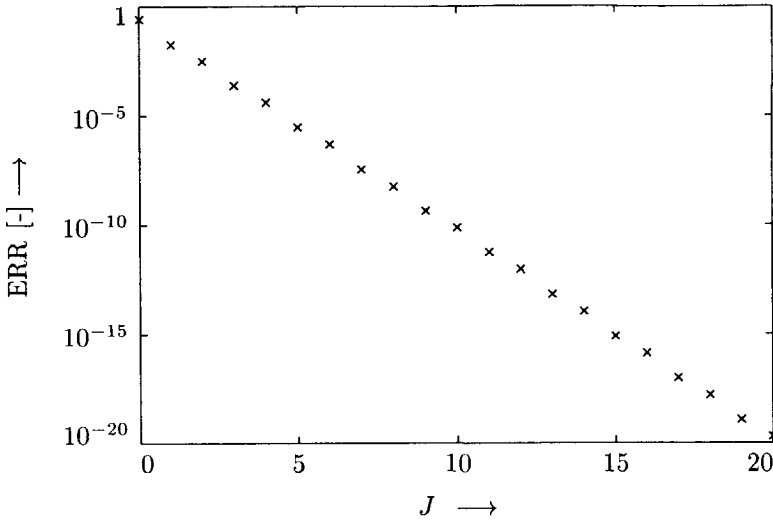
Figure 2.10: *The error ERR in the field versus the number of terms of the Bremmer coupling series.*
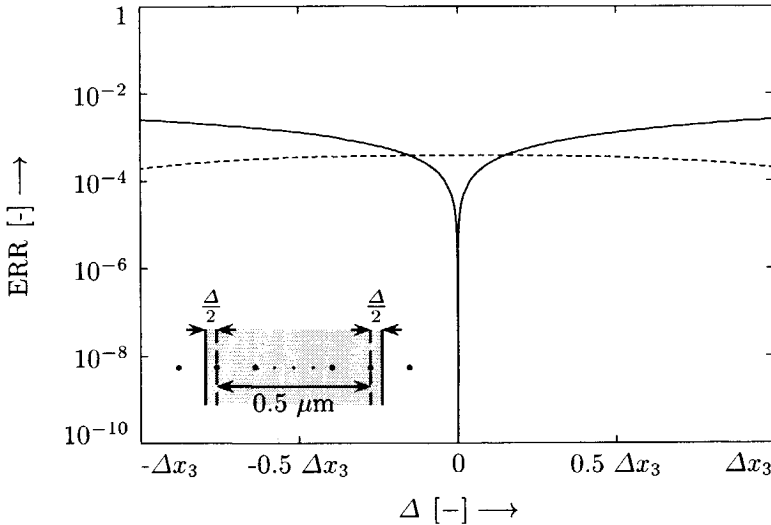
Figure 2.11: *The error ERR in the field when changing the barrier's width from 0.5 μm$-\Delta x_3$ to 0.5 μm$+\Delta x_3$. The position of the barrier's center is not changed. The deviation is denoted as Δ (see inset); the barrier's width is 0.5 μm$+\Delta$. The dashed curve corresponds to a smoothed medium, while the full curve corresponds to the original discretized medium.*

larger distance between the interface and the grid point.

Time-domain results

Time-domain results of a pulsed magnetic sheet source are obtained with a discrete time-Fourier transformation. The source excitation is translated into an initial field at $x_3 = 0$ according to $\hat{E}_2 = \hat{K}_1^{(e)}$. This short-pulse excitation estimates the transient-pulse response of the configuration. Here, the pulse used has a source signature with trapezoidal spectrum, as depicted in Figure 2.12. Its positive corner frequencies are 100, 200, 250 and 400 THz ($\lambda_0 \approx 3.0$, 1.5, 1.2, 0.75 μm, respectively)[c]. The negative corner frequencies are -100, -200, -250, -400 THz. Now, $\hat{E}(\omega)$ is an even function of ω and $\mathcal{E}(t)$ is real. Therefore, to compute the inverse Fourier transform we can restrict ourselves to positive frequencies

$$\mathcal{E}(t) = 2\,\mathrm{Re}\left[\frac{1}{2\pi}\int_0^\infty e^{j\omega t}\hat{E}(\omega)\,d\omega\right]. \tag{2.90}$$

Thus

$$\hat{E}_{\max}^{-1}\mathcal{E}_2(t) = \frac{\omega_1}{\pi t(\omega_1 - \omega_2)}[\sin(\omega_2 t) - \sin(\omega_1 t)] + \frac{1}{\pi t}[\sin(\omega_3 t) - \sin(\omega_2 t)]$$

$$+ \frac{\omega_4}{\pi t(\omega_4 - \omega_3)}[\sin(\omega_4 t) - \sin(\omega_3 t)] + \frac{1}{\pi t^2(\omega_2 - \omega_1)}[\cos(\omega_2 t) - \cos(\omega_1 t)]$$

$$+ \frac{1}{\pi t^2(\omega_3 - \omega_4)}[\cos(\omega_4 t) - \cos(\omega_3 t)] + \frac{1}{\pi t(\omega_2 - \omega_1)}[\omega_2 \sin(\omega_2 t) - \omega_1 \sin(\omega_1 t)]$$

$$+ \frac{1}{\pi t(\omega_3 - \omega_4)}[\omega_4 \sin(\omega_4 t) - \omega_3 \sin(\omega_3 t)], \qquad t \neq 0, \tag{2.91}$$

and

$$\hat{E}_{\max}^{-1}\mathcal{E}_2(0) = \frac{1}{2\pi}(\omega_3 + \omega_4 - \omega_1 - \omega_2), \tag{2.92}$$

where ω_1, ω_2, ω_3 and ω_4 are the positive angular corner frequencies and $\hat{E}_{\max}$ is the maximum value of $\hat{E}(\omega)$. Numerically, the inverse Fourier transform is discretized as

$$\mathcal{E}(t) \approx 2\sum_{n=1}^{N_{\mathrm{FT}}} \Delta f\,\mathrm{Re}\left[e^{j\omega t}\hat{E}(2\pi n\Delta f)\right], \tag{2.93}$$

with $\Delta f = 1/(2\Delta T N_{\mathrm{FT}})$. We have taken an inverse Fourier transformation with $N_{\mathrm{FT}} = 512$ points and $\Delta T = 0.4$ fs. The pulse shape is shown by letting the wave propagate through the free space, see Figure 2.12. The time- and x_3-axis are then interchangeable. In the same figure, a snapshot of the electromagnetic field $\mathcal{E}_2$ in the configuration of Figure 2.1 at 40 fs and its *reflected part* are shown (i.e. all terms exact the first one). We chose $x_3^{\mathrm{exit}} = 10$ μm, $\min(\hat{\varepsilon}_{\mathrm{r}}) = 1$, $\max(\hat{\varepsilon}_{\mathrm{r}}) = 4.2$ and $\Delta x_3 = 0.1$ μm.

---

[c]In acoustic configurations, we choose the corner frequencies as 10, 20, 25 and 40 Hz.
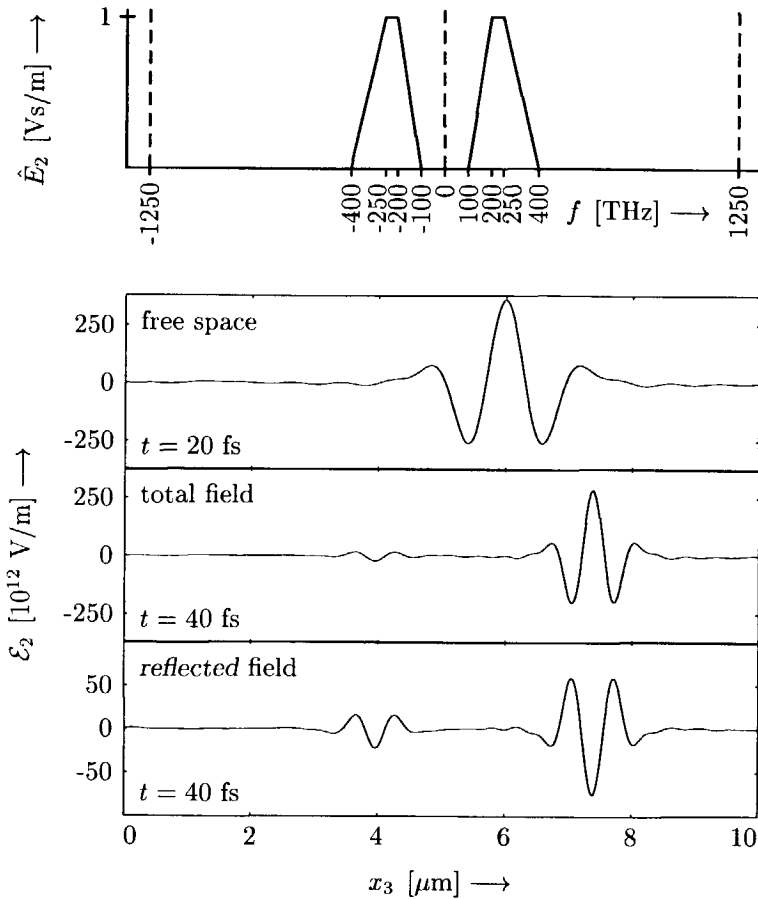
Figure 2.12: *Spectrum of the source and three computed snapshots of the electromagnetic field $\mathcal{E}_2$. The Nyquist frequency is 1250 THz. The first snapshot is made at 20 fs in free space ($\hat{\varepsilon}_r = 1$). The two other snapshots are made at 40 fs and correspond to the configuration described in Figure 2.1: the second snapshot shows the total field, while the last snapshot shows the reflected field. We used $x_3^{\text{exit}} = 10$ μm, $\min(\hat{\varepsilon}_r) = 1$, $\max(\hat{\varepsilon}_r) = 4.2$ and $\Delta x_3 = 0.1$ μm.*

2.7   Discussion of the results

We have introduced the Bremmer coupling series for the scattering problem along the longitudinal direction. A new numerical implementation has been developed. Numerical simulations showed good results which provides a reason to use the Bremmer coupling series also for the longitudinal scattering problem in higher-dimensional configurations (see Chapter 3 and 6).

CHAPTER 3

Directional Wave-Field Decomposition in a Two-dimensional, Isotropic, Dielectric Configuration

In the previous chapter, the longitudinal scattering problem was introduced in a one-dimensional configuration. In this chapter, this theory is extended to TE-polarized waves in *two-dimensional*, isotropic dielectric media. The equations are equivalent to those for acoustic waves in a two-dimensional configuration with a constant volume density of mass ρ.

This chapter is organized as follows. In Section 3.1, the configuration is described. Following the previous chapter, we rewrite the Maxwell equations into a differential equation for the field matrix (Section 3.2). Application of the directional decomposition introduces the wave matrix. Its differential equation (Section 3.3) is transformed into an integral equation (Section 3.4). The numerical scheme for the longitudinal scattering problem is derived in Section 3.5. Finally, the results are discussed in Section 3.6.

This chapter contains one appendix, in which the relation between the forward and backward Green functions is described.

3.1 Description of the configuration

The configuration has already been described in Section 1.3. In this chapter, we only consider one transverse direction.

3.2   Differential equation for the field matrix

In this section, the Maxwell equations are rewritten into a form suitable for the directional wave-field decomposition.

In a source-free isotropic configuration with invariance in *one* transverse direction ($\partial_2 \equiv 0$), the equations of Maxwell in frequency domain, (1.30) and (1.31), decompose into two independent sets of equations, namely one for transverse electric fields (TE: $\{\hat{E}_2, \hat{H}_1, \hat{H}_3\} \neq 0$) and one for transverse magnetic fields (TM: $\{\hat{H}_2, \hat{E}_1, \hat{E}_3\} \neq 0$). In this chapter, we only consider *TE fields* in dielectric media ($\hat{\varepsilon} = \varepsilon_0 \hat{\varepsilon}_r, \hat{\mu} = \mu_0$). We assume that the permittivity $\hat{\varepsilon}$ is a smooth, i.e., an infinitely differentiable function of the position. The Maxwell equations, (1.30)-(1.31), then simplify into

$$\partial_3 \hat{E}_2 - \mathrm{j}\omega\mu_0 \hat{H}_1 \qquad\qquad = 0, \qquad\qquad (3.1)$$

$$\partial_3 \hat{H}_1 - \mathrm{j}\omega\hat{\varepsilon} \hat{E}_2 \quad - \partial_1 \hat{H}_3 = 0, \qquad\qquad (3.2)$$

$$\mathrm{j}\omega\mu_0 \hat{H}_3 + \partial_1 \hat{E}_2 = 0. \qquad\qquad (3.3)$$

Before applying the directional wave-field decomposition along the longitudinal x_3 direction, we introduce the field matrix $\hat{F}_I$ as

$$\hat{F} = \begin{pmatrix} \hat{E}_2 \\ -\hat{H}_1 \end{pmatrix}. \qquad\qquad (3.4)$$

Due to this choice, the complex Poynting vector component in the preferred direction equals $\hat{S}_3 = \hat{F}_1 \hat{F}_2^*$. The resulting differential equation for the field matrix is

$$\partial_3 \hat{F}_I + \mathrm{j}\omega \hat{A}_{I,J} \hat{F}_J = 0, \qquad\qquad (3.5)$$

with the electromagnetic system matrix operator $\hat{A}_{I,J}$[a]

$$\hat{A}_{1,1}(x_1, x_3) = 0,$$

$$\hat{A}_{1,2}(x_1, x_3) = \mu_0,$$

$$\hat{A}_{2,1}(x_1, x_3) = \hat{\varepsilon}(x_1, x_3) + \mu_0^{-1}\omega^{-2}\partial_1^2,$$

$$\hat{A}_{2,2}(x_1, x_3) = 0.$$

This equation is often referred to as a two-way wave equation. In contrast to the one-dimensional configuration, $\hat{A}_{2,1}$ is now a differential operator. Since the matrix $\hat{A}_{I,J}$ depends on x_3, we cannot construct a simple analytic solution. For further computations it is more convenient to introduce the wave matrix.

---

[a]In this notation, operator $\hat{A}_{2,1}$ interacts with the function $\hat{h}$ as

$$(\hat{A}_{2,1}\hat{h})(x_1, x_3) = \hat{\varepsilon}(x_1, x_3)\hat{h}(x_1, x_3) + \mu_0^{-1}\omega^{-2}(\partial_1^2\hat{h})(x_1, x_3).$$

Acoustic field matrix and system matrix

When starting with the acoustic wave equations, one introduces the field matrix $\hat{F}_I$ as

$$\hat{F} = \begin{pmatrix} \hat{p} \\ \hat{v}_3 \end{pmatrix}. \tag{3.6}$$

Due to this choice, the complex Poynting vector component in the preferred direction equals $\hat{S}_3 = \hat{p}\hat{v}_3^* = \hat{F}_1 \hat{F}_2^*$. In order to obtain equivalent equations to those for TE-polarized electromagnetic waves, we assume that the volume density of mass ρ is constant. The compressibility κ is a smooth function of the position. The nonzero elements of the system matrix $\hat{A}_{I,J}$ are

$$\hat{A}_{1,2}(x_1, x_3) = \rho, \tag{3.7}$$

$$\hat{A}_{2,1}(x_1, x_3) = \kappa(x_1, x_3) + \omega^{-2}\hat{\rho}^{-1}\partial_1^2. \tag{3.8}$$

Thus, the compressibility κ is equivalent to the permittivity $\hat{\varepsilon}$ in this chapter. In the remainder of the chapter, we concentrate on the electromagnetic equations. The acoustic analog is found by some simple substitutions

$$\mu_0 \quad \to \rho,$$
$$\hat{\varepsilon}(x_1, x_3) \to \kappa(x_1, x_3).$$

3.3 Differential equation for the wave matrix

Below, the field is decomposed into waves traveling forward and backward with respect to the preferred direction.

3.3.1 Diagonalization procedure

The two-way wave equation can be transformed into a one-way wave equation by formally diagonalizing the matrix operator $\hat{A}_{I,J}$, i.e.,

$$\hat{A}_{I,J}\hat{L}_{J,M} = \hat{L}_{I,J}\hat{A}_{J,M}. \tag{3.9}$$

The elements of the diagonal matrix operator $\hat{A}_{J,M}$ are denoted as the operators $\hat{\Gamma}$ and $-\hat{\Gamma}$

$$\hat{\Lambda} = \begin{pmatrix} \hat{\Gamma} & 0 \\ 0 & -\hat{\Gamma} \end{pmatrix}. \tag{3.10}$$

The matrix operator $\hat{L}_{J,M}$ is called the composition matrix operator.

This diagonalization is the fundamental step in the directional wave-field decomposition. By applying it, the field is decomposed into a wave $\hat{W}_1 = \hat{W}^{(+)}(x_1, x_3)$

physically traveling in the positive x_3 direction and a wave $\hat{W}_2 = \hat{W}^{(-)}(x_1, x_3)$ physically traveling in the negative x_3 direction (see Figure 2.2). These waves are gathered in the wave matrix, which is defined through

$$\hat{W}_I = (\hat{L}^{-1})_{I,J} \hat{F}_J. \tag{3.11}$$

The resulting differential equation for the wave matrix is given by[b]

$$\partial_3 \hat{W}_I + j\omega \hat{\Lambda}_{I,M} \hat{W}_M = -(\hat{L}^{-1})_{I,J}(\partial_3 \hat{L}_{J,M})\hat{W}_M. \tag{3.13}$$

This equation is often called the one-way wave equation. The coupling matrix operator $-(\hat{L}^{-1})_{I,J}(\partial_3 \hat{L}_{J,M})$ has the general form

$$-\hat{L}^{-1}(\partial_3 \hat{L}) = \begin{pmatrix} \hat{T} & \hat{R} \\ \hat{R} & \hat{T} \end{pmatrix}, \tag{3.14}$$

in which $\hat{T}$ and $\hat{R}$ represent a transmission and reflection operator, respectively. The operators $\hat{T}$ and $\hat{R}$ vanish in homogeneous layers. This demonstrates that the two wave matrix components represent forward and backward waves, independently propagating in a homogeneous layer.

3.3.2   Electric-field strength normalization analog

It has been shown by De Hoop[49] that Equation (3.9) has nontrivial solutions if $\hat{A}_{I,J}$ is an off-diagonal matrix operator. Appendix 3.A contains some discussion about several choices for diagonalising $\hat{A}_{I,J}$. In the *electric-field strength normalization analog*[c] (EFN), the composition matrix operator is found as

$$\hat{L} = \begin{pmatrix} 1 & 1 \\ \hat{Y} & -\hat{Y} \end{pmatrix}, \tag{3.15}$$

and its inverse, the decomposition matrix operator, is given by

$$\hat{L}^{-1} = \tfrac{1}{2} \begin{pmatrix} 1 & Y^{-1} \\ 1 & -\hat{Y}^{-1} \end{pmatrix}, \tag{3.16}$$

where $\hat{Y}$ is the admittance operator

$$\hat{Y} = \hat{A}_{1,2}^{-1} \hat{\Gamma}. \tag{3.17}$$

---

[b]In this equation $(\partial_3 \hat{L}_{J,M})$ equals the commutator. This commutator has been introduced as the chain rule

$$[\partial_3, \hat{L}_{J,M}]\hat{W}_M = \underbrace{\partial_3(\hat{L}_{J,M}\hat{W}_M)}_{\partial_3 \hat{L}_{J,M}\hat{W}_M} - \hat{L}_{J,M}(\partial_3 \hat{W}_M) = (\partial_3 \hat{L}_{J,M})\hat{W}_M. \tag{3.12}$$

Note that, in general, $\partial_3 \hat{L} \neq (\partial_3 \hat{L})$: ∂_3 in $(\partial_3 \hat{L})$ act on the coefficients of $\hat{L}$ only.

[c]For acoustic waves: the acoustic-pressure normalization analog; see De Hoop[49].

In the EFN, the operator $\hat{\varGamma}$ equals

$$\hat{\varGamma} = (\hat{A}_{2,1}\hat{A}_{1,2})^{1/2} = (\mu_0\hat{\varepsilon} + \omega^{-2}\partial_1^2)^{1/2}, \tag{3.18}$$

which we call, in analogy with the 1-D case, the longitudinal slowness operator. From (3.18), we observe that $\hat{\varGamma}$ is a pseudo-differential operator (ΨDO). Some basic properties about pseudo-differential operators are discussed in Section 4. Until Section 4, we use only some operator properties of the pseudo-differential operators. For convenience, the symbol $\hat{A}$ is introduced as the square of $\hat{\varGamma}$

$$\hat{A} \stackrel{\text{def}}{=} \hat{\varGamma}^2 = \hat{A}_{2,1}\hat{A}_{1,2} = \mu_0\hat{\varepsilon} + \omega^{-2}\partial_1^2. \tag{3.19}$$

Note that $\hat{A}$ is a differential operator[d]. We call operator $\hat{A}$ the transverse Helmholtz operator, see also Fishman[23].

In the electric field strength normalization analog, we find for the electric field[e] $\hat{F}_1$

$$\hat{F}_1 = \left(\hat{W}^{(+)} + \hat{W}^{(-)}\right), \tag{3.20}$$

and for the magnetic field $\hat{F}_2$

$$\hat{F}_2 = \hat{Y}\left(\hat{W}^{(+)} - \hat{W}^{(-)}\right). \tag{3.21}$$

The wave matrices are then found as[f]

$$W^{(+)} = \tfrac{1}{2}\left(\hat{F}_1 + \hat{Y}^{-1}\hat{F}_2\right), \tag{3.22}$$

$$W^{(-)} = \tfrac{1}{2}\left(\hat{F}_1 - \hat{Y}^{-1}\hat{F}_2\right). \tag{3.23}$$

Further, we have

$$\hat{T} = -\hat{R} = -\tfrac{1}{2}\hat{Y}^{-1}(\partial_3\hat{Y}) = -\tfrac{1}{2}\hat{\varGamma}^{-1}(\partial_3\hat{\varGamma}). \tag{3.24}$$

The wave matrix differential equation is a coupled set of two one-way wave equations

$$\partial_3\hat{W}^{(+)} + \mathrm{j}\omega\,\hat{\varGamma}\hat{W}^{(+)} = \hat{T}\hat{W}^{(+)} + \hat{R}\hat{W}^{(-)}, \tag{3.25}$$

$$\partial_3\hat{W}^{(-)} - \mathrm{j}\omega\,\hat{\varGamma}\hat{W}^{(-)} = \hat{R}\hat{W}^{(+)} + \hat{T}\hat{W}^{(-)}. \tag{3.26}$$

In a longitudinal invariant configuration, the coupling terms vanish and two uncoupled one-way wave equations remain. They correspond to the left-hand sides of the above equations and are called the forward and backward one-way wave equations, respectively. Sometimes, the terms "forward and backward Helmholtz equations" are used, see März[133]. In a longitudinal invariant configuration, slowness operator $\hat{\varGamma}$ is also called the Dirichlet-to-Neumann operator, see Fishman[52]: it maps Dirichlet data ($\hat{E}_k$) to Neumann data ($\partial_3\hat{E}_k$), since according to (3.25), $\partial_3 \equiv -\mathrm{j}\omega\hat{\varGamma}$.

---

[d]For the acoustic waves: $\hat{A} = \rho\kappa + \omega^{-2}\partial_1^2$
[e]For the acoustic waves: $\hat{F}_1 = (\hat{W}^{(+)} + \hat{W}^{(-)})$.
[f]For the acoustic waves: $\hat{W}^{(\pm)} = \tfrac{1}{2}(\hat{F}_1 \pm \hat{Y}^{-1}\hat{F}_2)$.

3.4   Integral equations for the wave matrix

The solution of the set of two coupled one-way wave equations, (3.25) and (3.26), derived above are constructed by first transforming these equations into corresponding integral equations. For this transformation, we must assume, for the time being, the existence of the powers of the operator $\hat{A}$. We use the property that $\hat{A}$ and its square root are symmetric. In order to show this, we introduce a special bilinear form. Subsequently, we can derive the integral equations for the wave matrix using the Green functions. Finally, these equations are also expressed in terms of the evolution operators.

3.4.1   Symmetry of the longitudinal slowness operator

We introduce the L_2-inner product, discuss the symmetry of an operator and prove that the transverse Helmholtz operator $\hat{A}$ and the longitudinal slowness $\hat{\Gamma}$ are symmetric

Function spaces and inner product

The Hilbert space of all complex-valued square integrable functions is denoted by L_2. The L_2-inner product of the functions $\hat{u}(x_1)$ and $\hat{w}(x_1)$ is defined by

$$\langle \hat{u}, \hat{w} \rangle \stackrel{\text{def}}{=} \int_{x_1=-\infty}^{\infty} \hat{u}(x_1)\hat{w}^*(x_1)\, dx_1, \tag{3.27}$$

and the L_2-norm of $\hat{u}(x_1)$ by

$$\|\hat{u}\| = \langle \hat{u}, \hat{u} \rangle^{1/2}. \tag{3.28}$$

Here, we represent the complex conjugate of $\hat{w}$ by $\hat{w}^*$. Note that $\langle \hat{u}, \hat{w} \rangle = \langle \hat{w}, \hat{u} \rangle^*$. In this thesis, the notation $\langle \hat{u}, \hat{w} \rangle_b$ is reserved for the bilinear form, defined as

$$\langle \hat{u}, \hat{w} \rangle_b \stackrel{\text{def}}{=} \int_{x_1=-\infty}^{\infty} \hat{u}(x_1)\hat{w}(x_1)\, dx_1 = \langle \hat{u}, \hat{w}^* \rangle. \tag{3.29}$$

This is also known as the real or formal L_2-inner product[12].It is not an inner product in the mathematical sense because it is not positive definite.

The adjoint operator (or Hermite transposed) $\hat{B}^H$ of an operator $\hat{B}$ is defined as

$$\langle \hat{B}\hat{u}, \hat{w} \rangle_b \stackrel{\text{def}}{=} \langle \hat{u}, (\hat{B}^H)^* \hat{w} \rangle_b, \qquad \text{or} \qquad \langle \hat{B}\hat{u}, \hat{w} \rangle \stackrel{\text{def}}{=} \langle \hat{u}, \hat{B}^H \hat{w} \rangle. \tag{3.30}$$

The transposed operator $\hat{B}^T$ of an operator $\hat{B}$ is defined as

$$\langle \hat{B}\hat{u}, \hat{w} \rangle_b \stackrel{\text{def}}{=} \langle \hat{u}, \hat{B}^T \hat{w} \rangle_b, \qquad \text{or} \qquad \langle \hat{B}\hat{u}, \hat{w} \rangle \stackrel{\text{def}}{=} \langle \hat{u}, (\hat{B}^T)^* \hat{w} \rangle. \tag{3.31}$$

The above notation, the superscripts $^\text{T}$ and $^\text{H}$, is used to emphasize the equivalence with the linear algebra. We also define the terms *symmetric* and *skew-symmetric* in correspondance to their equivalent expressions in the linear algebra. An operator $\hat{B}$ is

$$
\begin{aligned}
&\textit{self-adjoint} && \text{if } \hat{B} = \hat{B}^\text{H}, \\
&\textit{symmetric} && \text{if } \hat{B} = \hat{B}^\text{T}, \text{ and,} \\
&\textit{skew-symmetric} && \text{if } \hat{B} = -\hat{B}^\text{T}.
\end{aligned}
$$

Now, we show that operator $\hat{A}$ and $\hat{\Gamma}$ are symmetric.

Symmetry of operator $\hat{A}$

From (3.29) follows that

$$\langle \hat{u}, \hat{w} \rangle_\text{b} = \langle \hat{w}, \hat{u} \rangle_\text{b}, \tag{3.32}$$

and

$$\langle \hat{\varepsilon}\hat{u}, \hat{w} \rangle_\text{b} = \langle \hat{u}, \hat{\varepsilon}\hat{w} \rangle_\text{b}. \tag{3.33}$$

Using the identity

$$-\hat{w}(\partial_1^2 \hat{u}) = -\partial_1(\hat{w}\partial_1 \hat{u}) + \partial_1(\hat{u}\partial_1 \hat{w}) - \hat{u}(\partial_1^2 \hat{w}), \tag{3.34}$$

Gauss' theorem and the causality condition that the field at infinity vanishes (also known as the outgoing radiation condition), it follows that

$$\langle \partial_1^2 \hat{u}, \hat{w} \rangle_\text{b} = \langle \hat{u}, \partial_1^2 \hat{w} \rangle_\text{b}. \tag{3.35}$$

Combining (3.33) and (3.35) yields that $\hat{A} = \mu_0\hat{\varepsilon} + \omega^{-2}\partial_1^2$ is symmetric, i.e.,

$$\hat{A} = \hat{A}^\text{T}. \tag{3.36}$$

If there are no losses, the permittivity is real-valued and the operator $\hat{A}$ is also self-adjoint.

Symmetry of operator $\hat{\Gamma}$

Let $\hat{\Gamma}_\text{s}$ be the symmetric part of $\hat{\Gamma}$

$$\hat{\Gamma}_\text{s} = \tfrac{1}{2}(\hat{\Gamma} + \hat{\Gamma}^\text{T}) = \hat{\Gamma}_\text{s}^\text{T}, \tag{3.37}$$

and let $\hat{\Gamma}_{-\text{s}}$ be the skew-symmetric part of $\hat{\Gamma}$

$$\hat{\Gamma}_{-\text{s}} = \tfrac{1}{2}(\hat{\Gamma} - \hat{\Gamma}^\text{T}) = -\hat{\Gamma}_{-\text{s}}^\text{T}, \tag{3.38}$$

so that

$$\hat{\varGamma} = \hat{\varGamma}_{\mathrm{s}} + \hat{\varGamma}_{-\mathrm{s}}. \tag{3.39}$$

Since $\hat{\mathrm{A}}$ is symmetric, the skew-symmetric part of $\hat{\varGamma}^2$ has to be 0 and thus

$$\hat{\varGamma}_{\mathrm{s}}\hat{\varGamma}_{-\mathrm{s}} = -\hat{\varGamma}_{-\mathrm{s}}\hat{\varGamma}_{\mathrm{s}}. \tag{3.40}$$

The symmetry properties of $\hat{\varGamma}$ depends on the choice of the square root. It is well known that the square root is a two-valued function. For energy conservation considerations, we show that there is only one physical choice for the square root and that within this choice, $\hat{\varGamma}$ is symmetric.

Consider a forward-travelling wave in an x_3-invariant configuration. The wave propagation is then described by the homogeneous version of Equation (3.25)

$$\partial_3 \hat{W}^+ + \mathrm{j}\omega\hat{\varGamma}\hat{W}^+ = 0. \tag{3.41}$$

The power transferred through the transverse plane at x_3 equals (see Equation (1.48))

$$\langle P \rangle_T(x_3) = \tfrac{1}{2}\mathrm{Re}\left(\langle \hat{S}_3, 1 \rangle\right), \tag{3.42}$$

with $\hat{S}_3 = \hat{F}_1\hat{F}_2^*$. Since we consider an x_3-invariant structure, the composition operator $\hat{Y} = \mu_0^{-1}\hat{\varGamma}$ is invariant, and therefore it is sufficient to show that $\partial_3\langle \hat{W}^+, \hat{W}^+ \rangle$ is negative (attenuation) or zero (no attenuation). Using (3.41) yields

$$\begin{aligned}
\partial_3\langle \hat{u}, \hat{w} \rangle &= \langle \partial_3\hat{u}, \hat{w} \rangle + \langle \hat{u}, \partial_3\hat{w} \rangle \\
&= \langle -\mathrm{j}\omega\hat{\varGamma}\hat{u}, \hat{w} \rangle + \langle \hat{u}, -\mathrm{j}\omega\hat{\varGamma}\hat{w} \rangle \\
&= -\mathrm{j}\omega \left\langle (\hat{\varGamma} - \hat{\varGamma}^{\mathrm{H}})\hat{u}, \hat{w} \right\rangle \\
&= -2\mathrm{j}\omega \left\langle \mathrm{Re}(\hat{\varGamma}_{-\mathrm{s}})\hat{u}, \hat{w} \right\rangle + 2\omega \left\langle \mathrm{Im}(\hat{\varGamma}_{\mathrm{s}})\hat{u}, \hat{w} \right\rangle. \tag{3.43}
\end{aligned}$$

Since (take $\hat{u} = \hat{w} = \hat{W}^+$)

$$\langle \mathrm{Re}(\hat{\varGamma}_{-\mathrm{s}})\hat{W}^+, \hat{W}^+ \rangle = -\langle \hat{W}^+, \mathrm{Re}(\hat{\varGamma}_{-\mathrm{s}})\hat{W}^+ \rangle = -\langle \mathrm{Re}(\hat{\varGamma}_{-\mathrm{s}})\hat{W}^+, \hat{W}^+ \rangle^*, \tag{3.44}$$

it is imaginary and the first term on the right-hand side of (3.43) is real valued (positive or negative). However,

$$\langle \mathrm{Im}(\hat{\varGamma}_{\mathrm{s}})\hat{W}^+, \hat{W}^+ \rangle = \langle \hat{W}^+, \mathrm{Im}(\hat{\varGamma}_{\mathrm{s}})\hat{W}^+ \rangle = \langle \mathrm{Im}(\hat{\varGamma}_{\mathrm{s}})\hat{W}^+, \hat{W}^+ \rangle^*, \tag{3.45}$$

and thus the second term on the right-hand side of (3.43) is also real valued. This term is negative if $-\mathrm{Im}(\hat{\varGamma}_{\mathrm{s}})$ is positive definite and thus if we choose $\mathrm{Im}[(.)^{1/2}] < 0$ for passive media.

In order to have a physical wave propagation, we have to choose a symmetrical $\hat{\Gamma}$

$$\hat{\Gamma} = \hat{\Gamma}_s = \hat{\Gamma}^\mathrm{T}. \tag{3.46}$$

For passive media, we choose a square root with $\mathrm{Im}[(.)^{1/2}] < 0$ (branch-cut along the real positive axis). For active media, one chooses $\mathrm{Re}[(.)]^{1/2} > 0$.

In the further computations, we use this symmetry property of operator $\hat{\Gamma}$. The same result can be obtained via an eigenvalue analysis, see Wapenaar and Grimbergen[134].

3.4.2 Green's functions

The solution of the set of two coupled one-way wave equations, (3.25) and (3.26) derived above is constructed by first transforming these equations into corresponding integral equations. In this approach, the behavior of the left-hand sides of these equations is required. The Green functions corresponding to the left-hand sides of (3.25) and (3.26), satisfy[g]

$$\partial_3 \hat{\mathcal{G}}^{(+)}(x_1, x_3; x_1', x_3') + \mathrm{j}\omega\hat{\Gamma}(x_1, x_3)\hat{\mathcal{G}}^{(+)}(x_1, x_3; x_1', x_3') = \delta(x_1 - x_1', x_3 - x_3'), \tag{3.47}$$

$$\partial_3 \hat{\mathcal{G}}^{(-)}(x_1, x_3; x_1', x_3') - \mathrm{j}\omega\hat{\Gamma}(x_1, x_3)\hat{\mathcal{G}}^{(-)}(x_1, x_3; x_1', x_3') = \delta(x_1 - x_1', x_3 - x_3'). \tag{3.48}$$

The explicit expressions is discussed later. Due to reciprocity, the relation between these Green functions is (see Appendix 3.A)

$$\hat{\mathcal{G}}^{(+)}(x_1, x_3; x_1', x_3') = -\hat{\mathcal{G}}^{(-)}(x_1', x_3'; x_1, x_3). \tag{3.49}$$

Using these Green functions, we can transform the differential equations for the wave matrices into the corresponding integral equations. Multiplication of Equation (3.25) by $\hat{\mathcal{G}}^{(-)}(x_1, x_3; x_1', x_3')$ and Equation (3.48) by $\hat{W}^{(+)}(x_1, x_3)$ yield

$$\hat{\mathcal{G}}^{(-)}\partial_3 \hat{W}^{(+)} + \hat{W}^{(+)}\partial_3 \hat{\mathcal{G}}^{(-)} + \hat{\mathcal{G}}^{(-)}\mathrm{j}\omega\hat{\Gamma}\hat{W}^{(+)} - \hat{W}^{(+)}\mathrm{j}\omega\hat{\Gamma}\hat{\mathcal{G}}^{(-)}$$
$$= \hat{\mathcal{G}}^{(-)}\hat{T}\hat{W}^{(+)} + \hat{\mathcal{G}}^{(-)}\hat{R}\hat{W}^{(-)} + \hat{W}^{(+)}\delta(x_1 - x_1', x_3 - x_3'). \tag{3.50}$$

Note that the last two terms on the left-hand side do not vanish. Using the symmetry of $\hat{\Gamma}$, the integration of these two terms over the interval $-\infty < x_1 < \infty$ yields

$$\langle \hat{\mathcal{G}}^{(-)}, \mathrm{j}\omega\hat{\Gamma}\hat{W}^{(+)}\rangle_\mathrm{b} - \langle \hat{W}^{(+)}, \mathrm{j}\omega\hat{\Gamma}\hat{\mathcal{G}}^{(-)}\rangle_\mathrm{b} = 0. \tag{3.51}$$

---

[g]In this notation $\hat{\Gamma}(x_1, x_3)\hat{\mathcal{G}}(x_1, x_3)$ stands for $(\hat{\Gamma}\hat{\mathcal{G}})(x_1, x_3)$.

The integration of (3.50) over the entire transverse x_1-line results in

$$\int_{x_1=-\infty}^{\infty} \partial_3 \left[\hat{\mathcal{G}}^{(-)}(x_1, x_3; x_1', x_3') \, \hat{W}^{(+)}(x_1, x_3) \right] \mathrm{d}x_1$$

$$= \int_{x_1=-\infty}^{\infty} \hat{\mathcal{G}}^{(-)}(x_1, x_3; x_1', x_3') \, \hat{T}(x_1, x_3) \, \hat{W}^{(+)}(x_1, x_3) \, \mathrm{d}x_1$$

$$+ \int_{x_1=-\infty}^{\infty} \hat{\mathcal{G}}^{(-)}(x_1, x_3; x_1', x_3') \, \hat{R}(x_1, x_3) \, \hat{W}^{(-)}(x_1, x_3) \, \mathrm{d}x_1$$

$$+ \hat{W}^{(+)}(x_1', x_3)\delta(x_3 - x_3'). \tag{3.52}$$

The next step is the integration of Equation (3.52) over the interval $0 < x_3 < x_3^{\mathrm{exit}}$: the finite section of the structure between the entrance plane $x_3 = 0$ and the exit plane $x_3 = x_3^{\mathrm{exit}}$. Using the relation

$$\int_{x_3=0}^{x_3^{\mathrm{exit}}} \int_{x_1=-\infty}^{\infty} \partial_3 \left[\hat{\mathcal{G}}^{(-)}(x_1, x_3; x_1', x_3')\hat{W}^{(+)}(x_1, x_3) \right] \mathrm{d}x_1 \mathrm{d}x_3$$

$$= - \int_{x_1=-\infty}^{\infty} \hat{\mathcal{G}}^{(-)}(x_1, 0; x_1', x_3')\hat{W}^{(+)}(x_1, 0) \, \mathrm{d}x_1, \tag{3.53}$$

where we substituted

$$\hat{G}^{(-)}(x_1, x_3^{\mathrm{exit}}; x_1', x_3') = 0, \qquad (x_3' < x_3^{\mathrm{exit}}), \tag{3.54}$$

and with (3.49) we find

$$\int_{x_1=-\infty}^{\infty} \hat{G}^{(+)}(x_1', x_3'; x_1, 0) \, \hat{W}^{(+)}(x_1, 0) \, \mathrm{d}x_1$$

$$= \hat{W}^{(+)}(x_1', x_3')$$

$$- \int_{x_3=0}^{x_3^{\mathrm{exit}}} \int_{x_1=-\infty}^{\infty} \hat{\mathcal{G}}^{(+)}(x_1', x_3'; x_1, x_3) \, \hat{T}(x_1, x_3)\hat{W}^{(+)}(x_1, x_3) \, \mathrm{d}x_1 \mathrm{d}x_3$$

$$- \int_{x_3=0}^{x_3^{\mathrm{exit}}} \int_{x_1=-\infty}^{\infty} \hat{\mathcal{G}}^{(+)}(x_1', x_3'; x_1, x_3) \, \hat{R}(x_1, x_3)\hat{W}^{(-)}(x_1, x_3) \, \mathrm{d}x_1 \mathrm{d}x_3. \tag{3.55}$$

In a similar way, we find

$$0 = \hat{W}^{(-)}(x_1', x_3')$$

$$- \int_{x_3=0}^{x_3^{\mathrm{exit}}} \int_{x_1=-\infty}^{\infty} \hat{\mathcal{G}}^{(-)}(x_1', x_3'; x_1, x_3) \, \hat{R}(x_1, x_3)\hat{W}^{(+)}(x_1, x_3) \, \mathrm{d}x_1 \mathrm{d}x_3$$

$$- \int_{x_3=0}^{x_3^{\mathrm{exit}}} \int_{x_1=-\infty}^{\infty} \hat{\mathcal{G}}^{(-)}(x_1', x_3'; x_1, x_3) \, \hat{T}(x_1, x_3)\hat{W}^{(-)}(x_1, x_3) \, \mathrm{d}x_1 \mathrm{d}x_3. \tag{3.56}$$

Knowing the Green functions $\hat{\mathcal{G}}^{(+)}$ and $\hat{\mathcal{G}}^{(-)}$ (solutions of (3.47) and (3.48)), we can also use the superposition principle to obtain the above relations directly from Equations (3.25) and (3.26). In a compact operator form, the integral equations for the wave matrix reads

$$(\delta_{I,J} - \hat{K}_{I,J})(x_1, x_3)\hat{W}_J(x_1, x_3) = \hat{W}_J^{(0)}(x_1, x_3),\tag{3.57}$$

where

$$\hat{W}_1^{(0)}(x_1, x_3) = \int_{x_1' = -\infty}^{\infty} \hat{\mathcal{G}}^{(+)}(x_1, x_3; x_1', 0)\, \hat{W}^{(+)}(x_1', 0)\, dx_1',\tag{3.58}$$

$$\hat{W}_2^{(0)}(x_1, x_3) = 0,\tag{3.59}$$

are the direct waves and the terms

$$\left(\hat{K}_{1,1}\hat{W}^{(+)}\right)(x_1, x_3) = \int_{\zeta=0}^{x_3} \int_{x_1' = -\infty}^{\infty} \hat{\mathcal{G}}^{(+)}(x_1, x_3; x_1', \zeta)\left(\hat{T}\hat{W}^{(+)}\right)(x_1', \zeta)\, dx_1' d\zeta,\tag{3.60}$$

$$\left(\hat{K}_{1,2}\hat{W}^{(-)}\right)(x_1, x_3) = \int_{\zeta=0}^{x_3} \int_{x_1' = -\infty}^{\infty} \hat{\mathcal{G}}^{(+)}(x_1, x_3; x_1', \zeta)\left(\hat{R}\hat{W}^{(-)}\right)(x_1', \zeta)\, dx_1' d\zeta,\tag{3.61}$$

$$\left(\hat{K}_{2,1}\hat{W}^{(+)}\right)(x_1, x_3) = \int_{\zeta=x_3}^{x_3^{\text{exit}}} \int_{x_1' = -\infty}^{\infty} \hat{\mathcal{G}}^{(-)}(x_1, x_3; x_1', \zeta)\left(\hat{R}\hat{W}^{(+)}\right)(x_1', \zeta)\, dx_1' d\zeta,\tag{3.62}$$

$$\left(\hat{K}_{2,2}\hat{W}^{(-)}\right)(x_1, x_3) = \int_{\zeta=x_3}^{x_3^{\text{exit}}} \int_{x_1' = -\infty}^{\infty} \hat{\mathcal{G}}^{(-)}(x_1, x_3; x_1', \zeta)\left(\hat{T}\hat{W}^{(-)}\right)(x_1', \zeta)\, dx_1' d\zeta,\tag{3.63}$$

describe the interaction between the forward- and backward-propagating waves. Because $\hat{T} = -\hat{R}$, the above four terms can be combined into two terms.

3.4.3 Evolution operators

In some approaches, the expressions derived above are rewritten in terms of evolution operators, which are also called Green's operators or propagators. This has the advantage of a compact notational form and it serves also as basis for the numerical implementation. The relation between the evolution operators and the Green functions is shown first.

Multiplying (3.47) by some test function $\hat{u}(x_1', x_3')$ and integrating over the in-
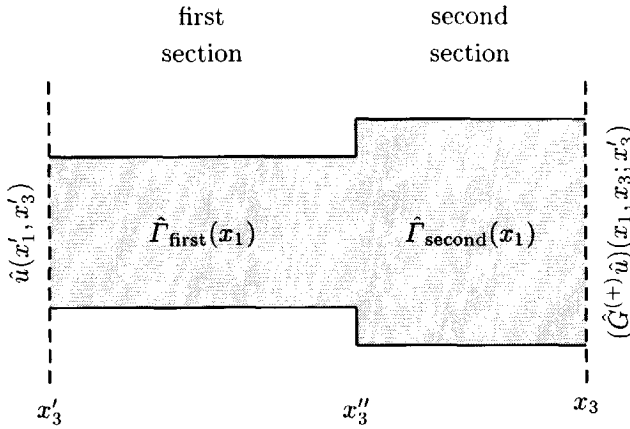
Figure 3.1: *Two longitudinal invariant sections.*

terval $-\infty < x_1' < \infty$ yield

$$\partial_3 \int_{x_1'=-\infty}^{\infty} \hat{\mathcal{G}}^{(+)}(x_1, x_3; x_1', x_3')\hat{u}(x_1', x_3') \, \mathrm{d}x_1'$$

$$+ \mathrm{j}\omega\hat{\Gamma}(x_1, x_3) \int_{x_1'=-\infty}^{\infty} \hat{\mathcal{G}}^{(+)}(x_1, x_3; x_1', x_3')\hat{u}(x_1', x_3') \, \mathrm{d}x_1'$$

$$= \hat{u}(x_1, x_3')\delta(x_3 - x_3'). \quad (3.64)$$

We now introduce the forward evolution operator or forward Green operator $\hat{G}^{(+)}$ as

$$(\hat{G}^{(+)}\hat{u})(x_1, x_3; x_3') \stackrel{\text{def}}{=} \int_{x_1'=-\infty}^{\infty} \hat{\mathcal{G}}^{(+)}(x_1, x_3; x_1', x_3')\hat{u}(x_1', x_3') \, \mathrm{d}x_1'. \tag{3.65}$$

Equation (3.64) reduces to

$$\partial_3(\hat{G}^{(+)}\hat{u})(x_1, x_3; x_3') + \mathrm{j}\omega\hat{\Gamma}(x_1, x_3)(\hat{G}^{(+)}\hat{u})(x_1, x_3; x_3') = \hat{u}(x_1, x_3')\delta(x_3 - x_3'). \tag{3.66}$$

For the construction of the forward evolution operator $\hat{G}^{(+)}$ we first examine a longitudinal invariant section. With a simple substitution and using the causality conditions

$$(\hat{G}^{(+)}\hat{u})(x_1, x_3; x_3') = 0, \qquad \text{for } x_3 < x_3', \tag{3.67}$$

it is checked whether the evolution operator in a longitudinal invariant section equals

$$(\hat{G}^{(+)}\hat{u})(x_1, x_3; x_3') = H(x_3 - x_3') \exp\left[-\mathrm{j}\omega(x_3 - x_3')\hat{\Gamma}(x_1)\right] \hat{u}(x_1, x_3'). \tag{3.68}$$
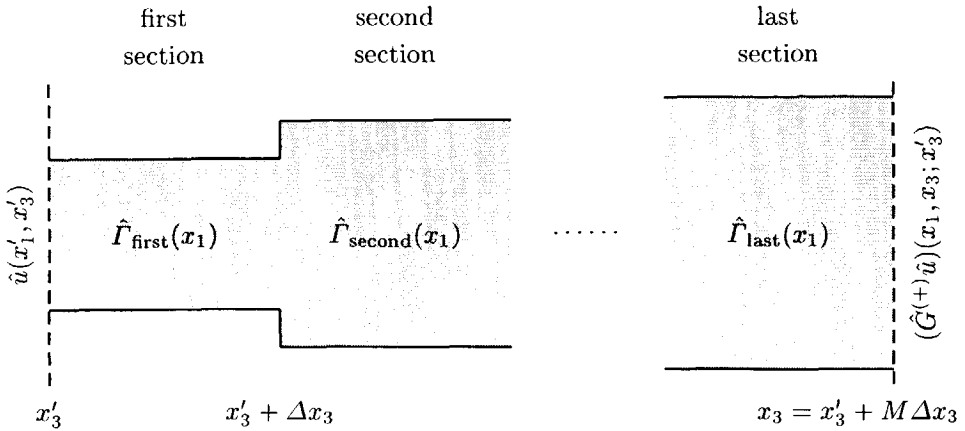
Figure 3.2: *Cascading of M longitudinal invariant sections.*

By considering two longitudinal invariant sections, as shown in Figure 3.1, the overall evolution operator results from the cascading of two forward evolution operators

$$
\begin{aligned}
(G^{(+)}u)(x_1, x_3; x_3') &= (G_{\text{second}}^{(+)} \hat{G}_{\text{first}}^{(+)} \hat{u})(x_1, x_3; x_3') \\
&= H(x_3 - x_3'') \exp\left[-\mathrm{j}\omega(x_3 - x_3'')\hat{\Gamma}_{\text{second}}(x_1)\right] \\
&\quad H(x_3'' - x_3') \exp\left[-\mathrm{j}\omega(x_3'' - x_3')\hat{\Gamma}_{\text{first}}(x_1)\right] \hat{u}(x_1, x_3').
\end{aligned}
$$

$$(3.69)$$

Note that the operators in the exponents do not commute in general. The full-range evolution operator over an arbitrary longitudinal variant structure is derived by first cascading M evolution operators which are chosen such that they span the full range (x_3', x_3), and by subsequently taking the limit $M \to \infty$ with $\Delta x_3 = (x_3 - x_3')/M > 0$ (see Figure 3.2)

$$
\begin{aligned}
(\hat{G}^{(+)}\hat{u})(x_1, x_3; x_3') &= (\hat{G}_{\text{last}}^{(+)} \cdots \hat{G}_{\text{second}}^{(+)} \hat{G}_{\text{first}}^{(+)} \hat{u})(x_1, x_3; x_3') \\
&= H(x_3 - x_3') \lim_{M \to \infty} \exp\left[-\mathrm{j}\omega\Delta x_3 \hat{\Gamma}_{\text{last}}(x_1)\right] \quad \cdots \\
&\quad \exp\left[-\mathrm{j}\omega\Delta x_3 \hat{\Gamma}_{\text{second}}(x_1)\right] \exp\left[-\mathrm{j}\omega\Delta x_3 \hat{\Gamma}_{\text{first}}(x_1)\right] \hat{u}(x_1, x_3') \\
&= H(x_3 - x_3') \lim_{M \to \infty} \exp\left\{-\mathrm{j}\omega\Delta x_3 \hat{\Gamma}[x_1, x_3' + (M - \tfrac{1}{2})\Delta x_3]\right\} \quad \cdots \\
&\quad \exp\left[-\mathrm{j}\omega\Delta x_3 \hat{\Gamma}(x_1, x_3' + \tfrac{3}{2}\Delta x_3)\right] \exp\left[-\mathrm{j}\omega\Delta x_3 \hat{\Gamma}(x_1, x_3' + \tfrac{1}{2}\Delta x_3)\right] \hat{u}(x_1, x_3')
\end{aligned}
$$

$$\stackrel{\text{def}}{=} H(x_3 - x_3') \left\{ \prod_{z=x_3'}^{x_3} \exp\left[-\mathrm{j}\omega\hat{\Gamma}(x_1, z)\,\mathrm{d}z\right] \right\} \hat{u}(x_1, x_3'). \tag{3.70}$$

Here we introduced the product integral, for which the above ordering rules apply (see DeWitt-Morette, Maheshwari and Nelson[135]). With a similar analysis we find the full range backward evolution operator as

$$(\hat{G}^{(-)}\hat{u})(x_1, x_3; x_3') \stackrel{\text{def}}{=} \int_{x_1'=-\infty}^{\infty} \hat{\mathcal{G}}^{(-)}(x_1, x_3; x_1', x_3')\hat{u}(x_1', x_3')\mathrm{d}x_1'$$

$$= -H(x_3' - x_3) \left\{ \prod_{z=x_3'}^{x_3} \exp[\mathrm{j}\omega\hat{\Gamma}(x_1, z)\mathrm{d}z] \right\} \hat{u}(x_1, x_3').$$

$$\tag{3.71}$$

Using these explicit expressions of the evolution operators in terms of product integrals, the Equations (3.58)-(3.63) transform into for $0 < x_3 < x_3^{\text{exit}}$

$$\hat{W}_1^{(0)}(x_1, x_3) = H(x_3 - x_3') \left\{ \prod_{z=x_3'}^{x_3} \exp[-\mathrm{j}\omega\hat{\Gamma}(x_1, z)\,\mathrm{d}z] \right\} \hat{W}_1(x_1, 0), \tag{3.72}$$

$$\hat{W}_2^{(0)}(x_1, x_3) = 0, \tag{3.73}$$

$$\left(\hat{K}_{1,1}\hat{W}^{(+)}\right)(x_1, x_3)$$

$$= \int_{\zeta=0}^{x_3} \left\{ \prod_{z=\zeta}^{x_3} \exp[-\mathrm{j}\omega\hat{\Gamma}(x_1, z)\,\mathrm{d}z] \right\} \left(\hat{T}\hat{W}^{(+)}\right)(x_1, \zeta)\,\mathrm{d}\zeta, \tag{3.74}$$

$$\left(\hat{K}_{1,2}\hat{W}^{(-)}\right)(x_1, x_3)$$

$$= \int_{\zeta=0}^{x_3} \left\{ \prod_{z=\zeta}^{x_3} \exp[-\mathrm{j}\omega\hat{\Gamma}(x_1, z)\,\mathrm{d}z] \right\} \left(\hat{R}\hat{W}^{(-)}\right)(x_1, \zeta)\,\mathrm{d}\zeta, \tag{3.75}$$

$$\left(\hat{K}_{2,1}\hat{W}^{(+)}\right)(x_1, x_3)$$

$$= -\int_{\zeta=x_3}^{x_3^{\text{exit}}} \left\{ \prod_{z=\zeta}^{x_3} \exp[\mathrm{j}\omega\hat{\Gamma}(x_1, z)\,\mathrm{d}z] \right\} \left(\hat{R}\hat{W}^{(+)}\right)(x_1, \zeta)\,\mathrm{d}\zeta, \tag{3.76}$$

$$\left(\hat{K}_{2,2}\hat{W}^{(-)}\right)(x_1, x_3)$$

$$= -\int_{\zeta=x_3}^{x_3^{\text{exit}}} \left\{ \prod_{z=\zeta}^{x_3} \exp[\mathrm{j}\omega\hat{\Gamma}(x_1, z)\,\mathrm{d}z] \right\} \left(\hat{T}\hat{W}^{(-)}\right)(x_1, \zeta)\,\mathrm{d}\zeta. \tag{3.77}$$

3.5 Numerical aspects of the Bremmer coupling series

In the previous sections, we have derived the Bremmer coupling series. Assuming that the square root operator $\hat{\Gamma}$ is known, we discuss the numerical aspects of the BPM-type approach and the Bremmer series in this section.

The directional wave-field decomposition method contains three main steps:

① directional decomposition of the field of the given incident wave (compare with (3.20))

$$\hat{W}^{(+)}(x_1, 0) = \hat{E}_2^{\text{incident}}(x_1, 0), \tag{3.78}$$

if the electric field is predescribed, and

$$\hat{W}^{(+)}(x_1, 0) = -\hat{Y}^{-1} \hat{H}_1^{\text{incident}}(x_1, 0), \tag{3.79}$$

if the magnetic field is predescribed,

② computation of the counter-propagating waves inside the configuration by solving the integral Equation (3.57), and,

③ composition of the counter-propagating waves into the electromagnetic fields at the positions of interest (Equations (3.20) and (3.21)).

The numerical implementation is thus split into two scattering problems: one in the longitudinal direction and one in the transverse direction. In here, we have discussed only the scattering problem in the longitudinal directional. Its numerical implementation is similar to that in 1-D structures and is discussed below. For this, we consider two methods: the classical BPM-type approach and the approach using the Bremmer coupling series. In the next two chapters, the scattering problem in the transverse direction will be discussed.

3.5.1 BPM-type approach

The classical BPM-type approaches assume that the medium properties vary slowly in the longitudinal direction. In such configurations, the influence of operator $\hat{K}_{I,J}$ in (3.57) can be neglected and the forward-directed transmitted field is dominant, hence

$$\hat{W}^{(+)}(x_1, x_3) \simeq \hat{W}_1^{(0)}(x_1, x_3), \tag{3.80}$$

$$\hat{W}^{(-)}(x_1, x_3) \simeq 0. \tag{3.81}$$

The calculation of these forward-directed waves is performed with a recurrent scheme. In this recurrent scheme, the forward-directed wave at a particular transverse plane

(or slice) $x_3 = m\Delta x_3$ is related to the forward-directed wave at the **previous** transverse plane $x_3 = (m-1)\Delta x_3$. The configuration is then divided into M points and the forward-directed waves are only calculated at the transverse planes $x_3 = 0, \Delta x_3, \cdots, m\Delta x_3, \cdots, M\Delta x_3$ ($\Delta x_3 = x_3^{\mathrm{exit}}/M$), see Figure 2.5. It is, however, not necessary to use a fixed propagation step Δx_3: Δx_3 may vary along the longitudinal direction. This recurrent scheme follows from rewriting Equation (3.72) as

$$\hat{W}_1^{(0)}(x_1, 0) = \hat{W}^{(+)}(x_1, 0) \tag{3.82}$$

$$\hat{W}_1^{(0)}(x_1, m\Delta x_3) = \hat{P}(x_1, m)\hat{W}_1^{(0)}[x_1, (m-1)\Delta x_3], \qquad m \geq 1, \tag{3.83}$$

where the operator $\hat{P}(x_1, m)$ equals

$$\hat{P}(x_1, m) = \left\{ \prod_{z=(m-1)\Delta x_3}^{m\Delta x_3} \exp\left[-\mathrm{j}\omega\hat{\Gamma}(x_1, z)\,\mathrm{d}z \right] \right\}. \tag{3.84}$$

The distance Δx_3 is often called the propagation step. In the numerical implementation, we can approximate $\hat{P}(x_1, m)$ by its half-way value

$$\hat{P}(x_1, m) \simeq \exp\left\{ -\mathrm{j}\omega\hat{\Gamma}\left[x_1, (m-\tfrac{1}{2})\Delta x_3 \right] \Delta x_3 \right\} + \mathcal{O}(\Delta x_3), \tag{3.85}$$

or by taking a higher approximation as

$$\hat{P}(x_1, m) \simeq \exp\left[-\mathrm{j}\omega\tfrac{1}{2}\hat{\Gamma}\left(x_1, m\Delta x_3 \right) \Delta x_3 \right]$$
$$\exp\left\{ -\mathrm{j}\omega\tfrac{1}{2}\hat{\Gamma}\left[x_1, (m-1)\Delta x_3 \right] \Delta x_3 \right\} + \mathcal{O}(\Delta x_3^2) \tag{3 86}$$

We refer this numerical scheme to the two-dimensional *forward BPM-type scheme*.

3.5.2   Bremmer coupling series

In many applications in the field of integrated optics, geoelectromagnetics and acoustics the interaction between the counter-propagating waves is weak. In such a case we may assume that the norm of the operator $\hat{K}_{I,J}$ is less than 1, so that the Neumann expansion can be applied to the inverse of $(\delta_{I,J} - \hat{K}_{I,J})$ in Equation (3.57). This leads to the Bremmer coupling series[49, 131]

$$\hat{W}_I = \sum_{j=0}^{\infty} (\hat{K}^j)_{I,J}\hat{W}_J^{(0)} = \hat{W}_I^{(0)} + \hat{K}_{I,J}\hat{W}_J^{(0)} + (\hat{K}^2)_{I,J}\hat{W}_J^{(0)} + \cdots. \tag{3.87}$$

To emphasize the physical nature of the expansion, we write

$$\hat{W}_I = \sum_{j=0}^{\infty} \hat{W}_I^{(j)}, \tag{3.88}$$

in which

$$\hat{W}_I^{(j)} = \hat{K}_{I,J}\hat{W}_J^{(j-1)}, \qquad (j \geq 1), \tag{3.89}$$

can be interpreted by the j-times reflected/transmitted or scattered wave. This equation shows that the solution is found by solving an iterative scheme. The separate terms are subsequently determined in a similar way.

To show the numerical implementation of each term of the Bremmer coupling series, we first consider one element on the right-hand side of (3.89), e.g. $\hat{K}_{1,1}\hat{W}_1^{(j-1)}$. For convenience, we introduce the shorthand notation

$$\hat{Q}_I^{(j)}(x_1, \zeta) \overset{\text{def}}{=} \left(\hat{T}\hat{W}_I^{(j-1)}\right)(x_1, \zeta), \tag{3.90}$$

$$\hat{I}_{I,1}^{(j)}(x_1, m) \overset{\text{def}}{=} \left(\hat{K}_{I,1}\hat{W}_1^{(j-1)}\right)(x_1, m\Delta x_3), \tag{3.91}$$

and

$$\hat{I}_{I,2}^{(j)}(x_1, m) \overset{\text{def}}{=} \left(\hat{K}_{I,2}\hat{W}_2^{(j-1)}\right)(x_1, m\Delta x_3). \tag{3.92}$$

Similarly to the case of the forward BPM-type scheme, a recursive scheme for $\hat{I}_{1,1}^{(j)}(x_1, m)$ is constructed

$$\hat{I}_{1,1}^{(j)}(x_1, m) = \int_{\zeta=0}^{m\Delta x_3} \left\{\prod_{z=\zeta}^{m\Delta x_3} \exp\left[-j\omega\hat{\Gamma}(x_1, z)\,dz\right]\right\} \hat{Q}_1^{(j)}(x_1, \zeta)\,d\zeta$$

$$= \left\{\prod_{z=(m-1)\Delta x_3}^{m\Delta x_3} \exp\left[-j\omega\hat{\Gamma}(x_1, z)\,dz\right]\right\}$$

$$\int_{\zeta=0}^{(m-1)\Delta x_3} \left\{\prod_{z=\zeta}^{m\Delta x_3} \exp\left[-j\omega\hat{\Gamma}(x_1, z)\,dz\right]\right\} \hat{Q}_1^{(j)}(x_1, \zeta)\,d\zeta$$

$$+ \int_{\zeta=(m-1)\Delta x_3}^{m\Delta x_3} \left\{\prod_{z=\zeta}^{m\Delta x_3} \exp\left[-j\omega\hat{\Gamma}(x_1, z)\,dz\right]\right\} \hat{Q}_1^{(j)}(x_1, \zeta)\,d\zeta$$

$$= \hat{P}(x_1, m)\hat{I}_{1,1}^{(j)}(x_1, m-1) + \hat{q}_{1,1}^{(j)}(x_1, m), \tag{3.93}$$

where the operator $\hat{P}(x_1, m)$ is given in (3.84) and

$$\hat{I}_{1,1}^{(j)}(x_1, 0) = 0, \tag{3.94}$$

$$\hat{q}_{1,1}^{(j)}(x_1, m) = \int_{\zeta=(m-1)\Delta x_3}^{m\Delta x_3} \left\{\prod_{z=\zeta}^{m\Delta x_3} \exp\left[-j\omega\hat{\Gamma}(x_1, z)\,dz\right]\right\} \hat{Q}_1^{(j)}(x_1, \zeta)\,d\zeta. \tag{3.95}$$

In the numerical implementation, we apply an approximation to the product integral in $\hat{q}_{1,1}^{(j)}(x_1, m)$

$$\hat{q}_{1,1}^{(j)}(x_1, m) \simeq \tfrac{1}{2}\Delta x_3 \left\{ \hat{Q}_1^{(j)}(x_1, m\Delta x_3) + \hat{P}(x_1, m)\hat{Q}_1^{(j)}[x_1, (m-1)\Delta x_3] \right\} + \mathcal{O}[(\Delta x_3)^2]. \quad (3.96)$$

The other terms on the right-hand side of (3.89) can be determined in a similar way. Our numerical scheme for the j-times, reflected wave reads

$$\hat{W}_1^{(j)}(x_1, m\Delta x_3) = \hat{I}_{1,1}^{(j)}(x_1, m) - \hat{I}_{1,2}^{(j)}(x_1, m), \quad (3.97)$$

$$\hat{W}_2^{(j)}(x_1, m\Delta x_3) = -\hat{I}_{2,1}^{(j)}(x_1, m) + \hat{I}_{2,2}^{(j)}(x_1, m), \quad (3.98)$$

$(j, m = 0, 1, 2, \cdots)$ with

$$\hat{I}_{1,J}^{(j)}(x_1, m) = \hat{P}(x_1, m) \quad \hat{I}_{1,J}^{(j)}(x_1, m-1) + \hat{q}_{1,J}^{(j)}(x_1, m), \quad m \geq 1, \quad (3.99)$$

$$\hat{I}_{2,J}^{(j)}(x_1, m) = \hat{P}(x_1, m+1)\hat{I}_{2,J}^{(j)}(x_1, m+1) + \hat{q}_{2,J}^{(j)}(x_1, m), \quad m \leq M-1, \quad (3.100)$$

in which

$$\hat{q}_{1,J}^{(j)}(x_1, m) = \int_{\zeta=(m-1)\Delta x_3}^{m\Delta x_3} \left\{ \prod_{z=\zeta}^{m\Delta x_3} \exp\left[-j\omega\hat{\Gamma}(x_1, z)\,dz\right] \right\} \hat{Q}_J^{(j)}(x_1, \zeta)\,d\zeta$$

$$\simeq \tfrac{1}{2}\Delta x_3 \left\{ \hat{Q}_J^{(j)}(x_1, m\Delta x_3) + \hat{P}(x_1, m)\hat{Q}_J^{(j)}[x_1, (m-1)\Delta x_3] \right\}, \quad (3.101)$$

$$\hat{q}_{2,J}^{(j)}(x_1, m) = \int_{\zeta=(m+1)\Delta x_3}^{m\Delta x_3} \left\{ \prod_{z=m\Delta x_3}^{\zeta} \exp\left[-j\omega\hat{\Gamma}(x_1, z)\,dz\right] \right\} \hat{Q}_J^{(j)}(x_1, \zeta)\,d\zeta$$

$$\simeq -\tfrac{1}{2}\Delta x_3 \left\{ \hat{Q}_J^{(j)}(x_1, m\Delta x_3) + \hat{P}(x_1, m+1)\hat{Q}_J^{(j)}[x_1, (m+1)\Delta x_3] \right\}, \quad (3.102)$$

in which

$$\hat{Q}_J^{(j)}(x_1, m\Delta x_3) = \left(\hat{T}\hat{W}_J^{(j-1)}\right)(x_1, m\Delta x_3), \quad j \geq 0, \quad (3.103)$$

and with the initial values

$$\hat{I}_{1,J}^{(0)}(x_1, 0) \quad = \hat{W}^{(+)}(x_1, 0), \quad (3.104)$$

$$\hat{I}_{1,J}^{(j)}(x_1, 0) \quad = 0, \quad (3.105)$$

$$\hat{I}_{2,J}^{(j)}(x_1, M) \quad = 0, \quad (3.106)$$

$$\hat{Q}_J^{(0)}(x_1, m\Delta x_3) = 0. \quad (3.107)$$

The flow chart for this numerical scheme is very similar to the flow chart of the 1-D scheme, see Figure 2.8. Observe that $\hat{I}_{1,1}^{(j)}$ and $\hat{I}_{1,2}^{(j)}$ (and also $\hat{I}_{2,1}^{(j)}$ and $\hat{I}_{2,2}^{(j)}$) can be computed simultaneously.

The computer capacity for data storing might be too small, because in every term j of the Bremmer coupling series, the reflected and transmitted field $\hat{Q}_j^{(j+1)}(x_1, m\Delta x_3)$ must be calculated and stored. In an x_3-invariant section, however, $\hat{Q}_j^{(j+1)}(x_1, m\Delta x_3) = 0$. If the variation in the x_3 direction is very slow, the transmitted and reflected fields are small and can be neglected. An energy criterion for detecting these small fields can be introduced by which the amount of data to be stored is reduced. The energy criterion rules can be determined by some numerical tests.

In this Bremmer coupling series, we still need to compute the operators $\hat{P}(x_1, m)$ and $\hat{T}(x_1, m\Delta x_3)$. Besides, for the computation of the magnetic fields one also needs to calculate the operator $\hat{\Gamma}$ (see Equation (3.21)). If the magnetic field of the incident wave is prescribed, then the decomposition operator $\hat{\Gamma}^{-1}$ has to be determined, too. These operators are all determined by the description of the scattering problem in the transverse direction. This is discussed in the next chapter.

3.6 Discussion of the results

In analogy with the 1-D configuration, we have introduced the Bremmer coupling series for the scattering problem along the longitudinal direction. Assuming that the scattering in the transverse direction is known, a new numerical implementation has been developed. The only thing which has still to be done, is computing the square root operator $\hat{\Gamma}$ for describing the scattering problem in the transverse direction. In this chapter, we showed that this operator is symmetric. In the next chapter, the square root operator will be analyzed.

Appendix

3.A   Relation between the forward and backward Green functions

To construct the Bremmer series in Section 3.4, we need the relation between the forward and backward Green functions. This relation is derived with use of the reciprocal forward Green function.

We introduce the reciprocal forward Green function $\hat{\mathcal{G}}_T^{(+)}(x_1, x_3; x_1', x_3')$ as

$$\hat{\mathcal{G}}_T^{(+)}(x_1, x_3; x_1', x_3') \stackrel{\text{def}}{=} -\hat{\mathcal{G}}^{(+)}(x_1', x_3'; x_1, x_3). \tag{3A.1}$$

We now derive the differential equation for $\hat{\mathcal{G}}_T^{(+)}(x_1, x_3; x_1', x_3')$.

Consider the differential Equation (3.47) for $\hat{\mathcal{G}}^{(+)}$. By multiplying this equation by $\hat{\mathcal{G}}_T^{(+)}$ and integrating over x_1 and x_3, we find the following global relation

$$\int_{x_3=-\infty}^{\infty} \langle \partial_3 \hat{\mathcal{G}}^{(+)} + \mathrm{j}\omega \hat{\Gamma} \hat{\mathcal{G}}^{(+)}, \hat{\mathcal{G}}_T^{(+)} \rangle \; \mathrm{d}x_3$$

$$= \int_{x_3=-\infty}^{\infty} \langle \delta(x_1 - x_1', x_3 - x_3'), \hat{\mathcal{G}}_T^{(+)} \rangle \; \mathrm{d}x_3. \tag{3A.2}$$

The integrand on the right-hand side can be rewritten

$$\langle \delta(x_1 - x_1', x_3 - x_3'), \hat{\mathcal{G}}_T^{(+)} \rangle$$

$$= \int_{x_1=-\infty}^{\infty} \hat{\mathcal{G}}_T^{(+)}(x_1, x_3; x_1', x_3') \delta(x_1 - x_1', x_3 - x_3') \; \mathrm{d}x_1$$

$$= \int_{x_1=-\infty}^{\infty} \hat{\mathcal{G}}_T^{(+)}(x_1', x_3'; x_1, x_3) \delta(x_1 - x_1', x_3 - x_3') \; \mathrm{d}x_1$$

$$= \int_{x_1=-\infty}^{\infty} -\hat{\mathcal{G}}^{(+)}(x_1, x_3; x_1', x_3') \delta(x_1 - x_1', x_3 - x_3') \; \mathrm{d}x_1$$

$$= \langle \hat{\mathcal{G}}^{(+)}, -\delta(x_1 - x_1', x_3 - x_3') \rangle. \tag{3A.3}$$

Since

$$0 = \int_{x_3=-\infty}^{\infty} \partial_3 (\hat{\mathcal{G}}^{(+)} \hat{\mathcal{G}}_T^{(+)}) \; \mathrm{d}x_3 = \int_{x_3=-\infty}^{\infty} \left[(\partial_3 \hat{\mathcal{G}}^{(+)}) \hat{\mathcal{G}}_T^{(+)} + \hat{\mathcal{G}}^{(+)} (\partial_3 \hat{\mathcal{G}}_T^{(+)}) \right] \; \mathrm{d}x_3,$$

$$\tag{3A.4}$$

and operator $\hat{\Gamma}$ is symmetric (see Equation (3.46)), the left-hand side of Equation (3A.2) equals

$$\int_{x_3=-\infty}^{\infty} \langle \partial_3 \hat{\mathcal{G}}^{(+)} + \mathrm{j}\omega \hat{\Gamma} \hat{\mathcal{G}}^{(+)}, \hat{\mathcal{G}}_T^{(+)} \rangle \; \mathrm{d}x_3$$

$$= \int_{x_3=-\infty}^{\infty} \langle \hat{\mathcal{G}}^{(+)}, -\partial_3 \hat{\mathcal{G}}_T^{(+)} + \mathrm{j}\omega \hat{\Gamma} \hat{\mathcal{G}}_T^{(+)} \rangle \; \mathrm{d}x_3. \tag{3A.5}$$

$$-\hat{\mathcal{G}}^{(+)}(x_1', x_3'; x_1, x_3)$$

$$(x_1', x_3')$$

$$(x_1, x_3)$$

$$\hat{\mathcal{G}}^{(-)}(x_1, x_3; x_1', x_3')$$
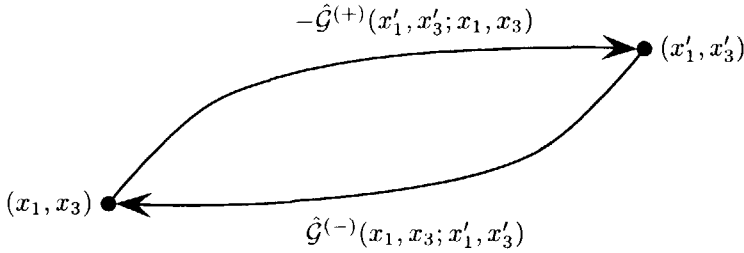
Figure 3.3: *The forward and backward Green functions between* (x_1, x_3) *and* (x_1', x_3').

From Equations (3A.3) and (3A.5) we find the differential equation for the reciprocal forward Green operator

$$\partial_3 \hat{\mathcal{G}}_{\mathrm{T}}^{(+)} - \mathrm{j}\omega \hat{\Gamma} \hat{\mathcal{G}}_{\mathrm{T}}^{(+)} = \delta(x_1 - x_1', x_3 - x_3'). \tag{3A.6}$$

This equation is the transposed version of Equation (3.47). By comparing this equation and equation (3.48) we can conclude that

$$\hat{\mathcal{G}}_{\mathrm{T}}^{(+)}(x_1, x_3; x_1', x_3') = \hat{\mathcal{G}}^{(-)}(x_1, x_3; x_1', x_3'). \tag{3A.7}$$

Thus the relation between the forward and backward Green functions is (compare with Equation (3A.1))

$$\hat{\mathcal{G}}^{(-)}(x_1, x_3; x_1', x_3') = -\hat{\mathcal{G}}^{(+)}(x_1', x_3'; x_1, x_3). \tag{3A.8}$$

Figure 3.3 shows this relationship graphically.

CHAPTER 4

Scattering in the transverse direction: pseudo-differential operators

In this chapter we consider the longitudinal slowness operator $\hat{\Gamma}$

$$\hat{\Gamma}(x_1, x_3) = \left[\mu_0 \hat{\varepsilon}(x_1, x_3) + \omega^{-2} \partial_1^2 \right]^{1/2} . \tag{4.1}$$

This operator describes the scattering problem in the transverse direction. Due to the x_1-dependence of $\hat{\varepsilon}$ and due to the square root, the numerical implementation is not trivial. For instance, if $\hat{\varepsilon}$ were independent of the transverse coordinate x_1, we could use a Fourier transformation with respect to x_1 in order to simplify the operator into a multiplication (see Section 4.1). Similarly, if the square root were not present, a finite-difference or a finite-element method could be directly used for the numerical implementation. From asymptotic considerations, we know that $\hat{\Gamma} \to |\partial_1|$, if the second derivative is dominant in (4.1), and $\hat{\Gamma} \to (\mu_0 \hat{\varepsilon})^{1/2}$, if $\mu_0 \hat{\varepsilon}$ dominates.

Our main goal is a fast numerical algorithm. A numerical scheme can be fast if, e.g., it contains a sparse matrix representation of $\hat{\Gamma}$. To derive such a scheme, we consider the calculus of pseudo-differential operators (ΨDO), since the longitudinal slowness operator $\hat{\Gamma}$ is a pseudo-differential operator. In this section, we discuss some basic properties of pseudo-differential operators. First, we take a closer look to the operators involved in a transverse homogeneous space (Section 4.1). In Section 4.2, we give a sketchy overview of some properties of the pseudo-differential operators. For more details about the pseudo-differential operator calculus, we refer to Hörmander[27], Taylor[28] and Duistermaat[29]. For an overview of the occurence of

the pseudo-differential operators in directional wave-field decomposition, we refer to Fishman and McCoy[23,24], Fishman[25], McCoy and Frazer[26], de Hoop[49] and Haines and de Hoop[53].

Sections 4.3 and 4.4 are dedicated to two configurations leading to analytical results: the quadratic profile and the step-index waveguides, respectively. For these media, analytic expressions of the functions which are introduced in Section 4.2 can be found. Section 4.3 deals with a waveguide with a quadratic profile, while Section 4.4 deals with a step-index waveguide. A derivation using the modal expansion has been chosen: thus the relation between the normal mode expansion and pseudo-differential operators is elucidated. These results have been presented at an international meeting, see de Hoop *et al.*[136]. Exact solutions of the Weyl and left symbol for some analytical profiles have already been found by Fishman[52,137]: general quadratic case[52] (and as a special limit, the linear case), delta function profile, discontinuity profile, square well profile[137] and certain cases from the hyperbolic function profile[52].

In Section 4.5, the results are discussed. This chapter contains one appendix, in which formulae of special functions referred to from other books are listed.

Since the longitudinal slowness operator $\hat{\Gamma}$ describes only the scattering in the transverse plane, we freely omit the longitudinal dependence (x_3) of $\hat{\Gamma}$ in this section.

4.1   Transverse homogeneous medium

In this section, the longitudinal slowness operator $\hat{\Gamma}$ in a transverse homogeneous medium is analyzed. First we introduce its symbol and analyze the corresponding dispersion curve. Subsequently, we discuss the parabolic approximation and derive the corresponding wavefront. Finally, the operators of interest are given.

Symbol and dispersion curve

When investigating a transverse homogeneous space, where the permittivity $\hat{\varepsilon}$ is independent of x_1, it is advantegeous to introduce the Fourier transform $\mathcal{F}$ with respect to the transverse coordinate x_1

$$\tilde{u}(\alpha_1) = (\mathcal{F}\hat{u})(\alpha_1) = \int_{-\infty}^{\infty} e^{j\omega\alpha_1 x_1}\, \hat{u}(x_1)\, dx_1, \qquad (4.2)$$

where α_1 is a normalized transformation parameter and is called the transverse slowness in analogy with the longitudinal slowness operator $\hat{\Gamma}$. The inverse Fourier transform is given by

$$\hat{u}(x_1) = (\mathcal{F}^{-1}\tilde{u})(x_1) = \frac{\omega}{2\pi}\int_{-\infty}^{\infty} e^{-j\omega\alpha_1 x_1}\, \hat{u}(\alpha_1)\, d\alpha_1. \qquad (4.3)$$

Let us consider the transverse Helmholtz operator $\hat{A} = \mu_0\hat{\varepsilon} + \omega^{-2}\partial_1^2$ in Equation (3.19), but now $\hat{\varepsilon}$ is independent of x_1. The Fourier transform of $(\hat{A}\tilde{u})(x_1)$ equals $(\hat{a}\tilde{u})(\tilde{\alpha}_1)$, where

$$\hat{a}(x_1, \alpha_1) = \hat{a}(\alpha_1) = \mu_0\hat{\varepsilon} - \alpha_1^2, \tag{4.4}$$

is called the symbol of operator $\hat{A}$. Similarly, the Fourier transform of $(\hat{\Gamma}\tilde{u})(x_1)$ equals $(\hat{\gamma}\tilde{u})(\tilde{\alpha}_1)$, where the longitudinal slowness

$$\hat{\gamma}(x_1, \alpha_1) = \hat{\gamma}(\alpha_1) = (\hat{a})^{1/2} = (\mu_0\hat{\varepsilon} - \alpha_1^2)^{1/2}, \qquad \text{Im}(.)^{1/2} < 0, \tag{4.5}$$

is the symbol of operator $\hat{\Gamma}$. It is closely related to the longitudinal wave number k_3

$$k_3 = \omega\hat{\gamma}. \tag{4.6}$$

The slownesses $\hat{\gamma}$ and α_1 satisfy the dispersion relation

$$\hat{\gamma}^2 + \alpha_1^2 = \hat{c}^{-2}, \tag{4.7}$$

where $\hat{c} = (\mu_0\hat{\varepsilon})^{-1/2}$ is the complex wave speed of the medium. In analogy with $\hat{\gamma}$, α_1 is related to the transverse wave number k_1 (remember that $\omega > 0$)

$$k_1 = \omega\alpha_1. \tag{4.8}$$

Let us rewrite (4.5) as

$$c\hat{\gamma} = \left[1 - (c\alpha_1)^2\right]^{1/2}. \tag{4.9}$$

In Figure 4.1, the slowness $c\hat{\gamma}$ and the dispersion curve are shown. The interval $c\alpha_1 \in [-1, 1]$ corresponds to the wave propagation under an angle from -90 to 90 degrees and is called the pre-critical region. The interval $c\alpha_1 \in (-\infty, -1) \cup (1, \infty)$ corresponds to the evanescent wave constituents and is called the post-critical region. The terms *critical* refers to the critical angle from Snell's law (90°). The dispersion curve is commonly used to analyze the wide-angle properties of an approximate one-way wave equation, see Claerbout[138], and Beats and Lagasse[139].

Parabolic approximation

In order to gain more insight into the parabolic approximation in the theory of the one-way wave equation, we take a closer look at the parabolic approximation (the first-order Taylor expansion of the square root with respect to 1)

$$c\hat{\gamma} \approx 1 - \tfrac{1}{2}(c\alpha_1)^2. \tag{4.10}$$

Because this relation is quadratic, this approximation is known as the parabolic approximation. The exact and parabolic slownesses are plotted in Figure 4.1. We observe that the parabolic approximation is valid for small values of $|\alpha_1|$: the paraxial region. Note, that the wave propagation is no longer isotropic in the parabolic approximation and that the evanescent waves become propagating waves. These waves have a lower wave speed than the exact waves.
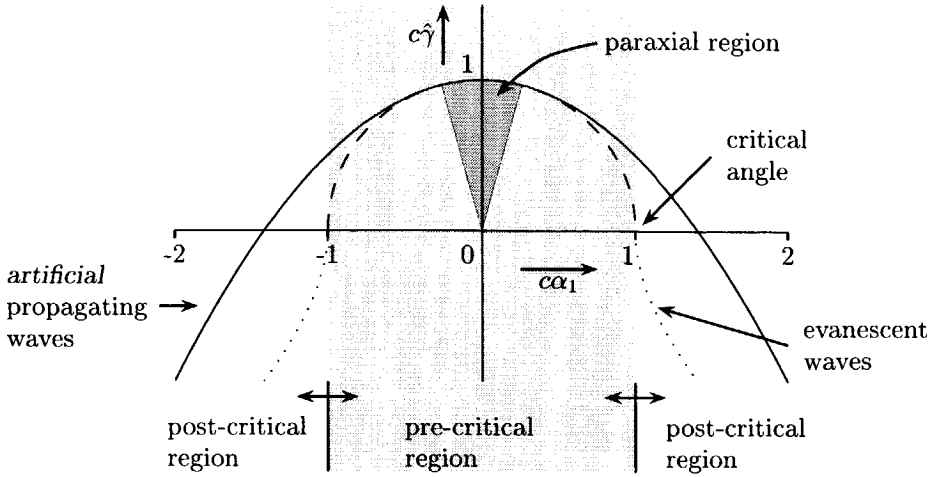
Figure 4.1: *Dispersion curve: the longitudinal slowness (c$\hat{\gamma}$) as a function of the transverse slowness cα_1. The dashed curve corresponds to the exact slowness (real part), while the solid curve corresponds to the slowness in the parabolic approximation. The imaginairy part of the exact slowness is dotted. Some terms used in the text are indicated.*

Wavefront

Some transient wave phenomena can be extracted from the slowness. We will now show the relation between the slowness and the wavefront.

The time-domain expression for steady-state plane waves in a homogeneous medium is

$$u(x_1, x_3, t) = \text{Re}\{\exp[\ j\omega t - j\omega(\alpha_1 x_1 + \hat{\gamma}x_3)]\}. \tag{4.11}$$

The wavefront (x_1, x_3) at time t is found from

$$\alpha_1 x_1 + \hat{\gamma}x_3 = t. \tag{4.12}$$

Differentiate both sides with respect to $\hat{\gamma}$ and note that $\hat{\gamma} = (\mu_0 \hat{\varepsilon} - \alpha_1^2)^{1/2}$ is independent of time t and the coordinates x_1 and x_3 ($\hat{\varepsilon} = $ constant)

$$\frac{d\alpha_1}{d\hat{\gamma}}x_1 + x_3 = 0. \tag{4.13}$$

Substituting this result in (4.12) yields

$$\alpha_1 x_1 - \hat{\gamma}\frac{d\alpha_1}{d\hat{\gamma}}x_1 = t. \tag{4.14}$$
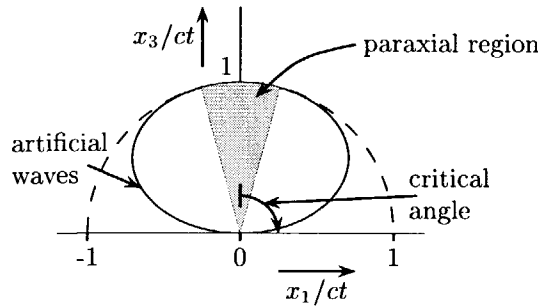
Figure 4.2: *The wavefront corrsponding to the slownesses in Figure 4.1. The dashed curve corresponds to the exact wavefront, while the solid curve corresponds to the wavefront in the parabolic approximation. Some terms used in the text are indicated.*

Thus

$$x_1 = \frac{t}{\alpha_1 - \hat{\gamma}\, \dfrac{\mathrm{d}\alpha_1}{\mathrm{d}\hat{\gamma}}}, \tag{4.15}$$

and

$$x_3 = \frac{t}{\hat{\gamma} - \alpha_1\, \dfrac{\mathrm{d}\hat{\gamma}}{\mathrm{d}\alpha_1}}, \tag{4.16}$$

describe the wavefront at time t. The graphical construction of the wavefront is described by Aki and Richards[15].

Figure 4.2 shows the wavefront of the exact slowness and the wavefront of the slowness in the parabolic approximation. Again, we note that the parabolic equation is only valid in the paraxial region. Since we are dealing with a one-way wave equation, the wavefront is only present for $x_3 > 0$. We see that in the parabolic approximation there is no critical angle.

Operators of interest

In a tranverse homogeneous space, a Fourier transformation with respect to the transverse coordinate x_1 can be applied to the operators of interest (compare with Equations (3.85) and (3.24))

$$\tilde{P}(\alpha_1, m) \quad \approx \exp\left\{-\mathrm{j}\omega\hat{\gamma}\left[\alpha_1, (m - \tfrac{1}{2})\Delta x_3\right]\Delta x_3\right\}, \tag{4.17}$$

$$\tilde{T}(\alpha_1, m\Delta x_3) \approx -\tfrac{1}{2}\left(\hat{\gamma}^{-1}\partial_3\hat{\gamma}\right)(\alpha_1, m\Delta x_3). \tag{4.18}$$

As an example, Figure 4.3 shows the propagator $\tilde{P}$.
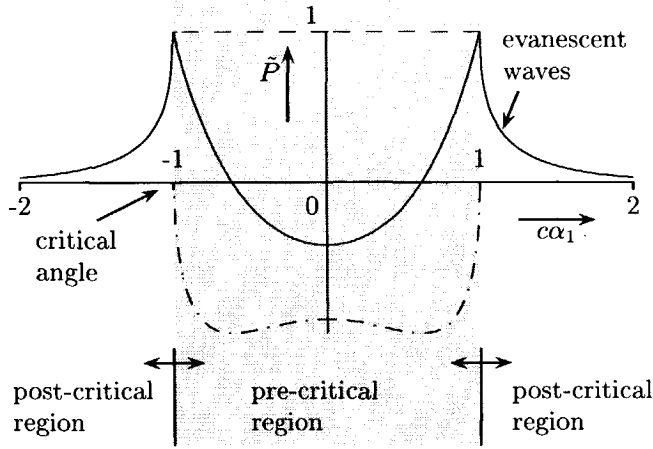
Figure 4.3:   *The propagator $\tilde{P}$: the real part (solid), the imaginairy part (dash-dot) and the absolute value (dashed). Here $\hat{\varepsilon}_r = 1$ and $k_0 \Delta x_3 = 2$. Some terms used in the text are indicated.*

4.2   Transverse inhomogeneous medium

We review some tools for pseudo-differential operators. We do that, in arbitrary order, ① by reviewing some basic tools for (partial differential) operators, ② by extending some parts of the theory on pseudo-differential operators in the s-domain to the ω-domain and ③ by integrating the modal analysis of waveguides with the theory of pseudo-differential operators.

We first take a closer look at the partial differential operator $\hat{A}$ (Subsection 4.2.1) and subsequently the pseudo-differential operator $\hat{\Gamma}$.

4.2.1   Partial differential operator $\hat{A}$

Now, we consider the partial differential operator $\hat{A} = \hat{\Gamma}^2 = \mu_0 \hat{\varepsilon} + \omega^{-2} \partial_1^2$ on $\mathbb{C}$, as defined in (3.19). The permittivity $\hat{\varepsilon}(x_1)$ may vary along the transverse direction x_1. The operator is well defined on the space $\mathcal{C}_0^\infty$ of smooth functions with compact support in $\mathbb{C}$. It can be extended as a bounded operator in an appropriate Sobolev space[49].

It is noted that in the time-Laplace transform domain (s-domain) the transverse Helmholtz operator $\hat{A}(s) = \mu_0 \hat{\varepsilon} - s^{-2} \partial_1^2$ is elliptic and positive definite. In the ω-domain where our analysis is performed, the operator $\hat{A}$ is neither elliptic nor positive definite (see Figure 4.4). Consequently, the analysis becomes more complex: artificial singularities are introduced (branch-cut of the square root) and the symbol is purely imaginary for real $\hat{\varepsilon}$ in the post-critical region. Most proofs come from the s-domain[49] and are translated to the ω-domain by the arguments of modal analysis.
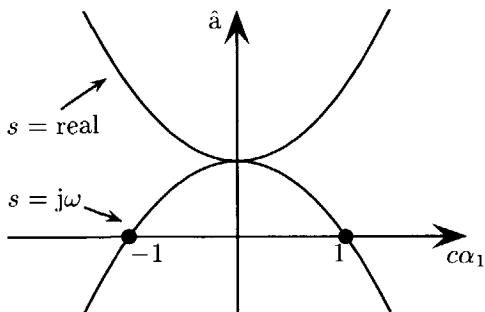
Figure 4.4: *The symbol of the elliptic operator $\hat{A}(x_1; s)$ and the nonelliptic operator $\hat{A}(x_1; j\omega)$. $\hat{A}(x_1; j\omega)$ is not elliptic, since its symbol $\hat{a}$ only positive between $c\alpha_1 = -1$ and $c\alpha_1 = 1$.*

Note that we always consider $s = j\omega + \delta$ with $\delta > 0$ (see Equation (1.29)).

Sobolev space

The Sobolev space $H^r(\mathbb{C})$ is the totality of functions $f(x)$ such that for all $|l| \leq r$, the derivatives $\partial_1^l f(x)$ in the sense of distributions belong to $L_2(\mathbb{C})$

$$H^r = \{\hat{u} \in \mathcal{I}' | (c^{-2} - s^{-2}\partial_1^2)^{r/2}\hat{u} \in L_2(\mathbb{C})\}, \tag{4.19}$$

which is a Banach space provided with the norm

$$\|\hat{u}\|_{H^r} = \|(c^{-2} - s^{-2}\partial_1^2)^{r/2}\hat{u}\|_{L_2}. \tag{4.20}$$

It is observed that the Sobolev space H^0 equals the space L_2.

Note that operator $\hat{A} : L_2 \to H^{-2}$ is a bounded operator, while $\hat{A} : L_2 \to L_2$ is not bounded. A Sobolev space of lower class contains rougher functions and distributions. A good example of such an operator is the second-order derivative ∂_1^2. The Heaviside function $H(x_1)$ is bounded in L_2, while $\partial_1^2 H(x_1) = \delta'(x_1)$ is not bounded in L_2, but it is bounded in H^{-2}.

Schwartz kernel of $\hat{A}$

In the operational context of the partial differential operator $\hat{A}$, it is useful to introduce the with this operator associated Schwartz kernel $\hat{\mathcal{A}}$. The operator $\hat{A}$ is related to its Schwartz kernel $\hat{\mathcal{A}}$ as

$$(\hat{A}\hat{u})(x_1) = \int_{x_1' = -\infty}^{\infty} \hat{\mathcal{A}}(x_1, x_1') u(x_1') \, dx_1'. \tag{4.21}$$

This Schwartz kernel is a distribution, i.e.,

$$\hat{\mathcal{A}}(x_1, x_1') = \mu_0 \hat{\varepsilon} \, \delta(x_1 - x_1') + \omega^{-2}\delta''(x_1 - x_1'), \tag{4.22}$$

in which $'$ indicates the differentiation with respect to its argument.
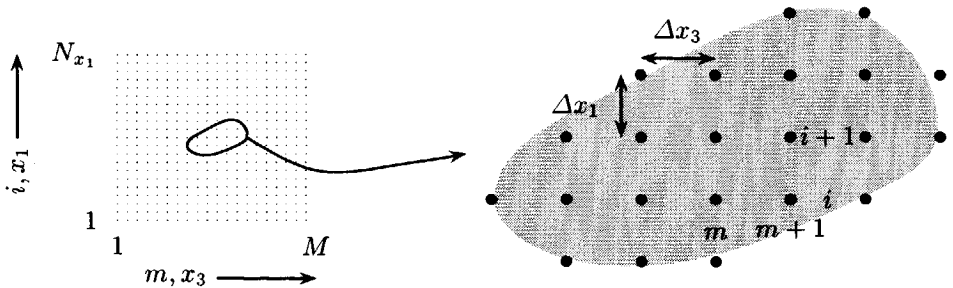
Figure 4.5:   *Uniform numerical grid. There are N_{x_1} grid points along the transverse direction x_1. The transverse sampling interval is Δx_1. There are M grid points along the longitudinal direction x_3. The longitudinal sampling interval is Δx_3.*

Matrix representation

The Schwartz kernel of an operator is closely related to the matrix representation of the operator $\hat{A}$. In order to show this, we introduce a numerical uniform grid in the transverse direction x_1, see Figure 4.5. The discretization in the x_3 direction has already been introduced by the Bremmer series.

In the previous sections, we showed that the discretization in the longitudinal direction can be nonuniform. The transverse sampling interval is denoted as Δx_1. To arrive at an explicit matrix representation for $\hat{A}$, we introduce the array

$$\hat{u}_i(x_3) = \hat{u}(x_{1i}, x_3), \tag{4.23}$$

where

$$x_{1i} = i \Delta x_1, \tag{4.24}$$

and $i = 1, \cdots, N_{x_1}$ labels the samples in the tranverse direction. In this notation, the matrix equivalent of Equation (4.21) is

$$(\hat{A}\hat{u})_i = \hat{A}_{i,j} \hat{u}_j. \tag{4.25}$$

By replacing $\delta(x_1 - x_1')$ by the identity matrix $\delta_{i,j}$ and its second derivative $\delta''(x_1 - x_1')$ by $\left(\frac{2}{\Delta x_1} \sinh^{-1} \frac{\delta_1}{2} \right)^2_{i,j}$ (see Mitchell and Griffiths[140]), the matrix representation of $\hat{A}$ is found as

$$\hat{A}_{i,j} = \mu_0 \hat{\varepsilon}(i \Delta x_1) \delta_{i,j} + \omega^{-2} \left(\frac{2}{\Delta x_1} \sinh^{-1} \frac{\delta_1}{2} \right)^2_{i,j}. \tag{4.26}$$

Here, δ_1 is the central difference operator in the x_1 direction

$$\delta_1 \hat{u}(x_1) = \hat{u}(x_1 + \tfrac{1}{2}\Delta x_1) - \hat{u}(x_1 - \tfrac{1}{2}\Delta x_1). \tag{4.27}$$

In this notation we have

$$(\delta_1)_{i,j}^2 = \begin{bmatrix} \ddots & \ddots & \ddots & & \\ & 1 & -2 & 1 & \\ & & 1 & -2 & 1 \\ & & & \ddots & \ddots & \ddots \end{bmatrix}. \tag{4.28}$$

Artifacts occur at the finite boundaries of the computational window and are an important numerical issue (see Section 5.4).

Spectrum

The spectrum of the operator $\hat{A}$ is defined as $\sigma(\hat{A})$. In analogy with matrices, the elements $\lambda^{(j)} \in \sigma(\hat{A})$ of the spectrum are found as the eigenvalues of $\hat{A}$

$$(\hat{A}\hat{\phi}^{(j)})(x_1) = \lambda^{(j)}\hat{\phi}^{(j)}(x_1). \tag{4.29}$$

The corresponding functions $\hat{\phi}^{(j)}(x_1)$ are the eigenfunctions of $\hat{A}$. In general, the spectrum contains a discrete set of J eigenfunctions $\{\phi^{(j)}(x_1), j = 0, \cdots, J-1\}$ and a continuum $\{\hat{\phi}_A(x_1, \lambda), \lambda \in \mathcal{B}_A\}$. Here, $\mathcal{B}_A$ stands for the branch-cut, see Blok[141]. Thus, the spectrum equals

$$\sigma(\hat{A}) = \{\lambda^{(j)}, j = 0, \cdots, J-1; \lambda \in \mathcal{B}_A\}. \tag{4.30}$$

Figure 4.6 shows spectra for some typical configurations: homogeneous space, quadratic gradient waveguide and step-index slab waveguide. For simplicity, we have chosen those eigenfunctions which are normalized as

$$\int_{x_1=-\infty}^{\infty} \hat{\phi}^{(i)}(x_1)\hat{\phi}^{(j)}(x_1)\, dx_1 = \delta_{i,j}, \tag{4.31}$$

$$\int_{x_1=-\infty}^{\infty} \hat{\phi}^{(i)}(x_1)\hat{\phi}_A(x_1; \lambda)\, dx_1 = 0, \tag{4.32}$$

$$\int_{x_1=-\infty}^{\infty} \hat{\phi}_A(x_1; \lambda')\hat{\phi}_A(x_1; \lambda'')\, dx_1 = \frac{1}{2\pi}\delta(\lambda' - \lambda''). \tag{4.33}$$

These eigenmodes $\hat{\phi}^{(j)}$ satisfy the completeness relation

$$\sum_j \hat{\phi}^{(j)}(x_1')\hat{\phi}^{(j)}(x_1'') = \delta(x_1' - x_1''). \tag{4.34}$$
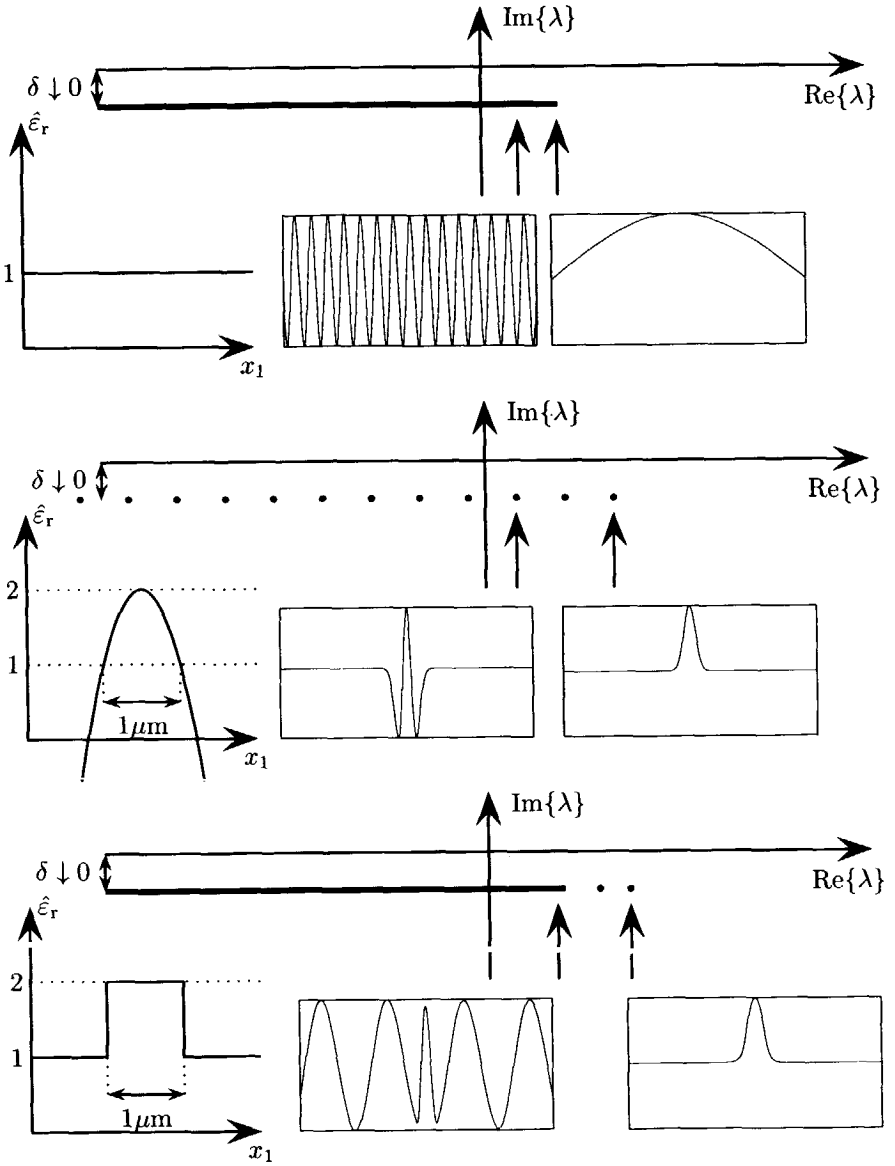
Figure 4.6:   Spectra of the free space (upper), a waveguide with a parabolic per-
              mittivity profile (middle) and a step-index slab waveguide (lower).
              For each spectrum two eigenmodes $\hat{\phi}^{(j)}(x_1)$ are shown. Here the
              free-space wavelength λ_0 is 1 μm.

Here, we used the above shorthand notation for notationally merging the discrete set and the continuum. Substituting (4.21) in (4.29) yields for one mode

$$\int_{x_1'=-\infty}^{\infty} \hat{\mathcal{A}}(x_1, x_1')\hat{\phi}^{(j)}(x_1') \, dx_1' = \lambda^{(j)}\hat{\phi}^{(j)}(x_1).$$ (4.35)

Multiplying both sides by $\hat{\phi}^{(j)}(x_1'')$ and taking the summation over all j give

$$\sum_j \hat{\phi}^{(j)}(x_1'') \int_{x_1'=-\infty}^{\infty} \hat{\mathcal{A}}(x_1, x_1')\hat{\phi}^{(j)}(x_1') \, dx_1' = \sum_j \hat{\phi}^{(j)}(x_1'')\hat{\phi}^{(j)}(x_1)\lambda^{(j)}.$$ (4.36)

With use of the completeness relation (4.34) we recognize the modal expansion of the Schwartz kernel $\hat{\mathcal{A}}$

$$\hat{\mathcal{A}}(x_1, x_1'') = \sum_j \hat{\phi}^{(j)}(x_1'')\hat{\phi}^{(j)}(x_1)\lambda^{(j)}.$$ (4.37)

This expansion has only meaning in the *distributional sense*, since interchanging the summation and integration is only allowed under some restricted conditions.

Resolvent and Helmholtz-Green's function

Let λ be a complex variable. The resolvent $\hat{R}_\lambda$ of $\hat{A}$ satisfies the relation

$$(\hat{A} - \lambda I)\hat{R}_\lambda = I,$$ (4.38)

where I is the identity operator. It exists for $\lambda \notin \sigma(\hat{A})$. Since $\hat{A}$ is a partial differential operator, $\hat{R}_\lambda$ is an operator of the indefinite integration type. The resolvent can be expressed in its kernel $\hat{\mathcal{R}}_\lambda(x_1, x_1')$ as

$$(\hat{R}_\lambda u)(x_1) = \int_{x_1'=-\infty}^{\infty} \hat{\mathcal{R}}_\lambda(x_1, x_1')u(x_1') \, dx_1'.$$ (4.39)

From (4.38) and (4.39) follows

$$\left[\omega^{-2}\partial_1^2 + \mu_0\hat{\varepsilon}(x_1) - \lambda\right]\hat{\mathcal{R}}_\lambda(x_1, x_1') = \delta(x_1 - x_1').$$ (4.40)

This equation is very similar to the 2-D Helmholz equation with an x_3-invariant permittivity $\hat{\varepsilon}$. The Green function $\hat{\mathcal{G}}(x_1, x_3; x_1', x_3')$ corresponding to this Helmholtz equation satisfies

$$\left[\partial_1^2 + \partial_3^2 + \omega^2\mu_0\hat{\varepsilon}(x_1)\right]\hat{\mathcal{G}}(x_1, x_3; x_1', x_3') = -\delta(x_1 - x_1', x_3 - x_3').$$ (4.41)

Since in the latter equation $\hat{\varepsilon}$ is x_3-invariant, we can apply a longitudinal Fourier transformation with respect to $(x_3 - x_3')$

$$\left[\partial_1^2 - k_3^2 + \omega^2\mu_0\hat{\varepsilon}(x_1)\right]\tilde{\mathcal{G}}(x_1, x_1'; k_3) = -\delta(x_1 - x_1'), \tag{4.42}$$

where k_3 is the longitudinal Fourier parameter or wave number (see Equation (2.8) and (4.6)). Comparison of (4.42) and (4.40) yields a relation between the resolvent and the Green function corresponding to the x_3-invariant, 2-D Helmholtz equation

$$\hat{\mathcal{R}}_\lambda(x_1, x_1') = -\omega^2\tilde{\mathcal{G}}\left(x_1, x_1'; \omega\lambda^{1/2}\right). \tag{4.43}$$

Hence for a fixed value of x_3, the spectrum of $\hat{A}$ is related to the spectrum of $\hat{\mathcal{G}}$. In the case of a local waveguiding structure, we interpret the discrete set of eigenfunctions of $\hat{A}$ as the discrete set of guided modes of the local waveguide and the continuum of eigenfunctions of $\hat{A}$ as the continuum of radiation modes of the local waveguide. For more details about the modal theory of waveguides, we refer the reader to Blok[141], Marcuse[142], Snyder and Love[143] and Vassallo[144]. In the case of non-guiding structures, only a continuum of eigenfunctions is present.

The resolvent can also be expressed in the the solutions $\hat{\psi}^\pm(x_1)$ of the homogeneous equation (compare with Equation (4.40))

$$\left[\omega^{-2}\partial_1^2 - \lambda + \mu_0\hat{\varepsilon}(x_1)\right]\hat{\psi}^\pm(x_1) = 0, \tag{4.44}$$

with

$$\hat{\psi}^\pm(x_1) = 0, \qquad \text{for } x_1 \to \pm\infty. \tag{4.45}$$

Then the Schwartz kernel of the resolvent equals

$$\hat{\mathcal{R}}_\lambda(x_1, x_1') = -\omega^2 W^{-1}(x_1')\left[H(x_1' - x_1)\hat{\psi}^+(x_1')\hat{\psi}^-(x_1)\right.$$
$$\left. + H(x_1 - x_1')\hat{\psi}^+(x_1)\hat{\psi}^-(x_1')\right], \tag{4.46}$$

where $W(x_1') = W$ is the Wronskian, defined through

$$W(x_1') = \hat{\psi}^+(x_1')\partial_{x_1'}\hat{\psi}^-(x_1') - \hat{\psi}^-(x_1')\partial_{x_1'}\hat{\psi}^+(x_1'), \tag{4.47}$$

and is independent of x_1'.

4.2.2 Pseudo-differential operator $\hat{\Gamma}$

Below, we introduce fractional powers of $\hat{A}$, the left symbol, the Schwartz kernel and the co-kernel of pseudo-differential operators. Subsequently, we discuss several ways to construct the left symbol: several composition equations and the polyhomogeneous and uniform expansion.
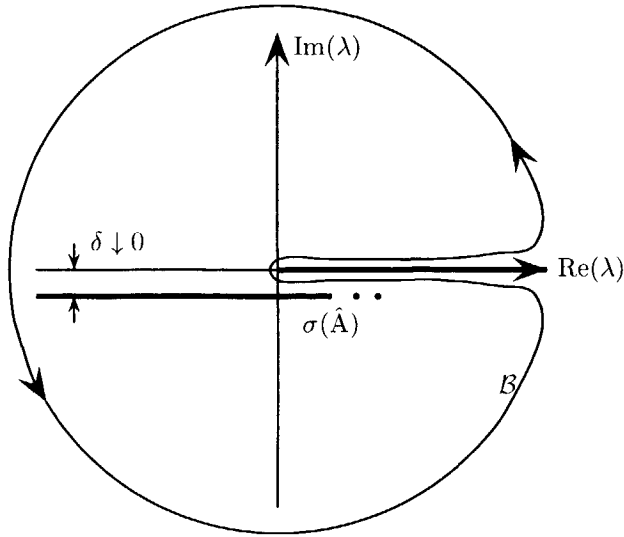
Figure 4.7: *The integration contour $\mathcal{B}$ for the Dunford integral. The contour $\mathcal{B}$ is along a semicircular arc at infinity in the upper and lower half of the λ-plane. The branch cut of λ^z ($z < 0$) is along the positive real axis. The spectrum $\sigma(\hat{A})$ of a passive configuration lies in the lower half of the λ-plane.*

Negative fractional powers of the operator $\hat{A}$

Let the power λ^z of a complex variable λ with $z \in \mathbb{R}$ be defined as[49]

$$\lambda^z = |\lambda|^z \exp[jz \arg(\lambda)], \qquad (4.48)$$

with $\arg(\lambda) \in (0, 2\pi)$. With this definition, the branch cut of λ^z is along the positive real axis, see Subsection 3.4.1. Let $\mathcal{B}$ be a contour of integration in the λ plane around the branch cut of λ^z, counter-clockwise oriented, staying away a small but finite distance from the origin (the branch point), not intersecting the spectrum $\sigma(\hat{A})$, and going along a semicircular arc at infinity in the upper and lower hf of the λ plane (see Figure 4.7). Then, for $z < 0$, the Dunford integral

$$\hat{A}_z = \frac{1}{2\pi j} \int_{\lambda \in \mathcal{B}} \lambda^z \hat{R}_\lambda \, d\lambda, \qquad (4.49)$$

converges in the operator norm $\|.\|_{r, r-2z}$ on the Sobolev space H^r (see de Hoop[49]). The Schwartz kernel of $\hat{A}_z$ is given by

$$\hat{\mathcal{A}}_z(x_1, x_1') = \frac{1}{2\pi j} \int_{\lambda \in \mathcal{B}} \lambda^z \hat{\mathcal{R}}_\lambda(x_1, x_1') \, d\lambda. \qquad (4.50)$$

The Dunford integral representation satisfies the *composition equation*

$$\hat{A}_z \hat{A}_w = \hat{A}_{z+w}, \tag{4.51}$$

for $z, w < 0$ (see de Hoop[49]). Thus for negative powers of $\hat{A}$ ($z < 0$)

$$\hat{A}^z = \hat{A}_z. \tag{4.52}$$

Nonnegative fractional powers of the operator $\hat{A}$

With the aid of Equation (4.49) a nonnegative fractional power of $\hat{A}$ can be readily introduced through[49]

$$\hat{A}^z = \hat{A}^k \hat{A}_{z-k}, \tag{4.53}$$

where k is an integer such that $k > z$. The resulting operators behave, again, like ordinary powers, i.e.,

$$\hat{A}^z \hat{A}^w = \hat{A}^{z+w}, \tag{4.54}$$

(note that $\hat{A}$ and its resolvent commute). Thus

$$\hat{\Gamma} = \hat{A}^{1/2} = \hat{A} \hat{A}_{-1/2}. \tag{4.55}$$

Functions of $\hat{A}$ (spectrum)

The Schwartz kernel of $\hat{A}^z$ with $\text{Re}(z) < 0$ can be expressed in the eigenfunctions and eigenvalues of $\hat{A}$

$$\hat{\mathcal{A}}_z(x_1, x_1') = \sum_j \hat{\phi}^{(j)}(x_1') \hat{\phi}^{(j)}(x_1) (\lambda^{(j)})^z. \tag{4.56}$$

To prove this, we start with (4.53) where the positive powers of $\hat{A}$ are found as

$$
\begin{aligned}
(\hat{A}^z \hat{u})(x_1) &= \hat{A}^k \int_{x_1=-\infty}^{\infty} \hat{\mathcal{A}}_{z-k}(x_1, x_1') \hat{u}(x_1') \, dx_1' \\
&= \int_{x_1=-\infty}^{\infty} \sum_j \hat{\phi}^{(j)}(x_1') \left[\hat{A}^k \hat{\phi}^{(j)}(x_1) \right] (\lambda^{(j)})^{z-k} \hat{u}(x_1') \, dx_1' \\
&= \int_{x_1=-\infty}^{\infty} \sum_j \hat{\phi}^{(j)}(x_1') \left[(\lambda^{(j)})^k \hat{\phi}^{(j)}(x_1) \right] (\lambda^{(j)})^{z-k} \hat{u}(x_1') \, dx_1' \\
&= \int_{x_1=-\infty}^{\infty} \sum_j \hat{\phi}^{(j)}(x_1') \hat{\phi}^{(j)}(x_1) (\lambda^{(j)})^z \hat{u}(x_1') \, dx_1'.
\end{aligned}
\tag{4.57}
$$

The corresponding Schwartz kernel equals Equation (4.56) in the distributional sense. We can generalize this to more general functions $f(\hat{A})$ of $\hat{A}$. The Schwartz kernel belonging to the operator $f(\hat{A})$ equals

$$\sum_j \hat{\phi}^{(j)}(x_1')\hat{\phi}^{(j)}(x_1)f(\lambda^{(j)}). \tag{4.58}$$

We now consider a few examples of these functions of the operator $\hat{A}$. If $f(\hat{A}) = 1$, the completeness relation of the eigenfunctions is retained (see Equation (4.34))

$$\delta(x_1 - x_1') = \sum_j \hat{\phi}^{(j)}(x_1')\hat{\phi}^{(j)}(x_1). \tag{4.59}$$

If $f(\hat{A}) = H(x_3 - x_3') \exp[-j\omega\hat{A}^{1/2}(x_3 - x_3')]$, we find the forward one-way wave Green function

$$\hat{\mathcal{G}}^{(+)}(x_1, x_3; x_1', x_3') = H(x_3 - x_3') \sum_j \hat{\phi}^{(j)}(x_1')\hat{\phi}^{(j)}(x_1) \exp\left[-jk_0 n_{\text{eff}}^{(j)}(x_3 - x_3')\right],$$

$$\tag{4.60}$$

where $n_{\text{eff}}^{(j)} = c_0(\lambda^{(j)})^{1/2}$ is the effective refractive index of eigenfunction $\hat{\phi}^{(j)}(x_1)$. The forward one-way wave Green function is the Schwartz kernel of the evolution operator (see Equation (3.65)).

If $f(\hat{A}) = -H(x_3' - x_3) \exp[j\omega\hat{A}^{1/2}(x_3 - x_3')]$, we find the backward one-wave way Green function

$$\hat{\mathcal{G}}^{(-)}(x_1, x_3; x_1', x_3') = -H(x_3' - x_3) \sum_j \hat{\phi}^{(j)}(x_1')\hat{\phi}^{(j)}(x_1) \exp\left[jk_0 n_{\text{eff}}^{(j)}(x_3 - x_3')\right].$$

$$\tag{4.61}$$

For the function $f(\hat{A}) = (2j\omega\hat{A}^{1/2})^{-1} \exp(-j\omega\hat{A}^{1/2}|x_3 - x_3'|)$, the modal representation (see Blok[141]) of the Helmholtz Green function in Equation (4.41) is found as

$$\hat{\mathcal{G}}(x_1, x_3; x_1', x_3') = \sum_j \frac{\hat{\phi}^{(j)}(x_1')\hat{\phi}^{(j)}(x_1)}{2jk_0 n_{\text{eff}}^{(j)}} \exp\left(-jk_0 n_{\text{eff}}^{(j)}|x_3 - x_3'|\right). \tag{4.62}$$

In particular, we are interested in the propagator $\hat{P}(x_1, m)$ in (3.85) and the transmission operator $\hat{T}(x_1, m\Delta x_3)$ in (3.24). The Schwartz kernel of the approximation of $\hat{P}(x_1, m)$ in (3.85) is found as

$$\hat{P}(x_1, x_1', m) \approx \sum_j \hat{\phi}^{(j)}(x_1')\hat{\phi}^{(j)}(x_1) \exp\left\{-jk_0\Delta x_3 n_{\text{eff}}^{(j)}\left[(m - \tfrac{1}{2})\Delta x_3\right]\right\}. \tag{4.63}$$

Note that the eigenfunctions $\hat{\phi}^{(j)}(x_1)$ may vary along the x_3-axis. The Schwartz kernel of the transmission operator equals (compare with Equation (3.24))

$$
\hat{\mathcal{T}}(x_1, x_1', m) = -\tfrac{1}{2} \int_{x_1''=-\infty}^{\infty} \left[\sum_j \hat{\phi}^{(j)}(x_1'')\hat{\phi}^{(j)}(x_1)(n_{\text{eff}}^{(j)})^{-1} \right]
$$
$$
\partial_3 \left[\sum_j \hat{\phi}^{(j)}(x_1'')\hat{\phi}^{(j)}(x_1')n_{\text{eff}}^{(j)} \right] dx_1''. \quad (4.64)
$$

The Schwartz kernel corresponding to $\hat{\varGamma}$ and its inverse $\hat{\varGamma}^{-1}$ are

$$
\hat{\mathcal{C}}(x_1, x_1') = \sum_j \hat{\phi}^{(j)}(x_1')\hat{\phi}^{(j)}(x_1) \, (\lambda^{(j)})^{1/2}, \quad (4.65)
$$

and

$$
\hat{\mathcal{C}}_{-1}(x_1, x_1') = \sum_j \hat{\phi}^{(j)}(x_1')\hat{\phi}^{(j)}(x_1)(\lambda^{(j)})^{-1/2}, \quad (4.66)
$$

respectively. Again, we have to emphasize that Equation (4.64) and (4.65) have only meaning in distributional sense. In order to arrive at a convergent expression, a special regularization procedure has to be performed.

Left symbol

A linear partial differential operator $\hat{\mathrm{A}}(x_1, D_1)$ is defined as a polynomial in $D_1 = \mathrm{j}\omega^{-1}\partial_1$

$$
\hat{\mathrm{A}}(x_1, D_1) = \sum_{i=0}^{\infty} \hat{\mathrm{A}}^{(i)}(x_1)D_1^i. \quad (4.67)
$$

We can reformulate $(\hat{\mathrm{A}}\hat{u})(x_1)$ by means of the transverse spatial Fourier transformation (see (4.2)-(4.3))

$$
(\hat{\mathrm{A}}\hat{u})(x_1) = \sum_{i=0}^{\infty} \hat{\mathrm{A}}^{(i)}(x_1)D_1^i \left[\frac{\omega}{2\pi} \int_{\alpha_1=-\infty}^{\infty} \mathrm{e}^{-\mathrm{j}\omega\alpha_1 x_1}\tilde{u}(\alpha_1)\, \mathrm{d}\alpha_1 \right]
$$
$$
= \sum_{i=0}^{\infty} \hat{\mathrm{A}}^{(i)}(x_1)\frac{\omega}{2\pi} \int_{\alpha_1=-\infty}^{\infty} \mathrm{e}^{-\mathrm{j}\omega\alpha_1 x_1}\alpha_1^i \tilde{u}(\alpha_1)\, \mathrm{d}\alpha_1
$$
$$
= \frac{\omega}{2\pi} \int_{\alpha_1=-\infty}^{\infty} \mathrm{e}^{-\mathrm{j}\omega\alpha_1 x_1}\hat{\mathrm{a}}(x_1, \alpha_1)\tilde{u}(\alpha_1)\, \mathrm{d}\alpha_1, \quad (4.68)
$$

where

$$
\hat{\mathrm{a}}(x_1, \alpha_1) = \sum_{i=0}^{\infty} \hat{\mathrm{A}}^{(i)}(x_1)\alpha_1^i, \quad (4.69)
$$

denotes the left symbol of operator $\hat{A}$. As an example, the symbol $\hat{a}(x_1, \alpha_1) = \mu_0 \hat{\varepsilon}(x_1) - \alpha_1^2$ is associated with the operator $\hat{A}(x_1, j\omega^{-1}\partial_1) = \mu_0 \hat{\varepsilon}(x_1) + \omega^{-2}\partial_1^2$. This equation can be generalized by replacing the polynomial $\hat{a}(x_1, \alpha_1)$ in α_1 by an arbitrary function in such a way that the integral still makes sense. The longitudinal slowness operator can be expressed in its left (or standard) symbol $\hat{\gamma}(x_1, \alpha_1)$ as

$$(\hat{\Gamma}\hat{u})(x_1) = \frac{\omega}{2\pi} \int_{\alpha_1 = -\infty}^{\infty} e^{-j\omega\alpha_1 x_1} \hat{\gamma}(x_1, \alpha_1) \tilde{u}(\alpha_1) \, d\alpha_1. \tag{4.70}$$

All operators of this kind are called pseudo-differential operators. We note that the left symbol $\hat{\gamma}(x_1, \alpha_1)$ of the longitudinal slowness operator $\hat{\Gamma}(x_1, -j\omega^{-1}\partial_1) = (\mu_0 \hat{\varepsilon}(x_1) + \omega^{-2}\partial_1^2)^{1/2}$ is, in general, not equal to $(\mu_0 \hat{\varepsilon}(x_1) - \alpha_1^2)^{1/2}$. This is only true in a transverse homogeneous section ($\hat{\varepsilon}(x_1) = \hat{\varepsilon} = $ constant). Equation (4.70) implies that

$$\hat{\Gamma}(x_1, D_1) e^{-j\omega\alpha_1 x_1} = \hat{\gamma}(x_1, \alpha_1) e^{-j\omega\alpha_1 x_1}. \tag{4.71}$$

This is a plane-wave decomposition. The left symbol of an operator is defined through the plane-wave interaction with the same operator. The left symbol generalizes the longitudinal slowness in transversely homogeneous media to transversely inhomogeneous media. Therefore it is also called the generalized slowness. Note that the left symbol of a partial differential operator is a local operator. The left symbol of a pseudo-differential operator is pseudo-local[27].

In the following two sections, the physical interpretation is elucidated with aid of two analytical examples. In a similar way, the tight and Weyl symbols can be introduced, see see McCoy and Frazer[26] and Hörmander[27].

Schwartz kernel of $\hat{\Gamma}$

The pseudo-differential operator can be expressed in its Schwartz kernel. First, we replace $\tilde{u}(\alpha_1)$ explicitly by applying the spatial Fourier transformation for $\hat{u}(x_1)$ in (4.70) and subsequently we collect all terms in the integrand

$$\hat{\Gamma}(x_1, D_1)\hat{u}(x_1) = \frac{\omega}{2\pi} \int_{\alpha_1 = -\infty}^{\infty} \left[\int_{x_1' = -\infty}^{\infty} e^{j\omega\alpha_1(x_1' - x_1)} \hat{\gamma}(x_1, \alpha_1) \hat{u}(x_1') \, dx_1' \right] d\alpha_1. \tag{4.72}$$

Interchanging the integrals in (4.72) results in

$$(\hat{\Gamma}\hat{u})(x_1) = \int_{x_1' = -\infty}^{\infty} \hat{C}(x_1, x_1') \hat{u}(x_1') \, dx_1', \tag{4.73}$$

where we introduced the Schwartz kernel $\hat{C}(x_1, x_1')$ as

$$\hat{C}(x_1, x_1') = \frac{\omega}{2\pi} \int_{\alpha_1 = -\infty}^{\infty} e^{j\omega\alpha_1(x_1' - x_1)} \hat{\gamma}(x_1, \alpha_1) \, d\alpha_1. \tag{4.74}$$

The left symbol is related to the Schwartz kernel through the transverse spatial Fourier transform

$$\hat{\gamma}(x_1, \alpha_1) = \int_{x_1' = -\infty}^{\infty} e^{-j\omega\alpha_1(x_1' - x_1)} \hat{\mathcal{C}}(x_1, x_1') \, dx_1'. \tag{4.75}$$

The left symbol $\hat{\gamma}(x_1, \alpha_1)$ can also be expressed in its spectrum

$$\hat{\gamma}(x_1, \alpha_1) = e^{j\omega\alpha_1 x_1} \sum_j \hat{\phi}^{(j)}(x_1) \tilde{\phi}^{(j)}(\alpha_1) (\lambda^{(j)})^{1/2}. \tag{4.76}$$

Note that the modal expansion was introduced for Schwartz kernels in the distributional sense (see (4.37)). The left symbol itself is not a distribution. The summation is, in general, not convergent. A special regularization procedure should be applied, see Chapter 4 for some examples.

Co-kernel

A transverse space-Fourier transformation to (4.70) results in

$$
\begin{aligned}
(\tilde{\Gamma}\tilde{u})(\alpha_1) &= \int_{x_1 = -\infty}^{\infty} e^{j\omega\alpha_1 x_1} (\hat{\Gamma}\hat{u})(x_1) \, dx_1 \\
&= \frac{\omega}{2\pi} \int_{\alpha_1 = -\infty}^{\infty} \left[\int_{x_1 = -\infty}^{\infty} e^{j\omega(\alpha_1 - \alpha_1')x_1} \hat{\gamma}(x_1, \alpha_1') \, dx_1 \right] \tilde{u}(\alpha_1') \, d\alpha_1' \\
&= \frac{\omega}{2\pi} \int_{\alpha_1 = -\infty}^{\infty} \tilde{\gamma}(\alpha_1 - \alpha_1', \alpha_1') \tilde{u}(\alpha_1') \, d\alpha_1',
\end{aligned} \tag{4.77}
$$

where $\tilde{\gamma}$ is the co-kernel of $\hat{\Gamma}$

$$\tilde{\gamma}(\alpha_1, \alpha_1') = \int_{x_1 = -\infty}^{\infty} e^{j\omega\alpha_1 x_1} \hat{\gamma}(x_1, \alpha_1') \, dx_1. \tag{4.78}$$

The co-kernel $\tilde{\gamma}(\alpha_1, \alpha_1')$ can also be expressed in its spectrum

$$\tilde{\gamma}(\alpha_1, \alpha_1') = \sum_j \tilde{\phi}^{(j)}(\alpha_1) \tilde{\phi}^{(j)}(\alpha_1' - \alpha_1) (\lambda^{(j)})^{1/2}. \tag{4.79}$$

Since

$$
\begin{aligned}
(\tilde{A}\tilde{u})(\alpha_1) &= \left\{ \left[(\mu_0 \tilde{\varepsilon}*) - \alpha_1^2 \right] \tilde{u} \right\} (\alpha_1) \\
&= \frac{\omega}{2\pi} \int_{\alpha_1' = -\infty}^{\infty} \left[\mu_0 \tilde{\varepsilon}(\alpha_1 - \alpha_1') - \alpha_1^2 \right] \tilde{u}(\alpha_1') \, d\alpha_1,
\end{aligned} \tag{4.80}
$$

('$*$' indicates the convolution operator with respect to α_1) the co-kernel of $\hat{A}$ equals

$$\tilde{a}(\alpha_1, \alpha_1') = \mu_0 \tilde{\varepsilon}(\alpha_1) - (\alpha_1 + \alpha_1')^2. \tag{4.81}$$

Composition equation for operators, kernels, symbols and co-kernels

A construction method for the left symbol is based upon the composition equation for left symbols. We now present the derivation of this equation. Substitution of the standard operator form (4.73) in the composition equattion for operators

$$[\hat{A}(x_1, D_1)\hat{u}](x_1) = \{\hat{\Gamma}(x_1, D_1)[\hat{\Gamma}(x_1, D_1)\hat{u}]\}(x_1), \tag{4.82}$$

yields

$$\int_{x_1'=-\infty}^{\infty} \hat{\mathcal{A}}(x_1, x_1')\hat{u}(x_1') \, dx_1'$$

$$= \int_{x_1''=-\infty}^{\infty} \hat{\mathcal{C}}(x_1, x_1'') \left[\int_{x_1'=-\infty}^{\infty} \hat{\mathcal{C}}(x_1'', x_1')\hat{u}(x_1') \, dx_1' \right] dx_1''$$

$$= \int_{x_1'=-\infty}^{\infty} \left[\int_{x_1''=-\infty}^{\infty} \hat{\mathcal{C}}(x_1, x_1'')\hat{\mathcal{C}}(x_1'', x_1') \, dx_1'' \right] \hat{u}(x_1') \, dx_1'. \tag{4.83}$$

The outer integrals are equal on both sides and therefore the Schwartz kernel equals

$$\hat{\mathcal{A}}(x_1, x_1') = \int_{x_1''=-\infty}^{\infty} \hat{\mathcal{C}}(x_1, x_1'')\hat{\mathcal{C}}(x_1'', x_1') \, dx_1''. \tag{4.84}$$

This is the *composition equation for the Schwartz kernels*. The corresponding left symbol follows from Equation (4.75)

$$\hat{a}(x_1, \alpha_1) = \int_{x_1'=-\infty}^{\infty} e^{-j\omega\alpha_1(x_1'-x_1)} \left[\int_{x_1''=-\infty}^{\infty} \hat{\mathcal{C}}(x_1, x_1'')\hat{\mathcal{C}}(x_1'', x_1') \, dx_1'' \right] dx_1'. \tag{4.85}$$

Using the definition of the Schwartz kernels (4.74) yields

$$\hat{a}(x_1, \alpha_1) = \frac{\omega}{2\pi} \int_{x_1'=-\infty}^{\infty} \int_{x_1''=-\infty}^{\infty} \int_{\alpha_1'=-\infty}^{\infty} \int_{\alpha_1''=-\infty}^{\infty} e^{-j\omega\alpha_1(x_1'-x_1)}$$

$$e^{j\omega\alpha_1'(x_1''-x_1)} e^{-j\omega\alpha_1''(x_1'-x_1'')} \hat{\gamma}(x_1, \alpha_1')\hat{\gamma}(x_1'', \alpha_1'') \, d\alpha_1'' \, d\alpha_1' \, dx_1'' \, dx_1', \tag{4.86}$$

and subsequently performing two of the integrations yields the *composition equation for left symbols*

$$\hat{a}(x_1, \alpha_1) = \frac{\omega}{2\pi} \int_{x_1''=-\infty}^{\infty} \int_{\alpha_1'=-\infty}^{\infty} e^{j\omega(\alpha_1-\alpha_1')(x_1-x_1'')} \hat{\gamma}(x_1, \alpha_1')\hat{\gamma}(x_1'', \alpha_1) \, d\alpha_1' dx_1''. \tag{4.87}$$

Note that as $\omega \to \infty$, the composition of the left symbol tends to an ordinary multiplication, and the solution of Equation (4.87) reduces to the principal parts of the symbols.

Composition equation for co-kernels

Another construction method is based upon the composition equation for co-kernels. Its derivation starts by substituting the composition equation for left symbols in Equation (4.78) for ã and subsequently interchanging some integrals

$$\tilde{a}(\alpha_1'', \alpha_1) = \int_{x_1=-\infty}^{\infty} e^{j\omega\alpha_1''x_1}\hat{a}(x_1, \alpha_1)\,dx_1$$

$$= \frac{\omega}{2\pi}\int_{\alpha_1'=-\infty}^{\infty} \tilde{\gamma}(\alpha_1 + \alpha_1'' - \alpha_1', \alpha_1')\tilde{\gamma}(\alpha_1' - \alpha_1, \alpha_1)\,d\alpha_1'. \qquad (4.88)$$

Symbol class

A symbol class $S^d(\mathbb{R} \times \mathbb{R})$ for a real number d is defined in the following way. The symbol $\hat{a}_d$ lies in a space $S^d(\mathbb{R} \times \mathbb{R})$ if there is a constant $C_{m,n}$ such that

$$|(\partial_1^m \partial_1^n \hat{\gamma})| \leq C_{m,n}[(c^{-2} + \alpha_1^2)^{1/2}]^{d-m}, \qquad (4.89)$$

for all $x_1 \in \mathbb{R}$ and $\alpha_1 \in \mathbb{R}$. The corresponding operator has the same degree: $\hat{A}^z : H^0 \to H^{-2z}$. As an example, the operator $\hat{A}^{-1}$ is of the (double) integration-type: it produces smoother functions and distributions. However, the operator $\hat{A}$ is of the second-order differentiation type: it produces rougher functions and distributions. The elements of successive lower symbol classes corresponds to successive *smoother* operators. A complex-valued function b is called *positively homogeneous of degree* m, if[49]

$$b(x_1, t\alpha_1) = t^m b(x_1, \alpha_1). \qquad (4.90)$$

Polyhomogeneous expansion of the left symbol

An approximate symbol construction as a solution of this composition equation is discussed by de Hoop[49]. If s is real, the left symbol is an elliptic operator and an approximate construction is the polyhomogeneous expansion of the left symbol

$$\hat{\gamma}(x_1, \alpha_1) = (\mu_0\hat{\varepsilon} + \alpha_1^2)^{1/2}\Big\{ 1$$

$$+ \tfrac{1}{2}(\mu_0\hat{\varepsilon} + \alpha_1^2)^{-2}\left[-\tfrac{1}{2}j\alpha_1 s^{-1}(\partial_1\mu_0\hat{\varepsilon}) + s^{-2}(\partial_1^2\mu_0\hat{\varepsilon})\right]$$

$$+ (\mu_0\hat{\varepsilon} + \alpha_1^2)^{-4} \quad \cdots \quad \Big\}. \qquad (4.91)$$

This is an asymptotic expansion in homogeneous functions of α_1 of decreasing orders. The lower-order symbols have smoother contributions. If $s = j\omega$, the left symbol is no longer elliptic. Consequently, the asymptotic expansion of the left symbol for

$\omega \to \infty$ contains, besides an algebraic branch (as above with $s = \mathrm{j}\omega$),

$$\hat{\gamma}(x_1, \alpha_1) = (\mu_0 \hat{\varepsilon} - \alpha_1^2)^{1/2} \bigg\{ 1$$
$$+ \tfrac{1}{2}(\mu_0 \hat{\varepsilon} - \alpha_1^2)^{-2} \left[\tfrac{1}{2}\mathrm{j}\alpha_1 \omega^{-1}(\partial_1 \mu_0 \hat{\varepsilon}) - \omega^{-2}(\partial_1^2 \mu_0 \hat{\varepsilon}) \right]$$
$$+ (\mu_0 \hat{\varepsilon} - \alpha_1^2)^{-4} \quad \cdots \quad \bigg\}, \tag{4.92}$$

also an oscillatory exponential branch (see Fishman[52]). Neglecting this oscillatory exponential branch leads to inaccuracy for the post-critical phenomena[52]. The leading term of the polyhomogeneous expansion, $(\mu_0 \hat{\varepsilon} - \alpha_1^2)^{1/2}$, is called the principal part of the left symbol: it contains the main contribution of the behavior of the left symbol.

Ray theory restricts itself to the principal part, the high-frequency limit. Using the generalized slowness, e.g., the first terms of the polyhomogeneous expansion, instead of its high-frequency equivalent, extends the ray theory to lower frequencies.

The left symbol is pseudo-local. In a locally transverse homogeneous region, the left symbol equals its principal part $(\mu_0 \hat{\varepsilon} - \alpha_1^2)^{1/2}$. In transversely varying media, only the properties of the medium in the vicinity of x_1 influence the left symbol. This property is very useful when making fast numerical schemes and analyzing the accuracy of those numerical schemes.

Uniform expansion

For $s = \mathrm{j}\omega$, the polyhomogeneous expansion no longer provides a uniformly valid, phase space, operator symbol approximation, but is only valid in the *outer* phase space regime. Fishman, Gautesen and Sun[51] constructed a uniform expasion of the symbol. They start with the identity

$$\hat{\gamma}(x_1, \alpha_1) = (c^{-2} - \alpha_1^2)^{1/2} + \left[\hat{\gamma}(x_1, \alpha_1) - (c^{-2} - \alpha_1^2)^{1/2} \right]. \tag{4.93}$$

in order to extract the singular term (first term), which corresponds to the locally homogeneous or high-frequency limit. We subsequently rewrite the retaining non-singular term with use of the Helmholtz Green function (see Equation (4.41)) and apply the WKB method to determine the $\omega \to \infty$ asymptotic expansion. For more details, we refer to Fishman, Gautesen and Sun[51].

4.3   Quadratic profile waveguide

The pseudo-differential operator theory is now applied to the longitudinal slowness operator $\hat{\Gamma}$ corresponding to a medium with a quadratic profile for $\hat{\varepsilon}_{\mathrm{r}}$

$$\hat{\varepsilon}_{\mathrm{r}}(x_1) = a - \tfrac{1}{4}\, b\, x_1^2, \tag{4.94}$$
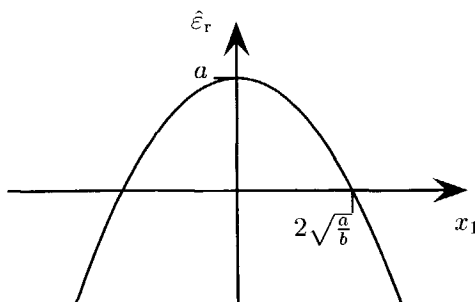
Figure 4.8:   *Medium with a quadratic profile for the relative permittivity $\hat{\varepsilon}_r$.*

as depicted in Figure 4.8. Here, we consider $b \in \mathbb{R}^+$; the configuration is a waveguide (a focussing medium). The quadratic medium with $b \in \mathbb{R}^-$ — an anti-waveguiding structure (a defocussing medium) has been analyzed by Fishman[52]. To ensure causality, we take $-\delta < \operatorname{Im}(a) < 0$, with $\delta \downarrow 0$. This is equivalent to assuming that ω has a small negative imaginary part.

For the derivation, we need some formulae from the "Handbook of Mathematical Function" by Abramowitz and Stegun[145], the "Table of Integrals, Series and Products" by Gradshteyn and Ryzhik[146] and the "Formulas and Theorems for the Special Functions of Mathematical Physics" by Magnus, Oberhettinger and Soni[147]. These formulae are repeated in Appendix 4.A.

This section is organized as follows. First, the theory is discussed, subsequently the numerical issues and, finally, the results.

4.3.1   Theory

Below, we derive the left symbol of the slowness operator, starting with the transverse Helmholtz operator, analyzing its spectrum and deforming the Dunford contour, and finally we arive at a summation over poles.

Consider the transverse Helmholtz operator $\hat{A}$

$$\hat{A}(x_1) = \mu_0 \hat{\varepsilon}(x_1) + \omega^{-2}\partial_1^2 = \omega^{-2}\partial_1^2 + c_0^{-2}(a - \tfrac{1}{4}bx_1^2). \tag{4.95}$$

The Schwartz kernel representation of the resolvent $\hat{R}_\lambda$ satisfies (compare with Equation (4.40) and (4.42))

$$\left[\partial_1^2 - k_0^2\left(-a + \tfrac{1}{4}bx_1^2 + c_0^2\lambda\right)\right]\left[-\omega^{-2}\hat{R}_\lambda(x_1, x_1')\right] = -\delta(x_1 - x_1'). \tag{4.96}$$

Now, introduce the new variables

$$\xi_1 = \left(b^{1/2}k_0\right)^{1/2} x_1, \tag{4.97}$$

$$Q\left[(b^{1/2}k_0)^{1/2}x_1, (b^{1/2}k_0)^{1/2}x_1'\right] = \left(b^{1/2}k_0\right)^{1/2}(-\omega^{-2}\hat{\mathcal{R}}_\lambda)(x_1, x_1'),$$
(4.98)

and

$$a_+(\lambda) \equiv (k_0/b^{1/2})\,(\lambda c_0^2 - a).$$
(4.99)

Here, ξ_1 can be interpreted as a scaled transverse coordinate and Q is the Green function of the 2-D Helmholtz equation (compare with Equation (4.43)). Using these abbreviations, we find the differential equation

$$\left[\partial_{\xi_1}^2 - (a_+ + \tfrac{1}{4}\xi_1^2)\right]Q(\xi_1, \xi_1') = -\delta(\xi_1 - \xi_1').$$
(4.100)

This equation is now written in the same form as Equation (4A.2).

The solutions of the homogeneous equation corresponding to (4.100) are Weber parabolic cylinder functions, $U(a_+, \pm\xi_1)$. From (4.100) follows (compare with Equation (4.46))

$$Q(\xi_1, \xi_1') = -\frac{1}{\sqrt{2\pi}}\Gamma(\tfrac{1}{2} + a_+)$$
$$\left[H(\xi_1' - \xi_1)U(a_+, -\xi_1)U(a_+, \xi_1') + H(\xi_1 - \xi_1')U(a_+, \xi_1)U(a_+, -\xi_1')\right]. \quad (4.101)$$

Note that the Wronskian

$$\hat{W}(\xi_1, \xi_1') = -\sqrt{2\pi}\,\Gamma^{-1}(\tfrac{1}{2} + a_+),$$
(4.102)

is independent of ξ_1 and ξ_1'. The singularities of the Gamma function $\Gamma(y)$ follow from Equation (4A.1)

$$\lim_{y \to -m}\frac{1}{\Gamma(y)} = 0, \qquad \text{for } m = 0, 1, 2, \cdots.$$
(4.103)

Therefore $\hat{\mathcal{R}}_\lambda(x_1, x_1')$ has poles at (see Figure 4.6)

$$\lambda = \lambda^{(m)} = c_0^{-2}\left(\frac{b^{1/2}}{k_0}a_{+,m} + a\right),$$
(4.104)

where

$$a_{+,m} = -\tfrac{1}{2} - m, \qquad \text{with } m = 0, 1, 2, \cdots.$$
(4.105)

In order to compute the Schwartz kernel $\hat{A}_z$ of operator $\hat{A}^z$, we start with the theorem of residues for calculating the scaled Schwartz kernel $\mathcal{Q}$ of $\hat{R}_\lambda$. By deforming the Dunford integration contour, the Dunford integral is then transformed into a summation over poles (compare with Equation (4.50))

$$\frac{1}{2\pi j}\int_{\lambda \in \mathcal{B}}\lambda^z\,\mathcal{Q}(\xi_1, \xi_1')\,d\lambda = \sum_{m=0}^{\infty}\lim_{\lambda \to \lambda^{(m)}}\mathcal{Q}(\xi_1, \xi_1')\,\lambda^z\,(\lambda - \lambda^{(m)}).$$
(4.106)

Here, we used that a, and thus also $\lambda^{(m)}$, has a small negative imaginary part (see also Figure 4.7). In order to compute this limit, we need two extra relations. Using (see Appendix 4.A)

$$\lim_{y \to -m} \Gamma(y)(y + m) = \frac{(-1)^m}{m!}, \quad m = 0, 1, 2, \cdots, \tag{4.107}$$

we find the first relation

$$\lim_{\lambda \to \lambda^{(m)}} \Gamma(\tfrac{1}{2} + a_+)(\lambda - \lambda^{(m)}) = \frac{b^{1/2}}{k_0 c_0^2} \lim_{a_+ \to -m-\frac{1}{2}} \Gamma(\tfrac{1}{2} + a_+)\left(a_+ + \tfrac{1}{2} + m\right)$$

$$= \frac{b^{1/2}}{k_0 c_0^2} \frac{(-1)^m}{m!}, \qquad m = 0, 1, 2, \cdots. \tag{4.108}$$

The parabolic cylindric function $U(a_+, \xi_1)$ is even for $a_+ = -m - \frac{1}{2}$ with m even

$$U(-m - \tfrac{1}{2}, \xi_1) = U(-m - \tfrac{1}{2}, -\xi_1), \qquad m = \cdots, -2, 0, 2, 4, \cdots, \tag{4.109}$$

and is odd for $a_+ = -m - \frac{1}{2}$ with m odd

$$U(-m - \tfrac{1}{2}, \xi_1) = -U(-m - \tfrac{1}{2}, -\xi_1), \qquad m = \cdots, -1, 1, 3, \cdots. \tag{4.110}$$

This leads to the second relation

$$H(\xi_1' - \xi_1)\, U(-m - \tfrac{1}{2}, -\xi_1')\, U(-m - \tfrac{1}{2}, \xi_1) +$$
$$H(\xi_1 - \xi_1')\, U(-m - \tfrac{1}{2}, \xi_1')\, U(-m - \tfrac{1}{2}, -\xi_1)$$
$$= (-1)^m U(-m - \tfrac{1}{2}, \xi_1')U(-m - \tfrac{1}{2}, \xi_1), \qquad \text{for } m \text{ integer.} \tag{4.111}$$

Combining these two relations yields

$$\frac{1}{2\pi \mathrm{j}} \int_{\lambda \in \mathcal{B}} \lambda^z \mathcal{Q}(\xi_1, \xi_1')\, \mathrm{d}\lambda$$

$$= \frac{b^{1/2}}{k_0 c_0^2} \sum_{m=0}^{\infty} -U(-m - \tfrac{1}{2}, \xi_1)\, U(-m - \tfrac{1}{2}, \xi_1') \frac{(\lambda^{(m)})^z}{(\sqrt{2\pi}\, m!)}. \tag{4.112}$$

The parabolic cylindric function $U(-m - \frac{1}{2}, \xi_1)$ $(m = 0, 1, 2, \cdots)$ can be expressed in the Hermite polynomials (see Equation (4A.3))

$$U(-m - \tfrac{1}{2}, \xi_1) = \mathrm{e}^{-\xi_1^2/4}\, H_m(\frac{\xi_1}{\sqrt{2}})\, 2^{-m/2}. \tag{4.113}$$

It is well known that these functions are the guided modes of a waveguide with quadratic profile[144]. They form an orthogonal and complete set. The Schwartz

kernel of $\hat{A}^z$ $(\mathrm{Re}\,(z) < 0)$ can be expressed in these modes

$$
\begin{aligned}
\hat{\mathcal{A}}_z(x_1, x_1') &= \frac{1}{2\pi\mathrm{j}} \int_{\lambda \in \hat{\mathcal{B}}} \lambda^z \hat{\mathcal{R}}_\lambda(x_1, x_1') \, \mathrm{d}\lambda \\
&= -\omega^2 (b^{1/2}k_0)^{-1/2} \frac{1}{2\pi\mathrm{j}} \int_{\lambda \in \mathcal{B}} \lambda^z \mathcal{Q} \left[(b^{1/2}k_0)^{1/2} x_1, (b^{1/2}k_0)^{1/2} x_1' \right] \, \mathrm{d}\lambda \\
&= (b^{1/2}k_0)^{1/2} \sum_{m=0}^{\infty} \frac{(\lambda^{(m)})^z}{(\sqrt{2\pi}\,m!)} U[-m - \tfrac{1}{2}, (b^{1/2}k_0)^{1/2} x_1] \\
&\hspace{4cm} U[-m - \tfrac{1}{2}, (b^{1/2}k_0)^{1/2} x_1']. \qquad (4.114)
\end{aligned}
$$

In particular (compare with Equation (4.59)),

$$
\hat{\mathcal{A}}_0(x_1, x_1') = \delta(x_1 - x_1'). \qquad (4.115)
$$

For $z > 0$, $\hat{A}_z$ becomes a higher-order distribution. With use of (see Equation (4A.5))

$$
\int_{\xi_1' = -\infty}^{\infty} \exp(-\mathrm{j}\omega\xi_1'\alpha_1') \mathrm{e}^{-(\xi_1')^2/4} H_m(\tfrac{\xi_1'}{\sqrt{2}}) \, \mathrm{d}\xi_1' = 2\sqrt{\pi}\,\mathrm{j}^m \mathrm{e}^{-(\omega\alpha_1')^2} H_m(-\sqrt{2}\omega\alpha_1'), \qquad (4.116)
$$

where α_1' is a rescaled transverse slowness

$$
\alpha_1' \equiv (b^{1/2}k_0)^{-1/2} \alpha_1, \qquad (4.117)
$$

the left symbol of $\hat{A}^z$ $(\mathrm{Re}\,(z) < 0)$ is found as (compare with Equation (4.76))

$$
\begin{aligned}
\hat{\mathrm{a}}_z(x_1, \alpha_1) &= \int_{x_1' = -\infty}^{\infty} \hat{\mathcal{A}}_z(x_1, x_1') \exp\left[\mathrm{j}\omega(x_1 - x_1')\alpha_1\right] \, \mathrm{d}x_1' \\
&= (b^{1/2}k_0)^{1/2} \sum_{m=0}^{\infty} \frac{(\lambda^{(m)})^z}{(\sqrt{2\pi}\,m!)} U[-m - \tfrac{1}{2}, (b^{1/2}k_0)^{1/2} x_1] \exp(\mathrm{j}\omega x_1 \alpha_1) \\
&\hspace{1cm} \int_{x_1' = -\infty}^{\infty} U[-m - \tfrac{1}{2}, (b^{1/2}k_0)^{1/2} x_1'] \exp(-\mathrm{j}\omega x_1' \alpha_1) \, \mathrm{d}x_1' \\
&= \sqrt{2} \exp\left(-\frac{k_0}{b^{1/2}} \alpha_1^2 + \mathrm{j}\omega x_1 \alpha_1 - \tfrac{1}{4} b^{1/2} k_0 x_1^2 \right) \\
&\hspace{0.5cm} \sum_{m=0}^{\infty} \left(\frac{-\mathrm{j}}{2} \right)^m \frac{(\lambda^{(m)})^z}{m!} H_m \left[\left(\frac{2k_0}{b^{1/2}} \right)^{1/2} \alpha_1 \right] H_m \left[\left(\tfrac{1}{2} b^{1/2} k_0 \right)^{1/2} x_1 \right].
\end{aligned}
$$
$$
(4.118)
$$

Here, we also used the *reflection Formula* (4A.9). Numerical tests show that convergence is also obtained for $z = 0$: $\hat{\mathrm{a}}_0(x_1, n_1) = 1$. This is in full agreement with

Equation (4A.7). For $\mathrm{Re}\,(z) > 0$, the above series is not convergent. This can be easily clarified with the Christoffel-Darboux Formula (4A.8) and the estimation of the Hermite polynomials (4A.4).

To make a convergent series for $\mathrm{Re}(z) > 0$, we can start with constructing the left symbol $\hat{\mathrm{a}}_z$ for $0 < \mathrm{Re}\,(z) < 1$. The composition equation for operators is (see Equation (4.54))

$$\hat{\mathrm{A}}^z = \hat{\mathrm{A}}\,\hat{\mathrm{A}}^{z-1}. \tag{4.119}$$

Higher-order powers of $\hat{\mathrm{A}}$ ($\mathrm{Re}\,(z) > 1$) are constructed by repeatedly applying the composition Equation (4.119). By letting the operators in (4.119) act on a plane wave and replace the operators then by their left symbol

$$\hat{\mathrm{a}}_z \mathrm{e}^{-jk_0 n_1 x_1} = \hat{\mathrm{A}}\hat{\mathrm{a}}_{z-1}\mathrm{e}^{-jk_0 n_1 x_1}, \tag{4.120}$$

we find an equation for computing the left symbol $\hat{\mathrm{a}}_z$ from $\hat{\mathrm{a}}_{z-1}$

$$\hat{\mathrm{a}}_z = \left[c_0^{-2}\left(a - \tfrac{1}{4}bx_1^2\right) - \alpha_1^2\right]\hat{\mathrm{a}}_{z-1} + \omega^{-2}\left(\partial_1^2\hat{\mathrm{a}}_{z-1}\right) - 2j\omega^{-1}\alpha_1\left(\partial_1\hat{\mathrm{a}}_{z-1}\right). \tag{4.121}$$

Substituting the series (4.118) for $\hat{\mathrm{a}}_{z-1}$ in the above equation, one might attempt to interchange the derivatives, ∂_1^2 and ∂_1, and the infinite summation. Doing thus, results in the same series as in (4.118), but now with $\mathrm{Re}\,(z) < 1$. Interchanging the infinite summation and the derivatives is, however, not allowed, and instead, a special regularization procedure should be used. We use Fourier-type filtering techniques to regularize the divergent series, as described in the next subsection.

4.3.2 Numerical issues

This subsection is addressed to computing the series (4.118). First, we discuss how to compute successively one term from the previous term with low numerical effort. Second, we discuss how to regularize the series in order to obtain a convergent series.

Individual terms

The series in (4.118) can be written in the form

$$\hat{\mathrm{a}}_z(x_1, \alpha_1) = C(x_1, \alpha_1)\sum_{m=0}^{\infty} T(m, z, \alpha_1, x_1), \tag{4.122}$$

with *constant* $C(x_1, \alpha_1)$ (independent of m)

$$C(x_1, \alpha_1) = \sqrt{2}\,\exp\left(-\frac{k_0}{b^{1/2}}\alpha_1^2 + j\omega x_1\alpha_1 - \tfrac{1}{4}b^{1/2}k_0 x_1^2\right), \tag{4.123}$$

and the terms $T(m, z, x_1, \alpha_1)$

$$T(m, z, x_1, \alpha_1) = \left(\frac{-j}{2}\right)^m \frac{(\lambda^{(m)})^z}{m!} H_m \left[\left(\frac{2k_0}{b^{1/2}}\right)^{1/2} \alpha_1\right] H_m \left[\left(\frac{1}{2}b^{1/2}k_0\right)^{1/2} x_1\right].$$

(4.124)

The numerical implementation of the Hermite polynomials is based upon the recursion Formula (4A.6). Because $m!$ and $(-j/2)^m$ occur also in $T(m, z, x_1, \alpha_1)$, numerical overflows will occur for higher order terms (for $m!$ already if $m > 200$). Therefore an alternative recursion scheme is employed. Set

$$T(m, x_1, \alpha_1) = T_m \left[\left(\frac{2k_0}{b^{1/2}}\right)^{1/2} \alpha_1\right] T_m \left[\left(\frac{1}{2}b^{1/2}k_0\right)^{1/2} x_1\right] (\lambda^{(m)})^z,$$

(4.125)

with the recursion relation for T_m

$$T_m(y) = 2y\ (j/2)^{1/2}\ m^{-1/2}\ T_{m-1}(y) - j(m-1)\ T_{m-2}[m(m-1)]^{-1/2},$$

(4.126)

and its initial conditions are $T_0(y) = 1$ and $T_1(y) = (2j)^{1/2}y$.

The series

The series for $\hat{a}_z$ in (4.118) is convergent for $\text{Re}(z) \leq 0$. Computing a finite number of terms gives a good approximation. The derivatives in the composition Equation (4.121) can be computed with a finite difference scheme. This is equivalent to computing the discrete derivative of the terms of the series directly. Slow convergence is obtained when taking a more accurate discrete derivative. Oscillation effects appear in $\hat{a}_z$. These effects are very similar to the Gibbs phenomena (see for instance Lanczos[148] or Scaife[149]). This prompted us to search for a similar approach to avoid oscillation effects and divergence of the series. We designed a very simple filter (see Figure 4.9) for this purpose

$$f(m) = \begin{cases} 1, & \text{if } m < M_1, \\ (M_1 - M_2)^{-1}\ m + (1 - M_1/M_2)^{-1}, & \text{if } m < M_2, \\ 0, & \text{if } m > M_2. \end{cases}$$

(4.127)

Every term of the series is now multiplied by the filter $f(m)$. Equation (4.122) becomes

$$\hat{a}_z(x_1, \alpha_1) = C(x_1, \alpha_1) \sum_{m=0}^{M_2} f(m)\ T(m, z, \alpha_1, x_1).$$

(4.128)

The infinite summation is now approximated by a finite sum with some filter in it. Now, it is permitted to change the order of the summation and the derivatives.
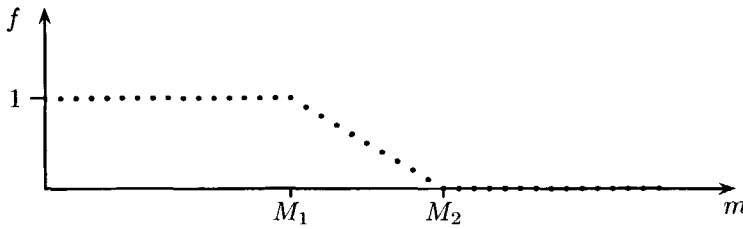
Figure 4.9: *Filter used to regularize the divergent series.*

We use Equation (4.128) for computing $\hat{a}_z$ with arbitrary z. In order to estimate the accuracy of the series, we compare the analytical left symbol $\hat{a}_1^{ex} = c_0^{-2}(a - \frac{1}{4}bx_1^2) - \alpha_1^2$ and the corresponding approximate left symbol $\hat{a}_1^{app}$ from Equation (4.128) with different $f(m)$. Since the convergence is slower for larger $\mathrm{Re}(z)$, the errors in computing $\hat{a}_{1/2}$ are smaller. This comparison indicates that the accuracy is high for $M_2 > 1000$.

4.3.3   Results

Having derived the left symbol for the slowness in a quadratic profile medium, we are now in a position to analyze it. For this purpose we consider a configuration with $a = 1$, $\omega = 1$ s^{-1}, $c_0 = 1$ m/s. Then, the transverse Helmholtz operator $\hat{A}$ simplifies into

$$\hat{A} = 1 - \tfrac{1}{4}\, b\, x_1^2 + \partial_1^2, \tag{4.129}$$

and the longitudinal slowness operator $\hat{\Gamma}$

$$\hat{\Gamma} = \left(1 - \tfrac{1}{4}\, b\, x_1^2 + \partial_1^2\right)^{1/2}. \tag{4.130}$$

Figure 4.10 illustrates the longitudinal slowness at the origin for several values of b, while Figure 4.11 illustrates the longitudinal slowness for two fixed values of b at different transverse positions x_1. We now discuss the asymptotic behavior and the physical interpretation.

Asymptotic behavior

It is clear from Figure 4.10 that for slowly varying media (b is small), the longitudinal slowness behaves as the longitudinal slowness in a homogeneous space. This corresponds to high frequencies. The asymptotic behavior for large transverse slownesses, $\alpha_1 \to \pm\infty$, is correct: $\hat{\gamma} \to -j|\alpha_1|$.

For high variation of the speed (b large: ≥ 4) the waveguiding properties (i.e. the real part equals 0) vanish and for higher values of b the attenuation becomes high. At the critical value $b = 4$, the first eigenvalue $\lambda^{(0)}$ equals 0 (see Equation (4.104)). For higher values of b, all eigenvalues $\lambda^{(m)}$ are imaginarily valued.

Physical interpretation

Wave phenomena in very slowly varying media are usually analyzed with ray theory. The ray theory describes waves in the high-frequency limit. In faster, varying media, the ray approximation is no longer accurate enough. When lowering the frequency (or increasing the medium variation), we can generalize the ray theory and examine the generalized slowness. The heterogeneity of the medium is then translated into anisotropic properties in the generalized slowness: heterogeneity and anisotropy are seen to coexist.

Wave propagation in slowly varying media ($b < 0.004$ m^{-2}) behaves like wave propagation in the homogeneous space and is close to the high-frequency asymptotics (half circle). From the number of oscillations in the slowness, we can estimate the number of propagating modes present in the waveguiding structure.

Figure 4.11 shows that at a positive off-set, the wave propagation towards the origin ($\alpha_1 < 0$) is stimulated. This can be seen from the shift of the amplified part of the longitudinal slowness ($\text{Im}(\hat{\gamma}) > 0$). This behavior characterizes waveguides.

The post-critical wave propagation is correctly described and can be used to investigate the artificial post-critical wave propagation in any approximate method. Some nonphysical phenomena occur due to the negative speeds in the outer regions of our waveguiding model.

The wave propagation depends on the frequency, which causes (waveguiding) dispersion. The local wavefront for one frequency component can be found through the path integral[135]. The one-dimensional lower theory of waveguiding modes is connected with transient phenomena through the left symbol. All the wave propagation information is inside the left symbol.

We showed the first graphs of the generalized slowness in waveguiding structures. The longitudinal slowness generalized ray theory to lower frequencies.

4.4 Symmetrical step-index slab waveguide

The pseudo-differential operator theory is now applied to the slowness operator for the case of a symmetrical step-index slab waveguide (see Figure 4.12) ("square well"). The refractive index is given by

$$n(x_1) = \begin{cases} n_{\text{co}}, & |x_1| < a, \\ n_{\text{cl}}, & |x_1| > a. \end{cases} \tag{4.131}$$

The thickness of the waveguide equals $2a$.

Here, we consider $n_{\text{co}} > n_{\text{cl}}$; the configuration is a waveguide (focussing medium). The anti-waveguiding structure (a defocussing medium $n_{\text{co}} < n_{\text{cl}}$) is not considered.

This section is organized as follows. First, the theory is discussed, subsequently the numerical issues, and finally the results.
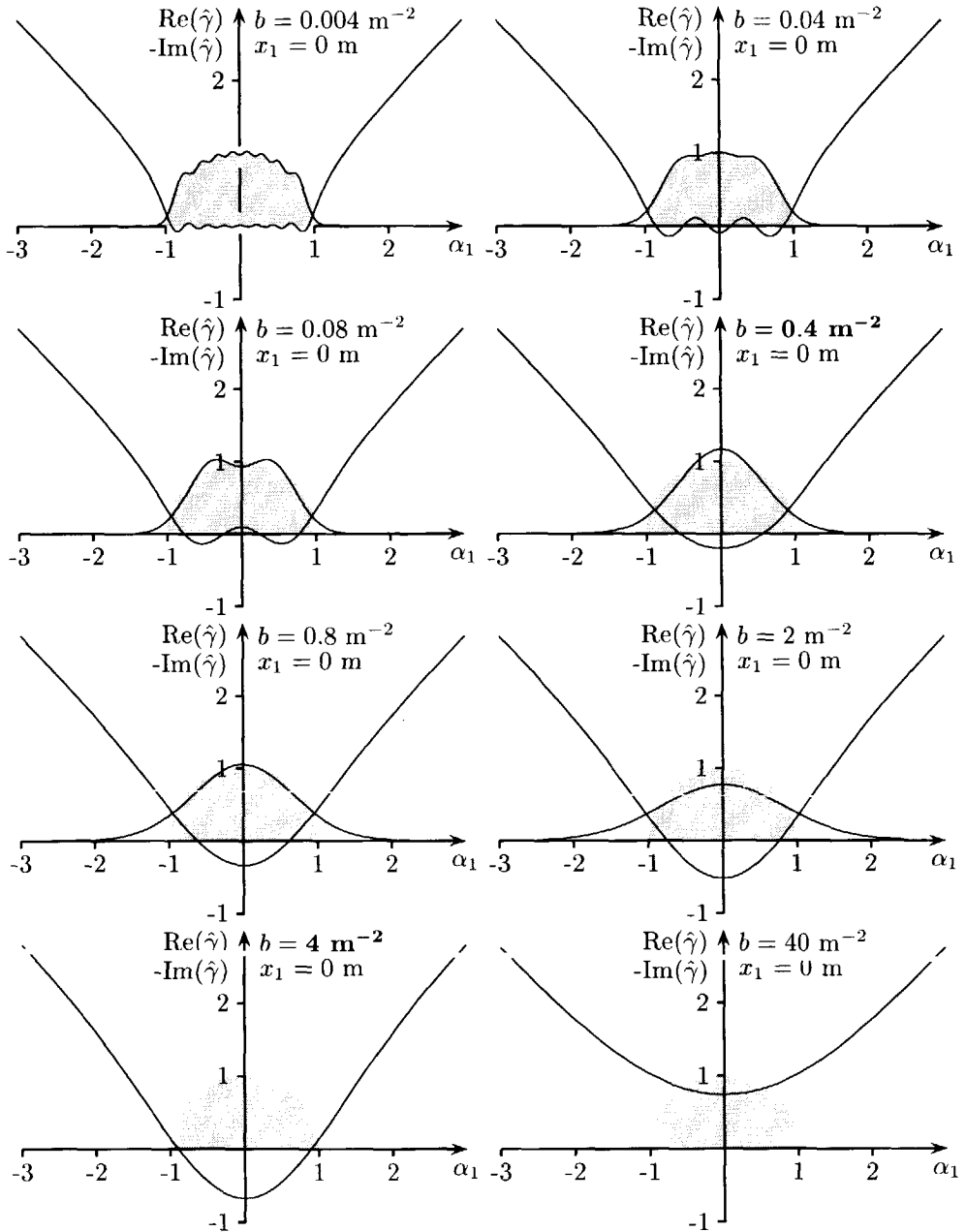
Figure 4.10: *The real and (negative) imaginary part of the left symbol $\hat{\gamma}$ in a waveguide with quadratic profile. The value of b varies in every figure; the position is fixed at the origin ($x_1 = 0$).*
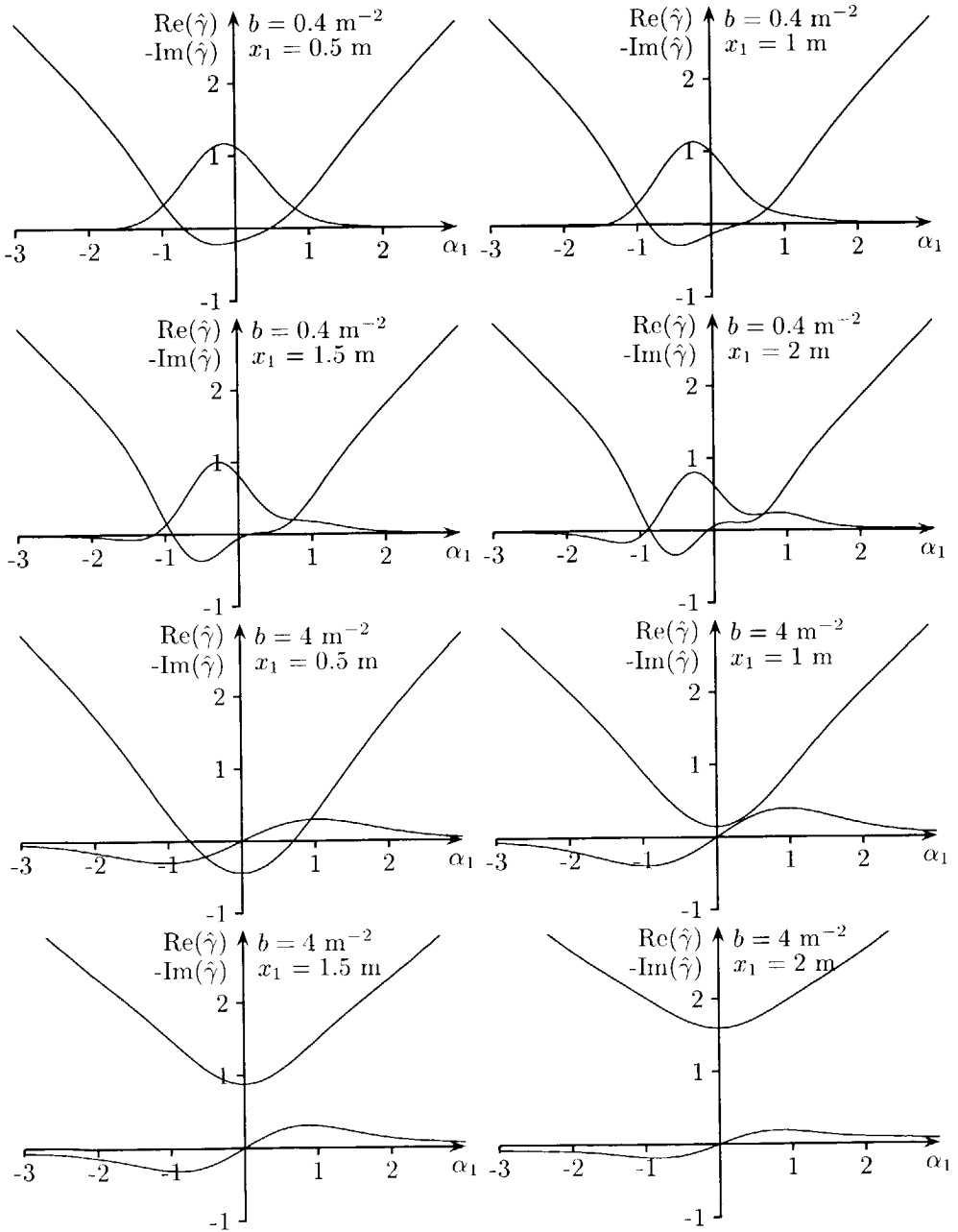
Figure 4.11: *The real and (negative) imaginary part of the left symbol $\hat{\gamma}$ in a waveguide with quadratic profile. The values of b and x_1 vary for every figure.*
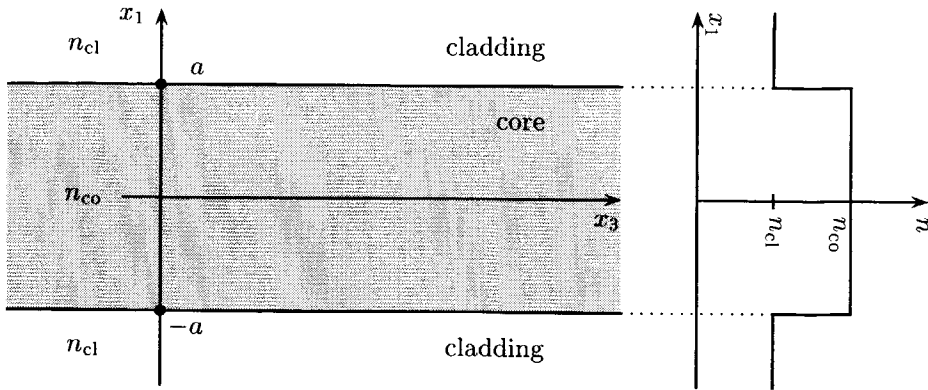
Figure 4.12: *Symmetrical slab dielectric waveguide. All the media are homogeneous, with permeability μ_0.*

4.4.1   Theory

In the derivation of the left symbols, we use the analytical expressions for the guided and radiating modes in a symmetrical (step-index) slab waveguide. These expressions are summarized in several books, see e.g., Marcuse[142], Snyder and Love[143], and Vassallo[144]. Below, we give a short summary of the modal analysis in a symmetrical step-index slab waveguide. First, we introduce some useful waveguiding parameters and, subsequently, we list the analytical expressions for the waveguide modes. Finally, the left symbol is derived.

Waveguide parameters

It is customary to introduce the normalized frequency

$$V = k_0 a \sqrt{n_{co}^2 - n_{cl}^2}, \tag{4.132}$$

the core parameters

$$\alpha = k_0 \sqrt{n_{co}^2 - n_{eff}^2}, \qquad\qquad U = k_0 a \sqrt{n_{co}^2 - n_{eff}^2} = \alpha a, \tag{4.133}$$

(n_{eff} is the effective index, see Equation (4.60)), the cladding parameters for bound modes

$$\kappa = k_0 \sqrt{n_{eff}^2 - n_{cl}^2}, \qquad\qquad W = k_0 a \sqrt{n_{eff}^2 - n_{cl}^2} = \kappa a, \tag{4.134}$$

and the cladding parameters for radiating modes

$$\nu = k_0 \sqrt{n_{cl}^2 - n_{eff}^2} = j\kappa, \qquad Q = k_0 a \sqrt{n_{cl}^2 - n_{eff}^2} = \nu a = jW. \tag{4.135}$$

We observe that the core parameter α depends on the cladding parameter ν

$$\alpha(\nu) = \sqrt{k_0^2(n_{\text{co}}^2 - n_{\text{cl}}^2) + \nu^2}, \tag{4.136}$$

and that the normalized frequency V satisfies

$$V^2 = U^2 + W^2, \qquad V^2 = U^2 - Q^2. \tag{4.137}$$

Here, the wave number in vacuum is $k_0 = \omega\sqrt{\varepsilon_0\mu_0}$. With these parameters, we can introduce the expressions for the guided and radiating modes.

Guided modes

The guided (or discrete) TE modes are found as

$$\hat{\phi}^{(j)}(x_1) = N_j^{-1/2} \begin{cases} \cos(\alpha x_1), & (|x_1| < a), \\ \cos(U)\exp[-\kappa(|x_1| - a)], & (|x_1| > a), \end{cases} \tag{4.138}$$

for even guided modes ($j = 0, 2, 4, \cdots$) with the dispersion relation

$$W = U\tan(U), \tag{4.139}$$

and

$$\hat{\phi}^{(j)}(x_1) = N_j^{-1/2} \begin{cases} \sin(\alpha x_1), & (|x_1| < a), \\ \text{sgn}(x_1)\sin(U)\exp[-\kappa(|x_1| - a)], & (|x_1| > a), \end{cases} \tag{4.140}$$

for odd guided modes ($j = 1, 3, 5, \cdots$) with the dispersion relation

$$W = -U/\tan(U). \tag{4.141}$$

The eigenvalues $\lambda^{(j)} = c_0^{-2}(n_{\text{eff}}^{(j)})^2$ follow from solving the corresponding dispersion equations. The effective refractive indices are real valued, positive and bounded by

$$n_{\text{cl}} < n_{\text{eff}}^{(j)} < n_{\text{co}}. \tag{4.142}$$

The norm of the discrete modes equals

$$N_j = a(1 + W_j^{-1}), \tag{4.143}$$

where W_j is the core parameter W of mode j. The guided modes satisfy the orthogonality relation (see Equation (4.31))

$$\int_{-\infty}^{\infty} \hat{\phi}^{(i)}(x_1)\hat{\phi}^{(j)}(x_1)\,\mathrm{d}x_1 = \delta_{i,j}. \tag{4.144}$$

Radiating modes

The even radiating TE modes are found as

$$
\hat{\phi}_{\text{even}}(x_1;\nu) = \pi^{-1/2} \begin{cases} \cos(\psi^{\text{e}})\cos^{-1}(U)\cos(\alpha x_1), & (|x_1| < a), \\ \cos[\nu(|x_1| - a) + \psi^{\text{e}}], & (|x_1| > a), \end{cases} \tag{4.145}
$$

while the odd radiating modes TE modes

$$
\hat{\phi}_{\text{odd}}(x_1;\nu) = \pi^{-1/2} \begin{cases} \sin(\psi^{\text{o}})\sin^{-1}(U)\sin(\alpha x_1), & (|x_1| < a), \\ \text{sgn}(x_1)\sin[\nu(|x_1| - a) + \psi^{\text{o}}], & (|x_1| > a). \end{cases} \tag{4.146}
$$

Here, the phase factor ψ is derived from

$$
\tan(\psi^{\text{e}}) = \frac{U}{Q}\tan(U), \tag{4.147}
$$

$$
\tan(\psi^{\text{o}}) = \frac{Q}{U}\tan(U). \tag{4.148}
$$

The radiating modes satisfy the orthogonality relation

$$
\int_{-\infty}^{\infty} \hat{\phi}_P(x_1;\nu)\hat{\phi}_R(x_1;\nu') \, dx_1 = \delta(\nu - \nu')\delta_{P,R}, \tag{4.149}
$$

with parity $P, R =$ even or odd.

Completeness relation

The completeness relation is given by (see Equation (4.34))

$$
\delta(x_1 - x_1') = \sum_{j=0}^{J-1} \hat{\phi}^{(j)}(x_1)\hat{\phi}^{(j)}(x_1')
$$

$$
+ \int_{\nu=0}^{\infty} \hat{\phi}_{\text{even}}(x_1';\nu) \, \hat{\phi}_{\text{even}}(x_1;\nu) \, d\nu
$$

$$
+ \int_{\nu=0}^{\infty} \hat{\phi}_{\text{odd}}(x_1;\nu) \, \hat{\phi}_{\text{odd}}(x_1';\nu) \, d\nu, \tag{4.150}
$$

where J is the number of guided modes. We note that the radiating modes are normalized in a different way than those in Section 4.2, see Equations (4.31)-(4.33). Here, the branch-cut integral is rewritten into an integral over ν from 0 to ∞.

Waveguide modes in spatial Fourier transform domain

To compute the left symbols, we need the Fourier transformations of the guided and radiating modes. The Fourier transform $\mathcal{F}$ with respect to the transverse coordinate x_1 was introduced in Equation (4.2). The even guided TE modes in spatial Fourier transform domain are

$$
\begin{aligned}
&\tilde{\phi}^{(j)}(\alpha_1) \\
&= -2N_j^{-1/2}\big\{(\alpha^2 - \omega^2\alpha_1^2)^{-1}\left[\omega\alpha_1\sin(a\omega\alpha_1)\cos(a\alpha) - \alpha\cos(a\omega\alpha_1)\sin(a\alpha)\right] \\
&\qquad\qquad + \cos(U)(\kappa^2 + \omega^2\alpha_1^2)^{-1}\left[\omega\alpha_1\sin(a\omega\alpha_1) - \kappa\cos(a\omega\alpha_1)\right]\big\}, \quad (4.151)
\end{aligned}
$$

while the odd guided TE modes in spatial Fourier transform domain are

$$
\begin{aligned}
&-\,\mathrm{j}\tilde{\phi}^{(j)}(\alpha_1) \\
&= -2N_j^{-1/2}\big\{(\alpha^2 - \omega^2\alpha_1^2)^{-1}\left[\omega\alpha_1\cos(a\omega\alpha_1)\sin(a\alpha) - \alpha\sin(a\omega\alpha_1)\cos(a\alpha)\right] \\
&\qquad\qquad + \sin(U)(\kappa^2 + \omega^2\alpha_1^2)^{-1}\left[\omega\alpha_1\cos(a\omega\alpha_1) + \kappa\sin(a\omega\alpha_1)\right]\big\}. \quad (4.152)
\end{aligned}
$$

The Fourier transformations of the even TE radiating modes are

$$
\begin{aligned}
\tilde{\phi}_{\mathrm{even}}(\alpha_1;\nu) &= 2\pi^{-1/2}\cos(\psi^{\mathrm{e}})\cos^{-1}(U)(\alpha^2 - \omega^2\alpha_1^2)^{-1} \\
&\quad\quad \left[\alpha\cos(a\omega\alpha_1)\sin(a\alpha) - \omega\alpha_1\sin(a\omega\alpha_1)\cos(a\alpha)\right] \\
&\quad - \pi^{-1/2}(\nu - \omega\alpha_1)^{-1}\sin(\psi^{\mathrm{e}} - a\omega\alpha_1) - \pi^{-1/2}(\nu + \omega\alpha_1)^{-1}\sin(\psi^{\mathrm{e}} + a\omega\alpha_1) \\
&\quad + \pi^{1/2}\delta(\nu - \omega\alpha_1)\cos(\psi^{\mathrm{e}} - a\omega\alpha_1) + \pi^{1/2}\delta(\nu + \omega\alpha_1)\cos(\psi^{\mathrm{e}} + a\omega\alpha_1), \quad (4.153)
\end{aligned}
$$

while the Fourier transformations of the odd TE radiating modes are

$$
\begin{aligned}
-\,\mathrm{j}\tilde{\phi}_{\mathrm{odd}}(\alpha_1;\nu) &= 2\pi^{-1/2}\sin(\psi^{\mathrm{o}})\sin^{-1}(U)(\alpha^2 - \omega^2\alpha_1^2)^{-1} \\
&\quad\quad \left[\alpha\sin(a\omega\alpha_1)\cos(a\alpha) - \omega\alpha_1\cos(a\omega\alpha_1)\sin(a\alpha)\right] \\
&\quad + \pi^{-1/2}(\nu - \omega\alpha_1)^{-1}\sin(\psi^{\mathrm{o}} - a\omega\alpha_1) - \pi^{-1/2}(\nu + \omega\alpha_1)^{-1}\sin(\psi^{\mathrm{o}} + a\omega\alpha_1) \\
&\quad - \pi^{1/2}\delta(\nu - \omega\alpha_1)\cos(\psi^{\mathrm{o}} - a\omega\alpha_1) + \pi^{1/2}\delta(\nu + \omega\alpha_1)\cos(\psi^{\mathrm{o}} + a\omega\alpha_1). \quad (4.154)
\end{aligned}
$$

There are two types of singularities at $\nu = \pm\omega\alpha_1$. First, there is an essential singularity due to the Dirac delta distribution. Second, there is a pole singularity. Note that the Fourier transformation of the even modes are real even functions of α_1, while the Fourier transformations of the odd modes are imaginary odd function of α_1.

Derivation of the left symbol

Consider the operator $\hat{\mathrm{A}}$

$$
\hat{\mathrm{A}}(x_1) = \mu_0\hat{\varepsilon}(x_1) + \omega^{-2}\partial_1^2, \tag{4.155}
$$

and its (fractional) power

$$\hat{A}^z(x_1) = (\mu_0\hat{\varepsilon}(x_1) + \omega^{-2}\partial_1^2)^z, \qquad (4.156)$$

with the permittivity $\hat{\varepsilon} = \varepsilon_0\hat{\varepsilon}_r = \varepsilon_0 n^2$. Special attention is given to $z = 1/2$: the longitudinal slowness

$$\hat{\Gamma} = \hat{A}^{1/2}. \qquad (4.157)$$

The symbol (left, right or Weyl) of operator $\hat{A}$ equals

$$\hat{a} = \mu_0\hat{\varepsilon}(x_1) - \alpha_1^2. \qquad (4.158)$$

The left symbol of operator $\hat{A}^z$ is found as (compare with Equation (4.76))

$$\begin{aligned}
\hat{a}_z(x_1, \alpha_1) = {}& e^{j\omega\alpha_1 x_1} \sum_{j=0}^{J-1} \hat{\phi}^{(j)}(x_1)\tilde{\phi}^{(j)}(\alpha_1)(\lambda^{(j)})^z \\
& + e^{j\omega\alpha_1 x_1} \int_{\nu=0}^{\infty} \hat{\phi}_{\text{even}}(x_1;\nu)\tilde{\phi}_{\text{even}}(\alpha_1;\nu)[\lambda(\nu)]^z \, d\nu \\
& + e^{j\omega\alpha_1 x_1} \int_{\nu=0}^{\infty} \hat{\phi}_{\text{odd}}(x_1;\nu)\,\tilde{\phi}_{\text{odd}}(\alpha_1;\nu)[\lambda(\nu)]^z \, d\nu. \quad (4.159)
\end{aligned}$$

The eigenvalues are

$$\lambda^{(j)} = c_0^{-2}\left(n_{\text{eff}}^{(j)}\right)^2, \qquad (4.160)$$

for discrete modes, and

$$\lambda(\nu) = c_0^{-2}n_{\text{cl}}^2 - \omega^{-2}\nu^2, \qquad (4.161)$$

for continuous modes.

4.4.2 Numerical issues

This section is addressed to compute the left symbol in (4.159). We split the expression in several parts and compute them separately. The left symbol can be decomposed in several parts

$$\hat{a}_z(x_1, \alpha_1) = \hat{a}_z^{\text{guided}} + \hat{a}_z^{\text{even radiating}} + \hat{a}_z^{\text{odd radiating}}, \qquad (4.162)$$

which are, on their turn, decomposed into

$$\hat{a}_z^{\text{even radiating}} = \hat{a}_z^{\text{er del}} + \hat{a}_z^{\text{er inv}} + \hat{a}_z^{\text{er}}, \qquad (4.163)$$

$$\hat{a}_z^{\text{odd radiating}} = \hat{a}_z^{\text{or del}} + \hat{a}_z^{\text{or inv}} + \hat{a}_z^{\text{or}}, \qquad (4.164)$$

$$\hat{a}_z^{\text{guided}} = \sum_{j=0}^{J-1} \hat{a}_z^{(j)}. \qquad (4.165)$$

This splitting is made in order to treat the several singularities separately. Due to symmetry properties (symmetry axis: $x_1 = \alpha_1$), we can restrict our analysis to $\alpha_1 \geq 0$. The two singularities have

- an essential nature ($\delta(\nu - \omega\alpha_1)$ in $\tilde{\phi}(\alpha_1; \nu)$), and,
- a discrete nature ($(\nu - \omega\alpha_1)^{-1}$ in $\tilde{\phi}(\alpha_1; \nu)$).

Their contributions deserve some more attention.

Contribution from the essential singularity

For very weak waveguiding, the essential singularities in $\tilde{\phi}(\alpha_1; \nu)$ dominates. The corresponding terms are

$$\hat{a}_z^{\text{er del}}(x_1, \alpha_1) = e^{j\omega\alpha_1 x_1} \cos[\psi^{e}(\omega\alpha_1) - a\omega\alpha_1] \cos[\psi^{e}(\omega\alpha_1)] \cos[u(\omega\alpha_1)]^{-1}$$
$$\cos[\alpha(\omega\alpha_1)x_1] \left[c_0^{-2}n_{\text{cl}}^2 - \alpha_1^2\right]^z, \qquad |x_1| < a, \quad (4.166)$$

$$\hat{a}_z^{\text{er del}}(x_1, \alpha_1) = e^{j\omega\alpha_1 x_1} \cos[\psi^{e}(\omega\alpha_1) - a\omega\alpha_1] \cos[\psi^{e}(\omega\alpha_1) + \omega\alpha_1(|x_1| - a)]$$
$$\left[c_0^{-2}n_{\text{cl}}^2 - \alpha_1^2\right]^z, \qquad |x_1| > a, \quad (4.167)$$

$$j\hat{a}_z^{\text{or del}}(x_1, \alpha_1) = e^{j\omega\alpha_1 x_1} \cos[\psi^{o}(\omega\alpha_1) - a\omega\alpha_1] \sin[\psi^{o}(\omega\alpha_1)] \sin[u(\omega\alpha_1)]^{-1}$$
$$\sin[\alpha(\omega\alpha_1)x_1] \left[c_0^{-2}n_{\text{cl}}^2 - \alpha_1^2\right]^z, \qquad |x_1| < a, \quad (4.168)$$

$$j\hat{a}_z^{\text{or del}}(x_1, \alpha_1) = e^{j\omega\alpha_1 x_1} \cos[\psi^{o}(\omega\alpha_1) - a\omega\alpha_1] \,\text{sgn}(x_1) \sin[\psi^{o}(\omega\alpha_1) + \omega\alpha_1(|x_1| - a)]$$
$$\left[c_0^{-2}n_{\text{cl}}^2 - \alpha_1^2\right]^z, \qquad |x_1| > a. \quad (4.169)$$

In the limit of a homogeneous space ($a \downarrow 0$) and in the low-frequencies limit ($\omega \downarrow 0$), we find

$$\hat{a}_z(x_1, \alpha_1) = (c_0^{-2}n_{\text{cl}}^2 - \alpha_1^2)^z. \qquad (4.170)$$

The essential singularity due to the Dirac delta distribution $\delta(\nu + \omega\alpha_1)$ lies outside the integration interval — we restrict ourselves to only $\alpha_1 \geq 0$; $\nu \geq 0$ — and therefore the corresponding integral vanishes.

Contribution from the discrete singularity

The pole singularity at $\nu = \nu_{\text{pole}} = \omega\alpha_1$ due to $\tilde{\phi}(\alpha_1; \nu)$ in Equations (4.153) and (4.154) is analytically integrated, using the identity

$$\int_0^{\nu_1} \frac{f(\nu)}{\nu - \nu_{\text{pole}}} \, d\nu = f(\nu_{\text{pole}}) \int_0^{\nu_1} (\nu - \nu_{\text{pole}})^{-1} \, d\nu + \int_0^{\nu_1} \frac{f(\nu) - f(\nu_{\text{pole}})}{\nu - \nu_{\text{pole}}} \, d\nu$$
$$= f(\nu_{\text{pole}}) \ln(\nu_1/\nu_{\text{pole}} - 1) + \int_0^{\nu_1} \frac{f(\nu) - f(\nu_{\text{pole}})}{\nu - \nu_{\text{pole}}} \, d\nu, \quad (4.171)$$

with $\nu_1 > \nu_{\text{pole}} > 0$. This trick is very similar to the one used for deriving the uniform expansion of the left symbol, see Equation (4.93). Choosing $\nu_1 = 2\nu_{\text{pole}}$ the first integral vanishes. The other integral has to be computed numerically. Numerical problems will arise when $\nu_{\text{pole}} \approx 0$. Therefore we choose a larger ν_1. For even functions (see (4.153))

$$f_{\text{even}}(x_1, \alpha_1; \nu) = -\pi^{-1/2} \sin[\psi^{\text{e}}(\nu) - a\omega\alpha_1] \hat{\phi}_{\text{even}}(x_1; \nu)(c_0^{-2} n_{\text{cl}}^2 - \nu^2)^z,$$
(4.172)

and for odd functions (see (4.154))

$$\mathrm{j} f_{\text{odd}}(x_1, \alpha_1; \nu) = -\pi^{-1/2} \sin[\psi^{\text{o}}(\nu) - a\omega\alpha_1] \hat{\phi}_{\text{odd}}(x_1; \nu)(c_0^{-2} n_{\text{cl}}^2 - \nu^2)^z.$$
(4.173)

The pole is situated at $\nu = \nu_{\text{pole}} = \omega\alpha_1$. Thus, in the numerical implementation, we compute $\hat{a}_z^{\text{er inv}}$ in three parts

$$\hat{a}_z^{\text{er inv}} = \hat{a}_z^{\text{eri 1}} + \hat{a}_z^{\text{eri 2}} + \hat{a}_z^{\text{eri 3}},$$
(4.174)

where

$$\hat{a}_z^{\text{eri 1}}(x_1, \alpha_1) = f_{\text{even}} \ln[\nu_1/(\omega\alpha_1) - 1],$$
(4.175)

$$\hat{a}_z^{\text{eri 2}}(x_1, \alpha_1) = \int_0^{\nu_1} \frac{f_{\text{even}}(\nu) - f_{\text{even}}(\nu_{\text{pole}})}{\nu - \nu_{\text{pole}}} \mathrm{d}\nu,$$
(4.176)

$$\hat{a}_z^{\text{eri 3}}(x_1, \alpha_1) = \int_{\nu_1}^{\infty} \frac{f_{\text{even}}(\nu)}{\nu - \nu_{\text{pole}}} \mathrm{d}\nu.$$
(4.177)

For the numerical implementation, a filter is used to compute the last two integrals. The same filter is present in computing $\hat{a}_z^{\text{er}}$. This Fourier-type filter regularize the divergent integral, as discussed in the previous section. For $z = 1$, this process has been numerically validated. Other numerical approaches are possible. In a similar way $\hat{a}_?^{\text{or inv}}$ is calculated. The numerical integration is done by an adaptive recursive Newton Cotes 8 panel rule, see the Matlab manual[150].

4.4.3   Results

Having introduced the left symbol of the slowness in a symmetrical step-index waveguide, we are in the position to analyze it. For this purpose, we consider a configuration with the following values

$$\lambda_0 = 1.5 \, \mu\text{m},$$
$$a = \frac{\lambda_0}{2\pi} \simeq 0.247 \, \mu\text{m},$$
$$n_{\text{cl}} = 1,$$
$$n_{\text{co}} = 1.5.$$

Then the transverse Helmholtz operator equals

$$c_0^2 \hat{\mathrm{A}}(x_1, \mathrm{j}\omega^{-1}\partial_1) = \hat{\varepsilon}_{\mathrm{r}}(x_1) + k_0^{-2}\partial_1^2, \tag{4.178}$$

and its left symbol equals

$$c_0^2 \hat{\mathrm{a}}(x_1, \alpha_1) = \hat{\varepsilon}_{\mathrm{r}}(x_1) - (c_0\alpha_1)^2. \tag{4.179}$$

Now, we compute the left symbol of the slowness operator at several transverse positions x_1: 0, 0.5a, 0.9a, 0.98a, 1.02a, 1.1a, 1.5a and 2a. Figure 4.13 shows the longitudinal slowness operator for the slab waveguide at several positions.

Asymptotic behavior

Toward the limit of transverse homogeneous medium, the essential singularity has the biggest contribution in the left symbol. From (4.170), it is observed that the left symbol equals the left symbol in a transverse homogeneous medium. The asymptotic behavior for large transverse slownesses, $\alpha_1 \to \pm\infty$, is also correct: $\hat{\gamma} = \pm\mathrm{j}|\alpha_1|$. For smaller values of the transverse slowness ($|\alpha_1| > 2$), the longitudinal slowness behaves as the local high-frequency slowness. For large transverse positions, $x_1 \to \pm\infty$, the outer refractive index dominates the left symbol. In this limit, the longitudinal slowness equals

$$c_0 \hat{\varGamma} \to (n_{\mathrm{cl}}^2 + k_0^{-2}\partial_1^2)^{1/2}, \qquad \text{as } x_1 \to \pm\infty. \tag{4.180}$$

In the middle of the core, the inner refractive index dominates.

The longitudinal slowness in the low-frequency limit equals

$$c_0 \hat{\varGamma} \to (n_{\mathrm{cl}}^2 + k_0^{-2}\partial_1^2)^{1/2}; \tag{4.181}$$

the slab waveguide is not visible for waves with low frequencies.

Physical interpretation

The left symbols still show the critical angle phenomena. Inside the waveguide, the imaginary part of $\hat{\gamma}$ is positive: wave propagation is stimulated. Outside the waveguide, only wave propagation towards the waveguide is stimulated. Especially wave propagation at the critical angle of the core is stimulated.

4.5 Discussion of the results

In this chapter, we took a closer look at the square root operator. First, we discussed the properties in a transverse homogeneous medium and subsequently in a transverse inhomogeneous medium. To describe the scattering problem in an inhomogeneous medium, we introduced two descriptions of the pseudo-differential operators under investigation.
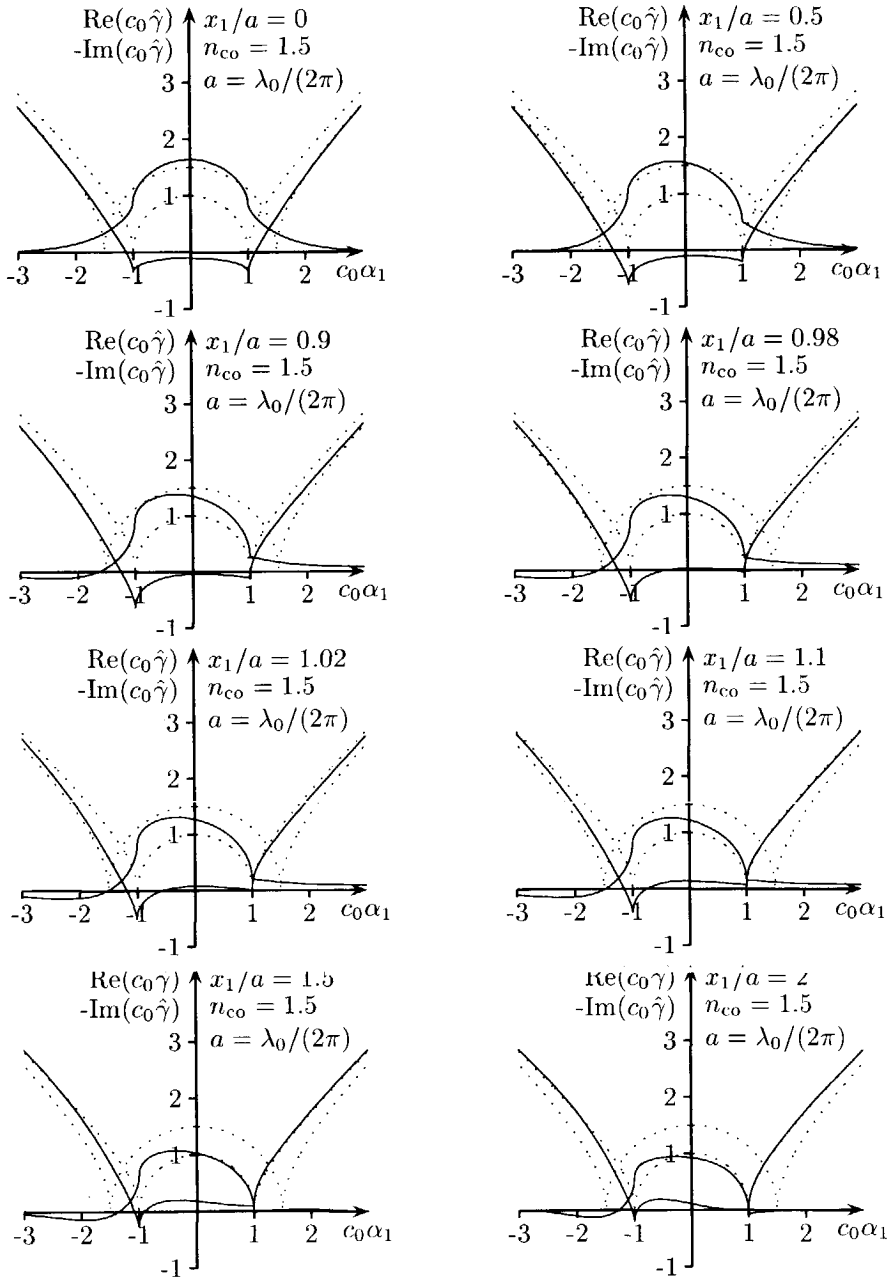
Figure 4.13: The real and (negative) imaginary part of the left symbol $\hat{\gamma}$ in a step-index slab waveguide. The position x_1 varies for every figure; the thickness $2a = \lambda_0/\pi$, wavelength $\lambda_0 = 1.55$ μm, $n_{\text{co}} = 1.5$.

The first description was based upon the eigenvalues and eigenfunctions. This description gives much insight into the relation between the well-known theory on waveguides and the pseudo-differential operator calculus. This description is, however, not useful for a fast numerical scheme, because for a high degree of numerical accuracy, many eigenfunctions should be determined. These eigenfunctions are globally defined and therefore their computation is a time-consuming task, especially for 3-D problems.

The second description was based upon the left symbol from the pseudo-differential operator calculus. This description will be used to make fast numerical schemes and analyzing the accuracy of those numerical schemes in the following chapter. The left symbols are (pseudo-)locally defined. In a locally transverse homogeneous region, the left symbols equal their principal parts. In transversely varying media, the left symbol is more complex and can be estimated from the polyhomogeneous expansion of the left symbol or from the composition equation. Since the longitudinal slowness operator is not elliptic if $s = j\omega$, the left symbol contains an oscillatory exponential branch. The influence of this branch cannot always be neglected.

The numerical implementation of the pseudo-differential operators will be done for the Schwartz kernel and its matrix representations. In this thesis, we chose to implement the square root operator by using a rational approximation. In addition, we also studied other promising techniques, like the Lanczos method. These methods are, however, beyond the scope of the thesis.

We presented a new method to compute the left symbol for *analytical* configurations. The method is based upon the eigenvalue analysis. A special regularization, which is similar to Fourier-type filtering techniques, has been introduced to compute the integrals over the spectrum. Results have been shown for the quadratic profile and the step-index slab waveguides. These results will be used to analyze the numerical schemes in the following chapter.

These analytical results can also be used to compose an accurate propagation scheme for more general profiles. In the transverse direction, the medium variations must be locally of the two discussed profiles or any other *analytical* profile, which has still to be constructed. This was discussed by de Hoop *et al.*[136].

Appendix

4.A   Formulae used

In Section 4.3, several formulae from other books were used. For convenience, they are repeated here.

From the "Handbook of Mathematical Function" by Abramowitz and Stegun[145], we used Equation (6.1.7) (poles of the Gamma function)

$$\lim_{z \to n} \frac{1}{\Gamma(-z)} = 0 = \frac{1}{(-n-1)!}, \qquad (n = 0, 1, 2, \cdots), \qquad (4A.1)$$

Equation (19.1.2), (differential equation for the Weber parabolic cylindric functions)

$$\frac{\mathrm{d}^2 y}{\mathrm{d}x^2} - (\tfrac{1}{4}x^2 + a)\, y = 0, \qquad (4A.2)$$

Equation (19.13.1) (when n is a nonnegative integer),

$$U(-n - \tfrac{1}{2}, x) = e^{-x^2/4} He_n(x) = 2^{-n/2}\, e^{-x^2/4} H_n(x/\sqrt{2}), \qquad (4A.3)$$

where

$$U(a, x) = \text{Weber parabolic cylindric function,}$$
$$H_n(x) = \text{Hermite polynomial,}$$
$$He_n(x) = 2^{-n/2} H_n(x/\sqrt{2}),$$

and Equation (22.14.17)

$$|H_n(x)| < e^{x^2/2}\, k\, 2^{n/2} \sqrt{n!}, \qquad k \approx 1.086435. \qquad (4A.4)$$

On page 255, the following remark is written:

> $\Gamma(z)$ *is single valued and analytic over the entire complex plane, save for the points $z = -n$ $(n = 0, 1, 2, \cdots)$ where it possesses simple poles with residue $(-1)^n/n!$.*

From "Table of Integrals, Series and Products" by Gradshteyn and Ryzhik[146] we used Equation (7.376.1)

$$\int_{-\infty}^{\infty} e^{jxy}\, e^{-x^2/2} H_n(x)\, \mathrm{d}x \;=\; (2\pi)^{1/2}\, e^{-y^2/2}\, H_n(y)\, j^n, \qquad (4A.5)$$

and the recursion Formula (8.952.2)

$$H_n(x) = 2x\, H_{n-1}(x) - 2(n-1)\, H_{n-2}(x), \qquad (4A.6)$$

with the initial condtions $H_0(x) = 1$ and $H_1(x) = 2x$ (see (8.956.1) and (8.956.2)).

From "Formulas and Theorems for the Special Functions of Mathematical Physics" by Magnus, Oberhettinger and Soni, we used

$$(1 - z^2)^{-1/2} \exp\left[\frac{x^2 - y^2}{2} - \frac{(x - yz)^2}{1 - z^2}\right]$$
$$= \sum_{n=0}^{\infty} e^{-(x^2+y^2)/2} \, He_n(x\sqrt{2}) \, He_n(y\sqrt{2}) \, \frac{z^n}{n!}, \quad |z| < 1, \quad (4A.7)$$

on page 253 and the Christoffel-Darboux Formula (see also Equation (22.12.1) in Abramowitz[145])

$$\sum_{m=0}^{n} \frac{2^{-m}}{m!} \, H_m(x) \, H_m(y) = \frac{2^{-n-1}}{n!} \left[\frac{H_{n+1}(x) \, H_n(y) - H_n(x)H_{n+1}(y)}{x - y}\right]. \quad (4A.8)$$

on page 255 and the reflection formula for Hermite polynomials (page 250)

$$H_n(-x) = (-1)^n H_n(x). \quad (4A.9)$$

CHAPTER 5

2-D Numerical Implementation: Third-Order Thiele Approximation

In the Bremmer series approach to the modeling of waveguiding structures, we encounter pseudo-differential operators in the directional (de)composition as well as in the forward and backward propagation, and in the reflections and transmissions due to variations in the medium properties in the preferred direction (de Hoop[48,49]). For the numerical implementation, we employ a total rational-approximation approach to find, upon discretization, sparse matrix representations of these pseudo-differential operators. The rational approximation has its roots in the parabolic equation (PE) method (Claerbout[31], and Tappert[151]), and has been extended and explored by Ma[152], Greene[153], Halpern and Trefethen[154], and Collins[155]. The rational approximation should be carried out in a delicate way, so as to ensure the conservation of power flow, see also Collins and Westwood[156]. For fixed sampling rates, allowing the numerical grid to be coarse, we consider optimizations of the matrix representations for the three steps, (de)composition, propagation and interaction, such that the numerical dispersion is minimized. The idea of optimization has been exploited by Collins[157], and Cederberg et al.[158]; the numerical dispersion has been carefully analyzed by Trefethen[159], Beaumont et al.[160], and Holberg[161,162].

The improvement in accuracy and efficiency, and extensions of rational approximation techniques still need significant attention. Recent advances in the application to exploration seismics can be found in Graves and Clayton[163], and Rühl et al.[164].

They controlled the errors at large scattering angles by initiating the propagation with a transversely homogeneous background phase shift. In the field of integrated optics, Hadley[97, 98] introduced the Padé approximation. Hoekstra *et al.*[99–101] also analyzed its accuracy.

The discretization of the *one-way* wave equation, the propagation step, is based on the third-order Thiele-type approximation of the longitudinal slowness symbol. We enforce the associated longitudinal slowness operator to be self-adjoint (*energy-conserving*), since the exact one is self-adjoint in the real L_2. This implies that we depart from the usual principal symbol analysis. The one-way wave equation is thus approximated by a partial differential equation. By discretizing the transverse derivatives (the Laplace operator) according to a rational approximation of its spectrum, this partial differential equation is transformed into a system of ordinary differential equations. The solution of this system is formally written as a product integral. The exponent in the discretized version of the product integral is then replaced by its (n, n)-Padé approximation. Such a procedure guarantees numerical stability. We pay most attention to the $(1, 1)$-Padé approximation, which yields the Crank-Nicolson implicit finite-difference scheme in the preferred direction. The resulting algebraic equations, which now involve sparse matrices, can be solved rapidly with standard procedures available in various software libraries. In two dimensions, direct matrix inversions are carried out; in three dimensions, iterative techniques are applied (see Chapter 6).

The longitudinal phase and group slownesses associated with the ultimate system of algebraic equations can be evaluated, and they are used to analyze the numerical artifacts introduced by the various rational approximations. The accuracy of the longitudinal group slowness as compared to the exact longitudinal slowness is indicative of the numerical anisotropy; the difference between the longitudinal phase and group slownesses is indicative of the numerical dissipation. To arrive at an optimal system of algebraic equations, fixing the bandwidth of the wave-field and the sampling rate, a simultaneous optimization of the Thiele-type approximation, the transverse finite-difference, and the longitudinal finite-difference representations is carried out. Since the optimization depends on the medium's wave speed, the optimal parameter set varies with frequency and position as well. The optimization procedure is repeated for the composition, decomposition, reflection and transmission operators. With the various matrix representations, the Bremmer coupling series solution of the wave equation can now be computed.

In Sections 5.1-5.3, the one-way wave equations are discretized for the purpose of solving the one-way Green's functions. In Section 5.4, transverse, transparent boundaries are introduced. In Section 5.5, the optimization procedure for the one-way propagation is explained. Sections 5.6 and 5.7 contain the discretizations and optimizations of the (de)composition and interaction operators. Our algorithm is illustrated in Section 5.8 by various numerical examples. Finally, we discuss the results in 5.9. This chapter contains one appendix, in which the FORTRAN code for constructing the involved matrices is discussed.

The major part of this material has been published in international journals, see

Stralen *et al.*[165, 166] and presented at international conferences[167, 168]. This chapter is written in the terminology of exploration seismics and underwater acoustics.

5.1 Rational approximation of the one-way wave propagator

Consider the homogeneous one-way wave equation (the homogeneous version of Equation (3.25))

$$\partial_3 \hat{W}_1^{(0)} + j\omega \hat{\Gamma} \hat{W}_1^{(0)} = 0, \qquad x_3 \in (0, x_3^{\text{exit}}], \tag{5.1}$$

which is satisfied by the leading-order term of the Bremmer series. In this chapter, we derive a sparse matrix representation for its propagator, $\hat{P}(x_1, m)$, see Equation (3.84). In the following approximations, we maintain the hyperbolicity of the time-domain-equivalent equations, but we deform the post-critical regime.

In this section, we introduce the third-order Thiele approximation, optimize it in the pre-critical region, introduce a small dissipation for reducing post-critical artifacts and employ the local co-moving frame of reference.

5.1.1 Third-order Thiele approximation

The principal part of the left longitudinal wave-slowness symbol is given by (see Equation (4.92))

$$\hat{\gamma}_{\text{pp}}(x_1, x_3, \alpha_1) = \left[c^{-2}(x_1, x_3) - \alpha_1^2 \right]^{1/2}, \tag{5.2}$$

and it is equal to the symbol in a transversely homogeneous space (see Equation (4.5)). For our numerical scheme, we consider Thiele's third-order continued fraction approximation of the left symbol (see Serafini and de Hoop[169] and de Hoop and de Hoop[170]). The Thiele approximation of the square root reads

$$(1 + x)^{1/2} \simeq 1 + (1 + \beta_3 x)^{-1} (\beta_1 x + \beta_2 x^2). \tag{5.3}$$

Applying this to (5.2) yields

$$\hat{\gamma}_{\text{pp}}^{\text{III}} = \frac{1}{c} + \left(1 - \beta_3 c^2 \alpha_1^2 \right)^{-1} \left(-\beta_1 c \alpha_1^2 + \beta_2 c^3 \alpha_1^4 \right). \tag{5.4}$$

The wavefront associated with this approximation is free from artificial cusps in a cone of propagation angles about the longitudinal axis, unlike the second-order approximation that is commonly used, see Figure 5.1. The operator associated with this left symbol is neither symmetric nor self-adjoint. To create a symmetric Thiele approximation, we extract the local wave speed c from the square root expression; then, the longitudinal slowness operator becomes

$$\hat{\Gamma} \approx c^{-1/2} (1 + \hat{\Xi})^{1/2} c^{-1/2}, \tag{5.5}$$
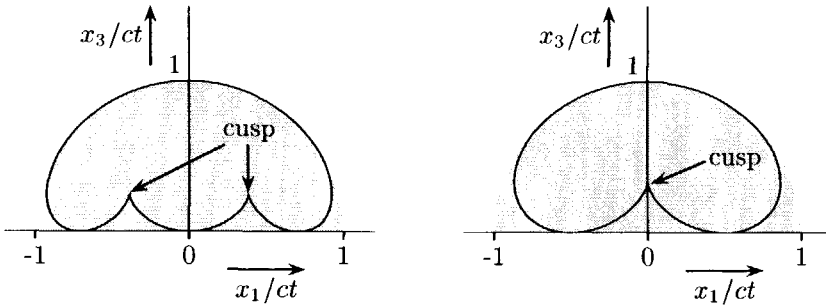
Figure 5.1: *The wavefront of the third (left) and second (right) order Thiele approximation of the longitudinal slowness. The second-order Thiele approximation has a cusp propagating along the logitudinal axis, while the cusps of the third-order Thiele approximation are only present at large angles (> 45°). See also Figure 4.2*

where

$$\hat{\Xi} \equiv \omega^{-2} \, c\partial_1^2 c. \tag{5.6}$$

This approximation is valid for small values of the commutator $[c, \omega^{-1}\partial_1]$, which will be the case for media varying smoothly on the scale of the dominant wavelength. Large differences between the media properties in the configuration are allowed.

The third-order Thiele approximation is now applied to the symbol of the operator $(1 + \hat{\Xi})^{1/2}$. This leads to a symmetric operator $\hat{\Gamma}^{III}$, the principal symbol of which still equals the expression in Equation (5.4),

$$\hat{\Gamma}^{III} = c^{-1/2} \left[1 + (1 + \beta_3\hat{\Xi})^{-1} \left(\beta_1\hat{\Xi} + \beta_2\hat{\Xi}^2\right) \right] c^{-1/2}. \tag{5.7}$$

The internal structure of $\hat{\Gamma}^{III}$ is such that its symbol captures some of the contributions beyond the principal part. From now on, we freely omit the superscript III.

5.1.2 Optimization

According to Thiele's formula, we have

$$\beta_1 = 1/2, \qquad \beta_2 = 1/8, \qquad \beta_3 = 1/2. \tag{5.8}$$

The parameters, β_1, β_2 and β_3, however, can be adjusted by minimizing the difference between the exact spectral-domain longitudinal slowness and its continued-fraction approximation, defined by Equation (5.4), with respect to the L_2 norm, over all the propagating waves (i.e., the real slowness surface). In this minimization, we
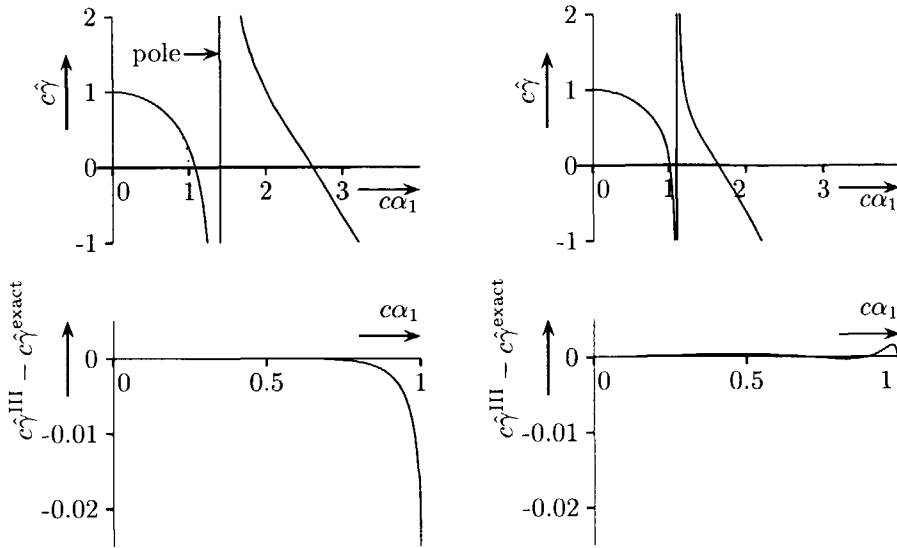
Figure 5.2: *The third-order Thiele approximation of the longitudinal slowness with $\beta_1 = 1/2$, $\beta_2 = 1/8$, $\beta_3 = 1/2$ (left) and with $\beta_1 = 0.531$, $\beta_2 = 0.364$, $\beta_3 = 0.825$ (right). The dotted line corresponds to the real part of the exact longitudinal slowness. In the bottom row the differences between the approximants and the exact expressions are shown.*

must be aware of the fact that the pole (at $(\alpha_1^\gamma)^2 = c^{-2}\beta_3^{-1}$), introduced by the Thiele-type approximation will lie outside the pre-critical region of the α_1-plane. The optimization procedure can be viewed as a replacement of Thiele's continued fraction by Newtonian interpolation.

Using an optimization routine based on the simplex method[171], the following values are obtained

$$\beta_1 = 0.526, \qquad \beta_2 = 0.364, \qquad \beta_3 = 0.825. \qquad (5.9)$$

When the propagation angles appearing in the wave-field are restricted, the optimization should be carried out accordingly. This type of optimization was also considered by Lee and Suh[172] and followed by Bunks[173].

Figure 5.2 shows the exact and approximated longitudinal slownesses with β_1, β_2 and β_3 as in Equation (5.8) and as in Equation (5.9), respectively. In the second row of figures, the differences with the exact slowness are drawn. In Figure 5.3, the real part of the longitudinal slownesses as a function of complex-valued $c\alpha_1$ is shown. In these figures, we recognize the singularities in the longitudinal slownesses: a branch cut from $c\alpha_1 = 1$ to $+\infty$ in the exact longitudinal slowness and poles at $\sqrt{2}$ and 1.10 for the two approximated longitudinal slownesses, respectively. Since
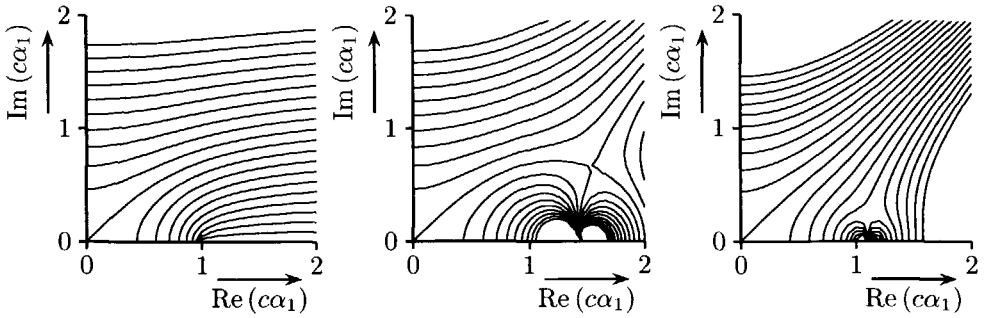
Figure 5.3:   The real parts of the exact (left) and approximated longitudinal
slownesses as functions of a complex α_1 are shown. The middle and
right figures corresponds to Equations (5.8) and (5.9), respectively.
The contour lines correspond to the values $0.1, 0.2, \cdots, 2.0$.
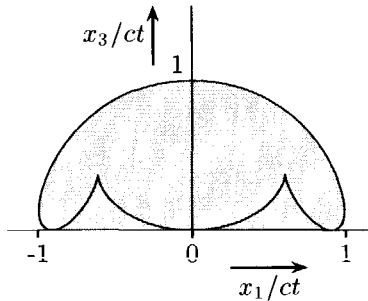
Figure 5.4:   The wavefront of the third-order optimized Thiele approximation of
the longitudinal slowness: $\beta_1 = 0.531$, $\beta_2 = 0.364$, $\beta_3 = 0.825$.

no singularities are present on the imaginary axis, the approximation is accurate for
a wide range of imaginary values of $c\alpha_1$. The corresponding wavefront is illustrated
in Figure 5.4.

Fundamental differences between the approximate and exact longitudinal slow-
nesses occur near the singularities in the transverse slowness plane. Since it is
impossible to approximate a branch cut with a finite set of poles from a rational
approximation, we have to restrict ourselves to approximating the pre-critical wave
propagation as completely as possible. The influences of the artificial post-critical
wave propagation must then be suppressed. A dissipation trick can be designed for
that purpose.

Figure 5.5: *The $\mathcal{Q}$-factor (left) and the corresponding amplification factor (right) associated with the dissipation trick in the third-order Thiele approximation; $\beta_1 = 0.526$, $\beta_2 = 0.364$ and $\beta_3 = 0.825$. The relative imaginary circular frequency $\Omega = 0.02$. Note that the notch occurs beyond the critical angle.*

5.1.3 Dissipation trick

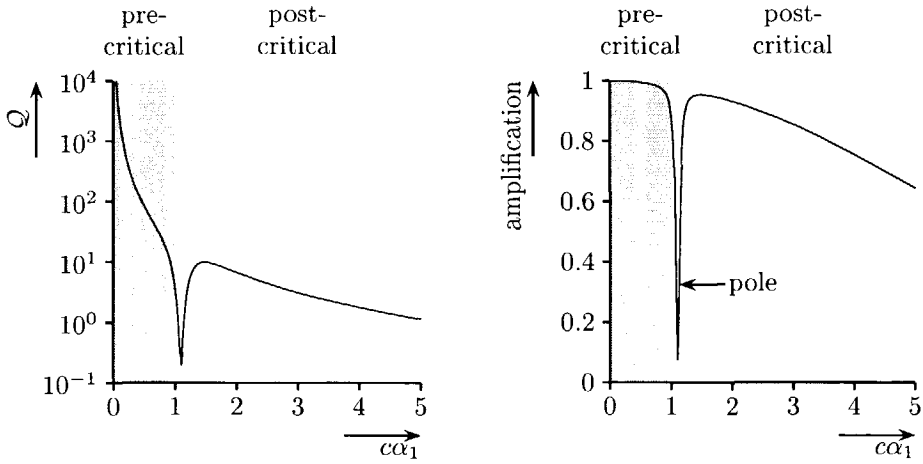To suppress artifacts and aliasing (which may arise in the discretization to be carried out in the transverse direction) from the large transverse wave number components, we may replace the real frequency ω by a complex one,

$$\omega' = \omega \left(1 - \mathrm{j}\Omega\right),$$

just in the expression for $\mathrm{j}\omega\hat{\Gamma}$ (and later in $\hat{\mathsf{M}}$ and $\hat{\mathsf{M}}'$, see equations (5.25)). The integration contour of the inverse Laplace Transformation (1.25) is now slightly deformed from the imaginary axis into the complex plane. In a homogeneous medium, this implies per Fourier component or plane wave, $\mathcal{A}(x_3, \alpha_1, \omega) \exp(-\mathrm{j}\omega\alpha_1 x_1)$, an amplification factor of the form

$$|\mathcal{A}(x_3 + \Delta x_3, \alpha_1, \omega)/\mathcal{A}(x_3, \alpha_1, \omega)| = \exp\left[-\frac{\omega\Delta x_3}{2c\,\mathcal{Q}(\alpha_1, \omega, \mathrm{j}\Omega)}\right]. \tag{5.10}$$

The amplification factor is attenuative in nature. The $\mathcal{Q}$-factor is given by

$$\mathcal{Q}(\alpha_1, \omega, \mathrm{j}\Omega) = \frac{1}{\mathrm{Im}\{2\,c\,\hat{\gamma}^{\mathrm{III}}[\alpha_1; \omega(1 - \mathrm{j}\Omega)]\}}, \tag{5.11}$$

for $c \in \mathbb{R}^+$ and is plotted in Figure 5.5. Here, Ω is assumed to be very small ($\Omega \ll 1$). This particular "complexification" results in a local band-limitation filter that suppresses the artifacts associated with the post-critically propagating waves.

5.1.4   Co-moving frame of reference

To reduce discretization artifacts in the longitudinal derivative, the numerical computations are done in a local co-moving frame of reference, traveling in the direction of preference. The accuracy is improved, since this transformation enables us to take exactly into account the leading phase shift. The change of frame yields (see Claerbout[31])

$$\hat{h}(x_k, \omega) = \exp[\,j\omega\tau(x_k)]\,\hat{W}_1^{(0)}(x_k, \omega),\tag{5.12}$$

in which

$$\tau(x_k) = \int_{\zeta=0}^{x_3} c^{-1}(x_1, \zeta)\,\mathrm{d}\zeta,\tag{5.13}$$

is the local longitudinal travel time. Substituting Equation (5.12) into Equation (5.1), leads to

$$\partial_3\hat{h} + j\omega\left[\exp(j\omega\tau)\,\hat{\Gamma}\exp(-j\omega\tau) - c^{-1}\right]\hat{h} = 0.\tag{5.14}$$

5.2   Discretization in the transverse direction

Now, we introduce the discretization in the transverse direction, of the partial differentiation ∂_1^2. In three-dimensional wave propagation this would be the two-dimensional Laplace operator, see Equation (7.33). Our starting point is a low-order, implicit, finite-difference approximation. The spectrum or symbol of the resulting operator is a rational function in the transverse slowness. The medium has to be smooth on the scale of the size of the operator. A uniform grid is employed in the transverse direction, see Figure 4.5. The transverse sampling interval is denoted as Δx_1. To ensure that the medium is smooth, we employ equivalent medium averaging at any point over a box that is twice the spatial sample size, see Coates and Schoenberg[174, 179].

The discretization of the one-dimensional Laplace operator is formulated in terms of recursive filters based on nearest-neighbors interaction (see Mitchell and Griffiths[140]). It is also known as the Douglas scheme, e.g. see Sun and Yip[84]. Our recursive filter acting on a function $\hat{h}$ is defined through

$$(1 + a_2\delta_1^2)\langle\partial_1^2\hat{h}\rangle = (\Delta x_1)^{-2}a_1\delta_1^2\hat{h},\tag{5.15}$$

where

$$\delta_1^2\hat{h} = \hat{h}(x_1 + \Delta x_1) - 2\hat{h}(x_1) + \hat{h}(x_1 - \Delta x_1).\tag{5.16}$$

In Equation (5.15), 1 denotes the identity operator and $\langle\partial_1^2\hat{h}\rangle = \langle\partial_1^2\rangle\hat{h}$ represents the approximate Laplace operator having acted on $\hat{h}$. Using a Taylor series expansion

of $\hat{h}$ at $x_1 \pm \Delta x_1$ about x_1, the following values of a_1 and a_2 are found (see Mitchell and Griffiths[140])

$$a_1 = 1, \qquad a_2 = 1/12. \tag{5.17}$$

Then

$$\langle \partial_1^2 \rangle = \partial_1^2 + \mathcal{O}[(\Delta x_1)^4]. \tag{5.18}$$

For a finite-bandwidth solution generated at a given sampling interval, however, we leave this order estimate, and use a_2 as a parameter to improve the overall accuracy. Requiring that in the limit $\Delta x_1 \downarrow 0$ the spectrum of $\langle \partial_1^2 \rangle$ tends to the spectrum of the Laplace operator up the lowest order, leads necessarily to $a_1 = 1$. The parameter a_2 is then determined by minimizing nonlinearly the difference between the approximate and the exact Laplace operator spectra with respect to the L_2 norm over the Nyquist interval. Thus a more accurate approximate spectrum is obtained over the spatial bandwidth as a whole. Using an optimization routine based on the simplex method[171], the following value for a_2 is obtained

$$a_2 = 0.130. \tag{5.19}$$

It is noted, however, that if it is known beforehand that the actual spatial bandwidth of the wave-field to be extrapolated is limited by a transverse wave number, less the Nyquist wave number $k_{1,\mathrm{Nyq}} = \pi/\Delta x_1$, the optimization should be carried out over this subband only.

Figure 5.6 illustrates the spectra of the exact and the approximate Laplace operators with a_1 and a_2 as in Equation (5.19) and as in Equation (5.17), respectively. The approximated Laplace operator has poles at

$$\alpha_1 = \alpha_1^{\mathrm{Laplace}} = (\omega \Delta x_1)^{-1} \left[\pm \arccos \left(1 - \tfrac{1}{2} a_2^{-1} \right) + 2m\pi \right], \tag{5.20}$$

($m = 0, \pm 1, \pm 2, \cdots$). In practice, $a_2 < 1$, and these poles are situated in the complex α_1-plane at $\mathrm{Re}(\alpha_1) = \pi/(\omega \Delta x_1)$ (determined by the Nyquist theorem), far away from the real axis.

The poles of the approximate Laplace operator carry over in the approximation of the longitudinal slowness operator. The longitudinal slowness symbol becomes periodic in accordance with the Nyquist theorem, and the Laplace poles are slightly shifted:

$$\alpha_1^{\mathrm{Laplace}} \to (\omega \Delta x_1)^{-1} \left\{ \pm \arccos \left[1 - \tfrac{1}{2} (a_2^{-1} + \omega \Delta x_1 \, \beta_3) \right] + 2m\pi \right\}, \tag{5.21}$$

see Figure 5.7. For example, taking $a_2 = 0.130$, $\beta_3 = 0.825$, and a sampling rate of 8 points per wavelength, the poles are located at

$$\alpha_1^\gamma = \pm 1.1023 + 8m, \qquad \text{and} \qquad \alpha_1^{\mathrm{Laplace}} = \pm(4 - 2.4010 \, \mathrm{j}) + 8m. \tag{5.22}$$
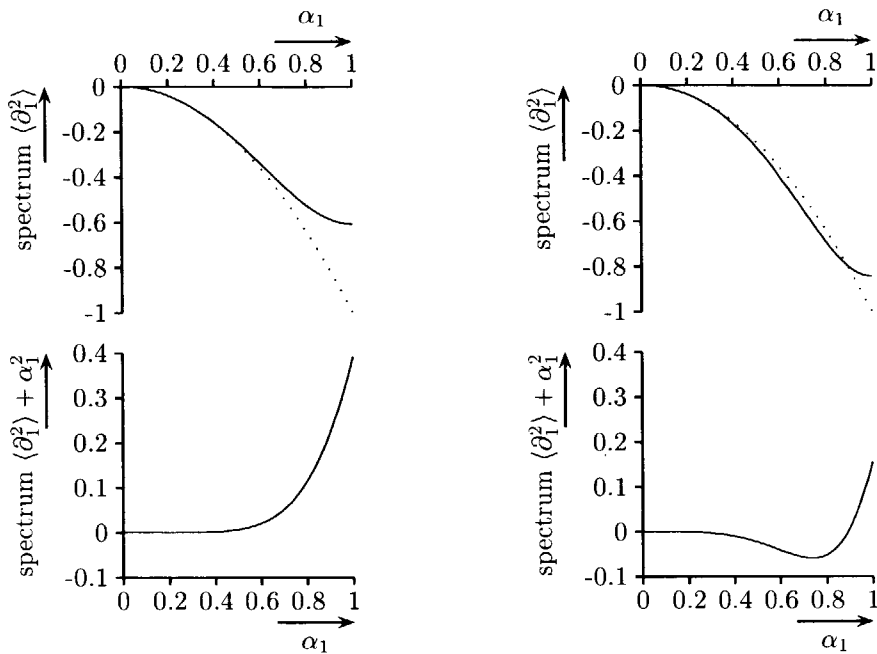
Figure 5.6:   *The spectra or symbols of the approximate ∂_1^2 operators with $a_2 = 1/12$ (upper left) and $a_2 = 0.130$ (upper right). The bottom figures show the corresponding differences with the exact spectra, which are also dotted in the upper figures. Here $\omega = 1$ s^{-1} and $\Delta x_1 = \pi$ m.*

5.3   Matrix representation of the one-way wave propagator

The discretized Laplace operator is now substituted into the one-way wave Equation (5.14). A system of ordinary differential equations is derived by integrating the longitudinal derivative and discretizing the field at a finite number of points.

5.3.1   System of ordinary differential equations

Substituting $\langle \partial_1^2 \rangle$, i.e., Equation (5.15), into Equation (5.6) and the result into the one-way wave equation (5.14) with longitudinal slowness (5.7), we obtain a system of ordinary differential equations of the form

$$\hat{\mathsf{M}}\,\partial_3 \hat{h} + \mathrm{j}\omega\,\hat{\mathsf{M}}'\hat{\mathsf{C}}^{-1}\hat{h} = 0. \tag{5.23}$$

The operators involved are $\hat{\mathsf{M}} = \hat{\mathsf{M}}(x_3, \omega; x_1, \delta_1^2, \Delta x_1)$, $\hat{\mathsf{M}}' = \hat{\mathsf{M}}'(x_3, \omega; x_1, \delta_1^2, \Delta x_1)$ and $\hat{\mathsf{C}} = \hat{\mathsf{C}}(x_3, \omega; x_1, \delta_1^2, \Delta x_1)$; they are sparse, viz., 3, 5 and 3 bands, respectively,
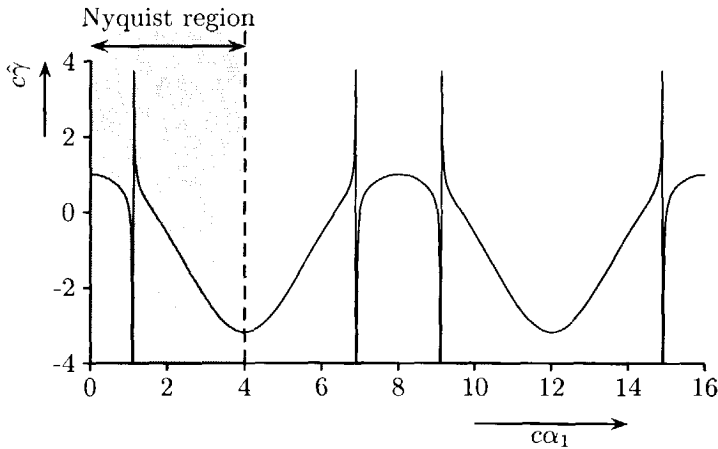
Figure 5.7:   *The third-order Thiele approximation of the longitudinal slowness symbol including the spectrum of the discretized Laplace operator ($a_2 = 0.130$, $\beta_1 = 0.526$, $\beta_2 = 0.364$, $\beta_3 = 0.825$, and a sampling rate of 8 points per wavelength). The poles are located at $\alpha_1 \approx 1.102, 6.898, 9.102, \cdots$.*

and are given by

$$\hat{\mathsf{M}} = \left(1 + a_2\delta_1^2\right) c^{-1/2} \exp(-\mathrm{j}\omega\tau) + \beta_3 r_{\mathrm{t}}^2 c^{-2}\delta_1^2 c^{3/2} \exp(-\mathrm{j}\omega\tau), \qquad (5.24)$$

$$\hat{\mathsf{M}}' = \beta_1 r_{\mathrm{t}}^2 c^{-2}\left(1 + a_2\delta_1^2\right)\delta_1^2 \qquad + \beta_2 r_{\mathrm{t}}^4 c^{-4}\delta_1^2 c^2 \delta_1^2, \qquad (5.25)$$

while

$$\hat{\mathsf{C}} = \exp(\mathrm{j}\omega\tau) \, c^{-1/2}\left(1 + a_2\delta_1^2\right), \qquad (5.26)$$

with reference transverse-sampling rate

$$r_{\mathrm{t}} = \frac{c}{\omega\Delta x_1}. \qquad (5.27)$$

The quantity $2\pi r_{\mathrm{t}}$ equals the number of grid points per wavelength in the local medium.

5.3.2   Integration of the longitudinal derivative

The solution of equation (5.23) can formally be written as a product integral. This product integral have to be evaluated, recursively, for every propagation step with size Δx_3. The product integral is given by (see also Equation (3.70))

$$\hat{h}(x_1, x_3 + \Delta x_3) = \prod_{\zeta=x_3}^{x_3+\Delta x_3} \exp\left[-\mathrm{j}\omega\,(\hat{\mathsf{M}}^{-1}\hat{\mathsf{M}}'\,\hat{\mathsf{C}}^{-1})(x_1, \zeta)\,\mathrm{d}\zeta\right] \hat{h}(x_1, x_3). \tag{5.28}$$

It is appoximated by

$$\hat{h}(x_1, x_3 + \Delta x_3) \simeq \exp\left[-j\omega\Delta x_3\,(\hat{M}^{-1}\hat{M}'\,\hat{C}^{-1})(x_1, x_3 + \tfrac{1}{2}\Delta x_3)\right]\hat{h}(x_1, x_3). \tag{5.29}$$

To speed up the computations, the exponent is approximated by the solution of a unitary matrix equation. The (n,n)-Padé approximants can be used for this purpose. They are given by (see Numerical Recipes[177])

$$\exp(Z) \simeq \begin{cases} \dfrac{1 + \beta_9 Z}{1 - \beta_9 Z}, & \text{lowest order: } (1,1), \\[3mm] \left(\dfrac{1 + \beta_{11} Z}{1 - \beta_{11} Z}\right)\left(\dfrac{1 + \beta_{10} Z}{1 - \beta_{10} Z}\right), & \text{higher order: } (2,2), \end{cases} \tag{5.30}$$

where

$$Z \equiv \Delta x_3\,\partial_3\bigg|_{x_3 + \Delta x_3/2}, \tag{5.31}$$

is the derivative that appears in Equation (5.23). The higher the order of the approximation is, the larger is the step size Δx_3. For stability considerations of the associated higher-order implicit finite-difference schemes, see Widlund[178].

According to Padé's formula, we have

$$\beta_9 = 1/2 . \tag{5.32}$$

Instead of taking this exact value, we let β_9 be a free parameter for an optimization procedure. Minimizing the difference for the pre-critical wave constituents, gives

$$\beta_9 = 0.766, \qquad \text{for 2\ \ points per wavelength,} \tag{5.33}$$

$$\beta_9 = 0.540, \qquad \text{for 5\ \ points per wavelength,} \tag{5.34}$$

$$\beta_9 = 0.510, \qquad \text{for 10 points per wavelength.} \tag{5.35}$$

The $(1,1)$-Padé approximation of the exponent yields the well-known Crank-Nicolson scheme (see Richtmeyer and Morton[179]), in our notation given by

$$(\hat{M}\hat{C})(x_3 + \tfrac{1}{2}\Delta x_3)\,(\delta_\| \hat{h}'(x_3))$$
$$= (-j\beta_9\,\omega\Delta x_3)\,\hat{M}'(x_3 + \tfrac{1}{2}\Delta x_3)\,[\hat{h}'(x_3) + \hat{h}'(x_3 + \Delta x_3)], \tag{5.36}$$

with

$$(\delta_\|\hat{h}')(x_3) = \hat{h}'(x_3 + \Delta x_3) - \hat{h}'(x_3), \tag{5.37}$$

where

$$\hat{h}'(\zeta) \stackrel{\text{def}}{=} \hat{C}^{-1}(x_3 + \tfrac{1}{2}\Delta x_3)\,\hat{h}(\zeta), \qquad \text{for} \qquad \zeta \in (x_3, x_3 + \Delta x_3]. \tag{5.38}$$

The scheme in Equation (5.36) should be interpreted as a centered difference approximation of the longitudinal derivative, and hence is accurate up to $\mathcal{O}[(\Delta x_3)^3]$.

5.3.3   Propagator matrix

To arrive at an explicit matrix representation for the one-way propagator, we introduce the array,

$$\hat{h}_i(x_3,\omega) = \hat{h}(x_{1i},x_3,\omega), \tag{5.39}$$

where

$$x_{1i} = i\Delta x_1, \tag{5.40}$$

and $i = 1, \cdots, N_{x_1}$ labels the samples in the tranverse direction. In this notation, with the aid of Equations (5.36) and (5.38), the approximate one-way wave propagation can finally be written in the matrix form

$$\hat{h}_i(x_3 + \Delta x_3,\omega) = \hat{C}_{i,j}(\hat{A}^{-1})_{j,k}\hat{A}'_{k,l}(\hat{C}^{-1})_{l,m}\Big|_{x_3 + \Delta x_3/2}\,\hat{h}_m(x_3,\omega), \tag{5.41}$$

where the matrices $\hat{A}$, $\hat{A}'$ and $\hat{C}$ are functions of x_3 and ω, and are constructed from the operators $\hat{M}$, $\hat{M}'$ and $\hat{C}$:

$$\hat{A} \ = \hat{M}\,\hat{C} + \mathrm{j}\beta_9\,\omega\Delta x_3\,\hat{M}', \tag{5.42}$$

$$\hat{A}' = \hat{M}\,\hat{C} - \mathrm{j}\beta_9\,\omega\Delta x_3\,\hat{M}'. \tag{5.43}$$

The matrices $\hat{A}$ and $\hat{A}'$ contain five nonvanishing bands, while $\hat{C}$ has three nonvanishing bands only. Observe that

$$\hat{A}'(\omega) = \hat{A}(-\omega), \tag{5.44}$$

thus $\hat{A}'(\omega) = \overline{\hat{A}(\omega)}$ if ω is real-valued ($\Omega = 0$).

    The numerical scheme following Equation (5.41), involves two matrix-vector multiplications and twice solving a matrix equation per propagation step:

$$\hat{C}_{l,m}\hat{h}'_m(x_3,\omega) = \hat{h}_l(x_3,\omega), \tag{5.45}$$

$$\hat{h}''_k(x_3,\omega) = \hat{A}'_{k,l}\hat{h}'_l(x_3,\omega), \tag{5.46}$$

$$\hat{A}_{j,k}\hat{h}'_k(x_3 + \Delta x_3,\omega) = \hat{h}''_j(x_3,\omega), \tag{5.47}$$

$$\hat{h}_i(x_3 + \Delta x_3,\omega) = \hat{C}_{i,j}\hat{h}'_j(x_3 + \Delta x_3,\omega). \tag{5.48}$$

The first and last steps adjust for the change to the co-moving frame of reference. Introduce the diagonal matrix $\hat{T}$, representing the change of frame, with diagonal elements (cf. Equation (5.12)) (no summation convention)

$$\hat{T}_{m,m}(x_3) = \exp[-\mathrm{j}\omega\tau(x_{1m},x_3)]. \tag{5.49}$$

Then the propagator matrix (cf. Equations (3.84) and (5.41)) is given by

$$\langle \hat{P} \rangle_{i,m}(m+1) = \hat{T}_{i,i'}(x_3 + \Delta x_3) \ \hat{C}_{i',j}(\hat{A}^{-1})_{j,k}\hat{A}'_{k,l}(\hat{C}^{-1})_{l,m}\Big|_{x_3 + \Delta x_3/2} \quad (5.50)$$

Appendix 5.A contains the FORTRAN code for constructing the various matrices. There are several techniques for carrying out the matrix inversions[180]. The inversion of the tridiagonal matrix $\hat{C}$ in Equation (5.45) is carried out by forward/backward substitution (see Numerical Recipes[177]).

5.4   Transverse boundaries

Our discretization coexists with applying periodic boundary conditions in the transverse direction. It is standard practice to make the boundaries of the computational domain absorbing, to simulate an unbounded configuration instead. Several approaches to this adjustment have been developed; we mention the work of Clayton and Engquist[181] based on the parabolic equation in the transverse directions. Competing approaches are the Transparent Boundary Condition (TBC) by Hadley[72, 73], and the one by Bérenger[182] based on a perfectly matched layer for absorption at the boundary. The latter approach is also applied in the BPM, see Vassallo and van der Keur[183]. We follow the methodology described by Arai et al.[184], which is a generalization of Hadley's approach. Arai et al. arrived at a linear boundary condition and made it adaptive. We employ its simplest form, the Robin conditions.

The Robin boundary condition employs the one-way wave equations (as in Equation (5.1)) in both transverse directions at the edges of the computational domain,

$$\partial_1 \hat{h} + j\omega\eta^{(\pm)}\hat{h} = 0, \quad \text{at } x_1 \stackrel{(-)}{=} 0 \ \text{ and at } x_1 \stackrel{(+)}{=} (N_{x_1} + 1)\Delta x_1.$$
$$(5.51)$$

By choosing $\eta^{(\pm)}$ adaptively, we will show that these boundary conditions can be made highly transparent.

The key matrices in our numerical scheme consist of five bands. We require estimates of the field at two discretization points outside the computational domain, in accordance with transparent boundary conditions. The estimate of the field at the farthest sample points is based on the additional constraint,

$$\partial_1^2 \hat{h} + j\omega\eta^{(\pm)}\partial_1 \hat{h} = \text{invariant}, \quad \text{at } x_1 \stackrel{(-)}{=} 0 \ \text{ and at } x_1 \stackrel{(+)}{=} (N_{x_1} + 1)\Delta x_1.$$
$$(5.52)$$

We will illustrate the estimation procedure at the left boundary at $x_1 = \Delta x_1$. Then the field samples $\hat{h}_0$ and $\hat{h}_{-1}$ have to be determined. In terms of a lowest-order finite-difference representation, Equation (5.51) becomes,

$$\hat{h}_1 - \hat{h}_0 + j\omega\Delta x_1\eta^{(-)}\hat{h}_0 = 0. \quad (5.53)$$

This leads to

$$\hat{h}_0 = (1 - j\omega \Delta x_1 \eta^{(-)})^{-1} \hat{h}_1. \qquad (5.54)$$

The constraint (5.52) is used to construct $\hat{h}_{-1}$, with the finite-difference representation

$$\frac{\hat{h}_1 - 2\hat{h}_0 + \hat{h}_{-1}}{(\Delta x_1)^2} + j\omega\eta^{(-)} \frac{\hat{h}_0 - \hat{h}_{-1}}{\Delta x_1} = \frac{\hat{h}_2 - 2\hat{h}_1 + \hat{h}_0}{(\Delta x_1)^2} + j\omega\eta^{(-)} \frac{\hat{h}_1 - \hat{h}_0}{\Delta x_1}, \qquad (5.55)$$

with the solution

$$\hat{h}_{-1} = \frac{\hat{h}_2 + \hat{h}_1 \left[j\omega\Delta x_1\eta^{(-)} - 3 + (1 - j\omega\Delta x_1\eta^{(-)})^{-1}(3 - 2j\omega\Delta x_1\eta^{(-)}) \right]}{1 - j\omega\Delta x_1\eta^{(-)}}. \qquad (5.56)$$

The numerical scheme associated with the Robin boundary condition is

- neutrally stable if $\mathrm{Re}(\eta^{(-)}) = 0$,

- stable if $\mathrm{Re}(\eta^{(-)}) < 0$,

- unstable if $\mathrm{Re}(\eta^{(-)}) > 0$.

The boundary conditions reduce to the Neumann boundary condition for $\eta^{(-)} = 0$, and to the Dirichlet boundary condition for $\eta^{(-)} \to \infty$.

We adapt the value of $\eta^{(\pm)}$ by assuming that the field behaves like a plane wave ($\sim \exp(-j\omega\eta^{(\pm)}x_1)$) near the computational boundaries. The transverse slowness associated with this plane wave can be estimated at the previous propagation step; at the current step, that value of $\eta^{(\pm)}$ can then be applied. At the left boundaries, with Equation (5.53), we get

$$\eta^{(-)} \simeq (j\omega\Delta x_1)^{-1} \left(1 - \frac{\hat{h}_2}{\hat{h}_1} \right). \qquad (5.57)$$

If the plane wave were to travel inward ($\mathrm{Re}(\eta^{(-)}) > 0$ at the left boundary), $\eta^{(\pm)}$ is reset to its imaginary part $\mathrm{Im}(\eta^{(\pm)})$. Thus, inward travelling waves are attenuated. The effectiveness of the transparent boundary conditions can be determined from the graph of the reflection coefficient associated with a plane wave hitting the boundary, see Clayton and Engquist[181]. Keys[185] extended the one-way absorbing boundary equation to the case where two distinguishable plane waves hit the computational boundary simultaneously.

In our numerical scheme, the transparent boundary conditions are translated into an adjustment of the outer elements of the matrices $\hat{A}'$ and $\hat{A}$. For example,

the left boundary elements of $\hat{\mathsf{A}}$ become (cf. Equations (5.54)-(5.56))

$$\hat{\mathsf{A}}_{1,1} \to \hat{\mathsf{A}}_{1,1} + (1 - j\omega\Delta x_1\eta^{(-)})^{-1}\Big\{\hat{\mathsf{A}}_{1,0} + \hat{\mathsf{A}}_{1,-1}$$

$$\Big[j\omega\Delta x_1\eta^{(-)} - 3 + (1 - j\omega\Delta x_1\eta^{(-)})^{-1}(3 - 2j\omega\Delta x_1\eta^{(-)})\Big]\Big\}, \quad (5.58)$$

$$\hat{\mathsf{A}}_{1,2} \to \hat{\mathsf{A}}_{1,2} + (1 - j\omega\Delta x_1\eta^{(-)})^{-1}\hat{\mathsf{A}}_{1,-1}, \quad (5.59)$$

$$\hat{\mathsf{A}}_{2,1} \to \hat{\mathsf{A}}_{2,1} + (1 - j\omega\Delta x_1\eta^{(-)})^{-1}\hat{\mathsf{A}}_{2,0}. \quad (5.60)$$

5.5 Longitudinal phase and group slownesses

In order to analyze and improve our numerical scheme, we study the longitudinal phase and group slownesses. First, we discuss their physical meaning, subsequently their form after discretization. We employ an optimization procedure to increase the accuracy and analyze the slowness in heterogeneous media. The wave-field in free space is analyzed.

An amplitude-modulated plane-wave constituent has the general form

$$w(x_1, x_3, t) = a(t) \cos\{\omega_c[t - \alpha_1 x_1 - \hat{\gamma}(\omega_c)x_3]\}, \quad (5.61)$$

where ω_c denotes the angular frequency of the carrier. The "amplitude" $a(t)$ of the signal is assumed to be frequency (band)limited with support $-\Delta\omega/2 < \omega < \Delta\omega/2$. For a pulsed amplitude function with Fourier transform

$$\hat{a}(\omega) = \begin{cases} (\Delta\omega)^{-1}, & \text{when} & -\Delta\omega/2 < \omega < \Delta\omega/2, \\ 0, & \text{when} & |\omega| > \Delta\omega/2, \end{cases} \quad (5.62)$$

and with $\Delta\omega/\omega_c$ small, the corresponding plane wave in the time domain is approximately

$$w(x_1, x_3, t) \simeq \pi^{-1}\text{sinc}\{(\Delta\omega/2)[t - \alpha_1 x_1 - \hat{\gamma}^{gr}(\omega_c)x_3]\}$$
$$\cos\{\omega_c[t - \alpha_1 x_1 - \hat{\gamma}^{ph}(\omega_c)x_3]\}, \quad (5.63)$$

with the group slowness

$$\hat{\gamma}^{gr} = \partial_\omega(\omega\hat{\gamma}^{ph}), \quad (5.64)$$

and the phase slowness $\hat{\gamma}^{ph} = \hat{\gamma}$. Equation (5.63) describes the distortion of a modulated sinc pulse traveling over a distance x_3. It elucidates the concepts of the longitudinal phase and group slownesses $\hat{\gamma}^{ph}$ and $\hat{\gamma}^{gr}$. Now, we derive expressions for $\hat{\gamma}^{ph}$ and $\hat{\gamma}^{gr}$. The analysis of the accuracy of finite-difference propagation schemes with phase and group velocities can be found in Trefethen[159]. Beaumont et al.[160] and Holberg[161, 162] assessed and improved the accuracy of such schemes.

5.5.1 Slownesses after discretization

Substitute a plane wave constituent into Equations (5.12) and (5.48):

$$\tilde{W}_1^{(0)}(x_1, \Delta x_3; \omega) = \exp(-\mathrm{j}\omega\hat{\gamma}^{\mathrm{ph}}\Delta x_3) \, \exp(-\mathrm{j}\omega\alpha_1 \Delta x_1), \tag{5.65}$$

or, in the moving frame of reference,

$$\hat{h}(x_1, \Delta x_3; \omega) = \exp(\mathrm{j}\omega\tau) \, \exp(-\mathrm{j}\omega\hat{\gamma}^{\mathrm{ph}}\Delta x_3) \, \exp(-\mathrm{j}\omega\alpha_1 \Delta x_1). \tag{5.66}$$

We then obtain the *amplification* factor of the finite-difference scheme (see Richtmeyer and Morton[179] and Equation (5.50)),

$$\mathsf{a}^{-1}\mathsf{a}' = \exp(-\mathrm{j}\omega\hat{\gamma}^{\mathrm{ph}}\Delta x_3) \, \exp(\mathrm{j}\omega c^{-1}\Delta x_3), \tag{5.67}$$

in which $\hat{\gamma}^{\mathrm{ph}}$, a and a' are the left symbols of the numerical representation for $\hat{\Gamma}$, $\hat{\mathsf{A}}$ and $\hat{\mathsf{A}}'$, respectively. For a homogeneous medium (constant c), we find

$$\mathsf{a} = \hat{\mathsf{A}}_{i,i} + 2\hat{\mathsf{A}}_{i,i+1}\cos(\omega\alpha_1\Delta x_1) + 2\hat{\mathsf{A}}_{i,i+2}\cos(2\omega\alpha_1\Delta x_1), \tag{5.68}$$

independent of i, together with a similar expression for a', replacing $\hat{\mathsf{A}}$ by $\hat{\mathsf{A}}'$. For real valued ω, we have $\mathsf{a}'(\omega) = \mathsf{a}(-\omega)$, thus $|\mathsf{a}^{-1}\mathsf{a}'| = 1$ in a homogeneous medium. The symbol of the finite difference scheme is the longitudinal phase slowness $\hat{\gamma}^{\mathrm{ph}}$ given by

$$\hat{\gamma}^{\mathrm{ph}}(\alpha_1, \omega) = c^{-1} - \frac{\ln(\mathsf{a}^{-1}\mathsf{a}')}{\mathrm{j}\omega\Delta x_3}, \tag{5.69}$$

which reduces, if ω is real-valued, to

$$\hat{\gamma}^{\mathrm{ph}}(\alpha_1, \omega) = c^{-1} + \frac{2}{\omega\Delta x_3}\arg(\mathsf{a}). \tag{5.70}$$

From the longitudinal phase slowness the longitudinal group slowness $\hat{\gamma}^{\mathrm{gr}}$ can be derived, viz.,

$$\hat{\gamma}^{\mathrm{gr}} = \partial_\omega(\omega\hat{\gamma}^{\mathrm{ph}}) = \hat{\gamma}^{\mathrm{ph}} + \omega(\partial_\omega\hat{\gamma}^{\mathrm{ph}}). \tag{5.71}$$

The second term can be related to $c\,(\partial_\omega\hat{\gamma}^{\mathrm{ph}})$, which can be identified with the delay of the envelope per wavelength. Together with Equation (5.67), this leads to

$$\hat{\gamma}^{\mathrm{gr}}(\alpha_1, \omega) = c^{-1} - \mathrm{j}(\Delta x_3)^{-1}\left[\mathsf{a}^{-1}\partial_\omega\mathsf{a} - (\mathsf{a}')^{-1}\partial_\omega\mathsf{a}'\right], \tag{5.72}$$

and reduces, if ω is real-valued, to

$$\hat{\gamma}^{\mathrm{gr}}(\alpha_1, \omega) = c^{-1} - 2(\Delta x_3)^{-1}\mathrm{Im}\left(\mathsf{a}^{-1}\partial_\omega\mathsf{a}\right). \tag{5.73}$$

It is observed that $\hat{\gamma}^{\mathrm{ph}}$ and $\hat{\gamma}^{\mathrm{gr}}$ are functions of the transverse and longitudinal sampling rates per wavelengths, $r_{\mathrm{t}} = c/(\omega\Delta x_1)$ and $r_{\mathrm{l}} = c/(\omega\Delta x_3)$. For a dense discretization ($\Delta x_1, \Delta x_3 \to 0$), the difference between the two slownesses disappear ($|\hat{\gamma}^{\mathrm{ph}} - \hat{\gamma}^{\mathrm{gr}}| \to 0$). Note that $\hat{\gamma}^{\mathrm{gr}} - \hat{\gamma}$ is indicative of the **numerical anisotropy**, whereas $\hat{\gamma}^{\mathrm{ph}} - \hat{\gamma}^{\mathrm{gr}}$ is indicative of the **numerical dissipation**.
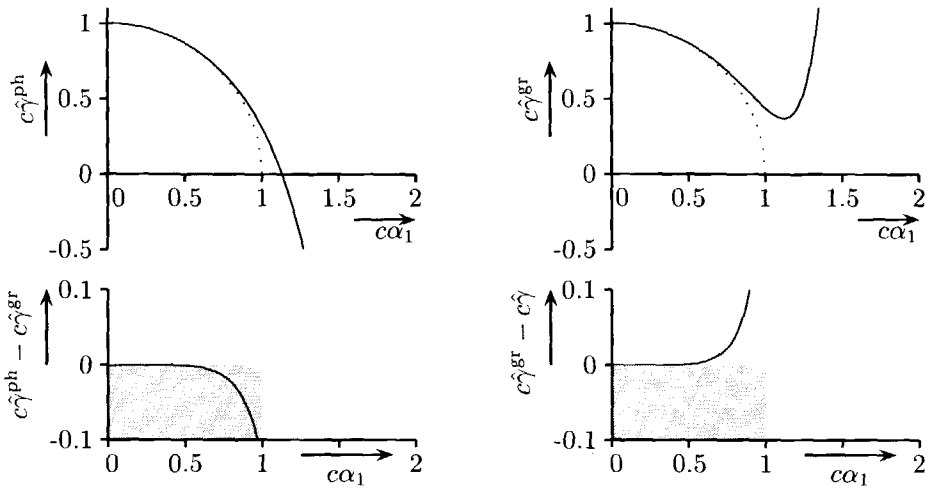
Figure 5.8:   *The phase slowness (upper left) and the group slowness (upper right) associated with the discretized, approximate, one-way wave equation with $\beta_1 = 1/2$, $\beta_2 = 1/8$, $\beta_3 = 1/2$, $a_2 = 1/12$ and $\beta_9 = 1/2$, and a sampling rate of 5 points per wavelength (parameter set 1). The real part of the exact longitudinal slowness is dotted. In the bottom row, the difference between the phase slowness and the group slowness, and the difference between the group slowness and the exact slowness are plotted.*

5.5.2   Optimization

The longitudinal phase and group slownesses are functions of our parameters $\{\beta_1, \beta_2, \beta_3, a_2, \beta_9, \Omega\}$ arising from the various approximations made to arrive at a sparse matrix representation for the propagator. So far, we have found two distinct parameter sets: one arising from consistent rational expansions, and one arising from step-wise optimization. For a sampling rate of 5 points per wavelength in both the transverse and longitudinal directions ($\Delta x_1 = \Delta x_3 = 0.2\lambda_0$) the phase and group slownesses for the first parameter set are shown in Figure 5.8. The exact longitudinal slowness is shown in the same graph. Significant deviations are observed for wide propagation angles. The parameter set corresponding to the step-wise optimization leads to a better result (Figure 5.9). In the step-wise optimization, however, it is hard to control the movement of the poles in the complex transverse slowness plane, which is introduced by the approximations. One can control this movement in an optimization scheme of the phase and group slownesses for all parameters together; then one expects a more accurate result as well.

The optimization of the phase and group slownesses results in a minimization of numerical anisotropy and numerical dissipation for the pre-critical wave constituents. In the optimization procedure, special attention must be paid to the
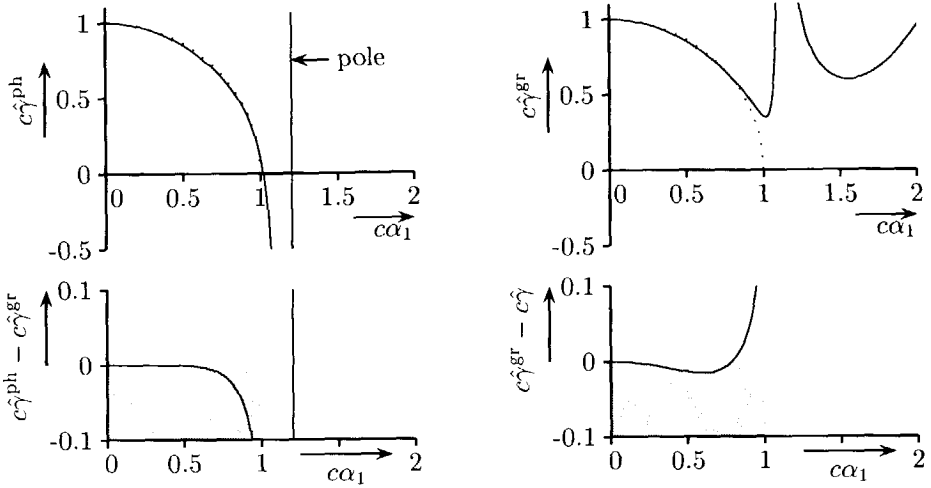
Figure 5.9: *Idem as for Figure 5.8, but now with parameter set 2: $\beta_1 = 0.526$, $\beta_2 = 0.364$, $\beta_3 = 0.825$, $a_2 = 0.0888$ and $\beta_9 = 0.529$.*
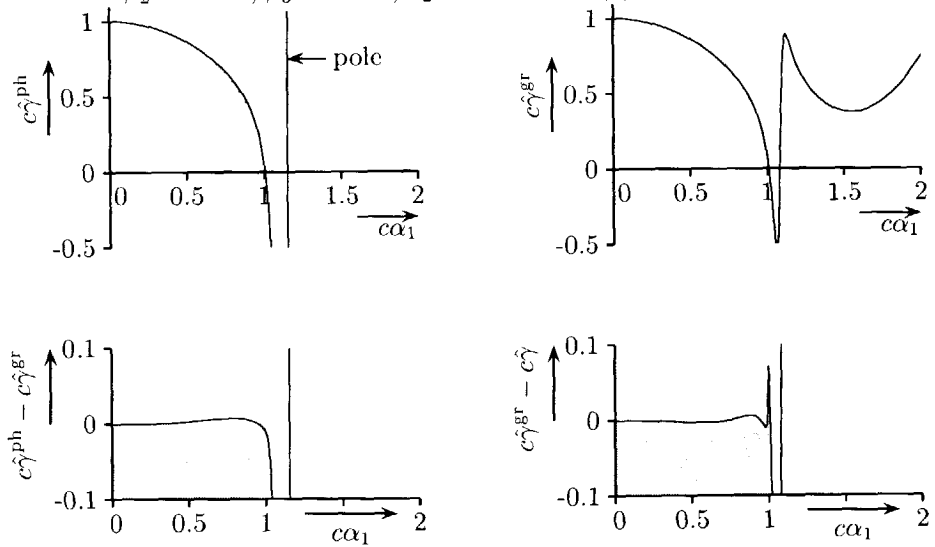

Figure 5.10: *Idem as for Figure 5.8, but now with parameter set 3: $\beta_1 = 0.486$, $\beta_2 = 0.349$, $\beta_3 = 0.841$, $a_2 = 0.114$ and $\beta_9 = 0.529$*

constraint that the poles of a stay outside the pre-critical region in the α_1-plane. The overall optimization is carried out for an objective function given by the sum of the squared differences between $\hat{\gamma}^{gr}$ and $\hat{\gamma}$, and $\hat{\gamma}^{ph}$ and $\hat{\gamma}^{gr}$. The results are illustrated in Figure 5.10, as before for 5 points per wavelength. From numerical tests, we find that the accuracy remains more or less the same when we vary the transverse sampling rate from 6 to 2.5 points per wavelength, keeping the longitudinal sampling rate the same. The procedure is even less sensitive to the longitudinal sampling rate.

Thus far, the optimization procedure has been focussed on the real slowness surface. However, as we have seen in the preceeding sections, the approximations lead to artifacts in the post-critical regime. In fact, the post-critical constituents have been mapped on propagating constituents (slow waves). We have designed a dissipation trick to attenuate these constituents. In addition to this trick, some of the artificial constituents are forced to leave the computational domain through the transparent boundary conditions. The dissipation trick induces a "complexification" of the parameters used in the optimization, and hence it seems to be natural to complexify the optimization procedure accordingly (see also Collins[186]). Pursuing this complexification, the optimization procedure is extended with the constraint that the post-critical power is attenuated markedly while the attenuation/amplification in the pre-critical region is kept minimal (less than 5%). The resulting parameter set is shown in the fourth column of Table 5.1. The first column of this table represents the expansion values, and the second column represents the values obtained by step-wise optimization. The accuracy of the complex parameter set is illustrated in Figure 5.11.

We note, however, that the complexification of parameters is not always desired. For example, in the application of our numerical scheme to long-range propagation in low-lossy waveguides, the accumulative power loss is of key importance. In such configurations, we set $\Omega = 0$ and keep the parameters real. The optimization leads to the third column of Table 5.1.

The poles arising in longitudinal phase slowness, for the different parameter sets, are given in Table 5.2.

5.5.3 Slowness in transverse varying media

Figures 5.12 and 5.13 show the real and imaginary parts of the discretized longitudinal slownesses in a transverse varying medium at several transverse positions. The medium is chosen to be a waveguide with quadratic waveguiding profile ($\varepsilon(x_1) = 1 - x_1^2/10$), for which the exact slowness is depicted in Figures 4.10 and 4.11. All graphs corresponds to densely discretized slownesses (16π points per wavelength). The first graph shows the slowness with a nonrationally discretized Laplace operator (thus $a_2 = 0$). The error appears to be small. Subsequently, we plotted the approximated slowness in Equation (5.5). Since we are especially interested in pre-critical wave propagation, we split this slowness into two contributions, one due to evanescent modes and the other due to propagation modes. Deviations appear
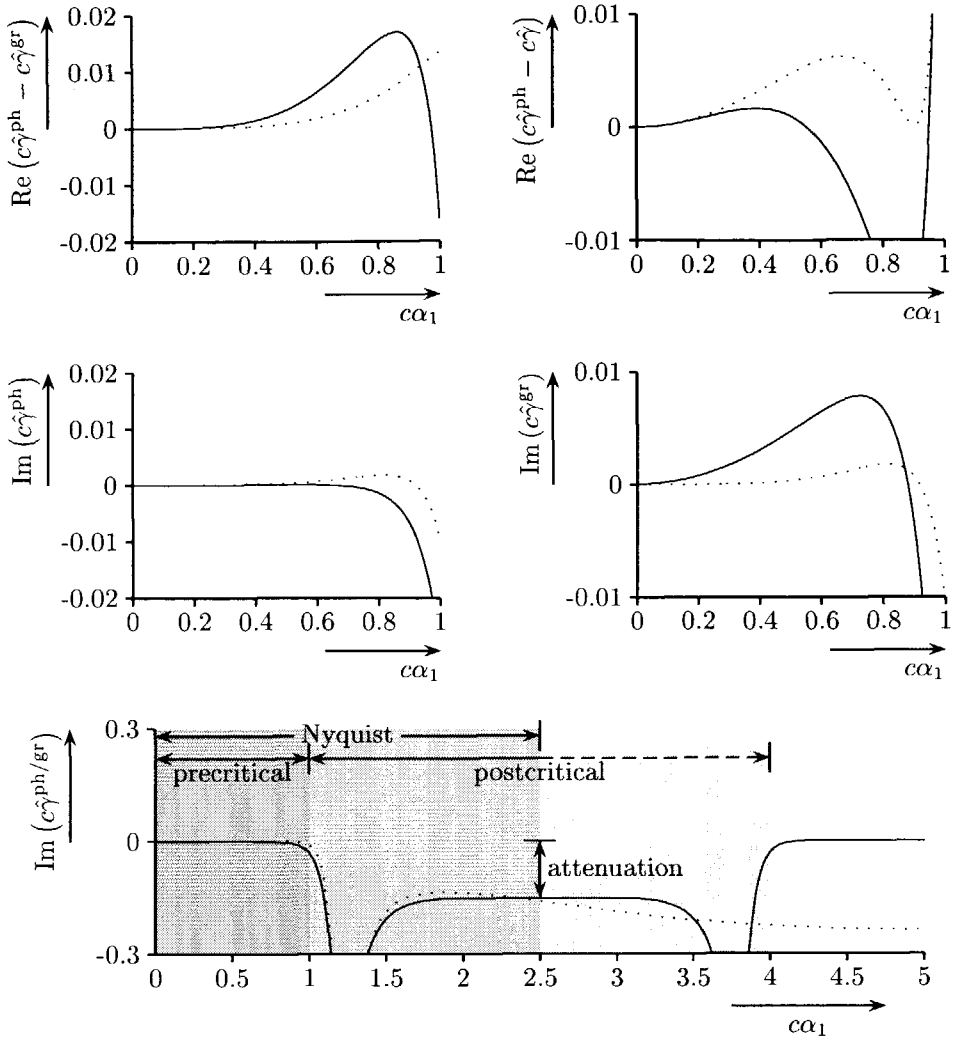
Figure 5.11: *The difference between the real parts of the phase slowness and the group slowness (upper left), and the difference between the real parts of the group slowness and the exact slowness (upper right). The middle row shows the imaginary parts of the phase slowness (left) and the group slowness (right). The parameter set is given in column 4 of Table 5.1. Two sampling rates are shown: 5 points per wave length (solid line) and 10 points per wave length (dotted line). The bottom figure shows the imaginary parts of the phase slowness (solid line) and the group slowness (dotted line) on a larger scale.*
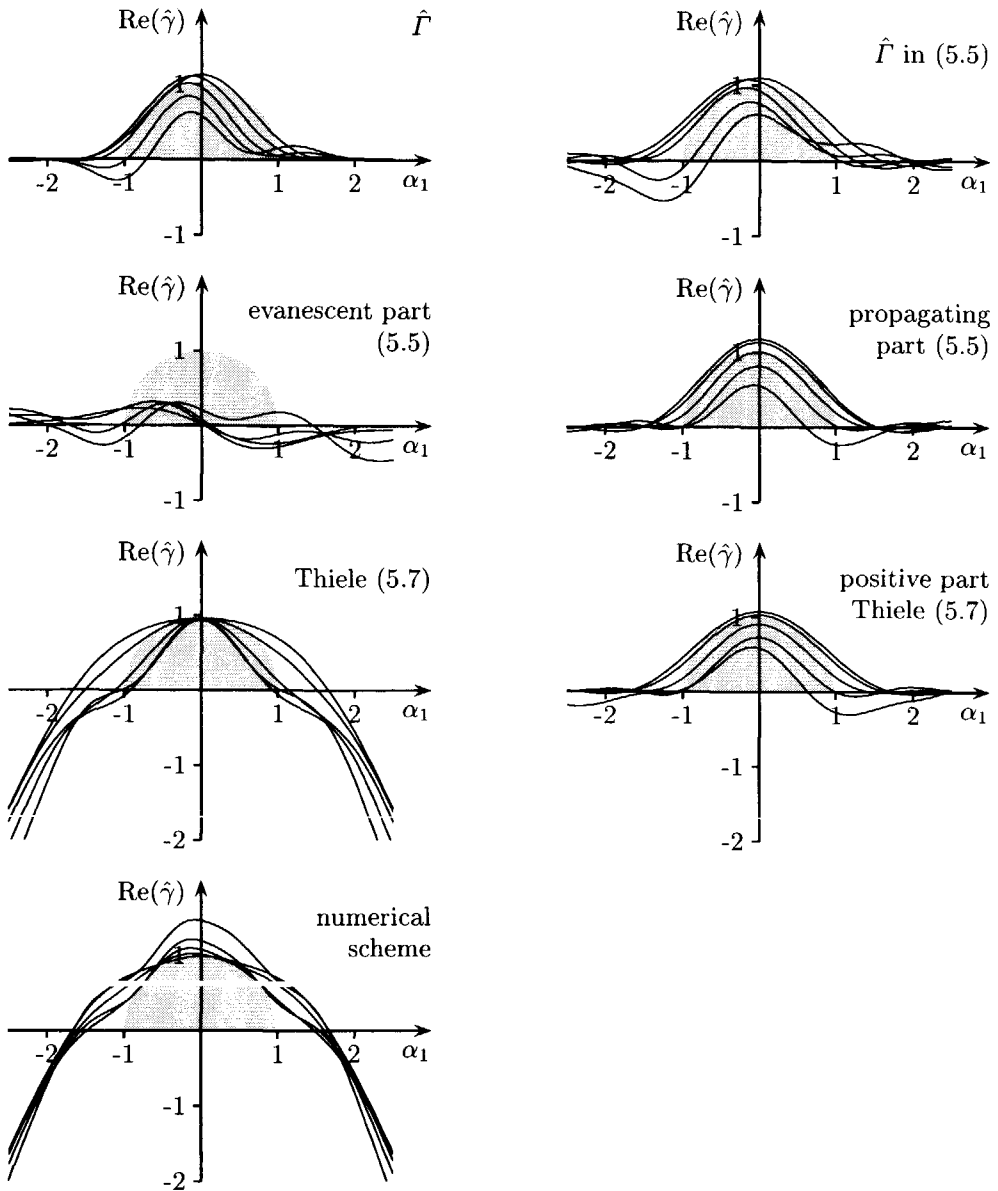
Figure 5.12: *The real part of the left symbol of our numerical scheme in a transverse heterogeneous medium with quatratic profile and Dirichlet conditions at the computational window. Here $\varepsilon(x_1) = 1 - x_1^2/10$ m^{-2}, $x_1 = 0$, 0.5, 1, 1.5, 2 m, $\Delta x = \Delta x_3 = 0.125$ m, $N_{x_1} = 64$ (last graph: $N_{x_1} = 256$).*

Figure 5.13: *Idem as in Figure 5.12, but now the imaginary part of the left symbol.*

Table 5.1:   *The parameter sets for propagation.*

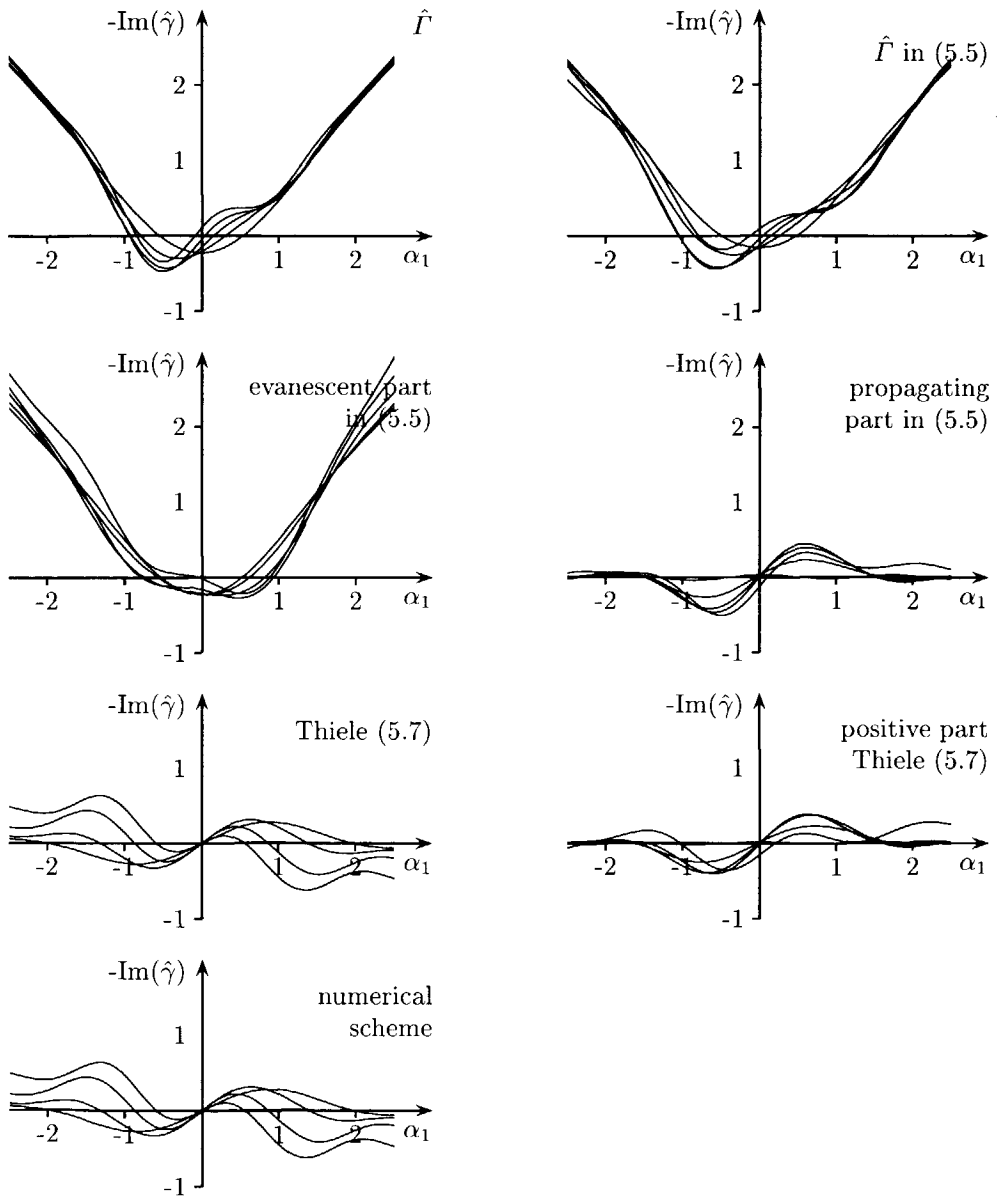| parameter set	1	2	3	4
$\Delta x_1/\lambda_0$	0.2	0.2	0.2	0.2
$\Delta x_3/\lambda_0$	0.2	0.2	0.2	0.2
$\mathrm{Re}\{\beta_1\}$	1/2	0.526	0.486	0.5104
$\mathrm{Im}\{\beta_1\}$	0	0	0	-0.0340
$\mathrm{Re}\{\beta_2\}$	1/8	0.364	0.349	0.2207
$\mathrm{Im}\{\beta_2\}$	0	0	0	-0.0131
$\mathrm{Re}\{\beta_3\}$	1/2	0.825	0.841	0.6685
$\mathrm{Im}\{\beta_3\}$	0	0	0	-0.0310
$\mathrm{Re}\{a_2\}$	1/12	0.089	0.114	0.1207
$\mathrm{Im}\{a_2\}$	0	0	0	0.0063
$\mathrm{Re}\{\beta_9\}$	1/2	0.540	0.529	0.4679
$\mathrm{Im}\{\beta_9\}$	0	0	0	-0.0066
Ω	0	0	0	0.0406
Figures	5.8 5.14	5.9	5.10 5.21,5.22	5.11, 5.15 5.18, 5.20 5.23-5.29

Table 5.2:   *The poles of the numerical longitudinal phase slowness.*

parameter set	pole 1	pole 2
1	$1.4588 + 0.2807\,j$	$1.7135 + 1.3074\,j$
2	$1.1054 - 0.0040\,j$	$2.2899 + 1.7530\,j$
3	$1.0762 - 0.0271\,j$	$1.3686 + 1.1214\,j$
4	$1.5974 - 1.1406\,j$	$1.1816 - 0.1211\,j$

for large transverse slownesses, mainly in the post-critical region. The contributions due to the evanescent and propagating modes are spread out into the pre-critical and post-critical regions, respectively. Subsequently, we plotted the left symbol of the a third-order Thiele approximation. Although it is different, we see in the next graph that the pre-critical part is well approximated. The last graph shows the left symbol of the whole numerical scheme. It is accurate for pre-critical wave propagtion.

When taking a higher-order Thiele approximation, the pre-critical part of the left symbol is better approximated, see Fishman[52]. However, when taking a Taylor approximation of the square root, only the pre-critical part in the high-frequency limit is well approximated. It is noted that we choose a local co-moving reference
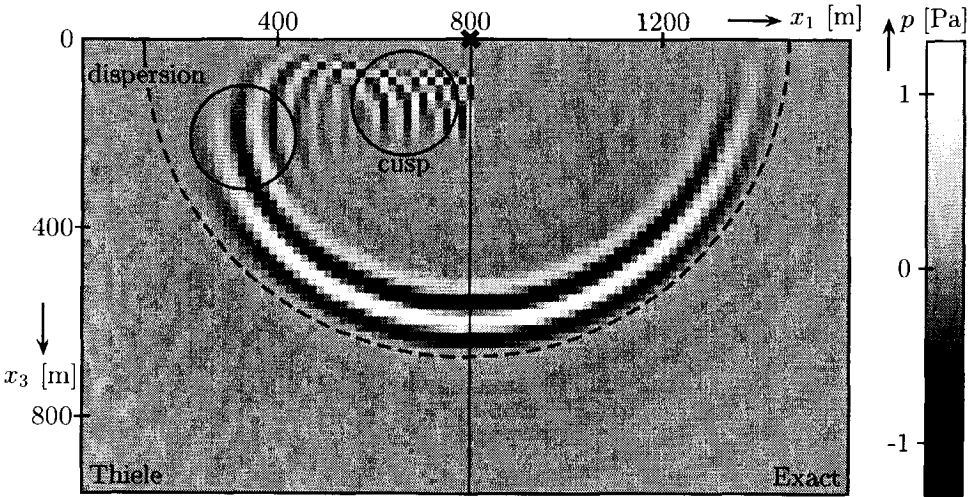
Figure 5.14: *Snapshot at $t = 0.3$ s of a vertical line-force response in a homogeneous medium ($c = 1900$ m/s). The right-hand side was obtained analytically, while the left-hand side wass obtained with our numerical scheme. Here, we used parameter set 1 of Table 5.1.*

frame for the Thiele approximation and therefore the accuracy of the approximated left symbol is independent of local permittivity, while it depends on the variation in the permittivity. This is in contrast to a transversely constant co-moving reference frame, where the slownesses are best approximated where the local permittivity is approximately equal to the reference permittivity.

5.5.4   Numerical example

We illustrate the final, optimized, one-way propagation by computing the wave-field excited by a line source in a homogeneous acoustic medium. The wave speed of the medium is chosen to be $c = 1900$ m/s. The numerical grid consists of 99 points along the x_1 direction and 60 points along the x_3 direction. The discretization step is 16 m in both directions. Given a source-signature with trapezoidal spectrum with corner frequencies 10, 20, 25, and 40 Hz (see Figure 2.12), we encounter sampling rates of 2.97 to 11.9 points per wavelength. The line source is located at $x_1 = 800$ m, $x_3 = 0$ m, and we show snapshots of the pressure field at $t = 0.3$ s. The source is a longitudinal line force. We have analytic expressions for this configuration.

In Figure 5.14, the snapshot is shown using the first parameter set, while in Figure 5.15, the snapshot for the fourth parameter set is shown. The left parts of the figures (0 m $< x_1 <$ 800 m) represent the numerical solutions, while the right parts (800 m$< x_1 <$ 1600 m) represent the exact solution. The errors occurring in
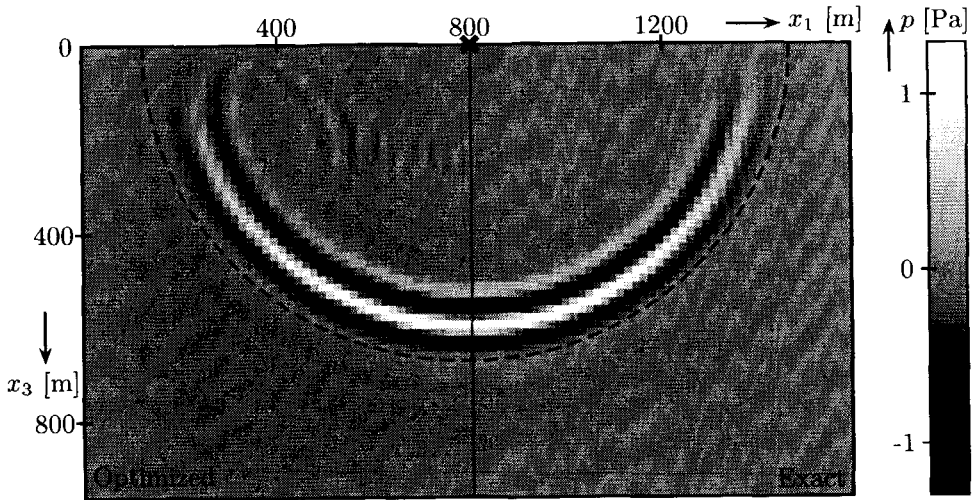
Figure 5.15: *Snapshot at* $t = 0.3$ *s of a vertical line-force response in a homogeneous medium* $(c = 1900$ *m/s). The right-hand side was obtained analytically, while the left-hand side was obtained with our numerical scheme. Here, we used parameter set 4 of Table 5.1.*
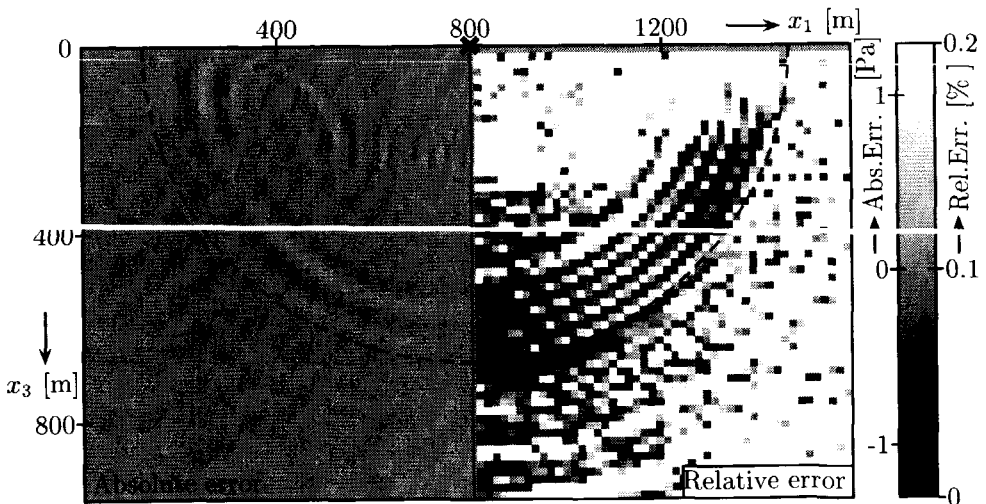

Figure 5.16: *The absolute error (0 m*$< x_1 < 800$ *m) and the relative error (800 m*$< x_1 < 1600$ *m) of the snapshot shown in the previous figure. The relative error is in %.*

Figure 5.15 are illustrated in Figure 5.16, the absolute ones for 0 m$< x_1 < 800$ m and the relative ones for 800 m$< x_1 < 1600$ m. From this figure we find that the relative error at the numerical wave front is less than 2.5% up to angles of approximately 65 degrees. Repeating this accuracy analysis for the other parameter sets, we conclude that the approximations are acceptable up to 20 degrees, 40 degrees, and 80 degrees for the standard parabolic approximation, parameter set 1, and parameter set 3, respectively. The third parameter set is more accurate for higher angles than the fourth parameter set; however, post-critical artifacts remain apparent in the numerical results obtained with this real-valued parameter set.

5.6 Sparse matrix representation of the (de)composition operator

The computation of the generalized Bremmer coupling series starts with the decomposition of the initial field into forward- and backward-traveling constituents, see also Equations (3.22)-(3.23)

$$\begin{pmatrix} \hat{W}_1 \\ \hat{W}_2 \end{pmatrix} = \frac{1}{2} \begin{pmatrix} 1 & \hat{Y}^{-1} \\ 1 & -\hat{Y}^{-1} \end{pmatrix} \begin{pmatrix} \hat{F}_1 \\ \hat{F}_2 \end{pmatrix}.$$

Upon completing the calculation of a sufficiently large number of terms of the Bremmer coupling series, the constituents are recomposed into observables, see also Equations (3.20)-(3.21)

$$\begin{pmatrix} \hat{F}_1 \\ \hat{F}_2 \end{pmatrix} = \begin{pmatrix} 1 & 1 \\ \hat{Y} & -\hat{Y} \end{pmatrix} \begin{pmatrix} \hat{W}_1 \\ \hat{W}_2 \end{pmatrix}.$$

In these procedures, the operator $\hat{\Gamma}$ and its inverse must be computed ($\hat{Y} = \mu_0^{-1}\hat{\Gamma}$). Here, using the results of Sections 5.3-5.5, we derive sparse matrix representations for these operators. A numerical example illustrates the accuracy.

5.6.1 Composition operator

The composition operator contains the longitudinal slowness operator. To find a sparse matrix representation for this operator, we use the same approximation as that in Equation (5.7) for one-way wave propagation. We write, however, the fraction in a slightly different way,

$$\hat{\Gamma}^{\text{III}} = c^{-1/2} \left[1 + \beta_4 \hat{\Xi} + (1 + \beta_3 \hat{\Xi})^{-1} \beta_5 \hat{\Xi} \right] c^{-1/2}, \tag{5.74}$$

with

$$\beta_4 = \frac{\beta_2}{\beta_3}, \qquad \beta_5 = \beta_1 - \frac{\beta_2}{\beta_3}. \tag{5.75}$$

We set

$$\hat{\varGamma}^{\mathrm{III}} = \hat{\varGamma}_1^{\mathrm{III}} + \hat{\varGamma}_2^{\mathrm{III}}, \qquad (5.76)$$

with

$$\hat{\varGamma}_1^{\mathrm{III}} = c^{-1/2}(1 + \beta_4\hat{\varXi})\,c^{-1/2}, \quad \hat{\varGamma}_2^{\mathrm{III}} = c^{-1/2}\left[\left(1 + \beta_3\hat{\varXi}\right)^{-1}\beta_5\hat{\varXi}\right]\,c^{-1/2}. \qquad (5.77)$$

Substituting discretization Equation (5.15) into Equation (5.6) and the result into these operators, yields

$$(1 + a_2\delta_1^2)\left(c^{-1/2}\langle\hat{\varGamma}_1^{\mathrm{III}}\hat{h}\rangle\right) = \left[(1 + a_2\delta_1^2)c^{-2} + \beta_4 r_t^2 c^{-2}\delta_1^2\right]\left(c^{1/2}\hat{h}\right), \qquad (5.78)$$

$$\left[(1 + a_2\delta_1^2)c^{-2} + \beta_3 r_t^2 c^{-2}\delta_1^2\right]\left(c^{3/2}\langle\hat{\varGamma}_2^{\mathrm{III}}\hat{h}\rangle\right) = \beta_5 r_t^2 c^{-2}\delta_1^2\left(c^{1/2}\hat{h}\right). \qquad (5.79)$$

The two equations contain tridiagonal matrices only. Hence, they can be solved rapidly with the forward/backward substitution procedure (see Numerical Recipes[177]).

5.6.2 Decomposition operator

The decomposition operator essentially contains the inverse of the longitudinal slowness operator. Using approximation (5.7) as before, we find that

$$c^{1/2}\hat{\varGamma}^{\mathrm{III}}c^{1/2} = \beta_2\,(1 + \beta_3\hat{\varXi})^{-1}[\beta_2^{-1} + \beta_2^{-1}(\beta_1 + \beta_3)\hat{\varXi} + \hat{\varXi}^2]. \qquad (5.80)$$

Factoring the operator between brackets, yields

$$\beta_2^{-1} + \beta_2^{-1}(\beta_1 + \beta_3)\hat{\varXi} + \hat{\varXi}^2 = (\beta_6 - \hat{\varXi})\,(\beta_7 - \hat{\varXi}), \qquad (5.81)$$

with

$$\beta_6 = (2\beta_2)^{-1}\left\{-\beta_1 - \beta_3 + \left[(\beta_1 + \beta_3)^2 - 4\beta_2\right]^{1/2}\right\}, \qquad (5.82)$$

$$\beta_7 = (2\beta_2)^{-1}\left\{-\beta_1 - \beta_3 - \left[(\beta_1 + \beta_3)^2 - 4\beta_2\right]^{1/2}\right\}. \qquad (5.83)$$

Then, it is straightforward to invert the longitudinal slowness operator, viz.,

$$\left(\hat{\varGamma}^{\mathrm{III}}\right)^{-1} = c^{1/2}\left[\beta_2^{-1}(\beta_7 - \hat{\varXi})^{-1}(\beta_6 - \hat{\varXi})^{-1}(1 + \beta_3\hat{\varXi})\right]c^{1/2}. \qquad (5.84)$$

Observe that the symbol of this operator has two poles on either side of the origin (the zero crossings of $\hat{\gamma}^{\mathrm{III}}$).

Using the factorization, we decompose the inverse longitudinal slowness into three operators,

$$(\hat{\Gamma}^{\mathrm{III}})^{-1} = \hat{\Upsilon}_3^{-1}\hat{\Upsilon}_2^{-1}\hat{\Upsilon}_1, \tag{5.85}$$

with

$$\hat{\Upsilon}_1 = (1 + \beta_3\hat{\Xi})c^{1/2}, \quad \hat{\Upsilon}_2 = (\beta_6 - \hat{\Xi}), \quad \hat{\Upsilon}_3 = (\beta_7 - \hat{\Xi})\beta_2 c^{-1/2}. \tag{5.86}$$

The inverse longitudinal slowness operator is then applied in two steps,

$$\hat{\Upsilon}_2\left\{\hat{\Upsilon}_3\left[\left(\hat{\Gamma}^{\mathrm{III}}\right)^{-1}\hat{h}\right]\right\} = \hat{\Upsilon}_1\hat{h}, \tag{5.87}$$

which involves twice solving an equation. Substituting Equation (5.6), with the aid of Equation (5.15), the two equations are discretized

$$\left[\beta_6(1 + a_2\delta_1^2) - r_{\mathrm{t}}^2 c^{-2}\delta_1^2 c^2\right]\left\{c^{-1}\langle\hat{\Upsilon}_3[(\hat{\Gamma}^{\mathrm{III}})^{-1}\hat{h}]\rangle\right\}$$
$$= \left[(1 + a_2\delta_1^2) + \beta_3 r_{\mathrm{t}}^2 c^{-2}\delta_1^2 c^2\right]\left(c^{-1/2}\hat{h}\right), \tag{5.88}$$

$$\beta_2\left[\beta_7(1 + a_2\delta_1^2) - r_{\mathrm{t}}^2 c^{-2}\delta_1^2 c^2\right]\left[c^{-3/2}\langle(\hat{\Gamma}^{\mathrm{III}})^{-1}\hat{h}\rangle\right]$$
$$= (1 + a_2\delta_1^2)\left\{c^{-1}\langle\hat{\Upsilon}_3[(\hat{\Gamma}^{\mathrm{III}})^{-1}\hat{h}]\rangle\right\}. \tag{5.89}$$

The associated tridiagonal matrices are inverted using the forward/backward substitution procedure (see Numerical Recipes[177]).

5.6.3 Numerical example

At the computational boundaries we apply, as before, the Robin boundary conditions (Section 5.4). We also employ an optimization procedure for the (de)composition operators, considering the parameter subset $\{\beta_1, \beta_2, \beta_3, a_2, \Omega\}$. To avoid instabilities, we have to move the poles arising in the symbols of the approximate operators into the complex transverse slowness plane. Table 5.3 contains the outcome of the optimization for a sampling rate of 5 points per wavelength. Figure 5.17 shows the symbols of the composition operator for different values of Ω.

To demonstrate the effect of wave-field decomposition, we have computed the pressure excited by an explosion line source. The configuration was otherwise the same as those in Figures 5.14-5.15. Figure 5.18 shows a snapshot at $t = 0.3$ s. The radiation pattern becomes close to isotropic.
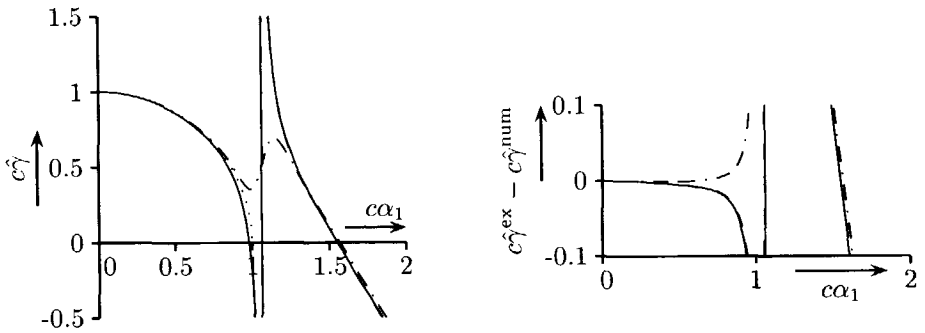
Figure 5.17: *The real part of the symbol of the vertical slowness (composition) operator (right figure) and its difference with the exact symbol (left figure). The dotted line corresponds to the real part of the exact slowness symbol; the other lines correspond to $\beta_1 = 0.526$, $\beta_2 = 0.364$, $\beta_3 = 0.825$ and $a_2 = 0.130$, while Ω equals 0 (solid line), 0.01 (dashed line) and 0.1 (dashdot line).*
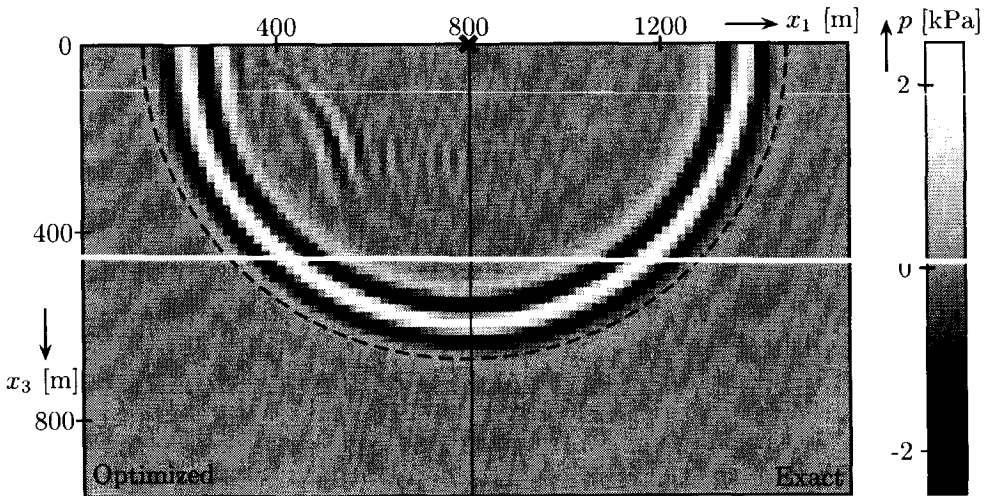
Figure 5.18: *Snapshot of an explosion line-source in a homogeneous medium ($c = 1900$ m/s). The right-hand side is obtained analytically, while the left-hand side is obtained with our numerical scheme.*

Table 5.3:   *The parameter set for the (de)composition operator.*

parameter set	2'
$\Delta x_1/\lambda_0$	0.2
$\Delta x_3/\lambda_0$	0.2
β_1	0.526
β_2	0.364
β_3	0.825
a_2	0.13
Ω	0.01

5.7   Sparse matrix representation of the reflection and transmission operators

The reflection and transmission operators describe the coupling between the forward- and backward-propagating waves. Using the results of the previous sections, we derive sparse matrix representations for these operators. A numerical example illustrates the accuracy.

From Equation (3.24), we obtain the reflection and transmission operators,

$$\hat{T} = -\hat{R} = -\tfrac{1}{2}\hat{\Gamma}^{-1}(\partial_3\hat{\Gamma}). \tag{5.90}$$

Up to principal parts, we can simplify these operators, since then

$$(\partial_3\hat{\Gamma}) \simeq \tfrac{1}{2}\hat{\Gamma}^{-1}(\partial_3 c^{-2}). \tag{5.91}$$

Substituting this approximation into Equation (5.90), yields

$$\hat{R} \simeq \tfrac{1}{4}\,\hat{A}^{-1}\,(\partial_3 c^{-2}); \tag{5.92}$$

no rational approximation is required to arrive at a sparse matrix representation, and its validity extends into the post-critical regime. To stay conceptually close to the original expression (5.90) we replace $\partial_3 c^{-2}$ by $2c^{-1}\partial_3 c^{-1}$. This replacement is justified prior to applying the finite-difference approximation only. In this approximation, we have

$$\tfrac{1}{2}c\,\partial_3 c^{-1} \xrightarrow{\text{F.D.}} \frac{1}{\Delta x_3}\frac{c^{-1}(x_3 + \tfrac{1}{2}\Delta x_3) - c^{-1}(x_3 - \tfrac{1}{2}\Delta x_3)}{c^{-1}(x_3 + \tfrac{1}{2}\Delta x_3) + c^{-1}(x_3 - \tfrac{1}{2}\Delta x_3)}, \tag{5.93}$$

which resembles the linearized reflection coefficient at normal incidence.

On the principal symbol level, the operator ordering can be further interchanged. Thus, the reflection operator can be written in the symmetric form

$$\hat{R} \simeq \tfrac{1}{2}c^{-1/2}(\partial_3 c^{-1})^{1/2}\hat{A}^{-1}c^{-1/2}(\partial_3 c^{-1})^{1/2}. \tag{5.94}$$

This form guarantees that the reflection/transmision operators vanish in any region where the medium is x_3 invariant. Upon discretizing this equation, using Equations (3.19) and (5.15), we get

$$2 \left[(1 + a_2 \delta_1^2) c^{-2} + r_t^2 c^{-2} \delta_1^2 \right] \left[(\partial_3 c^{-1})^{-1/2} c^{1/2} \langle \hat{R} \hat{h} \rangle \right]$$
$$= (1 + a_2 \delta_1^2) \left[c^{-1/2} (\partial_3 c^{-1})^{1/2} \hat{h} \right] . \quad (5.95)$$

Numerical example

The discretized reflection operator contains only two free parameters: a_2 and Ω, through r_t. To optimize for these parameters, we would have to consider every possible change in the wave speed. It turns out, however, that the optimization is rather insensitive to the medium changes, so that we can restrict ourselves to using a single parameter set,

$$a_2 = 1/12 , \qquad \Omega = 0.1. \quad (5.96)$$

The value of Ω is taken negative, to move the pole at 90 degrees propagation angle into the complex transverse slowness plane.

Figure 5.19 shows the symbol of the discretized reflection operator for $a_2 = 1/12$ and $\Omega = 0$ (the plane-wave reflection coefficient). In this figure are also shown the symbols for $\Omega = 0.05$ and $\Omega = 0.1$, as well as the exact reflection coefficient. In Figure 5.20, we show a snapshot of the pressure field corresponding to the first two terms of the Bremmer series, excited by a longitudinal line force in a two-layered medium. The numerical grid, and the position of the source, are the same as in Figures 5.14-5.15. The upper medium has a wave speed $c = 1900$ m/s and the lower medium has a wave speed $c = 3800$ m/s. The interface is located at $x_3 = 400$ m, and the snapshot time is 0.3 s, as before. The reflection and transmission are accurately modeled; the head wave, however, is only mimiced by our numerical scheme (for details, see de Hoop and de Hoop[187]).

5.8   Numerical simulations

In this section, we show examples of wave-field modeling in various configurations, using our Bremmer coupling series algorithm. First, we consider two examples that originate from integrated optics. Here, we have translated the first configuration into its acoustic counterpart. Second, we consider an example from exploration seismics, viz., a salt structure embedded in a sparse system of sedimentary layers.

5.8.1   Waveguide

Our first example is, in fact, a benchmark test (see Nolting[188]). It considers the propagation of a single mode through a waveguide (see, for example, Vassallo[144]),
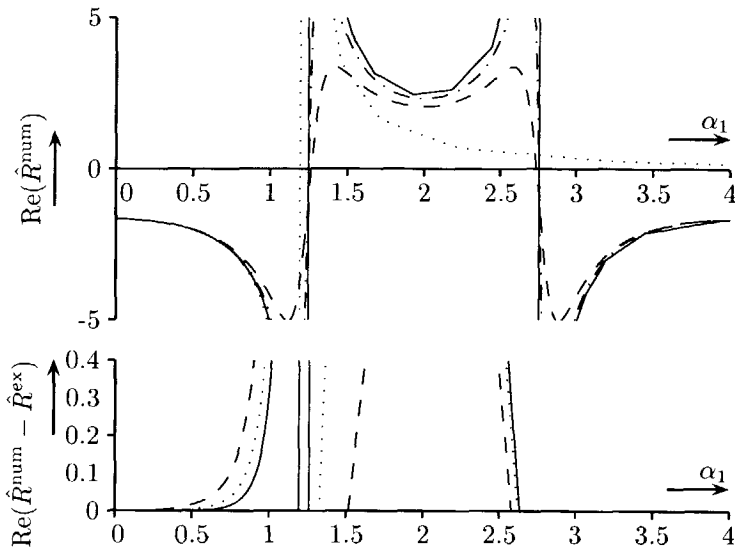
Figure 5.19: The real part of the symbols of the discretized and the exact (dotted line) reflection operators (plane-wave reflection coefficients). The differences between the discretized and exact symbols are plotted in the lower figure. The wave speed equals 1 above and 2 below the interface. We used $a_2 = 1/12$, and $\Omega = 0, 0.1, 0.05$ (solid, dashed and dashed-dotted lines, respectively).
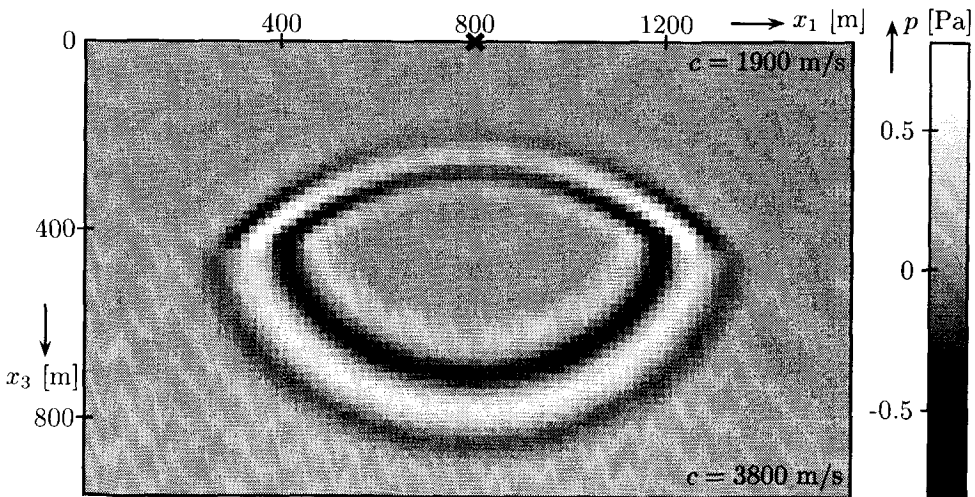

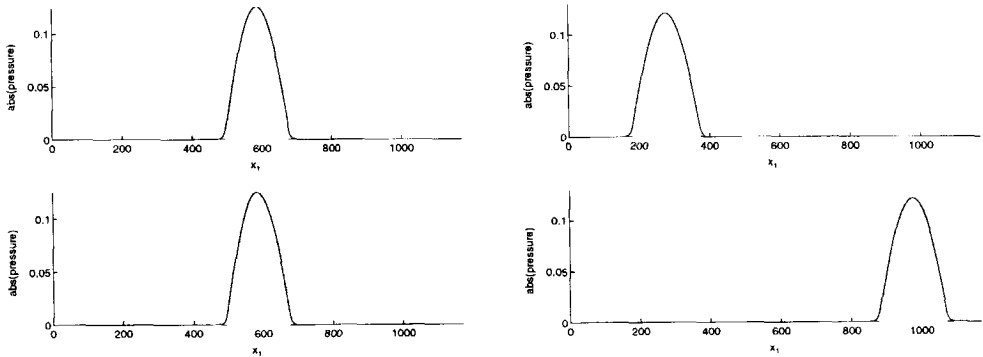Figure 5.20: Reflection and transmission at an interface.

Figure 5.21: *The fundamental waveguiding mode at the entrance plane (upper figure) and at the exit plane (bottom figure). The waveguide on the left-hand side is not tilted with respect to the coordinate system, while the waveguide on the right-hand side is tilted with an angle of 20 degrees with respect to the coordinate system. (Leading term of the Bremmer coupling series only).*

oriented under different angles with respect to the numerical grid. The details of this test configuration can be found in Nolting[188]. The wave speed is approximately 1825 m/s inside the waveguide and 1900 m/s outside. The waveguide has a thickness of approximately 180 m. The frequency is 190 Hz. We take a numerical grid with 779 points along the x_1 direction and 1360 points along the x_3 direction. The discretization step is approximately 1.5 m in both directions (about 6.7 points per wavelength). The total length of the waveguide is 2.04 km. In this simulation, we used the third (real-valued) parameter set. In this waveguide only 11 discrete modes can propagate.

Two of the waveguide modes (the fundamental and the tenth mode) are launched into the waveguide. In the first experiment the wall of the waveguide is parallel to the x_3-axis. In the second experiment, the waveguide is tilted with respect to the computational coordinate system by 20 degrees. The field at the output level plane is compared with the original field at the input level plane. Theoretically, these fields must be identical. Figure 5.21 shows the fundamental mode at the end of the longitudinal waveguide (left-hand side), and the fundamental mode at the end of the tilted waveguide (right-hand side). Figure 5.22 is the same, but then for the tenth-order mode. It is conjectured that some of the radiating modes (the propagating part) can be properly modeled with our scheme as well.

5.8.2   Block

The second example is an extension of the 1-D example in Figure 2.9 to two dimensions. We investigate the time-harmonic plane wave interaction in a homogeneous
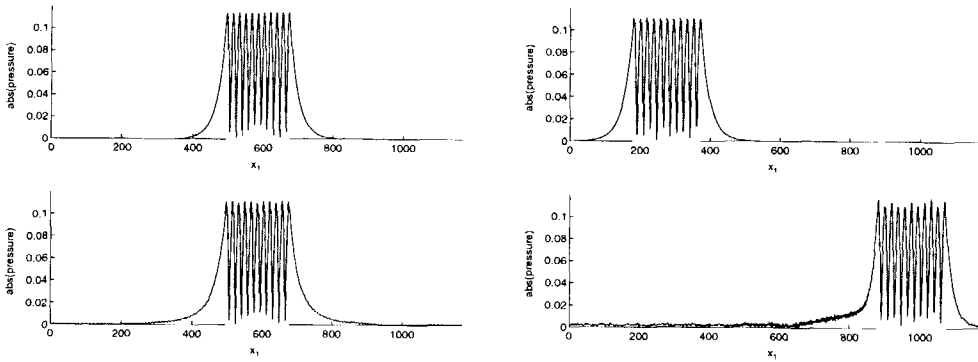
Figure 5.22:   *The tenth-order waveguide mode at the entrance plane (upper fig-
ure) and at the exit plane (bottom figure). The waveguide on the
left-hand side is not tilted with respect to the coordinate system,
while the waveguide on the right-hand side is tiltedwith an angle of
20 degrees with respect to the coordinate system. (Leading term of
the Bremmer coupling series only).*
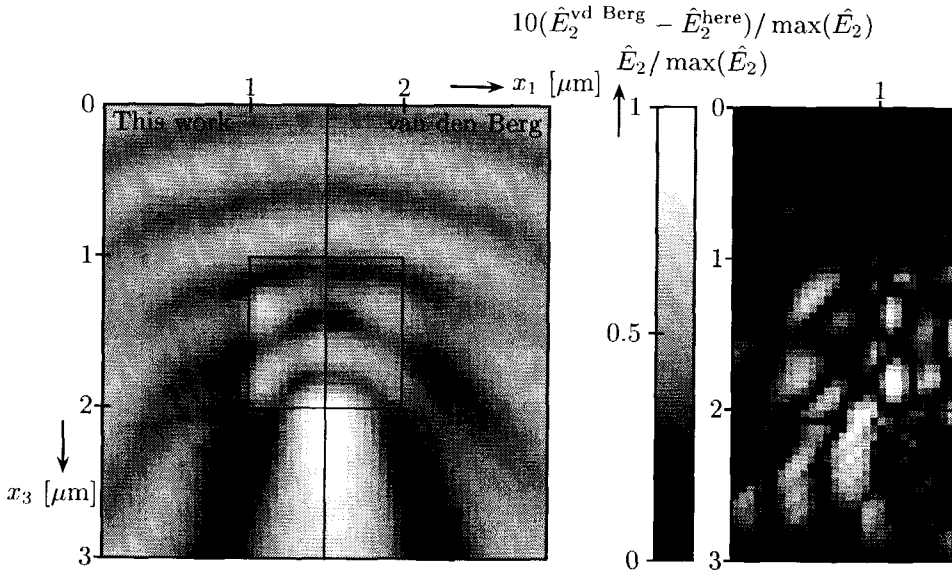
Figure 5.23:   *Plane wave (from the top) response in a configuration with a block
in a homogeneous embedding. The left half of the figure is the
Bremmer series solution, the right half is the full solution obtained
by an iterative integral-equation technique based upon minimizing
an integrated square error criterion (see van den Berg[189]). The
differences are indicated in the right figure.*
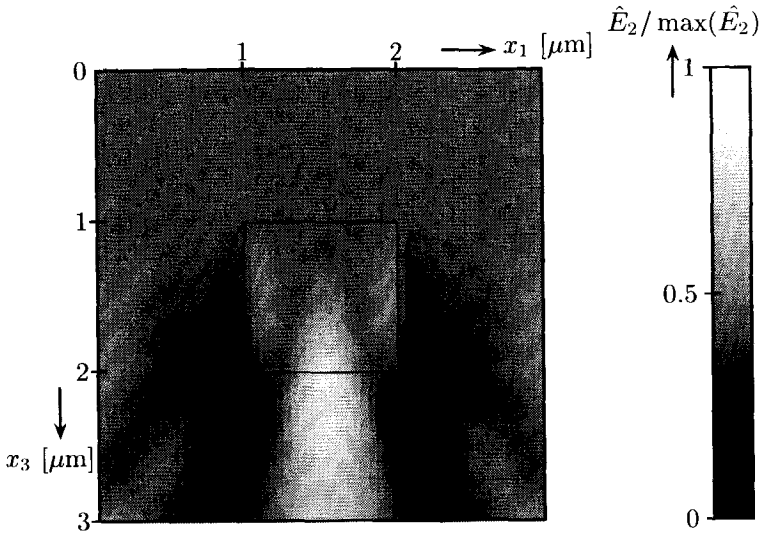
Figure 5.24: Plane wave (from the top) response in a configuration with a block in a homogeneous embedding. Leading term of the Bremmer coupling series.
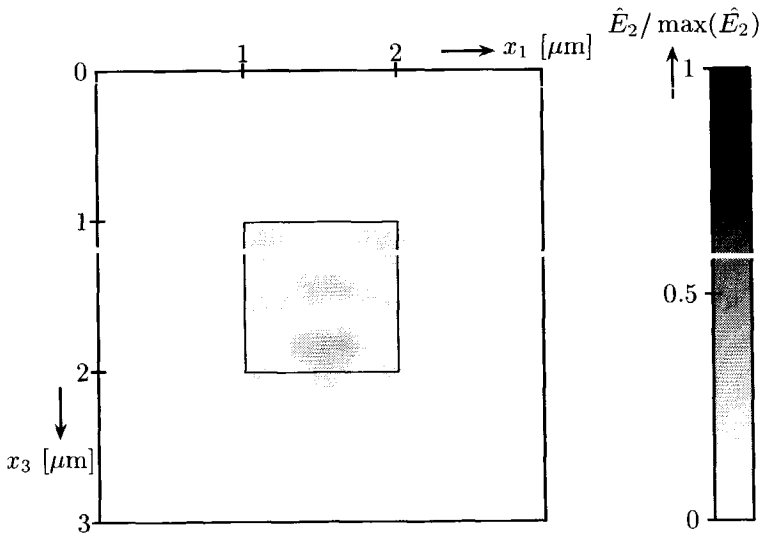
Figure 5.25: Plane wave (from the top) response in a configuration with a block in a homogeneous embedding. Second term of the Bremmer coupling series.
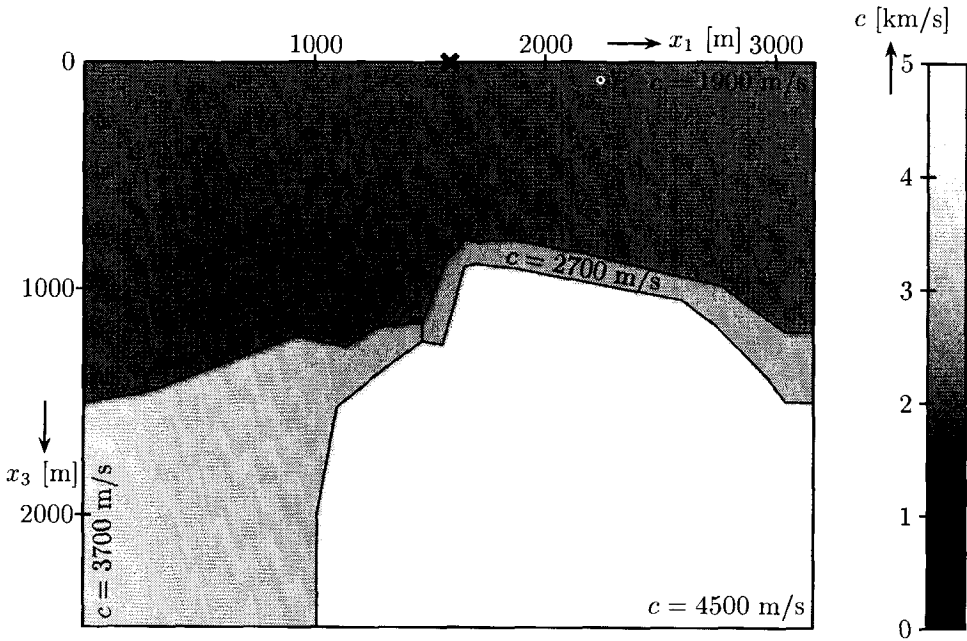
Figure 5.26: *Wave speeds of a two-dimensional salt model (see also Figure 1.2).*

medium ($n = 1$) with a square block (sized 1.05 μm by 1.05 μm) with a significantly larger refractive index ($n = 2$). The wavelength is 1 μm[a]. The numerical grid contains 99 points along the x_1 direction and 60 points along the x_3 direction. We plot only 59 points along the x_1 direction. The discretization step is 0.05 μm in both directions (14.8 grid points per wavelength inside the heterogeneity). Full, accurate, numerical responses have been presented by Martin et al.[122]. Our results, shown in Figure 5.23, are very similar to theirs. The left half of the figure is the Bremmer series solution, the right half is the full solution obtained by an iterative integral-equation technique based upon minimizing an integrated square error criterion (see van den Berg[189]). Figure 5.25 corresponds to the second term of the Bremmer coupling series, while Figure 5.24 shows the field corresponding to the leading term of the Bremmer coupling series. The higher-order terms in the Bremmer series become rapidly smaller. For the calculations, we used parameter set 4; in the reflection operator, we set $\Omega = 0.02$.
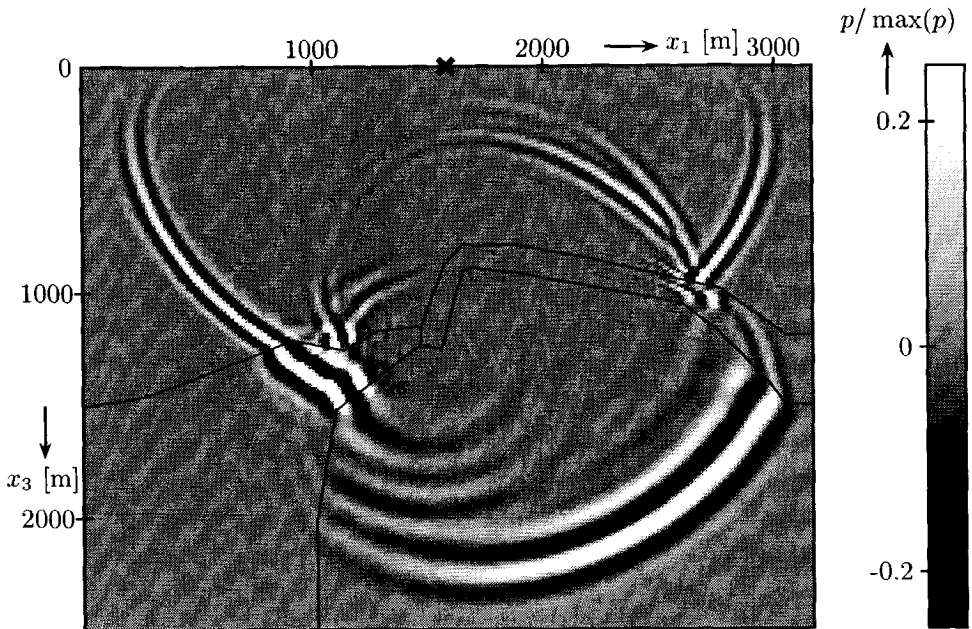
Figure 5.27: *Snapshot at t = 0.750 s of the acoustic pressure due to a vertical line force in the model of Figure 5.26. Six terms of the Bremmer coupling series.*

5.8.3 Geological dome

As a third example, we consider the salt model shown in Figure 5.26, see de Hoop[49]. This model contains three sedimentary layers. The wave speed is constant in the upper and bottom layers, while the wave speed varies linearly with x_1 (while constant in the x_2 direction) in the left part of the middle layer. An approximate, transient longitudinal line force is applied at $x_1 = 1600$ m, $x_3 = 0$ m. Figures 5.27-5.29 show snapshots at 0.75 s. For the calculations we used parameter set 4. The numerical grid contains 199 points in the x_1 direction and 156 points in the x_3 direction. The discretization step is 16 m in both directions. We used parameter set 4. In Figure 5.27, we calculated the first six terms of the Bremmer coupling series. The computation time was 50780 s on a Hewlett Packard 9000/735 workstation. Figures 5.28 and 5.29 show snapshots of the leading term (890 s CPU) and the second term of the series. We computed 512 frequencies in total.

This example illustrates that our approximate scheme models the transmitted and reflected body waves accurately up to large scattering angles. Also the line diffraction at the major kink of the second deepest interface is captured by the method. Some head-wave energy is mimiced by the artifacts of our approximations,

---

[a]The acoustic equivalent configuration has the media $c = 1900$ m/s and $c \simeq 1344$ m/s, sizes of 105 m by 105 m, frequency 19 Hz and a 5 m discretization step.
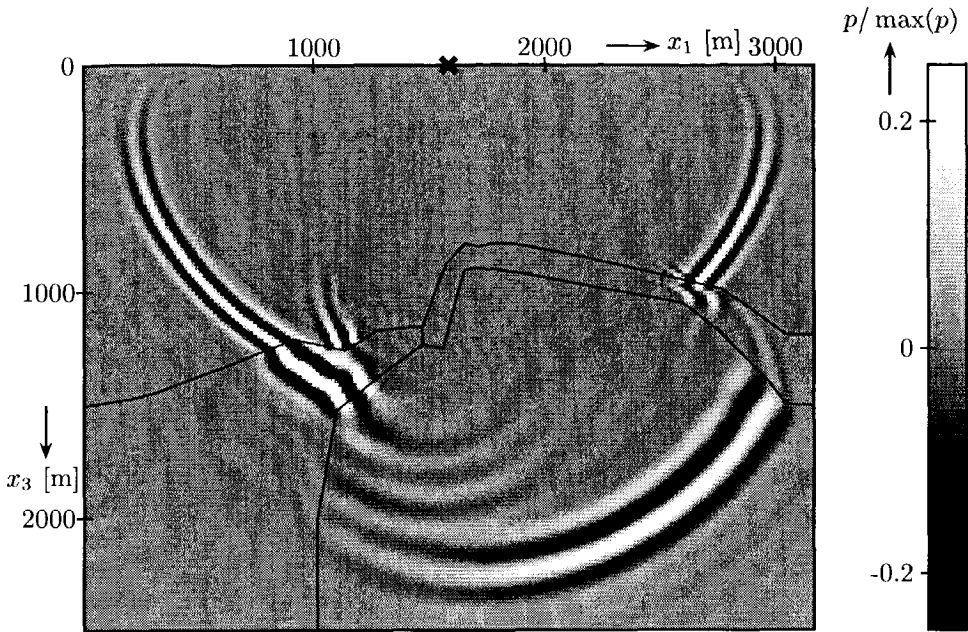
Figure 5.28: *Idem as for Figure 5.26. Leading term of the Bremmer coupling series.*
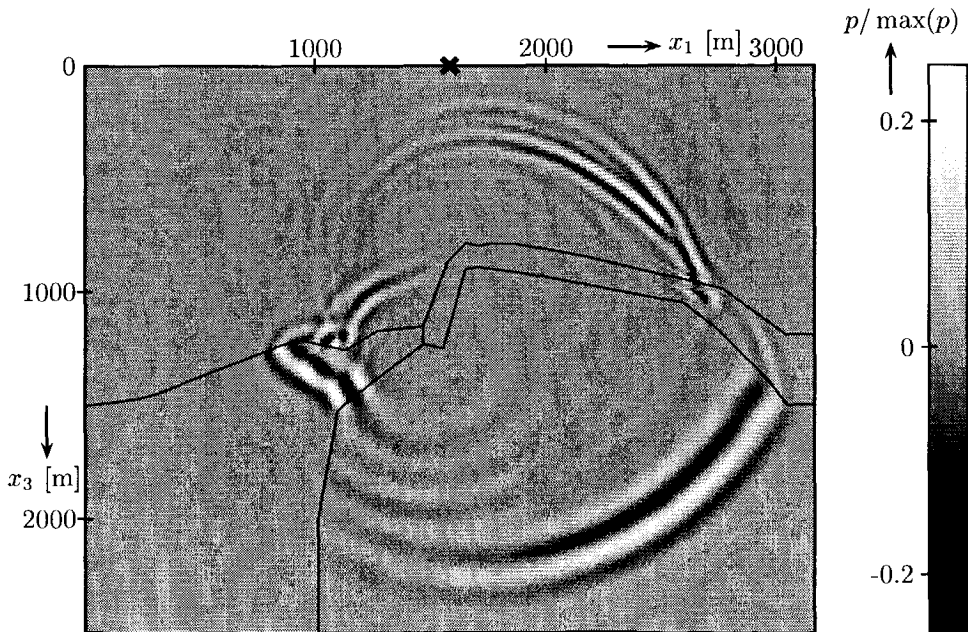
Figure 5.29: *Idem as for Figure 5.26. Second term of the Bremmer coupling series.*

but is inaccurate.

5.9   Discussion of the results

We have developed a fast numerical implementation of the Bremmer coupling series in two dimensions, for scattering angles up to critical. The key ingredient was a rational approximation of the longitudinal slowness in terms of the transverse slowness. Our scheme has added to the various existing one-way wave propagation and BPM schemes in the following ways: we considered the third-order Thiele approximation rather than the first- or second-order one, to enhance the accuracy and to remove artificial body waves around the longitudinal direction, we enhanced the accuracy by optimizing the phase and group slowness surfaces for any desired sampling rates; we have improved the transformation to a moving frame of reference; we introduced (de)composition operators to incorporate any desired source- or receiver-type with the appropriate radiation characteristics; we have taken care of the backscattered field with the aid of the Bremmer coupling series.

We have illustrated the generalized Bremmer series with rational approximation with various examples. The examples have been taken from the different fields of application of the method. With a view to exploration geophysics, the waveguide can be associated with a coal bed. In migration, the Bremmer series approach is particularly useful if multiple arrivals play a role in creating a proper image.

When critical angle phenomena (post-critical waves) are important, a more precise symbol for the longitudinal slowness operator has to be used. A candidate is the uniform expansion developed by Fishman, Gautesen and Sun[51]. Then the thin slab propagator is directly evaluated using Fourier transforms. The Lanczos algorithm, as described in Section 1.5, is another candidate.

A fast construction of the relevant matrices is not straight-forward. A special procedure has been written to compute the permittivity for many practical configurations, which can be input in a "user-friendly" way (see Appendix 5.A). At the time of publication, the numerical code has already been used by researchers as a design tool in integrated optics and as a migration tool in exploration seismics.

Appendix

5.A   FORTRAN code for constructing the involved matrices

The FORTRAN code for setting up the matrices in the propagation scheme, consists of two subroutines. In one subroutine, the following global constants are calculated, once for every frequency,

```
rt     = (1D0,0D0)/(omega*(1D0+(0D0,1D0)*omegIm)*DeltaX)**2
const = (0D0,1D0)*omega*DeltaX3*beta9
const1 = -2*beta2*rt*rt*const
const2 = beta1*rt*(1-4*a2)*const
const3 = (1-2*a2)*a2
const4 = -2*a2*beta3*rt
const5 = beta3*rt*(1-2*a2)
const6 = beta2*rt*rt*const
const7 = beta1*rt*(6*a2-2)*const
const8 = a2*a2
const9 = (1-2*a2)**2
const10 = beta3*rt*a2
const11 = -beta3*rt*2*(1-2*a2)
const12 = beta1*rt*a2*const
```

where `omegIm` $= \Omega$. In the second subroutine, the matrix elements of A and A' are evaluated. In this subroutine, we set

```
cp = c(i+1)
cc = c(i)
cm = c(i-1)
dp = 1D0/cp
dd = 1D0/cc
dm = 1D0/cm
gp = cp*cp
gg = cc*cc
gm = cm*cm
```

The function `c(i)` returns the value of c at position $x_1 = i\Delta x_1$. Since most configurations will contain large homogeneous regions, the above variables have not to be recalculated at every position.

The evaluation of the elements of matrices A and A' are very similar. We show the set up and storage of matrix A,

$$A(3,i+2) \quad = \quad A_{i,i+2} \, , \tag{5A.1}$$
$$A(4,i+1) \quad = \quad A_{i,i+1} \, , \tag{5A.2}$$
$$A(5,i) \quad = \quad A_{i,i} \, , \tag{5A.3}$$
$$A(6,i-1) \quad = \quad A_{i,i-1} \, , \tag{5A.4}$$
$$A(7,i-2) \quad = \quad A_{i,i-2} \, . \tag{5A.5}$$

The matrix elements follow as

```
    A(3,i+2) = const12+const6*gp+const8*dp+const10*cp
    A(4,i+1) = const1*(gg+gp)+const2+const3*(dd+dp)+const4*cc
&              +const5*cp
    A(5,i)   = const6*(4*gg+gm+gp)+const7+const8*dm+const9*dd
&              +const8*dp+const10*cm+const11*cc+const10*cp
    A(6,i-1) = const1*(gg+gm)+const2+const3*(dd+dm)+const4*cc
&              +const5*cm
    A(7,i-2) = const12+const6*gm+const8*dm+const10*cm
```

The matrix C is stored in a similar manner,

$$K(2,i+1) \quad = \quad C_{i,i+1} \, , \tag{5A.6}$$
$$K(3,i) \quad = \quad C_{i,i} \, , \tag{5A.7}$$
$$K(4,i-1) \quad = \quad C_{i,i-1} \, , \tag{5A.8}$$

and its elements follow as

```
    K(4,i-1) = a2*e(i)/sqrt(cc)
    K(3,i  ) = e(i)/sqrt(cc)*(1-2*a2)
    K(2.i+1) = a2*e(i)/sqrt(cc)
```

where the function $e(i)$ returns the value

```
    e = CDEXP((0D0,1D0)*DeltaX3/c(i)*Omega)
```

A special subroutine has been developed to compute the permittivity after equivalent medium averaging for many practical configurations. These configurations must be described by interfaces of which straight lines are their segments. In one-way wave propagation, the matrices at the next transverse plane are constructed from the previous matrices by adjusting only the elements where the medium changes.

CHAPTER 6

Directional Wave-Field Decomposition in a Three-dimensional, Anisotropic Dielectric Configuration

In Chapters 2 and 3, the longitudinal scattering problem was introduced in a one- and two-dimensional configuration. This chapter extends the theory to arbitrary polarized electromagnetic waves in a three-dimensional anisotropic dielectric configuration. With a simple reduction, the equivalent equations for acoustic waves in anisotropic fluids can be found. The chapter concentrates on the differences between Chapter 3 and this chapter. Special attention is paid to the different normalizations of the involved equations and, in connection to that, creating a stable forward numerical scheme.

This chapter is organized as follows. Section 6.1 describes the configuration under investigation. We distinguish two types of anisotropy: anisotropy with forward/backward symmetry, and general anisotropy. To increase the accuracy of discretizating rapidly varying media, we apply the equivalent medium theory. Then, an isotropic dielectric becomes an uniaxial anisotropic dielectric in the regions where the medium varies. Following Chapters 2 and 3, we rewrite the Maxwell equations into a differential equation for the field matrix (Section 6.2). Application of the directional wave-field decomposition introduces the wave matrix. We analyze both media with forward/backward symmetry (Section 6.3) as well as more general media

(Section 6.4). Special attention is paid to the different normalization analogs and symmetry properties of the involved operators. Section 6.5 briefly reports on 3-D aspects in deriving the Bremmer coupling series. Section 6.6 discusses the numerical aspects of the Bremmer coupling series. Special attention is addressed to the stability of the one-way wave equation and the symmetry relation of the matrices and operators. Finally, the results are discussed in Section 6.7.

This chapter contains one appendix. In Appendix 6.A, the notation is elucidated, some useful inner products are introduced and the symmetry properties of operators are discussed.

6.1   Description of the configuration

The configuration under investigation has already been described in Section 1.3. In Subsection 6.1, a distinction between two types of anisotropic dielectrics is made. The equivalent medium theory is employed to describe the medium on a numerical grid (Subsection 6.1): it turns out that a heterogeneous isotropic dielectric becomes a heterogeneous uniaxial dielectric after smoothing.

Anisotropic dielectrics

In this chapter, we distinguish two types of anisotropic dielectrics

① **restricted anisotropy** with the permittivity $(\varepsilon_{1,3} = \varepsilon_{2,3} = 0)$

$$\varepsilon = \begin{pmatrix} \varepsilon_{1,1} & \varepsilon_{1,2} & 0 \\ \varepsilon_{1,2} & \varepsilon_{2,2} & 0 \\ 0 & 0 & \varepsilon_{3,3} \end{pmatrix}, \tag{6.1}$$

and

② **general anisotropy** with the permittivity $(\varepsilon_{1,3}, \varepsilon_{2,3} \neq 0)$

$$\varepsilon = \begin{pmatrix} \varepsilon_{1,1} & \varepsilon_{1,2} & \varepsilon_{1,3} \\ \varepsilon_{1,2} & \varepsilon_{2,2} & \varepsilon_{2,3} \\ \varepsilon_{1,3} & \varepsilon_{2,3} & \varepsilon_{3,3} \end{pmatrix}. \tag{6.2}$$

Remember that the permeability tensor in a dielectric is constant and scalar

$$\mu_{j,p}(x_k) = \mu_0 \delta_{j,p}. \tag{6.3}$$

In the first class of anisotropic dielectrics, symmetry in forward and backward propagation occurs. In exploration seismics the name *up/down symmetry* is used (see e.g. de Hoop and de Hoop[190]). In integrated optics (see Vassallo[144]), the waveguide is said to be bidirectional: a field propagating in the forward direction can be transformed into a symmetrical field propagating reverse. Following Vassallo, we used the term **bidirectional anisotropy** for this class of anisotropy.
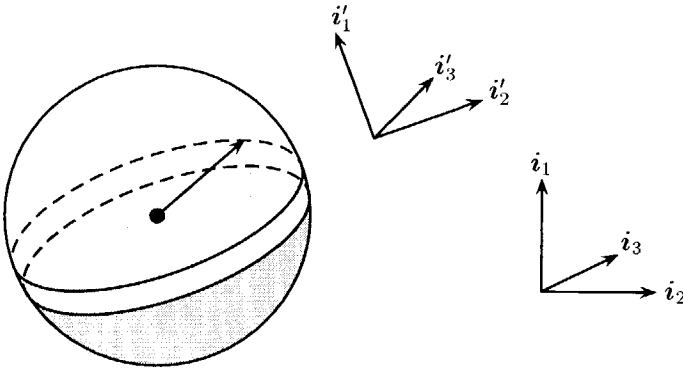
Figure 6.1: *Interface between two media in the neighborhood of a point in a local reference frame $\{i'_1, i'_2, i'_3\}$. The sphere represents the computational cell.*

Equivalent medium smoothing

In certain regions of the configuration, the medium properties may vary rapidly. We take these variations numerically into account by smoothing the medium. To ensure that the medium is numerically smooth, we employ the equivalent medium smoothing[175, 176] by averaging at any point over a computational cell, which is represented by a sphere in Figure 6.1. Thus, the local permittivity is replaced by a smoothed permittivity. Here, we present a short summary of this theory.

Consider a local Cartesian reference frame with three mutually perpendicular base vectors of unit length each, $\{i'_1, i'_2, i'_3\}$, which is obtained by rotating the original reference frame, see Figure 6.1. The permittivity is averaged over the computational cell. The electric flux density in the frequency domain, $\hat{D}_k$, equals (compare with Equation (1.18))

$$\hat{D}_k = \varepsilon_{k,r} \hat{E}_r. \tag{6.4}$$

At an interface between two media in the $x'_2 x'_3$ plane (see Figure 6.1), the components $\hat{D}_1, \hat{E}_2, \hat{E}_3$ are continuous, while $\hat{E}_1, \hat{D}_2, \hat{D}_3$ are discontinuous across the interface. Let us first consider isotropic dielectrics, then (compare with Equation (1.21))

$$\hat{D}_k = \varepsilon \hat{E}_k. \tag{6.5}$$

The relation between the discontinuous components $\hat{E}_1, \hat{D}_2, \hat{D}_3$ and the continuous components $\hat{D}_1, \hat{E}_2, \hat{E}_3$ follows as

$$\hat{E}_1 = \varepsilon^{-1} \hat{D}_1, \tag{6.6}$$

$$\hat{D}_2 = \varepsilon \hat{E}_2, \tag{6.7}$$

$$\hat{D}_3 = \varepsilon \hat{E}_3. \tag{6.8}$$

Averaging over a numerical cell with size Δx (notation: $\langle . \rangle$) and assuming that $\hat{D}_1, \hat{E}_2, \hat{E}_3$ are locally constant yields

$$\hat{D}_1 = \langle \varepsilon^{-1} \rangle^{-1} \hat{E}_1, \tag{6.9}$$

$$\hat{D}_2 = \langle \varepsilon \rangle \hat{E}_2, \tag{6.10}$$

$$\hat{D}_3 = \langle \varepsilon \rangle \hat{E}_3. \tag{6.11}$$

The validity of this assumption can be checked afterwards. Equations (6.9)-(6.11) show that an isotropic medium behaves after spatially averaging as a uniaxial anisotropic medium with the ordinary and extraordinary permittivities given by (see Equation (1.39))

$$\varepsilon^{(o)} = \langle \varepsilon \rangle, \tag{6.12}$$

$$\varepsilon^{(e)} = \langle \varepsilon^{-1} \rangle^{-1}. \tag{6.13}$$

Rotating back to the original reference frame, the permittivity is given as in (1.39) or, in case of bidirectional anisotropy, as in (1.42).

After a similar analysis for any arbitrary symmetric permittivity tensor $\varepsilon_{k,r}$, we find after averaging the substitution

$$\varepsilon_{1,1} \to \langle \varepsilon_{1,1}^{-1} \rangle^{-1}, \tag{6.14}$$

$$\varepsilon_{1,2} \to \langle \varepsilon_{1,1}^{-1} \rangle^{-1} \langle \frac{\varepsilon_{1,2}}{\varepsilon_{1,1}} \rangle, \tag{6.15}$$

$$\varepsilon_{1,3} \to \langle \varepsilon_{1,1}^{-1} \rangle^{-1} \langle \frac{\varepsilon_{1,3}}{\varepsilon_{1,1}} \rangle, \tag{6.16}$$

$$\varepsilon_{2,2} \to \langle \varepsilon_{1,1}^{-1} \rangle^{-1} \langle \frac{\varepsilon_{1,2}}{\varepsilon_{1,1}} \rangle^2 \quad + \langle \varepsilon_{2,2} - \frac{\varepsilon_{1,2}^2}{\varepsilon_{1,1}} \rangle, \tag{6.17}$$

$$\varepsilon_{2,3} \to \langle \varepsilon_{1,1}^{-1} \rangle^{-1} \langle \frac{\varepsilon_{1,2}}{\varepsilon_{1,1}} \rangle \langle \frac{\varepsilon_{1,3}}{\varepsilon_{1,1}} \rangle + \langle \varepsilon_{2,3} - \frac{\varepsilon_{1,3}\varepsilon_{2,3}}{\varepsilon_{1,1}} \rangle. \tag{6.18}$$

$$\varepsilon_{3,3} \to \langle \varepsilon_{1,1}^{-1} \rangle^{-1} \langle \frac{\varepsilon_{1,3}}{\varepsilon_{1,1}} \rangle^2 \quad + \langle \varepsilon_{3,3} - \frac{\varepsilon_{1,3}^2}{\varepsilon_{1,1}} \rangle. \tag{6.19}$$

The permittivity after averaging describes biaxial anisotropy. With the use of an eigenvalue analysis the permittivity can be transformed to its principal axis, with the elements: $\varepsilon^{(1)}$, $\varepsilon^{(2)}$ and $\varepsilon^{(3)}$. The permittivity diagonal can also be rotated back to the original reference frame $\{i_1, i_2, i_3\}$.

6.2   Differential equation for the field matrix

Below, Maxwell's equations are rewritten into a form suitable for the directional wave-field decomposition. We will discuss a hierarchy of increasing symmetry: the

generic case, anisotropic dielectrics, isotropic dielectrics and the semi-vectorial approximation. In the sequel of this chapter, we will constrain ourselves to anisotropic dielectrics.

6.2.1 Generic case

Directional wave-field decomposition requires a separate handling of the transverse components of the electromagnetic field $\{\hat{E}_r, \hat{H}_p\}$. Using Maxwell's equations in space-frequency domain, (1.30) and (1.31), the longitudinal components can be expressed in terms of the transverse ones:

$$\hat{H}_3 = \frac{\partial_2 \hat{E}_1 - \partial_1 \hat{E}_2}{j\omega\mu_{3,3}} - \frac{\mu_{3,1}}{\mu_{3,3}}\hat{H}_1 - \frac{\mu_{3,2}}{\mu_{3,3}}\hat{H}_2 - \frac{\hat{K}_3^e}{j\omega\mu_{3,3}}, \tag{6.20}$$

$$\hat{E}_3 = \frac{\partial_1 \hat{H}_2 - \partial_2 \hat{H}_1}{j\omega\varepsilon_{3,3}} - \frac{\varepsilon_{3,1}}{\varepsilon_{3,3}}\hat{E}_1 - \frac{\varepsilon_{3,2}}{\varepsilon_{3,3}}\hat{E}_2 - \frac{\hat{J}_3^e}{j\omega\varepsilon_{3,3}}, \tag{6.21}$$

leaving, upon substitution, the matrix differential equation — known as the two-way wave equation —

$$(\partial_3 \delta_{I,J} + j\omega \hat{A}_{I,J})\hat{F}_J = \hat{N}_I, \tag{6.22}$$

or, in tensor-product notation

$$\partial_3 \begin{pmatrix} \hat{F}_1 \\ \hat{F}_2 \end{pmatrix} + j\omega \begin{pmatrix} \hat{A}_{1,1} & \hat{A}_{1,2} \\ \hat{A}_{2,1} & \hat{A}_{2,2} \end{pmatrix} \begin{pmatrix} \hat{F}_1 \\ \hat{F}_2 \end{pmatrix} = \begin{pmatrix} \hat{N}_1 \\ \hat{N}_2 \end{pmatrix}. \tag{6.23}$$

The elements of $\hat{F}_J$ are chosen such that $\hat{F}_1^{\mathrm{T}} \hat{F}_2^*$ represents the longitudinal component $\hat{S}_3$ of the complex Poynting vector. A valid choice is

$$\hat{F}_1 = \begin{pmatrix} \hat{E}_1 \\ \hat{E}_2 \end{pmatrix}, \qquad \hat{F}_2 = \begin{pmatrix} \hat{H}_2 \\ -\hat{H}_1 \end{pmatrix}. \tag{6.24}$$

The electromagnetic system matrix operator $\hat{A}_{I,J}$ reveals a 2 by 2 block structure. Its entries are found to be operators

$$\hat{A}_{1,1} = (j\omega)^{-1} \begin{pmatrix} \partial_1 \varepsilon_{3,3}^{-1}\varepsilon_{1,3} + \mu_{3,3}^{-1}\mu_{2,3}\partial_2 & \partial_1 \varepsilon_{3,3}^{-1}\varepsilon_{2,3} - \mu_{3,3}^{-1}\mu_{2,3}\partial_1 \\ \partial_2 \varepsilon_{3,3}^{-1}\varepsilon_{1,3} - \mu_{3,3}^{-1}\mu_{1,3}\partial_2 & \partial_2 \varepsilon_{3,3}^{-1}\varepsilon_{2,3} + \mu_{3,3}^{-1}\mu_{1,3}\partial_1 \end{pmatrix}, \tag{6.25}$$

$$\hat{A}_{1,2} = \begin{pmatrix} \omega^{-2}\partial_1 \varepsilon_{3,3}^{-1}\partial_1 + \mu_{2,2}' & \omega^{-2}\partial_1 \varepsilon_{3,3}^{-1}\partial_2 - \mu_{2,1}' \\ \omega^{-2}\partial_2 \varepsilon_{3,3}^{-1}\partial_1 - \mu_{1,2}' & \omega^{-2}\partial_2 \varepsilon_{3,3}^{-1}\partial_2 + \mu_{1,1}' \end{pmatrix}, \tag{6.26}$$

$$\hat{A}_{2,1} = \begin{pmatrix} \omega^{-2}\partial_2 \mu_{3,3}^{-1}\partial_2 + \varepsilon_{1,1}' & -\omega^{-2}\partial_2 \mu_{3,3}^{-1}\partial_1 + \varepsilon_{1,2}' \\ -\omega^{-2}\partial_1 \mu_{3,3}^{-1}\partial_2 + \varepsilon_{2,1}' & \omega^{-2}\partial_1 \mu_{3,3}^{-1}\partial_1 + \varepsilon_{2,2}' \end{pmatrix}, \tag{6.27}$$

$$\hat{A}_{2,2} = (j\omega)^{-1} \begin{pmatrix} \varepsilon_{3,3}^{-1}\varepsilon_{1,3}\partial_1 + \partial_2 \mu_{3,3}^{-1}\mu_{2,3} & \varepsilon_{3,3}^{-1}\varepsilon_{1,3}\partial_2 - \partial_2 \mu_{3,3}^{-1}\mu_{1,3} \\ \varepsilon_{3,3}^{-1}\varepsilon_{2,3}\partial_1 - \partial_1 \mu_{3,3}^{-1}\mu_{2,3} & \varepsilon_{3,3}^{-1}\varepsilon_{2,3}\partial_2 + \partial_1 \mu_{3,3}^{-1}\mu_{1,3} \end{pmatrix}. \tag{6.28}$$

Here,

$$\varepsilon'_{\nu,\rho} = \varepsilon_{\nu,\rho} - \varepsilon_{3,3}^{-1}\varepsilon_{\nu,3}\varepsilon_{3,\rho}, \tag{6.29}$$

is the reduced 2 by 2 permittivity matrix, whereas

$$\mu'_{\nu,\rho} = \mu_{\nu,\rho} - \mu_{3,3}^{-1}\mu_{\nu,3}\mu_{3,\rho}. \tag{6.30}$$

is the reduced 2 by 2 permeability matrix. The elements of the source matrix are found as

$$\hat{N}_1 = \begin{pmatrix} -\hat{K}_2^{e} - \partial_1(j\omega\varepsilon_{3,3})^{-1}\hat{J}_3^{e} + \mu_{3,3}^{-1}\mu_{2,3}\hat{K}_3^{e} \\ \hat{K}_1^{e} - \partial_2(j\omega\varepsilon_{3,3}^{-1})^{-1}\hat{J}_3^{e} - \mu_{3,3}^{-1}\mu_{1,3}\hat{K}_3^{e} \end{pmatrix}, \tag{6.31}$$

$$\hat{N}_2 = \begin{pmatrix} -\hat{J}_1^{e} - \partial_2(j\omega\mu_{3,3})^{-1}\hat{K}_3^{e} + \varepsilon_{3,3}^{-1}\varepsilon_{1,3}\hat{J}_3^{e} \\ -\hat{J}_2^{e} + \partial_1(j\omega\mu_{3,3})^{-1}\hat{K}_3^{e} + \varepsilon_{3,3}^{-1}\varepsilon_{2,3}\hat{J}_3^{e} \end{pmatrix}. \tag{6.32}$$

Operator and symbol analysis

Assuming that the medium be reciprocal, the permeability and the permittivity tensors are *symmetric*. (One-way wave propagation in nonreciprocal magnetooptic waveguides is discussed by e.g. Shamonin[191] or Tsuji and Koshiba[192]). Then, with respect to the real L_2 inner product defined on the transverse (electric and magnetic) field components (see also Equation (6A.3)), $\hat{A}_{1,2}$ and $\hat{A}_{2,1}$ are symmetric, while $\hat{A}_{2,2} = -\hat{A}_{1,1}^{T}$. In absence of any loss mechanisms these operators are also Hermitean with respect to the complex L_2 inner product.

6.2.2   Anisotropic dielectrics

Now, we discuss the reduction of the above equations for anisotropic dielectrics.

In a dielectric, the permeability tensor is isotropic and constant, i.e.

$$\mu_{i,p}(x_m) = \mu_0\delta_{i,p}. \tag{6.33}$$

As a consequence of this constraint, we have $\mu_{\nu,3} = 0$ $(\nu = 1, 2)$ and

$$\mu' = \mu_0. \tag{6.34}$$

Hence, we can rewrite elements of the electromagnetic system matrix operator $\hat{A}$ as

$$\hat{A}_{1,1} = \quad (j\omega)^{-1} \begin{pmatrix} \partial_1 \\ \partial_2 \end{pmatrix} \varepsilon_{3,3}^{-1} \begin{pmatrix} \varepsilon_{1,3} & \varepsilon_{2,3} \end{pmatrix}, \tag{6.35}$$

$$\hat{A}_{1,2} = \mu_0 + \omega^{-2} \begin{pmatrix} \partial_1 \\ \partial_2 \end{pmatrix} \varepsilon_{3,3}^{-1} \begin{pmatrix} \partial_1 & \partial_2 \end{pmatrix}, \tag{6.36}$$

$$\hat{A}_{2,1} = \varepsilon' + \omega^{-2} \begin{pmatrix} \partial_2 \\ -\partial_1 \end{pmatrix} \mu_0^{-1} \begin{pmatrix} \partial_2 & -\partial_1 \end{pmatrix}, \tag{6.37}$$

$$\hat{A}_{2,2} = \quad (j\omega)^{-1} \begin{pmatrix} \varepsilon_{1,3} \\ \varepsilon_{2,3} \end{pmatrix} \varepsilon_{3,3}^{-1} \begin{pmatrix} \partial_1 & \partial_2 \end{pmatrix}. \tag{6.38}$$

Note that $\hat{A}_{1,2}$ and $\hat{A}_{2,1}$ are symmetric, i.e. (see Subappendix 6.A.2 for the definition of symmetry)

$$\hat{A}_{1,2}^{\mathrm{T}} = \hat{A}_{1,2}, \qquad \hat{A}_{2,1}^{\mathrm{T}} = \hat{A}_{2,1}. \tag{6.39}$$

If no losses occur, ε is real valued and

$$\hat{A}_{1,2}^{\mathrm{H}} = \hat{A}_{1,2}, \qquad \hat{A}_{2,1}^{\mathrm{H}} = \hat{A}_{2,1}, \tag{6.40}$$

while $\hat{A}_{2,2} = -\hat{A}_{1,1}^{\mathrm{T}}$.

Reduction for bidirectional anisotropy

Bidirectional anisotropy imposes the additional constraint of *forward/backward symmetry*[190]. Then

$$\varepsilon_{1,3} = \varepsilon_{2,3} = 0, \tag{6.41}$$

and as a consequence of this

$$\varepsilon'_{\nu,\rho} = \varepsilon_{\nu,\rho}, \tag{6.42}$$

while now

$$\hat{A}_{1,1} = 0, \qquad \text{and} \qquad \hat{A}_{2,2} = 0. \tag{6.43}$$

The system matrix operator $\hat{A}$ becomes block off-diagonal.

6.2.3   Isotropic dielectrics

Now, we discuss the reduction of the above equations to isotropic dielectrics.

In isotropic materials the permittivity tensor is reduced to a scalar

$$\varepsilon_{i,j} = \varepsilon \delta_{i,j}. \tag{6.44}$$

The isotropic system matrix operator has two nonzero symmetrical elements

$$\hat{A}_{1,2} = \mu_0 + \omega^{-2} \begin{pmatrix} \partial_1 \\ \partial_2 \end{pmatrix} \varepsilon^{-1} \begin{pmatrix} \partial_1 & \partial_2 \end{pmatrix}, \tag{6.45}$$

$$\hat{A}_{2,1} = \varepsilon \quad + \omega^{-2}\mu_0^{-1} \begin{pmatrix} \partial_2 \\ -\partial_1 \end{pmatrix} \begin{pmatrix} \partial_2 & -\partial_1 \end{pmatrix}. \tag{6.46}$$

6.2.4   Semi-vectorial approximation

In an isotropic dielectric, when one polarization component dominates the wave phenomena, the system matrix operator can be approximated in the following fashion. Distinguishing two different possible dominant polarizations (see Stern[193]), i.e., quasi-TE (with $\hat{E}_1 \equiv 0$) and quasi-TM (with $\hat{H}_1 \equiv 0$) leads to the following two reductions.

For quasi-TE scattering, we reduce the representation of $\hat{F}_1$ to $\hat{E}_2$ and in accordance with this reduction, we remove the first row of $\hat{A}_{1,2}$ as well as the first column of $\hat{A}_{2,1}$:

$$\hat{A}_{1,2} \stackrel{\mathrm{TE}}{=} \begin{pmatrix} \omega^{-2}\partial_2\varepsilon^{-1}\partial_1 & \mu_0 + \omega^{-2}\partial_2\varepsilon^{-1}\partial_2 \end{pmatrix}, \tag{6.47}$$

$$\hat{A}_{2,1} \stackrel{\mathrm{TE}}{=} \begin{pmatrix} -\mu_0^{-1}\omega^{-2}\partial_1\partial_2 \\ \varepsilon + \mu_0^{-1}\omega^{-2}\partial_1\partial_1 \end{pmatrix}. \tag{6.48}$$

For quasi-TM scattering, we reduce the representation of $\hat{F}_2$ to $\hat{H}_2$ and in accordance with this reduction, we remove the second column of $\hat{A}_{1,2}$ as well as the second row of $\hat{A}_{2,1}$:

$$\hat{A}_{1,2} \stackrel{\mathrm{TM}}{=} \begin{pmatrix} \mu_0 + \omega^{-2}\partial_1\varepsilon^{-1}\partial_1 \\ \omega^{-2}\partial_2\varepsilon^{-1}\partial_1 \end{pmatrix}, \tag{6.49}$$

$$\hat{A}_{2,1} = \begin{pmatrix} \varepsilon + \mu_0^{-1}\omega^{-2}\partial_2^2 & -\mu_0^{-1}\omega^{-2}\partial_1\partial_2 \end{pmatrix}. \tag{6.50}$$

These approximations are commonly referred to as the *semi-vectorial* approximations. In effect, they neglect the coupling to $\hat{E}_1$ (TE) or the coupling to $\hat{H}_1$ (TM).

6.3   Differential equation of the wave matrix: bidirectional anisotropy

In this section, the electromagnetic field in a bidirectionally anisotropic dielectric is decomposed into waves traveling forward and backward. First, we formulate the diagonalization procedure for the system matrix. Subsequently, we discuss two different normalizations: one based on the electric field and one based on the magnetic field. These normalizations can be transformed to one another. Finally, we analyze the properties of the associated transverse Helmholtz operator.

6.3.1 Diagonalization procedure

To distinguish forward- and backward-traveling constituents in the wave-field, we construct an appropriate operator $\hat{L}_{I,J}$ with

$$\hat{F}_I = \hat{L}_{I,J}\hat{W}_J, \tag{6.51}$$

that, with aid of the commutation relation,

$$(\partial_3 \hat{L}_{I,J}) = [\partial_3, \hat{L}_{I,J}], \tag{6.52}$$

([.,.] denotes the commutator), transforms Equation (6.22) into

$$\hat{L}_{I,J}\,(\partial_3 \delta_{J,M} + \mathrm{j}\omega\hat{A}_{J,M})\hat{W}_M = -(\partial_3 \hat{L}_{I,J})\,\hat{W}_J + \hat{N}_I, \tag{6.53}$$

so as to make $\hat{A}_{J,M}$, satisfying

$$\hat{A}_{I,J}\hat{L}_{J,M} = \hat{L}_{I,J}\hat{A}_{J,M}, \tag{6.54}$$

a diagonal matrix of matrix operators. We denote $\hat{L}_{I,J}$ as the *composition* operator and $\hat{W}_M$ as the wave matrix. The expression in parentheses on the left-hand side of Equation (6.53) represents the two *one-way* wave operators. The first term on the right-hand side of Equation (6.53) is representative of the scattering due to variations of the medium properties in the longitudinal direction. The scattering due to variations of the medium properties in the transverse directions is contained in $\hat{A}_{J,M}$ and, implicitly, in $\hat{L}_{I,J}$.

To investigate whether solutions to Equation (6.54) exist, we introduce the column matrix (generalized eigenvector) operators $\hat{L}_I^{(\pm)}$ according to

$$\hat{L}_I^{(+)} = \hat{L}_{I,1}, \qquad \hat{L}_I^{(-)} = \hat{L}_{I,2}. \tag{6.55}$$

Upon writing the (block-)diagonal entries (generalized eigenvalues) of $\hat{A}_{J,M}$ as

$$\hat{A}_{1,1} = \hat{\Gamma}^{(+)}, \qquad \hat{A}_{2,2} = \hat{\Gamma}^{(-)}, \tag{6.56}$$

Equation (6.54) decomposes into two systems of equations

$$\hat{A}_{I,J}\hat{L}_J^{(\pm)} = \hat{L}_I^{\pm}\hat{\Gamma}^{(\pm)}. \tag{6.57}$$

In analogy with the case where the medium is translationally invariant in the transverse directions, we denote $\hat{\Gamma}^{(\pm)}$ as the *longitudinal slowness* operators. Note that the operators $\hat{L}_1^{(\pm)}$ compose the electric field and that the operators $\hat{L}_2^{(\pm)}$ compose the magnetic field. Through mutual elimination, the equations for $\hat{L}_1^{(\pm)}$ and $\hat{L}_2^{(\pm)}$ can be decoupled as follows

$$\hat{A}_{1,2}\hat{A}_{2,1}\hat{L}_1^{(\pm)} = \hat{L}_1^{(\pm)}\hat{\Gamma}^{(\pm)}\hat{\Gamma}^{(\pm)}, \tag{6.58}$$

$$\hat{A}_{2,1}\hat{A}_{1,2}\hat{L}_2^{(\pm)} = \hat{L}_2^{(\pm)}\hat{\Gamma}^{(\pm)}\hat{\Gamma}^{(\pm)}. \tag{6.59}$$

The partial differential operators on the left-hand sides differ from each another.

To ensure that nontrivial solutions of Equations (6.58) and (6.59) exist, one equation must imply the other. To construct a formal solution, an Ansatz is introduced in the form of a commutation relation for one of the components $\hat{L}_J^\pm$ that restricts the freedom in the choice for the other component. We now consider two choices[49]: the electric-field strength normalization analog and the magnetic-field strength normalization analog.

6.3.2   Electric-field strength normalization analog

In the *electric-field strength normalization* analog (EFN) one assumes that $\hat{L}_2^{(\pm)}$ can be chosen such that[49]

$$\hat{A}_{2,1}\hat{A}_{1,2}\hat{L}_2^{(\pm)} = \hat{L}_2^{(\pm)}\hat{A}_{1,2}\hat{A}_{2,1}. \tag{6.60}$$

In view of Equation (6.59), the slowness operator in the EFN, $\hat{\Gamma}_{\text{EFN}}^{(\pm)}$, must then satisfy

$$\hat{A}_{1,2}\hat{A}_{2,1} - \hat{\Gamma}_{\text{EFN}}^{(\pm)}\hat{\Gamma}_{\text{EFN}}^{(\pm)} = 0. \tag{6.61}$$

The relation for $\hat{L}_1^{(\pm)}$ follows as

$$\hat{A}_{1,2}\hat{A}_{2,1}\hat{L}_1^{(\pm)} = \hat{L}_1^{(\pm)}\hat{A}_{1,2}\hat{A}_{2,1}, \tag{6.62}$$

and a possible solution to Equation (6.57) (and thus also a possible solution to Equation (6.54)) is

$$\hat{L}_1^{(\pm)} = 1, \qquad \hat{L}_2^{(\pm)} = \pm\hat{Y}. \tag{6.63}$$

Here, we introduce the *admittance* operator $\hat{Y}$ according to

$$\hat{Y} = \hat{A}_{1,2}^{-1}\hat{\Gamma}_{\text{EFN}}^{(+)}. \tag{6.64}$$

Since $\hat{L}_2^{(\pm)}$ as given by Equation (6.63) satisfies (6.60), the Ansatz is justified. The solutions of Equation (6.61) are written as

$$\hat{\Gamma}_{\text{EFN}}^{(+)} = -\hat{\Gamma}_{\text{EFN}}^{(-)} = \hat{\Gamma}_{\text{EFN}} = \hat{A}_{\text{EFN}}^{1/2}, \qquad \hat{A}_{\text{EFN}} = \hat{A}_{1,2}\hat{A}_{2,1}. \tag{6.65}$$

We denote operator $\hat{A}$ as the *transverse (vectorial) Helmholtz* operator. Operator $\hat{A} : H^r \to H^{r-2}$ is a partial differential operator of order 2, while $\hat{\Gamma} : H^r \to H^{r-1}$ is a pseudo-differential operator of order 1. Both operators are nonelliptic. The composition matrix operator becomes

$$\hat{L}_{\text{EFN}} = \begin{pmatrix} 1 & 1 \\ \hat{Y} & -\hat{Y} \end{pmatrix}. \tag{6.66}$$

Its inverse, the *decomposition* matrix operator, becomes

$$\hat{L}_{\text{EFN}}^{-1} = \tfrac{1}{2} \begin{pmatrix} 1 & \hat{Y}^{-1} \\ 1 & -\hat{Y}^{-1} \end{pmatrix}. \tag{6.67}$$

Thus the electric field is represented by

$$\hat{F}_1 = \hat{W}_{\text{EFN}}^{(+)} + \hat{W}_{\text{EFN}}^{(-)}, \tag{6.68}$$

while the magnetic field is represented by

$$\hat{F}_2 = \hat{Y} \left(\hat{W}_{\text{EFN}}^{(+)} - \hat{W}_{\text{EFN}}^{(-)} \right). \tag{6.69}$$

6.3.3   Magnetic-field strength normalization analog

In the *magnetic-field strength normalization* analog (MFN), one assumes that $\hat{L}_2^{(\pm)}$ can be chosen such that

$$\hat{A}_{2,1} \hat{A}_{1,2} \hat{L}_1^{(\pm)} = \hat{L}_1^{(\pm)} \hat{A}_{2,1} \hat{A}_{1,2}. \tag{6.70}$$

We find the longitudinal slowness operator and the transverse Helmholtz operator

$$\hat{\Gamma}_{\text{MFN}}^{(+)} = -\hat{\Gamma}_{\text{MFN}}^{(-)} = \hat{\Gamma}_{\text{MFN}} = \hat{A}_{\text{MFN}}^{1/2}, \qquad \hat{A}_{\text{MFN}} = \hat{A}_{2,1} \hat{A}_{1,2}, \tag{6.71}$$

The composition operator and decomposition operators follow as

$$\hat{L}_{\text{MFN}} = \begin{pmatrix} \hat{Z} & -\hat{Z} \\ 1 & 1 \end{pmatrix}, \qquad \hat{L}_{\text{MFN}}^{-1} = \tfrac{1}{2} \begin{pmatrix} \hat{Z}^{-1} & 1 \\ -\hat{Z}^{-1} & 1 \end{pmatrix}. \tag{6.72}$$

Here, $\hat{Z}$ is the *impedance*

$$\hat{Z} = \hat{A}_{2,1}^{-1} \hat{\Gamma}_{\text{MFN}}. \tag{6.73}$$

The electric field is found as

$$\hat{F}_1 = \hat{Z} \left(\hat{W}_{\text{MFN}}^{(+)} - \hat{W}_{\text{MFN}}^{(-)} \right), \tag{6.74}$$

and the magnetic field as

$$\hat{F}_2 = \hat{W}_{\text{MFN}}^{(+)} + \hat{W}_{\text{MFN}}^{(-)}. \tag{6.75}$$

6.3.4 Transformation between the two normalization analogs

We now discuss the relation between the two introduced normalization analogs, EFN and MFN.

Since the operators $\hat{A}_{1,2}$ and $\hat{A}_{2,1}$ are symmetric (see Equation (6.39)), the transverse Helmholtz operator in the MFN is the transpose of the transverse Helmholtz operator in the EFN

$$\hat{A}_{\text{MFN}} = \hat{A}_{\text{EFN}}^{\text{T}}. \tag{6.76}$$

This prompts us to introduce an alternative vector inner product, see Subappendix 6.A.2. As a consequence of (6.76) the longitudinal slowness operators are related in a similar way

$$\hat{\Gamma}_{\text{MFN}} = \hat{\Gamma}_{\text{EFN}}^{\text{T}}. \tag{6.77}$$

We can derive the following equivalent expressions for the impedance operator (use Equations (6.61), (6.64), (6.71), (6.73) and (6.77))

$$\hat{Z} = \hat{A}_{2,1}^{-1}\hat{\Gamma}_{\text{MFN}} = \hat{A}_{1,2}\hat{\Gamma}_{\text{MFN}}^{-1} = \hat{\Gamma}_{\text{EFN}}\hat{A}_{2,1}^{-1} = \hat{\Gamma}_{\text{EFN}}^{-1}\hat{A}_{1,2} = \hat{Y}^{-1} = \hat{Z}^{\text{T}}, \tag{6.78}$$

in a similar way, we find the equivalent expressions for the admittance operator

$$\hat{Y} = \hat{A}_{1,2}^{-1}\hat{\Gamma}_{\text{EFN}} = \hat{A}_{2,1}\hat{\Gamma}_{\text{EFN}}^{-1} = \hat{\Gamma}_{\text{MFN}}\hat{A}_{1,2}^{-1} = \hat{\Gamma}_{\text{MFN}}^{-1}\hat{A}_{2,1} = \hat{Z}^{-1} = \hat{Y}^{\text{T}}. \tag{6.79}$$

Observe the absence of derivatives of the medium parameters in the expression for $\hat{A}_{2,1}$ (Equation (6.37)). However, $\hat{A}_{1,2}$ contains such derivatives (Equation (6.36)). Hence, for computational convenience, the expressions without $\hat{A}_{1,2}$ are the preferred ones.

The (de)composition operators in the two normalizations are related as

$$\hat{L}_{\text{MFN}}^{\text{T}} = 2\hat{L}_{\text{EFN}}^{-1}J, \qquad \hat{L}_{\text{EFN}}^{\text{T}} = 2\hat{L}_{\text{MFN}}^{-1}J, \tag{6.80}$$

with $J = \begin{pmatrix} 0 & 1 \\ 1 & 0 \end{pmatrix}$. The relation between the waves in the two different normalizations is

$$\hat{W}_{\text{MFN}}^{(\pm)} = \pm\hat{Y}\hat{W}_{\text{EFN}}^{(\pm)}. \tag{6.81}$$

6.3.5 Transverse Helmholtz operator and its properties

In this subsection, we take a closer look at the transverse Helmholtz operator.

Now, we can write the transverse Helmholtz operator $\hat{A}_{EFN} = \hat{A}_{MFN}^{T} = \hat{A}_{1,2}\hat{A}_{2,1}$ as

$$\hat{A}_{EFN} = \hat{A}_{MFN}^{T} = \mu_0 \varepsilon' + \omega^{-2}\left[\begin{pmatrix} \partial_1 \\ \partial_2 \end{pmatrix} \varepsilon_{3,3}^{-1} \begin{pmatrix} \partial_1 & \partial_2 \end{pmatrix} \varepsilon' + \begin{pmatrix} \partial_2 \\ -\partial_1 \end{pmatrix} \begin{pmatrix} \partial_2 & -\partial_1 \end{pmatrix}\right]$$

$$+ \omega^{-4}\mu_0^{-1}\begin{pmatrix} \partial_1 \\ \partial_2 \end{pmatrix} \varepsilon_{3,3}^{-1} \underbrace{\begin{pmatrix} \partial_1 & \partial_2 \end{pmatrix} \begin{pmatrix} \partial_2 \\ -\partial_1 \end{pmatrix}}_{= 0} \begin{pmatrix} \partial_2 & -\partial_1 \end{pmatrix}.$$

$$= 0 \tag{6.82}$$

In order to emphasize that the terms of order ω^{-4} vanish, we have written them explicitely. The transverse Helmholtz operator is *not* symmetric, but from the symmetries of $\hat{A}_{1,2}$ and $\hat{A}_{2,1}$ it follows that that

$$\hat{A}_{EFN}\hat{A}_{1,2} = \hat{A}_{1,2}\hat{A}_{EFN}^{T}, \qquad \hat{A}_{2,1}\hat{A}_{EFN} = \hat{A}_{EFN}^{T}\hat{A}_{2,1}. \tag{6.83}$$

In the transverse Helmholtz operator we distinguish three contributions, viz.,

$$\hat{A} = \hat{A}^{prop} + \hat{A}^{ani.pol} + \hat{A}^{iso.pol}, \tag{6.84}$$

where

$$\begin{aligned} \hat{A}_{EFN}^{prop} &= (\hat{A}_{MFN}^{prop})^{T} &= \mu_0\varepsilon' + \omega^{-2}\partial_\nu\partial_\nu \\ &= \hat{A}_{MFN}^{prop} &= (\hat{A}_{EFN}^{prop})^{T}, \end{aligned} \tag{6.85}$$

$$\hat{A}_{EFN}^{ani.pol} = (\hat{A}_{MFN}^{ani.pol})^{T} = \omega^{-2}\begin{pmatrix} \partial_1 \\ \partial_2 \end{pmatrix} \begin{pmatrix} \partial_1 & \partial_2 \end{pmatrix} (\varepsilon_{3,3}^{-1}\varepsilon' - 1), \tag{6.86}$$

$$\hat{A}_{EFN}^{iso.pol} = (\hat{A}_{MFN}^{iso.pol})^{T} = -\omega^{-2}\begin{pmatrix} \partial_1 \\ \partial_2 \end{pmatrix} \begin{pmatrix} (\partial_1\varepsilon_{3,3}^{-1}) & (\partial_2\varepsilon_{3,3}^{-1}) \end{pmatrix} \varepsilon'. \tag{6.87}$$

The *first* contribution controls the forward propagation; the *second* contribution contains two parts, the principal part represents the phenomenon that the polarizations are not aligned with the coordinate axes while the smoothing part represents the polarization interaction both due to the presence of anisotropy, and the *third* contribution describes polarization interaction solely due to transverse heterogeneity.

When investigating the operators in the MFN, the orders of the symbols are easily determined

$$\hat{a}_{MFN}^{prop} \in S^2,$$
$$\hat{a}_{MFN}^{ani.pol} \in S^2,$$
$$\hat{a}_{MFN}^{iso.pol} \in S^1.$$

Thus the orders of the geometrical polarization operator owing to heterogeneity is one degree lower than the principal part of the transverse Helmholtz operator. Consequently, it is a smoother operator and does not introduce new singularities in the wavefront.

Symmetry property of $\hat{A}$

Using the symmetry of $\hat{A}_{1,2}$ and $\hat{A}_{2,1}$, see Equations (6.39) and (6.39), the following symmetry properties of $\hat{A}_{EFN} = \hat{A}_{MFN}^T$ are found

$$\hat{A}_{EFN}\hat{A}_{1,2} = \hat{A}_{1,2}\hat{A}_{EFN}^T, \tag{6.88}$$

$$\hat{A}_{2,1}\hat{A}_{EFN} = \hat{A}_{EFN}^T\hat{A}_{2,1}. \tag{6.89}$$

Symmetry property of $\hat{\Gamma}$

Using the expressions for the admittance $\hat{Y}$ in (6.78), the following symmetry properties of $\hat{\Gamma}_{EFN} = \hat{\Gamma}_{MFN}^T$ are found

$$\hat{\Gamma}_{EFN}\hat{A}_{1,2} = \hat{A}_{1,2}\hat{\Gamma}_{EFN}^T, \tag{6.90}$$

$$\hat{A}_{2,1}\hat{\Gamma}_{EFN} = \hat{\Gamma}_{EFN}^T\hat{A}_{2,1}. \tag{6.91}$$

The longitudinal slowness operator is thus symmetric in sense of the bilinear form $\langle .,. \rangle_\beta$ (see Subappendix 6.A.2).

6.3.6   Coupled set of two one-way wave equations

Using the decomposition operator, Equation (6.53) transforms into

$$\partial_3 \hat{W}^{(+)} + j\omega\,\hat{\Gamma}\hat{W}^{(+)} = \hat{T}\hat{W}^{(+)} + \hat{R}\hat{W}^{(-)} + \hat{X}^{(+)}, \tag{6.92}$$

$$\partial_3 \hat{W}^{(-)} - j\omega\,\hat{\Gamma}\hat{W}^{(-)} - \hat{R}\hat{W}^{(+)} + \hat{T}\hat{W}^{(-)} + \hat{X}^{(-)}, \tag{6.93}$$

which can be interpreted as a coupled system of one-way wave equations. The coupling between the counter-propagating components, $\hat{W}^{(+)}$ and $\hat{W}^{(-)}$, is apparent in the source-like term on the right-hand side. We have the coupling matrix operator

$$-\hat{L}^{-1}(\partial_3\hat{L}) = \begin{pmatrix} \hat{T} & \hat{R} \\ \hat{R} & \hat{T} \end{pmatrix}, \tag{6.94}$$

in which $\hat{R}$ and $\hat{T}$ are given by

$$\hat{R}_{EFN} = -\hat{T}_{EFN} = \tfrac{1}{2}\hat{Y}^{-1}(\partial_3\hat{Y}), \tag{6.95}$$

$$\hat{R}_{MFN} = -\hat{T}_{MFN} = \tfrac{1}{2}\hat{Z}^{-1}(\partial_3\hat{Z}) = -\tfrac{1}{2}\hat{Y}^{-1}(\partial_3\hat{Y}) = \hat{T}_{EFN} = -\hat{R}_{EFN}, \tag{6.96}$$

and represent the *reflection* and *transmission* matrix operators, respectively. The source terms are

$$\hat{X}^{(+)} = (\hat{L}^{-1})_{1,M}\hat{N}_M, \tag{6.97}$$

$$\hat{X}^{(-)} = (\hat{L}^{-1})_{2,M}\hat{N}_M. \tag{6.98}$$

6.4 Differential equation of the wave matrix: general anisotropy

In this section, the electromagnetic field in a bidirectionally anisotropic dielectric is decomposed into waves traveling forward and backward. First, we formulate an approximate diagonalization procedure for the system matrix. Subsequently, we discuss two different normalizations: one based on the electric field and one based on the magnetic field. These normalizations can be transformed to one another. Finally, we analyze the properties of the associated transverse Helmholtz operator.

Diagonalization procedure

The diagonalization of a 2 by 2 matrix operator is not straightforward and an explicit diagonalization might be impossible. If so, one should search for a correction to an approximate diagonalization. Here, we discuss such a correcting method. It is noted that a similar problem arises in the decomposition into the polarization states, see Brent and Fishman[50]. They applied the diagonalization to the symbols on the principal symbol level.

Starting from the exact solution for the case that $\hat{A}_{1,1} = 0$, we construct an approximate diagonalization procedure for $\hat{A}_{1,1} \neq 0$. Let

$$\hat{L} = \begin{pmatrix} 1 & 1 \\ \hat{Y} & -\hat{Y} \end{pmatrix}, \tag{6.99}$$

and take $\hat{Y}$ the same as in Equation (6.79). Now, we search for a correction when $\hat{A}_{1,1} \neq 0$. For this purpose, we evaluate the full action

$$\hat{L}^{-1}\hat{A}\hat{L} = \hat{\Lambda} + \hat{\mathcal{R}}, \tag{6.100}$$

with

$$\hat{\Lambda} = \begin{pmatrix} \hat{\Gamma}^{(+)} & 0 \\ 0 & \hat{\Gamma}^{(-)} \end{pmatrix}. \tag{6.101}$$

Let

$$\hat{\Gamma}^{(\pm)} = \hat{A}_{1,1} \pm \hat{A}_{1,2}\hat{Y}, \tag{6.102}$$

then the rest matrix operator $\hat{\mathcal{R}}$ equals

$$\hat{\mathcal{R}} = \tfrac{1}{2}(\hat{A}_{1,1} + \hat{Y}^{-1}\hat{A}_{1,1}^{\mathrm{T}}\hat{Y}) \begin{pmatrix} -1 & 1 \\ 1 & -1 \end{pmatrix}, \tag{6.103}$$

which vanishes when $\hat{A}_{1,1} = 0$. Correcting the decomposition equation (6.100) yields

$$(\delta_{I,J} + \hat{\mathcal{U}}_{I,J})(\hat{L}^{-1})_{J,K}\hat{A}_{K,L}\hat{L}_{L,M} = \hat{\Lambda}_{I,M}, \tag{6.104}$$

where the correction matrix operator $\hat{\mathcal{U}}$ is found as

$$\hat{\mathcal{U}} = -\left(1 + \hat{\Lambda}\hat{\mathcal{R}}^{-1}\right)^{-1}. \tag{6.105}$$

Taking the first term of the Neumann expansion of the inverse operator in (6.105), the correction matrix operator $\hat{\mathcal{U}}$ becomes approximately

$$\hat{\mathcal{U}} \simeq -\hat{\mathcal{R}}\hat{\Lambda}^{-1}. \tag{6.106}$$

6.4.1 Electric-field strength normalization analog

In the *electric-field strength normalization analog* (EFN), the electric field is decomposed into two counterpropagating waves

$$\hat{F}_1 = \hat{F}_1^{(+)} + \hat{F}_1^{(-)} = \hat{W}_{\text{EFN}}^{(+)} + \hat{W}_{\text{EFN}}^{(-)}. \tag{6.107}$$

The admittances $\hat{Y}^{(+)}$ and $\hat{Y}^{(-)}$ interrelate the electric- and magnetic-field components according to

$$\hat{F}_2^{(\pm)} = \hat{Y}^{(\pm)}\hat{F}_1^{(\pm)}. \tag{6.108}$$

Now we search for an explicit expression for the admittance $\hat{Y}^{(\pm)}$ and slowness $\hat{\Gamma}^{(\pm)}$.
   Substituting (6.108) into Equation (6.54) yields the system of equations

$$\hat{A}_{1,1} + \hat{A}_{1,2}\hat{Y}^{(\pm)} = \Gamma^{(\pm)}, \tag{6.109}$$

$$\hat{A}_{2,1} - \hat{A}_{1,1}^{\text{T}}\hat{Y}^{(\pm)} = \hat{Y}^{(\pm)}\hat{\Gamma}^{(\pm)}. \tag{6.110}$$

Substituting Equation (6.109) into Equation (6.110) results in the quadratic equation

$$\hat{Y}\hat{A}_{1,2}\hat{Y} + \hat{Y}\hat{A}_{1,1} + \hat{A}_{1,1}^{\text{T}}\hat{Y} - \hat{A}_{2,1} = 0, \tag{6.111}$$

with solutions $\hat{Y}^{(\pm)}$. It is noted that $(\hat{Y}^{(\pm)})^{\text{T}}$ are also solutions of the quadratic equation. From these solutions, we can reconstruct the quadratic equation

$$\left[\hat{Y} - \left(\hat{Y}^{(\pm)}\right)^{(\text{T})}\right]\hat{A}_{1,2}\left(\hat{Y} - \hat{Y}^{(\mp)}\right) = 0 \tag{6.112}$$

and thus $\hat{Y}^{(+)}$ en $\hat{Y}^{(-)}$ are solutions of the quadratic equation in $\hat{Y}$. Then

$$\hat{Y}\hat{A}_{1,2}\hat{Y} - \left(\hat{Y}^{(\pm)}\right)^{(\text{T})}\hat{A}_{1,2}\hat{Y} - \hat{Y}\hat{A}_{1,2}\hat{Y}^{(\mp)} + \left(\hat{Y}^{(\pm)}\right)^{(\text{T})}\hat{A}_{1,2}\hat{Y}^{(\mp)} = 0. \tag{6.113}$$

Combining (6.111) and (6.113) yields

$$\left(\hat{Y}^{(\pm)}\right)^{(\mathrm{T})}\hat{A}_{1,2}\hat{Y}^{(\mp)} = -\hat{A}_{2,1}, \tag{6.114}$$

and

$$\left(\hat{Y}^{(\pm)}\right)^{(\mathrm{T})}\hat{A}_{1,2}\hat{Y} + \hat{Y}\hat{A}_{1,2}\hat{Y}^{(\mp)} + \hat{Y}\hat{A}_{1,1} + \hat{A}_{1,1}^{\mathrm{T}}\hat{Y} = 0. \tag{6.115}$$

The latter equation can only be fulfilled for a subset of $\hat{Y}$s.

Let us take a closer look at the same configuration apart from permittivity elements $\overline{\varepsilon}_{3,\nu} = -\varepsilon_{3,\nu}$ ($\nu = 1,2$). The corresponding system matrix $\overline{A}$ equals

$$\overline{A}_{1,1} = -\hat{A}_{1,1}, \tag{6.116}$$

$$\overline{A}_{1,2} = \hat{A}_{1,2}, \tag{6.117}$$

$$\overline{A}_{2,1} = \hat{A}_{2,1}. \tag{6.118}$$

From (6.114), we assume that $\hat{Y}^{(\pm)}$ is independent of $\hat{A}_{1,1}$. Under this assumption, the equivalent of Equations (6.109)-(6.110)

$$-\hat{A}_{1,1} + \hat{A}_{1,2}\hat{Y}^{(\pm)} = \overline{\Gamma}^{(\pm)}, \tag{6.119}$$

$$\hat{A}_{2,1} + \hat{A}_{1,1}^{\mathrm{T}}\hat{Y}^{(\pm)} = \hat{Y}^{(\pm)}\overline{\Gamma}^{(\pm)}. \tag{6.120}$$

Adding (6.119) to (6.109)

$$2\hat{A}_{1,2}\hat{Y}^{(\pm)} = \hat{\Gamma} + \overline{\Gamma}, \tag{6.121}$$

and adding (6.120) to (6.110)

$$2\hat{A}_{2,1} = \hat{Y}^{(\pm)}(\hat{\Gamma} + \overline{\Gamma}), \tag{6.122}$$

yield

$$\hat{A}_{2,1} = \hat{Y}^{(\pm)}\hat{A}_{1,2}\hat{Y}^{(\pm)}. \tag{6.123}$$

Substracting (6.119) from (6.109)

$$2\hat{A}_{1,1} = \hat{\Gamma} - \overline{\Gamma}, \tag{6.124}$$

and substracting (6.120) from (6.110)

$$-2\hat{A}_{1,1}\hat{Y}^{(\pm)} = \hat{Y}^{(\pm)}(\hat{\Gamma} - \overline{\Gamma}), \tag{6.125}$$

yield

$$-\hat{A}_{1,1}\hat{Y}^{(\pm)} = \hat{Y}^{(\pm)}\hat{A}_{1,1}. \tag{6.126}$$

Thus, under the assumption that $\hat{Y}^{(\pm)}$ is independent of $\hat{A}_{1,1}$, the rest matrix $\hat{\mathcal{R}}$ vanishes. Under this assumption, the admittance $\hat{Y}^{(\pm)}$ equals

$$
\begin{aligned}
\hat{Y} = \pm \hat{Y}^{(\pm)} &= \hat{A}_{1,2}^{-1} \left(\hat{A}_{1,2} \hat{A}_{2,1} \right)^{1/2} = \left(\hat{A}_{2,1} \hat{A}_{1,2} \right)^{1/2} \hat{A}_{1,2}^{-1} \\
&= \left(\hat{A}_{1,2} \hat{A}_{2,1} \right)^{-1/2} \hat{A}_{2,1} = \hat{A}_{2,1} \left(\hat{A}_{2,1} \hat{A}_{1,2} \right)^{-1/2} = \hat{Y}^{\mathrm{T}}, \quad (6.127)
\end{aligned}
$$

and the slowness $\hat{\varGamma}_{\mathrm{EFN}}^{(\pm)}$ equals

$$
\hat{\varGamma}_{\mathrm{EFN}}^{(\pm)} = \hat{A}_{1,1} \pm \left(\hat{A}_{1,2} \hat{A}_{2,1} \right)^{1/2}. \tag{6.128}
$$

6.4.2   Magnetic-field strength normalization analog

In the *magnetic-field strength normalization* analog (MFN), one decomposes the magentic field as

$$
\hat{F}_2 = \hat{F}_2^{(+)} + \hat{F}_2^{(-)} = \hat{W}_{\mathrm{MFN}}^{(+)} + \hat{W}_{\mathrm{MFN}}^{(-)}. \tag{6.129}
$$

The impedances $\hat{Z}^{(+)}$ and $\hat{Z}^{(-)}$ interrelate the electric- and magnetic-field components according to

$$
\hat{F}_1^{(\pm)} = \hat{Z}^{(\pm)} \hat{F}_2^{(\pm)}. \tag{6.130}
$$

With a similar analysis as above and under the assumption that $\hat{Z}^{(\pm)}$ is independent of $\hat{A}_{1,1}$, the impedance operator $\hat{Z}^{(\pm)}$ is found as

$$
\begin{aligned}
\hat{Z} = \pm \hat{Z}^{(\pm)} &= \left(\hat{A}_{1,2} \hat{A}_{2,1} \right)^{-1/2} \hat{A}_{1,2} = \hat{A}_{1,2} \left(\hat{A}_{2,1} \hat{A}_{1,2} \right)^{-1/2} \\
&= \hat{A}_{2,1}^{-1} \left(\hat{A}_{1,2} \hat{A}_{2,1} \right)^{1/2} = \left(\hat{A}_{2,1} \hat{A}_{1,2} \right)^{1/2} \hat{A}_{2,1}^{-1} = \hat{Y}^{-1} = \hat{Z}^{\mathrm{T}}, \quad (6.131)
\end{aligned}
$$

while the forward and backward slownesses $\hat{\varGamma}_{\mathrm{MFN}}^{(\pm)}$ are found as

$$
\hat{\varGamma}_{\mathrm{MFN}}^{(\pm)} = \hat{A}_{1,1}^{\mathrm{T}} \pm \left(\hat{A}_{2,1} \hat{A}_{1,2} \right)^{1/2}. \tag{6.132}
$$

6.4.3   Coupled set of two one-way wave equations

Using the decomposition operator $(\delta_{I,J} + \hat{\mathcal{U}}_{I,J}) \hat{M}_{J,K}$, Equation (6.53) transforms into

$$
\partial_3 \hat{W}^{(+)} + \mathrm{j}\omega\, \hat{\varGamma}^{(+)} \hat{W}^{(+)} = \hat{T}^{(+)} \hat{W}^{(+)} + \hat{R}^{(-)} \hat{W}^{(-)} + \hat{X}^{(+)}, \tag{6.133}
$$

$$
\partial_3 \hat{W}^{(-)} + \mathrm{j}\omega\, \hat{\varGamma}^{(-)} \hat{W}^{(-)} = \hat{R}^{(+)} \hat{W}^{(+)} + \hat{T}^{(-)} \hat{W}^{(-)} + \hat{X}^{(-)}, \tag{6.134}
$$

which can be interpreted as a coupled system of one-way wave equations. The coupling between the counter-propagating components, $\hat{W}^{(+)}$ and $\hat{W}^{(-)}$, is apparent in the source-like term on the right-hand side. We have the coupling matrix operator

$$-(\hat{M} + \hat{\mathcal{U}}\hat{M})(\partial_3 \hat{L}) = \begin{pmatrix} \hat{T}^{(+)} & \hat{R}^{(-)} \\ \hat{R}^{(+)} & \hat{T}^{(-)} \end{pmatrix}, \qquad (6.135)$$

in which $\hat{R}^{(\pm)}$ and $\hat{T}^{(\pm)}$ are given by

$$-2\hat{T}^{(+)} = (1+\hat{\mathcal{U}}_{1,1})\hat{Y}_{\mathrm{EFN}}^{-1}(\partial_3 \hat{Y}_{\mathrm{EFN}}^{(+)}) - \hat{\mathcal{U}}_{1,2}\ \hat{Y}_{\mathrm{EFN}}^{-1}(\partial_3 \hat{Y}_{\mathrm{EFN}}^{(+)}), \qquad (6.136)$$

$$-2\hat{R}^{(-)} = (1+\hat{\mathcal{U}}_{1,1})\hat{Y}_{\mathrm{EFN}}^{-1}(\partial_3 \hat{Y}_{\mathrm{EFN}}^{(-)}) - \hat{\mathcal{U}}_{1,2}\ \hat{Y}_{\mathrm{EFN}}^{-1}(\partial_3 \hat{Y}_{\mathrm{EFN}}^{(-)}), \qquad (6.137)$$

$$-2\hat{R}^{(+)} = \hat{\mathcal{U}}_{2,1}\ \hat{Y}_{\mathrm{EFN}}^{-1}(\partial_3 \hat{Y}_{\mathrm{EFN}}^{(+)}) - (1+\hat{\mathcal{U}}_{1,2})\hat{Y}_{\mathrm{EFN}}^{-1}(\partial_3 \hat{Y}_{\mathrm{EFN}}^{(+)}), \qquad (6.138)$$

$$-2\hat{T}^{(-)} = \hat{\mathcal{U}}_{2,1}\ \hat{Y}_{\mathrm{EFN}}^{-1}(\partial_3 \hat{Y}_{\mathrm{EFN}}^{(-)}) - (1+\hat{\mathcal{U}}_{1,2})\hat{Y}_{\mathrm{EFN}}^{-1}(\partial_3 \hat{Y}_{\mathrm{EFN}}^{(-)}), \qquad (6.139)$$

and represent the *reflection* and *transmission* matrix operators, respectively. The source terms are $\hat{X}^{(+)}$ and $\hat{X}^{(-)}$.

The decomposition matrix operator $\hat{M} + \hat{\mathcal{U}}\hat{M}$ needs only to be computed for the decomposition of the initial field or source and for the coupling operator.

6.5 Integral equation for the wave matrix

The derivation of the integral equation for 3-D wave propagation is very similar to the 2-D case. Below, we discuss only the main differences.

In the 3-D configurations, the transverse Helmholtz operator is a 2 by 2 matrix operator instead of a scalar operator. In the electric-field and magnetic-field strength normalization analog, the square root matrix operator $\hat{\Gamma}$ is not symmetric. Therefore, to derive the integral equation for the wave matrix, we start with the reciprocal forward Green function, instead of the backward Green function (see Equation (3.47)).

The solution of the two coupled one-way wave equations, (6.133) and (6.134) derived above, are constructed by first transforming these equations into corresponding integral equations. In this approach, the behaviour of the left-hand sides of these equations is required. The Green functions corresponding to the left-hand sides of (6.133) and (6.134), and satisfy

$$\partial_3 \hat{G}^{(+)}(x_k; x_k') + \mathrm{j}\omega \hat{\Gamma}^{(+)}(x_k)\hat{G}^{(+)}(x_k; x_k') = \delta(x_k - x_k'), \qquad (6.140)$$

$$\partial_3 \hat{G}^{(-)}(x_k; x_k') + \mathrm{j}\omega \hat{\Gamma}^{(-)}(x_k)\hat{G}^{(-)}(x_k; x_k') = \delta(x_k - x_k'), \qquad (6.141)$$

respectively. The explicit expressions will be derived later. To derive an integral representation for $\hat{W}^{(\pm)}$, we introduce the reciprocal Green functions $\hat{G}_{\mathrm{T}}$ through

$$\hat{G}_{\mathrm{T}}^{(\pm)}(x_k'; x_k) = -\hat{G}^{(\pm)}(x_k; x_k'). \qquad (6.142)$$

The reciprocal Green functions satisfy the transposed one-way wave equations

$$\partial_3 \hat{G}_{\mathrm{T}}^{(+)}(x_k; x_k') - \mathrm{j}\omega(\hat{\varGamma}^{(+)})^{\mathrm{T}}(x_k)\hat{G}_{\mathrm{T}}^{(+)}(x_k; x_k') = \delta(x_k - x_k'), \tag{6.143}$$

$$\partial_3 \hat{G}_{\mathrm{T}}^{(-)}(x_k; x_k') - \mathrm{j}\omega(\hat{\varGamma}^{(-)})^{\mathrm{T}}(x_k)\hat{G}_{\mathrm{T}}^{(-)}(x_k; x_k') = \delta(x_k - x_k'). \tag{6.144}$$

In fact, if $\hat{G}^{(\pm)} = \hat{G}_{\mathrm{EFN}}^{(\pm)}$ then $\hat{G}_{\mathrm{T}}^{(\pm)} = \hat{G}_{\mathrm{MFN}}^{(\pm)}$. Multiplying Equation (6.133) by $\hat{G}_{\mathrm{T}}^{(+)}(x_k; x_k')$ and Equation (6.141) by $\hat{W}^{(+)}$ yields

$$\hat{G}_{\mathrm{T}}^{(+)}\partial_3\hat{W}^{(+)} + \hat{W}^{(+)}\partial_3\hat{G}_{\mathrm{T}}^{(+)} + \mathrm{j}\omega\left[\hat{G}_{\mathrm{T}}^{(+)}\hat{\varGamma}^{(+)}\hat{W}^{(+)} + \hat{W}^{(+)}(\hat{\varGamma}^{(+)})^{\mathrm{T}}\hat{G}_{\mathrm{T}}^{(+)}\right]$$
$$= \hat{G}_{\mathrm{T}}^{(+)}\hat{T}^{(+)}\hat{W}^{(+)} + \hat{G}_{\mathrm{T}}^{(+)}\hat{R}^{(-)}\hat{W}^{(-)} + \hat{W}^{(+)}\delta(x_k - x_k'). \tag{6.145}$$

Note that the last two terms on the left-hand side do not vanish. After integrating over the entire transverse plane, these terms vanish because

$$\langle \hat{G}_{\mathrm{T}}^{(+)}, \hat{\varGamma}^{(+)}\hat{W}^{(+)} \rangle_{\mathrm{B}} = \langle \hat{W}^{(+)}, (\hat{\varGamma}^{(+)})^{\mathrm{T}}\hat{G}_{\mathrm{T}}^{(+)} \rangle_{\mathrm{B}}. \tag{6.146}$$

Integrating (6.145) over the entire transverse plane, and following the derivation in Subsection 3.4.2, yield the integral equations for the wave matrix, similar to Equations (3.57)-(3.63). In operator form

$$\left(\delta_{I,J} - \hat{K}_{I,J}\right)\hat{W}_J = \hat{W}_I^{(0)}, \tag{6.147}$$

with

$$\hat{W}_1^{(0)}(x_\nu, x_3) = H(x_3 - x_3')\left\{\prod_{z=x_3'}^{x_3}\exp\left[-\mathrm{j}\omega\hat{\varGamma}^{(+)}(x_\nu, z)\,\mathrm{d}z\right]\right\}\hat{W}_1(x_\nu, 0), \tag{6.148}$$

while

$$(\hat{K}_{1,1}\hat{W}_1)(x_\nu, x_3) = \int_{\zeta=0}^{x_3}\left\{\prod_{z=\zeta}^{x_3}\exp\left[-\mathrm{j}\omega\hat{\varGamma}^{(+)}(x_\nu, z)\,\mathrm{d}z\right]\right\}\left(\hat{T}^{(+)}\hat{W}^{(+)}\right)(x_1, \zeta)\,\mathrm{d}\zeta, \tag{6.149}$$

and so on.

6.6   Numerical aspects of the Bremmer coupling series

The numerical aspects of the Bremmer coupling series are nearly the same as for the 2-D case. We therefore refer to Section 3.5. Here, we discuss some aspects of the stability of the one-way wave equation: the BPM-type approach. In Section 6.6.2, the combined Bremmer series is discussed. For reasons of stability, the Bremmer series is computed twice: once in the electric-field strength normalization analog, and once in the magnetic-field strength normalization analog.
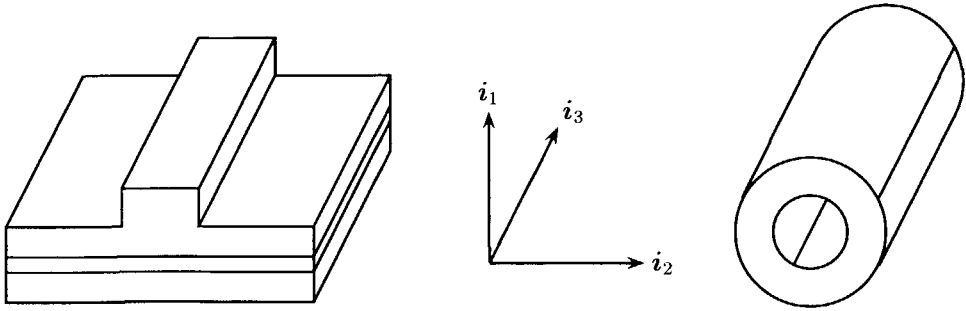
Figure 6.2: *Rib waveguide on an optical chip (right) and an optical fiber (left).*

6.6.1 BPM-type approach

The classical Beam Propagation Method (BPM) and many related methods assume that the medium properties vary slowly in the longitudinal direction. In such configurations, the influence of operator $\hat{K}_{I,J}$ vanishes. The forward-directed transmitted wave is then dominant

$$\hat{W}^{(+)}(x_3) \simeq \hat{W}_1^{(0)}(x_3), \tag{6.150}$$

$$\hat{W}^{(0)}(x_3) \simeq 0. \tag{6.151}$$

The numerical aspect of the scattering in the longitudinal direction is the same as those in the 1-D and 2-D configurations, see Sections 2.5 and 3.5. We now discuss the corresponding one-way wave equations and the power flow in longitudinal invariant media.

Wave propagation in longitudinally invariant structures

Consider a wave $\hat{W}_{\text{EFN}}^{r(+)}$ propagating in the positive x_3 direction in an x_3 invariant structure with bidirectional anisotropy: e.g., a waveguide (see Figure 6.2). Due to the invariance in the preferred direction, the corresponding one-way wave equations for the transverse electric and magnetic-field vectors are found to be (compare with Equation (6.92))

$$\partial_3 \hat{F}_1 + j\omega \hat{\Gamma}_{\text{EFN}} \, \hat{F}_1 = 0, \tag{6.152}$$

$$\partial_3 \hat{F}_2 + j\omega \hat{\Gamma}_{\text{MFN}} \hat{F}_2 = 0, \tag{6.153}$$

respectively. In this formulation, the decomposition and composition operators do not have to be computed. In the field of integrated optics, these equations are also known as the wide-angle BPM equations in the electric-field formulation and magnetic-field formulation, respectively. Both equations need to be evaluated in order to compute the guided power along the preferred axis x_3.

One-way power flow in longitudinal invariant media

By analyzing the power flow in longitudinal invariant media, one finds several importants properties of the one-way wave equation. We show that the power flow is stable for a special choice of the square root operator $\hat{\Gamma}$.

The symmetry properties of $\hat{\Gamma}_{\text{EFN}}$ depend on the choice of the square root. It is well known that the square root is a two-valued function. For energy conservation considerations, we show that there is only one physical choice for the square root.

Consider a forward-traveling wave in an x_3-invariant configuration. The wave propagation is then described by the homogeneous version of Equation (6.92)

$$\partial_3 \hat{W}^+_{\text{EFN}} + j\omega \hat{\Gamma}_{\text{EFN}} \hat{W}^+_{\text{EFN}} = 0. \tag{6.154}$$

The power transferred through the transverse plane at x_3 equals (see Equation (1.48))

$$\langle P \rangle_T(x_3) = \tfrac{1}{2}\text{Re}\left(\langle \hat{S}_3, 1 \rangle\right), \tag{6.155}$$

with $\hat{S}_3 = \hat{F}_1^T \hat{F}_2^*$. We must now show that $\langle \hat{S}_3, 1 \rangle = \partial_3 \langle \hat{W}^+_{\text{EFN}}, \hat{Y} \hat{W}^+_{\text{EFN}} \rangle$ is negative (attenuation) or zero (no attenuation). Substituting (6.154) in (6.155) yields

$$\partial_3 \langle \hat{W}^{(+)}_{\text{EFN}}, \hat{Y} \hat{W}^{(+)}_{\text{EFN}} \rangle = \langle \partial_3 \hat{W}^{(+)}_{\text{EFN}}, \hat{Y} \hat{W}^{(+)}_{\text{EFN}} \rangle + \langle \hat{W}^{(+)}_{\text{EFN}}, \hat{Y} \partial_3 \hat{W}^{(+)}_{\text{EFN}} \rangle$$

$$\hat{Y} \hat{W}^{(+)}_{\text{EFN}} \rangle + \langle \hat{W}^{(+)}_{\text{EFN}}, -j\omega \hat{Y} \hat{\Gamma}_{\text{EFN}} \hat{W}^{(+)}_{\text{EFN}} \rangle$$

$$= -j\omega \langle [\hat{\Gamma}_{\text{EFN}} - \hat{\Gamma}^*_{\text{EFN}}] \hat{W}^{(+)}_{\text{EFN}}, \hat{Y} \hat{W}^{(+)}_{\text{EFN}} \rangle$$

$$= 2\omega \langle \text{Im}(\hat{\Gamma}_{\text{EFN}}) \hat{W}^{(+)}_{\text{EFN}}, \hat{Y} \hat{W}^{(+)}_{\text{EFN}} \rangle, \tag{6.156}$$

where

$$\text{Im}(\hat{\Gamma}_{\text{EFN}}) = \tfrac{1}{2}(\hat{\Gamma}_{\text{EFN}} - \hat{\Gamma}^*_{\text{EFN}}). \tag{6.157}$$

Since

$$\text{Im}(\hat{\Gamma}_{\text{EFN}})^H \hat{Y} = \hat{Y}^* \text{Im}(\hat{\Gamma}_{\text{EFN}}), \tag{6.158}$$

the expression

$$\langle \text{Im}(\hat{\Gamma}_{\text{EFN}}) \hat{W}^+_{\text{EFN}}, \hat{Y} \hat{W}^+_{\text{EFN}} \rangle = \langle \text{Im}(\hat{\Gamma}_{\text{EFN}}) \hat{W}^+_{\text{EFN}}, \hat{Y} \hat{W}^+_{\text{EFN}} \rangle^*, \tag{6.159}$$

is real valued and thus the right-hand side of (6.156) is also real valued. This term is negative if $-\text{Im}(\hat{\Gamma}_{\text{EFN}})$ is positive definite and thus if we choose $\text{Im}[(.)^{1/2}] < 0$ for passive media. With this choice for the square root, stable power flow is ensured

$$\langle P \rangle_T(x_3) \leq \langle P \rangle_T(0). \tag{6.160}$$

6.6.2   Bremmer coupling series

Combined Bremmer coupling series

If, as we will see in the next chapter, in the numerical discretization procedure, the symmetry relations are lost, stability can no longer be guaranteed (although the instability might be small). In order to obtain a stable scheme, one should compute the wave propagation in both normalization analogs simultaneously: the electric-field strength normalization analog and its transposed analog, the magnetic-field strength normalization analog. Consequently, the corresponding numerical scheme becomes twice as time consuming, compared to a single one-way wave propagation scheme. The final magnetic field has to be computed from the waves in the magnetic-field strength normalization analog instead of from the final electric field. Then stability is ensured. Executing a similar analysis as above, starting with

$$\hat{F}_1 = \hat{W}_{\mathrm{EFN}}^{(+)}, \tag{6.161}$$

$$\hat{F}_2 = \hat{W}_{\mathrm{MFN}}^{(+)}, \tag{6.162}$$

yields (compare with Equation (6.156))

$$\partial_3 \langle W_{\mathrm{EFN}}^{(+)}, W_{\mathrm{MFN}}^{(+)} \rangle = 2\omega \langle \mathrm{Im}(\hat{\Gamma}_{\mathrm{EFN}}) \hat{W}_{\mathrm{EFN}}^{(+)}, \hat{W}_{\mathrm{MFN}}^{(+)} \rangle. \tag{6.163}$$

Again, stable power flow is ensured

$$\langle P \rangle_T(x_3) \leq \langle P \rangle_T(0). \tag{6.164}$$

In this alternative approach, the computation time is increased by a factor two.

Figure 6.3 illustrates the numerical implementation of the combined Bremmer coupling series; the Bremmer series is simultaneously computed in the electric-field and magnetic-field strength normalization analog. Note that in the derivation of the coupled set of two one-way wave integral equations, we used both normalization.

In different words, the one-way wave equation for the electric-field is not stable in the standard vector L_2 inner product, but it is stable in the alternative vector inner product in Equation (6A.5). This stability is only ensured if the slowness operator is symmetric in this inner product. If this condition is not met, stability can be enforced by doing the computations in both normalization analogs simultaneously. In practice, however, computing the magnetic field from the electric field gives often nearly stable results.

General anisotropy

In order to obtain a stable scheme for general anisotropy, the one-way wave equations should also be computed in one normalization analog (e.g., electric field) and its transposed normalization analog.
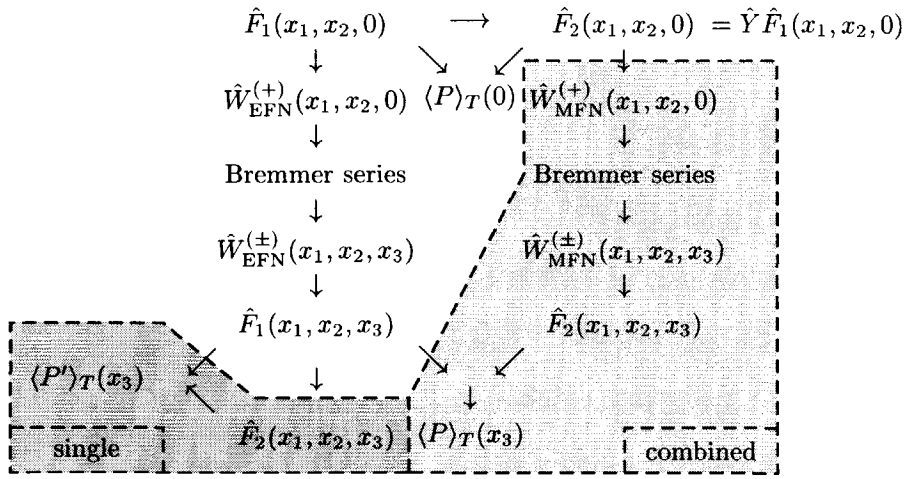
Figure 6.3:   *Flow chart of the numerical implementation of the three-dimensio-*
              nal combined and single Bremmer coupling series.

6.7   Discussion of the results

In analogy with the 1-D and 2-D configurations, we introduced the Bremmer cou-
pling series for the scattering problem along the longitudinal direction. We made a
distinction between two type of anisotropic dielectrics: bidirectional anisotropy and
general anisotropy. For the both classes, the directional wave-field decomposition
is analog with the lower dimensional configurations. For general anisotropy, a cor-
rection to an approximate diagonalization was derived. We discussed two types of
normalization analogs: the electric-field and magnetic-field strength normalization
analogs. These analogs are each other's transpose. We showed that stability of the
forward scheme is ensured as long as some symmetry relations are conserved. If
not, we introduced the combined Bremmer approach. The forward scheme is then
unconditionally stable.

The transverse scattering problem is described by slowness operator. We showed
its symmetry properties. It contains two contributions: a square root operator of
the transverse Helmholtz operator and a partial differential operator $(\hat{A}_{1,1})$. The

transverse Helmholtz operator can be decomposed into three operators, each of them describing a different physical effect: propagation, geometrical polarization and physical polarization. The operator $\hat{A}_{1,1}$ described the directional-dependent propagation. The geometrical polarization operator's symbol belongs to a lower symbol space. Consequently, the polarization interaction smooths the wave propagation.

Alternatively, we could have introduced the *electromagnetic power-flux normalization* analog (PFN), see de Hoop[49]. Then the transverse Helmholtz operator and its square root, the longitudinal slowness, are symmetric, which forces stability of the forward scheme. A disadvantage of the PFN is the numerical implementation; it is more difficult due to the occurance of the square root of the longitudinal slowness and its inverse in the composition and decomposition operators and the additional square root $\hat{A}_{1,2}^{1/2}$ in the slowness. Therefore, the electric-field or magnetic-field strength normalization analogs are preferred in our numerical implementation above the power-flux normalization analog. However, it is easier to ensure stability.

Appendix

6.A Notation

6.A.1 Matrix representations

See also Section 1.2. In this and the next chapter, four types of vectors and matrices are used

- ① scalars, denoted as a,

- ② vectors of length 2, denoted as (lower-case Greek letters will be used for subsripts: $\nu, \rho, \cdots = 1, 2$)

$$a = a_\nu = \begin{pmatrix} a_1 \\ a_2 \end{pmatrix},$$

  2 by 2 matrices, denoted as $a_{\nu,\rho}$,

- ③ vectors of length 3, denoted as (lower-case Latin letters will be used for subscripts: $k, r, \cdots = 1, 2, 3$)

$$a = a_k = \begin{pmatrix} a_1 \\ a_2 \\ a_3 \end{pmatrix},$$

  3 by 3 matrices, denoted as $a_{k,r}$,

- ④ vectors of length 4, containing two vectors of length 2, denoted as (upper-case Latin letters will be used for subscripts: $I, J, \cdots = 1, 2$)

$$a = a_I = \begin{pmatrix} a_1 \\ a_2 \end{pmatrix} = \begin{pmatrix} (a_1)_1 \\ (a_1)_2 \\ (a_2)_1 \\ (a_2)_2 \end{pmatrix},$$

  4 by 4 matrices, containing four 2 by 2 matrices, denoted as $a_{I,J}$.

As an example, the two elements of vector $a = \begin{pmatrix} b_\nu \\ c_\rho \end{pmatrix}$ are vectors of length 2:

$$b = b_\nu = a_1 = \begin{pmatrix} (a_1)_1 \\ (a_1)_2 \end{pmatrix} \text{ and } c = c_\nu = a_2 = \begin{pmatrix} (a_2)_1 \\ (a_2)_2 \end{pmatrix}.$$

The vectors of length 2 will be loosely written without subscript. In order to *emphasize* the inner product notation, we also use the following notation with superscript ^{T}

$$a_\nu a_\nu = a^T a.$$

For 2 by 2 matrices, the identity matrix $I = \begin{pmatrix} 1 & 0 \\ 0 & 1 \end{pmatrix}$ will be often neglected in multiplication with a scalar and often written as 1. The zero matrix $\begin{pmatrix} 0 & 0 \\ 0 & 0 \end{pmatrix}$ is often written as 0.

6.A.2 Function (tensor product) spaces, inner products

In this chapter, many mathematical manipulations with operators are performed. These operators are defined on a function space. These spaces and their inner products are introduced here.

L_2 inner product

The vector L_2 inner product of vector functions $\hat{v}_\nu(x_1)$ and $\hat{w}_\rho(x_1)$ is defined by (see also Equation (3.27))

$$\langle \hat{v}_\nu, \hat{w}_\nu \rangle \overset{\text{def}}{=} \int_{x_1=-\infty}^{\infty} \int_{x_2=-\infty}^{\infty} \hat{v}_\nu(x_1, x_2) \hat{w}_\nu^*(x_1, x_2) \, \mathrm{d}x_1 \mathrm{d}x_2, \qquad (6A.1)$$

where we used the summation convention. The L_2 norm of $\hat{v}(x_1)$ equals

$$\|\hat{v}\| = \langle \hat{v}_\nu, \hat{v}_\nu \rangle^{1/2}. \qquad (6A.2)$$

In this thesis, the notation $\langle \hat{v}, \hat{w} \rangle_{\text{B}}$ is reserved for the corresponding (vector) bilinear form, defined as (without complex conjugation)

$$\langle \hat{v}_\nu, \hat{w}_\nu \rangle_{\text{B}} \overset{\text{def}}{=} \int_{x_1=-\infty}^{\infty} \int_{x_2=-\infty}^{\infty} \hat{v}_\nu(x_1, x_2) \hat{w}_\nu(x_1, x_2) \, \mathrm{d}x_1 \mathrm{d}x_2 = \langle \hat{v}_\nu, \hat{w}_\nu^* \rangle. \qquad (6A.3)$$

Alternative inner product

Note that the transposed operator of $\hat{A}_{\text{EFN}}$ equals (compare with (6.76))

$$\hat{A}_{\text{EFN}}^{\text{T}} = \hat{A}_{2,1} \hat{A}_{1,2} = \hat{A}_{\text{MFN}}, \qquad (6A.4)$$

which is the transverse Helmholtz operator of the magnetic-field strength normalization analog (6.71): the equations in the electric-field strength normalization analog are the transposed equations of the magnetic-field strength normalization analog. This prompts us to introduce an alternative vector inner product

$$\langle \hat{v}_\nu, \hat{w}_\nu \rangle_\iota \overset{\text{def}}{=} \int_{x_1=-\infty}^{\infty} \int_{x_2=-\infty}^{\infty} (\hat{A}_{2,1})_{\nu,\rho} \hat{v}_\rho(x_1, x_2) \hat{w}_\nu^*(x_1, x_2) \, \mathrm{d}x_1 \mathrm{d}x_2$$
$$= \langle (\hat{A}_{2,1})_{\nu,\rho} \hat{v}_\rho, \hat{w}_\nu \rangle, \qquad (6A.5)$$

(for lossless bidirectionally anisotropic dielectrics) and an alternative vector bilinear form

$$\langle \hat{v}_\nu, \hat{w}_\nu \rangle_\beta \overset{\text{def}}{=} \int_{x_1=-\infty}^{\infty} \int_{x_2=-\infty}^{\infty} (\hat{A}_{2,1})_{\nu,\rho} \hat{v}_J(x_1, x_2) \hat{w}_\nu(x_1, x_2) \, \mathrm{d}x_1 \mathrm{d}x_2$$
$$= \langle (\hat{A}_{2,1})_{\nu,\rho} \hat{v}_\rho, \hat{w}_\nu^* \rangle, \qquad (6A.6)$$

(for bidirectionally anisotropic dielectrics) to analyze the wave propagation. Clearly — using the symmetry of $\hat{A}_{1,2}$ and $\hat{A}_{2,1}$, see Equations (6.39) and (6.39),

$$\langle \hat{A}\hat{v}, \hat{w} \rangle_\beta = \langle \hat{v}, \hat{A}\hat{w} \rangle_\beta. \tag{6A.7}$$

The transverse Helmholtz operator $\hat{A}$ is thus *self-adjoint* within this bilinear form. In the lossless case, the transverse Helmholtz operator is also *self-adjoint* within the above inner product, see also März[133].

For general anisotropy one should use a different inner product in which both counter-propagating waves, are included.

6.A.3 Operator symmetries

The adjoint operator $(\hat{B}^H)_{\nu,\rho} = (\hat{B}_{\rho,\nu})^H$ of the operator $\hat{B}_{\nu,\rho}$ is defined as

$$\langle \hat{B}_{\nu,\rho}\hat{v}_\rho, \hat{w}_\nu \rangle_B \stackrel{\text{def}}{=} \langle \hat{v}_\nu, (\hat{B}^H)^*_{\nu,\rho}\hat{w}_\rho \rangle_B, \qquad \text{or} \qquad \langle \hat{B}_{\nu,\rho}\hat{v}_\rho, \hat{w}_\nu \rangle \stackrel{\text{def}}{=} \langle \hat{v}_\nu, (\hat{B}^H)_{\nu,\rho}\hat{w}_\rho \rangle. \tag{6A.8}$$

The transposed operator $(\hat{B}^T)_{\nu,\rho} = (\hat{B}_{\rho,\nu})^T$ of the operator $\hat{B}_{\nu,\rho}$ is defined as

$$\langle \hat{B}_{\nu,\rho}\hat{v}_\rho, \hat{w}_\nu \rangle_B \stackrel{\text{def}}{=} \langle \hat{v}_\nu, (\hat{B}^T)_{\nu,\rho}\hat{w}_\rho \rangle_B, \qquad \text{or} \qquad \langle \hat{B}_{\nu,\rho}\hat{v}_\rho, \hat{w}_\nu \rangle \stackrel{\text{def}}{=} \langle \hat{v}_\nu, (\hat{B}^T)^*_{\nu,\rho}\hat{w}_\rho \rangle. \tag{6A.9}$$

The operator $\hat{B}$ is

$$
\begin{array}{ll}
\text{\textit{self-adjoint} if} & \hat{B}_{\nu,\rho} = (\hat{B}^H)_{\nu,\rho}, \\
\text{\textit{symmetric} if} & \hat{B}_{\nu,\rho} = (\hat{B}^T)_{\nu,\rho}, \\
\text{\textit{skew-symmetric} if} & \hat{B}_{\nu,\rho} = -(\hat{B}^T)_{\nu,\rho}.
\end{array}
$$

Three important examples are

$$\partial_\nu^T = -\partial_\nu, \qquad \text{for } \nu = 1, 2, \tag{6A.10}$$

$$(\varepsilon\partial_\nu)^T = -\partial_\nu\varepsilon, \qquad \text{for } \nu = 1, 2, \tag{6A.11}$$

$$(\partial_\nu\partial_\nu)^T = \partial_\nu\partial_\nu. \tag{6A.12}$$

CHAPTER 7

3-D Numerical Implementation: Third-Order Thiele Approximation on a Transverse Hexagonal Grid

This chapter extends the numerical total rational-approximation approach of Chapter 5 to a three-dimensional anisotropic configuration. The vectorial electromagnetic wave propagation is considered. Due to the increased complexity, some small changes are made in the numerical implementation. The extension to the acoustic wave propagation, which is mathematically simpler due to the absence of different polarization states, is not discussed and left as an exersize to the reader.

Several researchers have investigated and developed a vectorial Beam Propagation Method. Some of them are Rivera[114], Li[194], Huang et al.[195] and Lüsse et al.[196]. For an overview, we refer to Section 1.5. Some authors restrict themselves to semi-vectorial wave propagation. The coupling between the occuring states of polarization is then neglected, see Stern[193]. As far as the author knows, the inclusion of reflection in a 3-D vectorial scheme has only been considered by Pregla et al.[88], who developed the MoL-BPM, a beam propagation method based upon the method of lines.

In discretizing the coupled set of two one-way wave equations on a hexagonal grid, we can, in principle, follow two strategies. We now describe both strategies.

In the first strategy we optimize the discretization of the transverse Helmholtz

operator directly. By doing this, the propagation and the polarization coupling can be made accurate up to $\mathcal{O}[(\Delta x)^4]$, where Δx is the distance between two discretization points. The original building operators of the transverse Helmholtz operator, $\hat{A}_{1,2}$ and $\hat{A}_{2,1}$, cannot be extracted from the discretized transverse Helmholtz operator, and the symmetry relation (6.88) is lost. To create a stable numerical scheme, we must compute the wave propagation in both normalization analogs simultaneously: the electric-field strength normalization analog and its transposed analog, the magnetic-field strength normalization analog, see Section 6.6. Consequently, the corresponding numerical scheme becomes twice as time consuming, compared to a single one-way wave propagation scheme.

In the second strategy, we start with discretizing the original building operators, $\hat{A}_{1,2}$ and $\hat{A}_{2,1}$. In order to keep the matrices sparse, we replace each first-order derivative by an elementary difference operator. This approach conserves the symmetry relations and thus also the stability. The accuracy of the coupling term, however, is decreased to $\mathcal{O}[(\Delta x)]$. In order to save the symmetry relations for the rational finite difference operators, the corresponding matrices become denser. An alternative discretization scheme will lead to a more accurate polarization coupling term, but then the forward propagation looses its accuracy; reducing to $\mathcal{O}[(\Delta x)]$.

Choosing a different discretization scheme, which is not based upon discretizing $\hat{A}_{1,2}$ and $\hat{A}_{2,1}$ first, the term of order ω^{-4} will probably remain. Neglecting this term leads to instabilities, which must be suppressed by other means, as it is done in the modified Crank-Nicolson scheme (see Huang et al.[195] and Li[194]), or a combined Bremmer approach (as presented here, see Section 6.6).

This chapter is organized as follows. In Section 7.1, the one-way wave equation is simplified for the numerical scheme: the square root operator is approximated by a third-order Thiele-type approximation, the optimization procedure for improving the accuracy is addressed to, and the dissipation trick and co-moving reference frame are introduced. Section 7.2 describes the discretization on a transverse hexagonal grid. The derivatives are approximated by finite difference operators; their accuracy is discussed in detail. In Section 7.3, the numerical scheme in derived. The stability of the numerical scheme is emphasized. Section 7.4 discusses the transparent boundary conditions for decreasing the influence of the computational window. In Section 7.5, the group and phase slownesses are determined. An optimization procedure is introduced to minimize the numerical anisotropy and numerical dissipation. In Section 7.6 and Section 7.7, the composition and decomposition operators and the reflection operator are discretized, respectively. Finally, the results are discussed (Section 7.8).

This method has been presented at an international meeting, see van Stralen et al.[197].

7.1 Rational approximation of the one-way wave propagator

Consider the homogeneous one-way equation (the homogeneous version of Equations (6.133) and (6.134))

$$\partial_3 \hat{W}_1^{(0)} + j\omega \hat{\Gamma}^{(+)} \hat{W}_1^{(0)} = 0, \qquad x_3 \in (0, x_3^{\text{exit}}], \tag{7.1}$$

which is satisfied by the leading-order term of the Bremmer series. In this section, we derive a sparse matrix representation for its propagator, $\hat{P}(x_1, m)$ (3-D equivalent of $\hat{P}(x_1, m)$ in Equation (3.84)). In the associated approximations, we maintain the hyperbolicity of the time-domain-equivalent equations. The key towards sparsification is deforming the evanescent regime into an artificial propagating counterpart.

7.1.1 Third-order Thiele approximation

The longitudinal slowness operator contains a square root operator

$$\hat{\Gamma}^{(\pm)} = \hat{A}_{1,1} \pm c_{\text{ref}}^{-1} (1 + \hat{\Xi})^{1/2}. \tag{7.2}$$

Here, $c_{\text{ref}}(x_3)$ is some (transverse constant) reference wave speed and $\hat{\Xi}$ is a scaled and normalized transverse Helmholtz operator (or contrast transverse Helmholtz operator)

$$\hat{\Xi} = \left(c_{\text{ref}}^2 \hat{A} - 1 \right). \tag{7.3}$$

For our numerical scheme, we consider Thiele's third-order continued fractions approximation (see Equation (5.3)). The Thiele approximation of the square root reads

$$(1 + x)^{1/2} \simeq 1 + (1 + \beta_3 x)^{-1} (\beta_1 x + \beta_2 x^2). \tag{7.4}$$

The Thiele's third-order continued fractions approximation caries over to the slowness operator as

$$\hat{\Gamma}^{(\pm)} \simeq \hat{\Gamma}^{\text{III} \, (\pm)} = \hat{A}_{1,1} \pm c_{\text{ref}}^{-1} \pm c_{\text{ref}}^{-1} (1 + \beta_3 \hat{\Xi})^{-1} (\beta_1 \hat{\Xi} + \beta_2 \hat{\Xi}^2). \tag{7.5}$$

Because we use a transverse constant reference medium, the symmetry between the two normalization analogs, EFN and MFN, is preserved in the Thiele approximation. From now on, we freely omit the superscript $^{\text{III}}$.

Scaled transverse Helmholtz operator

The scaled transverse Helmholtz operator in the electric-field strength normalization analog (see Equations (6.82) and (6.128)) is given by

$$\hat{\Xi}_{\text{EFN}} = \chi + \left(\frac{c_{\text{ref}}}{\omega} \right)^2 \left[\begin{pmatrix} \partial_1 \\ \partial_2 \end{pmatrix} \varepsilon_{3,3}^{-1} \begin{pmatrix} \partial_1 & \partial_2 \end{pmatrix} \varepsilon' + \begin{pmatrix} \partial_2 \\ -\partial_1 \end{pmatrix} \begin{pmatrix} \partial_2 & -\partial_1 \end{pmatrix} \right]$$

In the magnetic-field strength normalization analog (see Equations (6.82) and (6.132)) we have

$$\hat{\Xi}_{\mathrm{MFN}} = \chi + \left(\frac{c_{\mathrm{ref}}}{\omega}\right)^2 \left[\varepsilon' \begin{pmatrix} \partial_1 \\ \partial_2 \end{pmatrix} \varepsilon_{3,3}^{-1} \begin{pmatrix} \partial_1 & \partial_2 \end{pmatrix} + \begin{pmatrix} \partial_2 \\ -\partial_1 \end{pmatrix} \begin{pmatrix} \partial_2 & -\partial_1 \end{pmatrix}\right]$$

In here, the contrast matrix χ is given by

$$\chi = \varepsilon_{\mathrm{ref}}^{-1}\varepsilon' - 1. \tag{7.6}$$

The scaled transverse Helmholtz operator is decomposed into three suboperators (see Equations (6.85)-(6.87))

$$\hat{\Xi} = \hat{\Xi}^{\mathrm{prop}} + \hat{\Xi}^{\mathrm{ani.pol}} + \hat{\Xi}^{\mathrm{iso.pol}}; \tag{7.7}$$

each operator describes a different physical phenomenon, namely

- propagation ($\hat{\Xi}^{\mathrm{prop}}$),

- physical polarization interaction owing to anisotropy ($\hat{\Xi}^{\mathrm{ani.pol}}$), and,

- geometrical polarization interaction owing to heterogeneity ($\hat{\Xi}^{\mathrm{iso.pol}}$).

It is noted that $\hat{A}_{1,1}$ in $\hat{\Gamma}$ contributes to the directionally varying propagation owing to general anisotropy. First, the forward propagation is described by the propagation term of the transverse Helmholtz operator (see Equation (6.85))

$$\hat{\Xi}_{\mathrm{EFN}}^{\mathrm{prop}} = (\hat{\Xi}_{\mathrm{MFN}}^{\mathrm{prop}})^{\mathrm{T}} = \chi + \left(\frac{c_{\mathrm{ref}}}{\omega}\right)^2 (\partial_1^2 + \partial_2^2) \begin{pmatrix} 1 & 0 \\ 0 & 1 \end{pmatrix}. \tag{7.8}$$

Second, the physical polarization coupling owing to anisotropy between the two polarization states is described by (compare with Equation (6.86))

$$\hat{\Xi}_{\mathrm{EFN}}^{\mathrm{ani.pol}} = (\hat{\Xi}_{\mathrm{MFN}}^{\mathrm{ani.pol}})^{\mathrm{T}} = \left(\frac{c_{\mathrm{ref}}}{\omega}\right)^2 \begin{pmatrix} \partial_1 \\ \partial_2 \end{pmatrix} \begin{pmatrix} \partial_1 & \partial_2 \end{pmatrix} (\varepsilon_{3,3}^{-1}\varepsilon' - 1), \tag{7.9}$$

Third, the geometrical polarization coupling owing to heterogeneity between two polarizations states is described by (see Equation (6.87))

$$\hat{\Xi}_{\mathrm{EFN}}^{\mathrm{iso.pol}} = (\hat{\Xi}_{\mathrm{MFN}}^{\mathrm{iso.pol}})^{\mathrm{T}} = -\left(\frac{c_{\mathrm{ref}}}{\omega}\right)^2 \begin{pmatrix} \partial_1 \\ \partial_2 \end{pmatrix} \left((\partial_1\varepsilon_{3,3}^{-1})(\partial_2\varepsilon_{3,3}^{-1})\right) \varepsilon'. \tag{7.10}$$

Operator $\hat{A}_{1,1}$ describes the directionally varying propagation owing to general anisotropy

$$\hat{A}_{1,1} = (\mathrm{j}\omega)^{-1} \begin{pmatrix} \partial_1 \\ \partial_2 \end{pmatrix} \begin{pmatrix} \varepsilon_{1,3}, \varepsilon_{2,3} \end{pmatrix} \varepsilon_{3,3}^{-1}. \tag{7.11}$$

Examining the above equations, we see that it is necesary to discretize the second-order derivatives ∂_1^2 and ∂_2^2, the first-order derivative ∂_1 and ∂_2 and the mixed second-order derivative $\partial_1\partial_2$.

7.1.2 Optimization

As in Section 5.1, the Thiele parameters are

$$\beta_1 = 1/2, \qquad \beta_2 = 1/8, \qquad \beta_3 = 1/2. \tag{7.12}$$

The parameters β_1, β_2 and β_3, however, can be adjusted by minimizing the difference between the principal parts of the longitudinal slowness and its continued-fraction approximation, defined by Equation (7.5), with respect to the L_2 norm over all the propagating modes (i.e., the real slowness surface). Thus, the artificial azimuthal anisotropy is minimized. The optimization is for the principal part of the left symbols, thus the polarization interaction owing to heterogeneity is excluded. For convenience, we restrict ourselves to isotropic media for the optimization procedure. The extension of the optimization procedure to anisotropic media is straightforward. Using an optimization routine based on the simplex method (E04CCF - NAG Fortran Library Routine), the following values are obtained for $c = c_{\text{ref}}$

$$\beta_1 = 0.531, \qquad \beta_2 = 0.379, \qquad \beta_3 = 0.835. \tag{7.13}$$

These values differ slightly from the values in (5.9), which belong to the 2-D wave propagation.

7.1.3 Dissipation trick

To suppress artifacts and aliasing (which may arise from the discretization to be carried out in the transverse direction) from the large transverse wave number components present in the wave-field, we may replace the real frequency ω by a complex one

$$\omega' = \omega(1 - j\Omega), \tag{7.14}$$

just in the expression for $j\omega\hat{\Gamma}$. See Subsection 5.1.3 for more details. This procedure results in a complexification of the expansion coefficient.

7.1.4 Co-moving frame of reference

To suppress artifacts in the longitudinal derivative, the numerical computations are done in a co-moving frame of reference, traveling in the direction of preference. In order to preserve the commutation relations between the internal terms of the longitudinal slowness ($\hat{\Xi}$s in Equation (7.5)), we introduce a co-moving reference frame in which $c_{\text{ref}}(x_3)$ is independent of x_1 and x_2. The change of frame yields

$$\hat{h}(x_k, \omega) = \exp(j\omega\tau_{\text{ref}})\hat{W}_1^{(0)}(x_k, \omega), \tag{7.15}$$

in which

$$\tau_{\text{ref}}(x_3) = \int_{\zeta=0}^{x_3} c_{\text{ref}}^{-1}(\zeta)\, d\zeta, \tag{7.16}$$

is a reference longitudinal travel time. Substituting (7.15) in (7.1) yields

$$\partial_3 \hat{h} + j\omega \left(\hat{\Gamma}^{(+)} - c_{\text{ref}}^{-1} \right) \hat{h} = 0. \tag{7.17}$$

Note that in Chapter 5, we introduced a local reference frame. This is especially useful for analyzing transient wave phenomena in media with large (but not fast) variations. Here, we introduced a transverse constant reference frame, because then the symmetry relations are preserved. These relations play an important role in the polarization coupling.

7.2 Discretization in the transverse directions

The transverse derivatives are approximated by finite-difference operators on a hexagonal grid. First, we discuss the criteria for discretizing. Subsequently, we analyze this hexagonal grid, the matrix reprentations of general finite-difference stencils and the elementary differencing. Then, we analyze some elementary difference operators, which are useful for analyzing the stability of the numerical scheme. Finally, we discuss the second-order derivatives, the first-order derivatives and the mixed second-order derivatives.

7.2.1 Discretization criteria

Our main goals are to create a **fast** numerical scheme with an as high as possible degree of **accuracy**. In discretizing the differential Equation (7.17), several criteria play a role. These criteria are now discussed. The final scheme will be a trade-off between these criteria. We first formulate our numerical goal. Subsequently, we discuss the representation in time-domain and summarize three reasons for using a hexagonal grid. Finally, we discuss our choices.

In order to create a **fast** numerical scheme, we must search for sparse and small matrix representations for the involved operators. A *sparse* matrix representation can be obtained by using finite-difference or finite-element approximations. It is noted that a finite-difference approximation and its rational extension require, under some conditions, the same density of the matrices for our rational approximation of the square root operator. Another important condition is that all rational approximations have the same denominator. However, this might have consequences for the accuracy. A *small* matrix representation can be obtained by reducing the computational window size with the aid of accurate absorbing boudary conditions and taking only a few discretization points per wavelength (the Nyquist limit is 2). Another possibility would be to use a nonuniform grid: there are many grid points in the neighborhood of the core of the configuration and fewer towards the outer regions. But when taking only a few points per wavelength, there is not much freedom left for varying the grid spacing.

In order to create an **accurate** numerical scheme, we must search for accurate approximations of the involved derivatives (first-order, second-order and mixed

second-order). It turns out that finite-difference approximations on a hexagonal grid maintain rotational symmetry in the leading order error term. This has considerable advantages in modeling wave propagation. A rational approximation does not necessarily lead to denser matrices. Using a rational finite-difference approximation of the involved derivatives is consistent with the third-order Thiele approximation of the square root and the (1,1) Padé approximation for integrating the longitudinal derivative. The rational spectral approximations have also consistent orders of accuracy: the matrices are not denser, but they are more difficult to invert due to the bad condition numbers.

Time-domain results are obtained by combining the computations at several frequencies. These computations should be performed at the same relative grid size: the number of points per wavelength in the reference medium should be the same for all frequencies. Consequently, the physical dimensions of the grid, Δx and Δx_3, differ between the frequencies. An interpolation procedure must be used to compute the field values at the grid, on which the numerical results are presented. This procedure has not yet been implemented.

The **reason** for using a hexagonal grid instead of an ordinary rectangular grid is threefold. First, the artificial azimuthal anisotropy due to the discretization in the transverse direction is the better suppressed, see Mersereau[198], and Peterson and Middleton[199]. Second, there is the advantage of the reduced number of grid points: a square grid requires 15.5% ($2/\sqrt{3}$) more grid points than a hexagonal grid in order to model the same Nyquist region. Third, rational approximations of the derivatives can be introduced to increase the accuray with two orders. These rational approximations do not increase the density of the final matrices in the Thiele approach, through which they are very attractive and useful. Besides, it is noted that a hexagonal grid is very attractive for a discrete Fourier transform, see also Mersereau[198], and Peterson and Middleton[199]. However, for the analysis presented here, no Fourier transform has been employed.

With the above discussion in mind, we choose for rational finite differences on a coarse uniform hexagonal grid. This is discussed in the remainder of this section.

7.2.2 Hexagonal grids, indices

A uniform hexagonal or triangular spatial grid (see Figure 7.1) is employed in the transverse $x_1 x_2$ plane. The mesh has the structure of a honey comb. Prisms form the cells of the mesh.

Since, in optoelectronic circuits, the waveguiding structures are often layered in one of the directions — this direction is perpendicular to the chip surface and is mostly called the transverse direction; it is common practice to draw it as the vertical direction in the plots — we choose the orientation of the grid according, see Figure 7.1. In addition, it is noted that the circular shape of optical glass fibers can be described very accurately on a hexagonal grid.
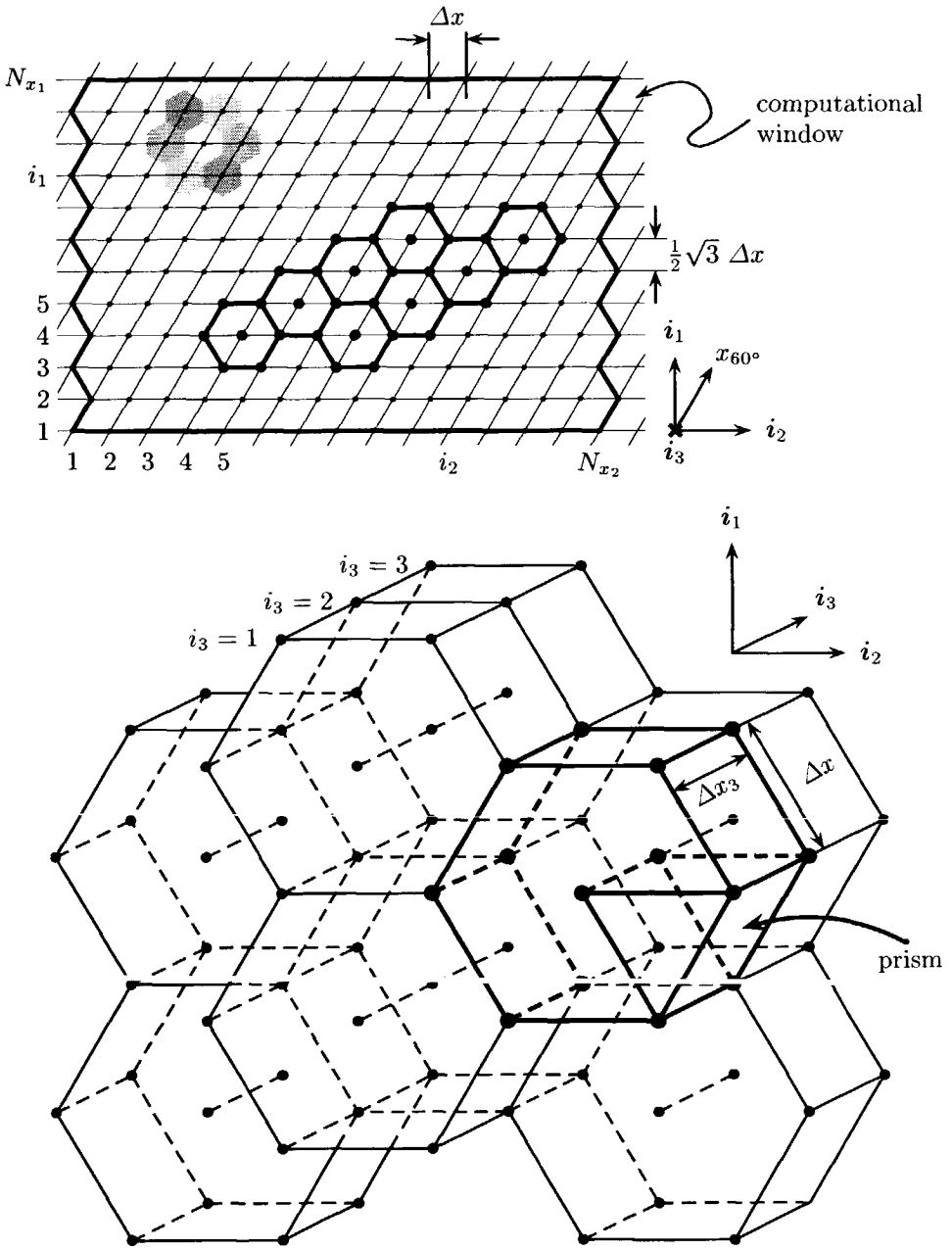
Figure 7.1:   Hexagonal grid. The upper figure shows the transverse cross-section of the 3-D grid in the lower figure. See text for the notation used.

The transverse sampling interval is denoted as Δx; the sampling interval equals

$$\Delta x_1 = \tfrac{1}{2}\sqrt{3}\Delta x, \qquad \Delta x_2 = \Delta x, \tag{7.18}$$

and the number of grid points equals N_{x_1} and N_{x_2} along the i_1-and i_2 directions, respectively. The total number of transverse grid points is $N_{x_\nu} = N_{x_1}N_{x_2}$. In the numerical implementation and in the figures in this thesis we choose N_{x_1} to be even. The edges of the outer cells constitute the computational window. The restriction introduced by this computational window causes numerical artifacts and therefore needs some special attention, see Section 7.4. The longitudinal grid spacing is denoted as Δx_3. This mesh parameter can be adaptively chosen along the preferred direction, which makes the grid nonuniform along the i_3 direction. In order to write the relevant operators in matrix form, we introduce a *slice index* i in the transverse plane (*slice*) according to

$$(i) = (..., (i_1, i_2 = 1), (i_1, 2), ..., (i_1, N_{x_2}), (i_1 + 1, 1), ...). \tag{7.19}$$

The ordering over first i_2 and subsequently over i_1 is preferred, since waveguiding properties in the x_2 direction are assumed to be weaker in many configurations under investigation. Thus, this formulation is a straightforward extension of the 2-D configuration.

The wave matrices, $\hat{W}^{(+)}$ and $\hat{W}^{(-)}$, and the field vector, $\hat{F}_1$ and $\hat{F}_2$, contain two components each. For the discretized vector the notation

$$\hat{h}_i(x_3; \omega) = \begin{cases} \hat{h}_1(x_{1;i}, x_{2;i}, x_3; \omega), & \text{if } 1 < i \le N_{x_\nu}, \\ \hat{h}_2(x'_{1;i-N_{x_\nu}}, x'_{2;i-N_{x_\nu}}, x_3; \omega), & \text{if } N_{x_\nu} < i \le 2N_{x_\nu}, \end{cases} \tag{7.20}$$

will be employed, where

$$x_{1;i} = i_1(i)\Delta x\sqrt{3}/2 = i_1(i)\Delta x_1, \tag{7.21}$$

$$x_{2;i} = [i_2(i) + 1/2]\Delta x - [i_1(i) \bmod 2]\Delta x/2, \tag{7.22}$$

with the transverse slice indices

$$i_1(i) = \text{int}[(i-1)/n_2] + 1, \tag{7.23}$$

$$i_2(i) = i \bmod n_2, \tag{7.24}$$

in which int[.] denotes the entier. Here, $x_{1;i}$ and $x_{2;i}$ are the coordinates of the first component and $x'_{1;i}$ and $x'_{2;i}$ are the coordinates of the second component of the field/wave matrix. For the second component, we use either the same grid (first strategy)

$$x'_{1;i} = x_{1;i}, \tag{7.25}$$
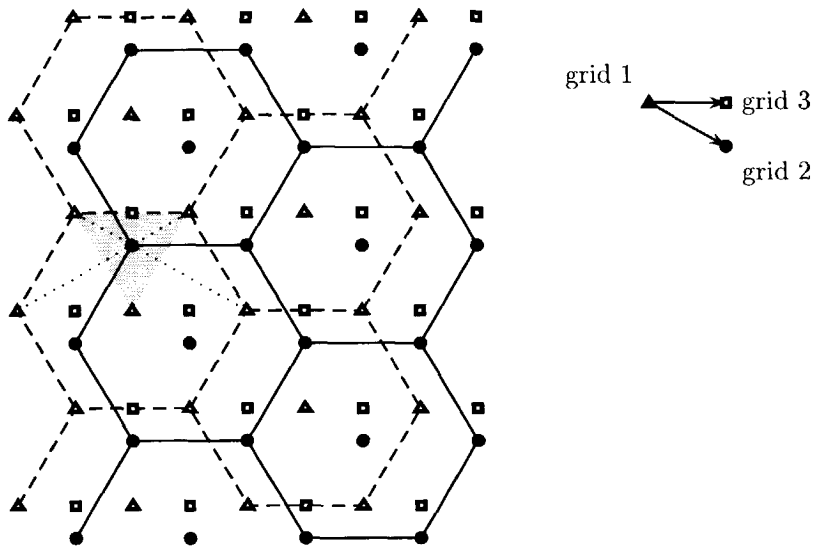
$$x'_{2;i} = x_{2;i}, \tag{7.26}$$

Figure 7.2:   The three grids: grid 1 (dashed line and triangular dots), grid 2 (solid lines and solid dots) and grid 3 (square dots).

or a shifted grid (second strategy)

$$x'_{1;i} = x_{1;i} - \Delta x_1/3 = [i_2(i) - 1/3]\Delta x_1, \tag{7.27}$$

$$x'_{2;i} = x_{2;i} + \Delta x/2 = [i_2(i) + 1]\Delta x - [i_1(i) \bmod 2]\Delta x/2. \tag{7.28}$$

In the second strategy, different grids (staggered grids) are used for the two components of each wave matrix $\hat{W}^{(+)}$ and $\hat{W}^{(-)}$ and one intermediate grid where the medium properties have to be evaluated (see Figure 7.2).

As for the longitudinal slowness, we employ a rational approximation of the spectra of the relevant partial differential operators.

7.2.3   Matrix representations of general finite-difference stencils

The discretization of the pseudo-differential equation is based upon a finite-difference scheme. The derivatives is replaced by fractions of finite-difference quotients. First, some basics of elementary finite-difference operators on hexagonal grids are discussed. Computational molecules represent these operators. They are also called stencils. The graphical symbolizations of the molecules used here are given in Figures 7.4, 7.5, 7.10, 7.12 and 7.13.

Let us consider a general molecule $M(x_1, x_2)$ on a hexagonal grid

$$(M\hat{u})(i_1\Delta x, i_2\Delta x_2)$$
$$\begin{aligned}
= \; & m_1(i)\hat{u}(x_1 + \sqrt{3}\Delta x/2, x_2 - \Delta x/2) & + \; & m_2(i)\hat{u}(x_1 + \sqrt{3}\Delta x/2, x_2 + \Delta x/2) \\
& + m_3(i)\hat{u}(x_1, x_2 - \Delta x) & & + m_4(i)\hat{u}(x_1, x_2) \\
& + m_5(i)\hat{u}(x_1, x_2 + \Delta x) & & + m_6(i)\hat{u}(x_1 - \sqrt{3}\Delta x/2, x_2 - \Delta x/2) \\
& + m_7(i)\hat{u}(x_1 - \sqrt{3}\Delta x/2, x_2 + \Delta x/2) & & + m_8(i)\hat{u}(x_1 + \sqrt{3}\Delta x/2, x_2 - 3\Delta x/2) \\
& + m_9(i)\hat{u}(x_1 - \sqrt{3}\Delta x/2, x_2 + 3\Delta x/2), & & \hspace{3cm} (7.29)
\end{aligned}$$

with its pictorial representation
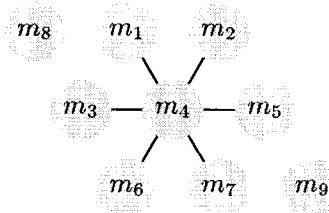
The structure of the corresponding matrix is shown in Figure 7.3. The matrix has three diagonal blocks that are themselves tridiagonal. This form is called *tridiagonal with fringes*. A Taylor series expansion of $\hat{u}$ about (x_1, x_2) will be used to determine the accuracy of the difference operator. The transposed molecule $M' = M^T$ of M is given by (left-hand side if i_1 is odd; right-hand side if i_1 is even)

$$\begin{aligned}
m_1'(i) &= m_7(i + N_{x_2} - 1), & m_1'(i) &= m_7(i + N_{x_2}), \\
m_2'(i) &= m_6(i + N_{x_2}), & m_2'(i) &= m_6(i + N_{x_2} + 1), \\
m_6'(i) &= m_2(i - N_{x_2}), & m_6'(i) &= m_2(i - N_{x_2} - 1), \\
m_7'(i) &= m_1(i - N_{x_2} + 1), & m_7'(i) &= m_1(i - N_{x_2}), \\
m_8'(i) &= m_1(i + N_{x_2} - 2), & m_8'(i) &= m_1(i + N_{x_2} - 1), \\
m_9'(i) &= m_1(i - N_{x_2} + 2), & m_9'(i) &= m_1(i - N_{x_2} + 1),
\end{aligned}$$

and

$$\begin{aligned}
m_3'(i) &= m_5(i - 1), \\
m_4'(i) &= m_4(i), \\
m_5'(i) &= m_3(i + 1).
\end{aligned}$$

A molecule M is said to be symmetric if $M^T = M$, skew-symmetric if $M^T = -M$, and self-adjoint if $M^H = (M^T)^* = M$. We will use only use 7-points (m_1-m_7) and 4-points molecules (m_4-m_6, m_9 or m_2-m_4, m_8 or m_1, m_3, m_4, m_6).

$m_4\,m_5$ $m_3\,m_4\,m_5$ $m_3\,m_4\,m_5$ $m_3\,m_4\,m_5$ $m_3\,m_4\,m_5$ $m_3\,m_4$	m_2 $m_1\,m_2$ $m_8\,m_1\,m_2$ $m_8\,m_1\,m_2$ $m_8\,m_1\,m_2$ $m_8\,m_1\,m_2$		$\ldots$
$m_6\,m_7\,m_9$ $m_6\,m_7\,m_9$ $m_6\,m_7\,m_9$ $m_6\,m_7\,m_9$ $m_6\,m_7$ m_6	$m_4\,m_5$ $m_3\,m_4\,m_5$ $m_3\,m_4\,m_5$ $m_3\,m_4\,m_5$ $m_3\,m_4\,m_5$ $m_3\,m_4$	$m_1\,m_2$ $m_8\,m_1\,m_2$ $m_8\,m_1\,m_2$ $m_8\,m_1\,m_2$ $m_8\,m_1\,m_2$ $m_8\,m_1$	$\ldots$
	$m_7\,m_9$ $m_6\,m_7\,m_9$ $m_6\,m_7\,m_9$ $m_6\,m_7\,m_9$ $m_6\,m_7\,m_9$ $m_6\,m_7$	$m_4\,m_5$ $m_3\,m_4\,m_5$ $m_3\,m_4\,m_5$ $m_3\,m_4\,m_5$ $m_3\,m_4\,m_5$ $m_3\,m_4$	$\ldots$
$\vdots$	$\vdots$	$\vdots$	$\ddots$

Figure 7.3: *The structure of the matrix corresponding to molecule* M. *Here,* $N_{x_1} = 6$. *All elements not shown are zero.*

7.2.4 Elementary differencing

Some elementary difference operators build up all other finite-difference operators. In this section, we investigate these elementary difference operators, which are the elementary molecules. Figure 7.4 shows the pictorial representation of these opera-~~tors~~.

The accuracy of these elementary difference operators can be analyzed using a Taylor series expansion. The gray dot indicates were the first-order derivative is approximated and reveals the shifts from one (input) grid to another shifted grid (output):

$$\bar{\bar{\delta}}_1,\ \bar{\delta}_2\ :\quad \text{grid 1} \rightarrow \text{grid 3},$$

$$\bar{\bar{\delta}}_1^{\mathrm{T}},\ \bar{\delta}_2^{\mathrm{T}}\ :\quad \text{grid 3} \rightarrow \text{grid 1},$$

$$\bar{\delta}_1\ \quad :\quad \text{grid 2} \rightarrow \text{grid 3},$$

$$\bar{\delta}_1^{\mathrm{T}}\ \quad :\quad \text{grid 3} \rightarrow \text{grid 2}.$$
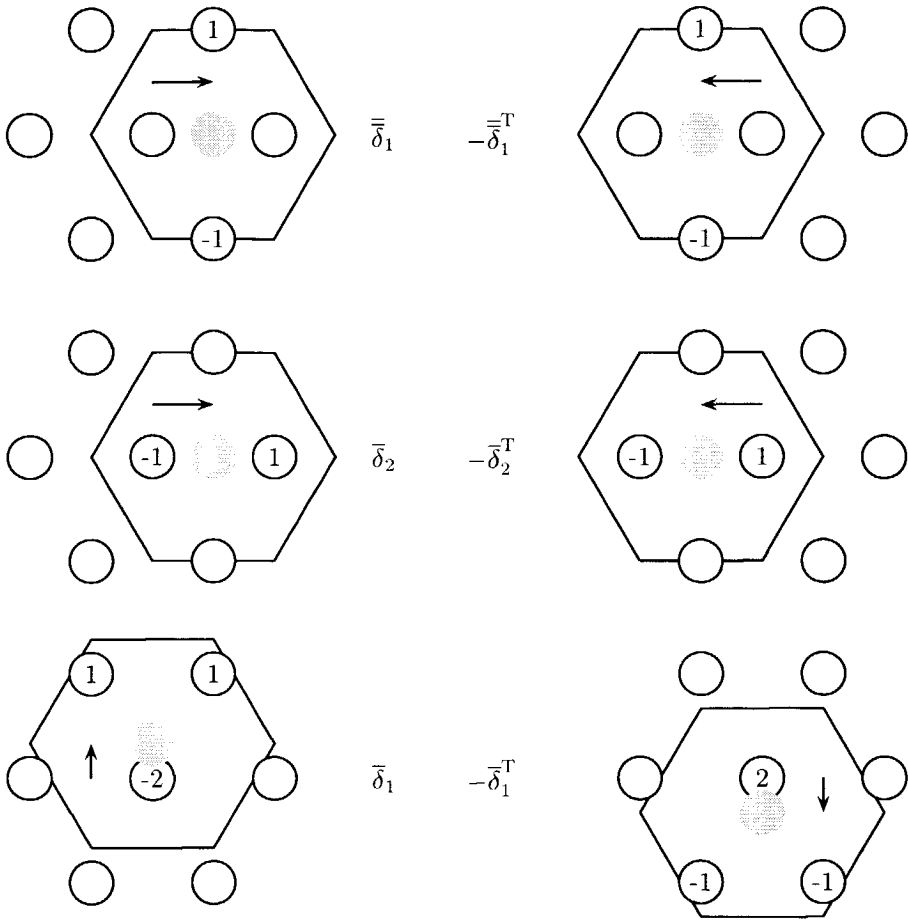
Figure 7.4: *Pictorial representation of the elementary difference operators. The gray dot indicates where the first-order derivative is approximated.*

The accuracy of the difference operators is found as

$$\bar{\bar{\delta}}_1 = \sqrt{3}\Delta x \partial_1 - \tfrac{1}{4}(\Delta x)^2(\partial_1^2 + \partial_2^2) + \tfrac{1}{24}\sqrt{3}(\Delta x)^3 \partial_1(\partial_1^2 + \partial_2^2) + \mathcal{O}[(\Delta x)^4],$$
(7.30)

$$\bar{\bar{\delta}}_1 = \sqrt{3}\Delta x \partial_1 + \tfrac{1}{8}\sqrt{3}(\Delta x)^3 \partial_1^3 + \mathcal{O}[(\Delta x)^5],$$
(7.31)

$$\bar{\bar{\delta}}_2 = \Delta x \partial_2 + \tfrac{1}{24}(\Delta x)^3 \partial_2^3 + \mathcal{O}[(\Delta x)^5].$$
(7.32)

The corresponding pictorial representations are shown in Figure 7.4. The arrows indicate the direction of the shifting of the grids. Note that leading order error term

in $\bar{\delta}_1$ is rotationally symmetric. In principal, the molecules $\bar{\bar{\delta}}_1$ and $\bar{\bar{\delta}}_2$ can be used to construct the numerical scheme. However, if we would like to construct the more general molecules only on the neighboring grid points, we must use the molecule $\bar{\delta}_1$. This is shown in the next subsections.

We also introduce a *neutral* difference operator δ_N for later use. The neutral operator equals 0 up to order $\mathcal{O}[(\Delta x)^2]$ (see Figure 7.10).

7.2.5 Laplace operator and second-order derivatives

In this section, the discretization of the Laplace operator $\partial_\nu \partial_\nu = \partial_1^2 + \partial_2^2$ and its two terms, the second-order derivatives ∂_1^2 and ∂_2^2 is discussed.

Laplace operator

The discretization of the Laplace operator ($\partial_\nu \partial_\nu = \partial_1^2 + \partial_2^2$) is formulated in terms of recursive filters based on nearest-neighbors interactions. Our recursive filter acting on a test function $\hat{u}$ is defined through

$$(1 + a_2 \delta_\perp^2)\langle \partial_\nu \partial_\nu \hat{u}\rangle = (\Delta x)^{-2} a_1 \delta_\perp^2 \hat{u}, \tag{7.33}$$

where the molecule $\delta_\perp^2$

$$
\begin{aligned}
(\delta_\perp^2 \hat{u})&(x_1, x_2) \\
&= \hat{u}(x_1, x_2 + \Delta x) + \hat{u}(x_1, x_2 - \Delta x) + \hat{u}(x_1 + \sqrt{3}\Delta x/2, x_2 + \Delta x/2) \\
&\quad + \hat{u}(x_1 - \sqrt{3}\Delta x/2, x_2 + \Delta x/2) \quad + \hat{u}(x_1 + \sqrt{3}\Delta x/2, x_2 - \Delta x/2) \\
&\quad + \hat{u}(x_1 - \sqrt{3}\Delta x/2, x_2 - \Delta x/2) \quad - 6\hat{u}(x_1, x_2),
\end{aligned} \tag{7.34}
$$

is graphically symbolized in Figure 7.5. In Equation (7.33), 1 denotes the identity and $\langle \partial_\nu \partial_\nu \hat{u}\rangle = \langle \partial_\nu \partial_\nu\rangle \hat{u}$ represents the approximate Laplace operator having acted on $\hat{u}$. The molecule $\delta_\perp^2$ is symmetric and thus the approximate Laplace operator is symmetric, too. The introduced rational approximation does not make the matrix representation of the longitudinal slowness denser. Using a Taylor series expansion of $\hat{u}$ about (x_1, x_2), $\delta_\perp^2$ is found as

$$\delta_\perp^2 = \left\{ \tfrac{3}{2}(\Delta x)^2 \partial_\kappa \partial_\kappa + \tfrac{3}{32}(\Delta x)^4 (\partial_\rho \partial_\rho)^2 + \mathcal{O}[(\Delta x)^6] \right\}. \tag{7.35}$$

Hence, the discretized Laplace operator equals

$$\langle \partial_\nu \partial_\nu\rangle = \tfrac{3}{2} a_1 \left\{ 1 + \tfrac{3}{2} a_2 (\Delta x)^2 \partial_\rho \partial_\rho + \mathcal{O}[(\Delta x)^4] \right\}^{-1}$$
$$\left\{ 1 + \tfrac{1}{16}(\Delta x)^2 \partial_\kappa \partial_\kappa + \mathcal{O}[(\Delta x)^4] \right\} \partial_\nu \partial_\nu. \tag{7.36}$$

Taking the following values of a_1 and a_2

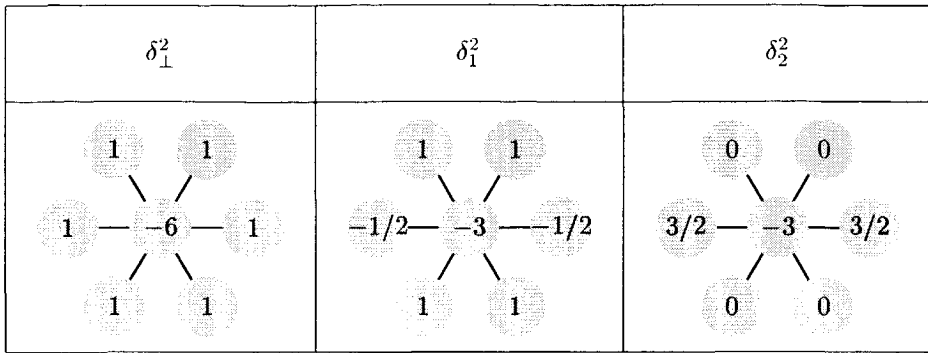$$a_1 = 2/3, \qquad a_2 = 1/24, \tag{7.37}$$

$\delta_\perp^2$	δ_1^2	δ_2^2

Figure 7.5: *The graphical symbolizations of the molecules $\delta_\perp^2$, δ_1^2 and δ_2^2, that correspond to the Laplace operator $\partial_\nu\partial_\nu$ and the operators ∂_1^2 and ∂_2^2.*

an error of order $\mathcal{O}[(\Delta x)^4]$ is obtained. The scheme is consistent and fourth-order accurate. Note that the leading order error term is rotationally symmetric. Instead, however, a_1 and a_2 are used as fitting parameters. Requiring that, in the limit $\Delta x \downarrow 0$, the spectrum (or left symbol) of $\langle\partial_\nu\partial_\nu\rangle$ tends to the spectrum of the Laplace operator up to the lowest order, leads necessarily to (using a Taylor series) $a_1 = 2/3$. The parameter a_2 is determined by minimizing nonlinearly the difference between the spectra of the approximate and the exact Laplace operators with respect to the L_2 norm over the Nyquist interval. Thus, a more accurate spectrum over the spatial bandwidth as a whole is obtained. Using an optimization routine based on the simplex method (E04CCF - NAG Fortran Library Routine), the following value for a_2 is obtained

$$a_2 = 0.0621. \tag{7.38}$$

It is noted, however, that if it is known beforehand that the actual bandwidth of the wave-field to be extrapolated, is limited by a radial transverse wave number $k_{\text{dis}} < k_{x,\text{Nyq}} = 2\pi/(\sqrt{3}\Delta x)$, the optimization should be carried out over this subband. This will be discussed later on. Figure 7.6 and Figure 7.7 illustrate the spectra of the exact and the approximated Laplace operators with a_1 and a_2 as in Equation (7.37) and as in Equation (7.38), respectively. A relatively large grid spacing is chosen to elucidate numerical artifacts. Note that the region between the azimuthal angles $0°$ and $30°$ contains all information of the spectrum. For comparison, Figure 7.8 illustrates the spectra of the approximated Laplace operator on a square grid. The corresponding discretized Laplace operator equals

$$\langle\partial_\nu\partial_\nu\rangle = \partial_\nu\partial_\nu + \tfrac{1}{12}(\Delta x)^2\left(\partial_1^4 + \partial_2^4\right) + \mathcal{O}[(\Delta x)^4]. \tag{7.39}$$

The leading order error term is no longer rotationally symmetric, which is apparent in the figure.
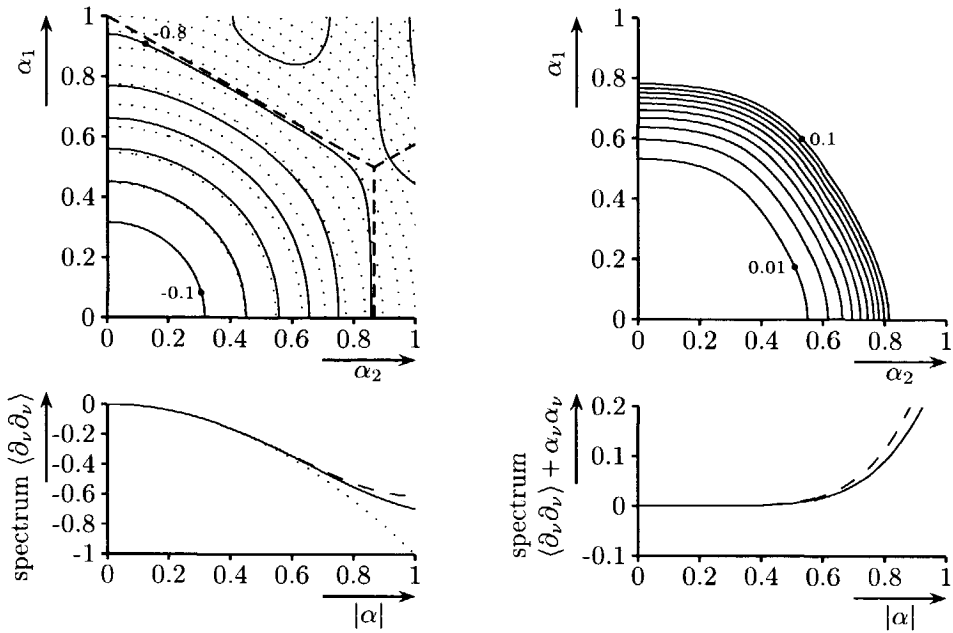
Figure 7.6:   *The spectrum or symbol of the approximate Laplace operator $\partial_\nu\partial_\nu$*
with $a_2 = 1/24$ (solid line; upper left), the exact Laplace operator
(dotted line; upper and lower left) and their difference (upper right).
The corresponding curves for $\alpha_1 = 0$ and $\alpha_2 = 0$ are drawn in the
lower figures (solid and dashed lines, respectively). The dashed line
in the upper figure indicates the borders of the Nyquist region and
the structure of the grid in the Fourier domain. Here, $\omega = 1$ s^{-1}
and $\Delta x_1 = \pi$ m.

Second-order derivatives

The Laplace molecule can be split into two parts

$$\delta_\perp^2 = \delta_1^2 + \delta_2^2. \tag{7.40}$$

The difference operators δ_1^2 and δ_2^2 correspond to derivatives ∂_1^2 and ∂_2^2, respectively.
They are graphically symbolized in Figure 7.5. The leading order error term is not
rotationally symmetric

$$\tfrac{2}{3}\delta_2^2\hat{u} = (\Delta x)^2\partial_2^2\hat{u} + \tfrac{1}{12}(\Delta x)^4\partial_2^4\hat{u} + \mathcal{O}[(\Delta x)^6]. \tag{7.41}$$
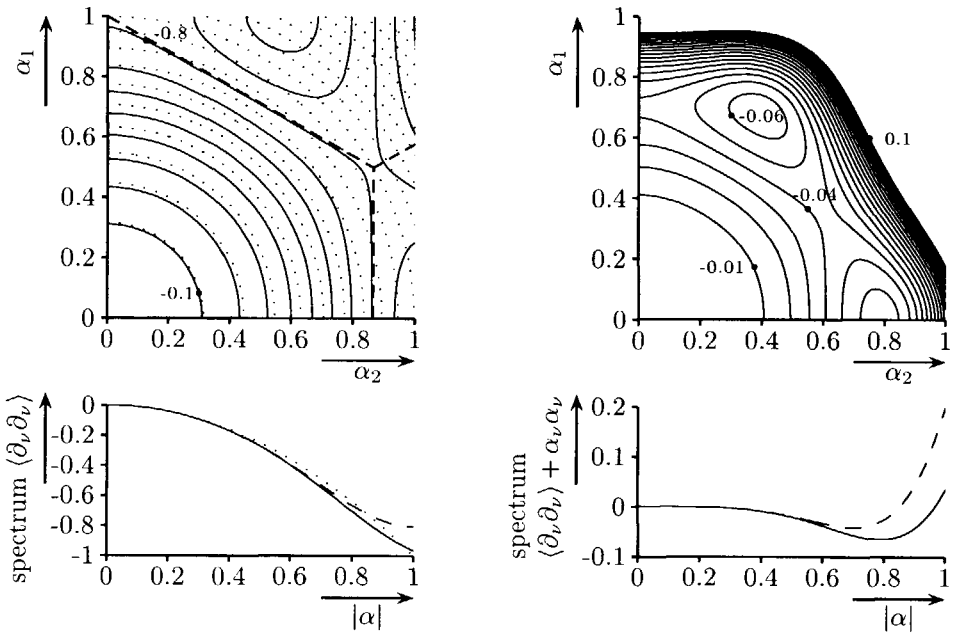
Figure 7.7:   *Idem as for Figure 7.6, but now with $a_2 = 0.0621$.*

The difference operators δ_1^2 and δ_2^2 can be split into compositions of two corresponding elementary difference operators,

$$\delta_1^2 = -\tfrac{1}{2}\overline{\delta}_1^{\mathrm{T}}\overline{\delta}_1, \tag{7.42}$$

$$\delta_2^2 = -\tfrac{3}{2}\overline{\delta}_2^{\mathrm{T}}\overline{\delta}_2. \tag{7.43}$$

Figure 7.9 shows the spectrum of the approximated second-order derivatives δ_1^2 and δ_2^2.

7.2.6   First-order derivatives

Here, the discretization of the first-order derivatives ∂_1 and ∂_2 is discussed.

The discretization of the polarization coupling operator is also formulated in terms of recursive filters based upon nearest-neighbours interactions. These polarization coupling terms contain the first-order derivatives ∂_1 and ∂_2. Our recursive filter acting on $\hat{u}$ is defined through

$$(1 + a_4\delta_\perp^2)\langle\partial_\nu\hat{u}_\nu\rangle = (\Delta x)^{-1}a_3(\delta_\nu\hat{u}_\nu), \tag{7.44}$$
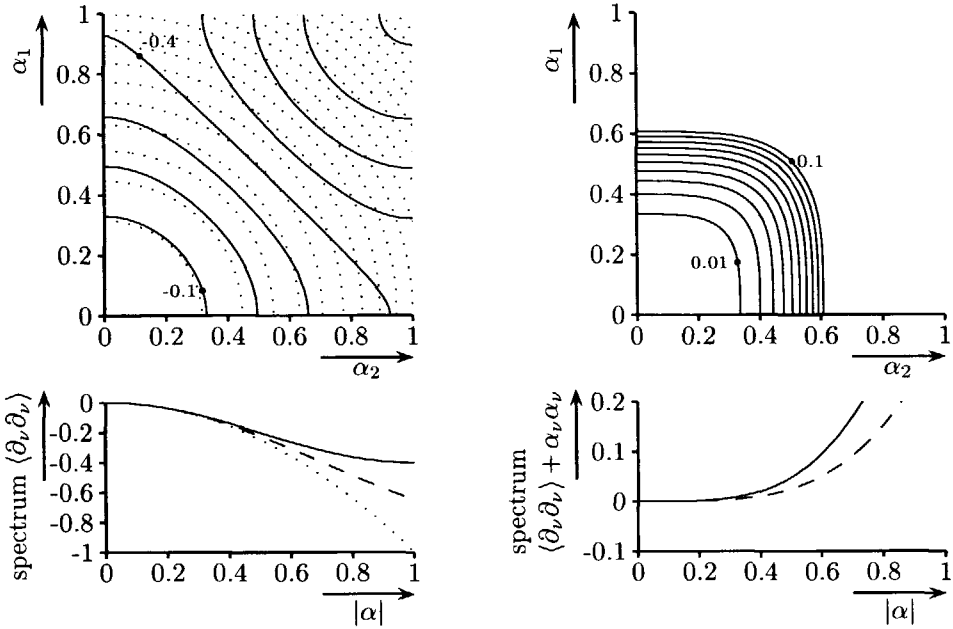
Figure 7.8:   *Idem as for Figure 7.6, but now for a square grid and $\Delta x = \pi$ m. Thus with 15.5% more grid points than a hexagonal grid with $\Delta x_1 = \pi$ m. The lower curves correspond to $\alpha_1 = 0$ (dashed) and $\alpha_1 = \alpha_2$ (solid).*

Figure 7.9:   *The real part of the spectrum or symbol of the approximate (solid) and exact (dotted) second-order derivatives ∂_1^2 (left) and ∂_2^2 (right) with $a_2 = 0.0621$. Here $\omega = 1$ s^{-1} and $\Delta x_1 = \pi$ m.*

δ_1	δ_2	δ_N
$\sqrt{3}$ $\sqrt{3}$ \ / $0 - 0 - 0$ / \ $-\sqrt{3}$ $-\sqrt{3}$	-1 1 \ / $-2 - 0 - 2$ / \ -1 1	-1 1 \ / $1 - 0 - -1$ / \ -1 1

Figure 7.10: *The graphical symbolizations of the molecules δ_1, δ_2 and δ_N that correspond to the first derivatives ∂_1 and ∂_2, and the zero matrix up to $\mathcal{O}[(\Delta x)^3]$.*

where the molecules δ_1 and δ_2 are
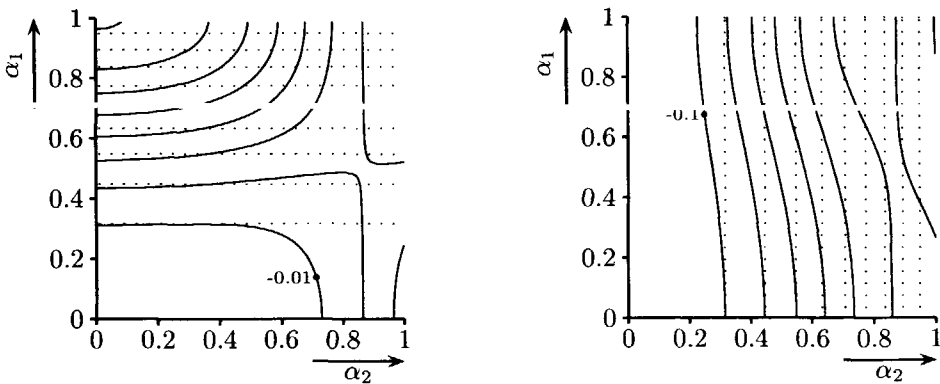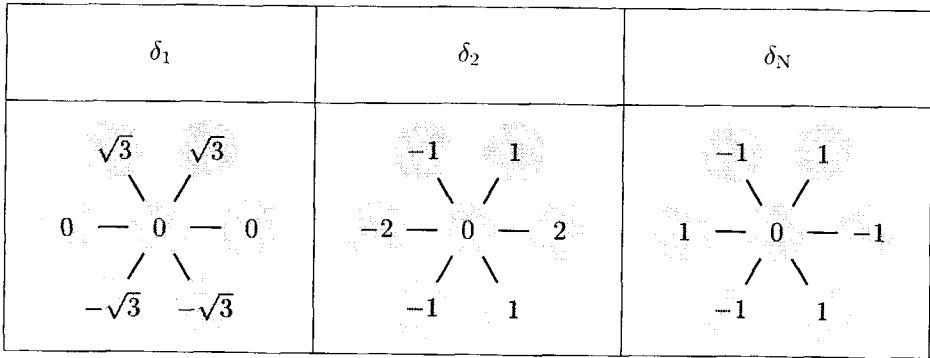
$$(\delta_1 \hat{u})(x_1, x_2) = \sqrt{3}\left[\hat{u}(x_1 + \sqrt{3}\Delta x/2, x_2 + \Delta x/2) - \hat{u}(x_1 - \sqrt{3}\Delta x/2, x_2 - \Delta x/2) \right.$$
$$\left. -\hat{u}(x_1 - \sqrt{3}\Delta x/2, x_2 + \Delta x/2) + \hat{u}(x_1 + \sqrt{3}\Delta x/2, x_2 - \Delta x/2) \right],$$

$$(7.45)$$

and

$$(\delta_2 \hat{u})(x_1, x_2) = 2\ \hat{u}(x_1, x_2 + \Delta x) \qquad\qquad - 2\ \hat{u}(x_1, x_2 - \Delta x)$$
$$+ \hat{u}(x_1 + \sqrt{3}\Delta x/2, x_2 + \Delta x/2) + \quad \hat{u}(x_1 - \sqrt{3}\Delta x/2, x_2 + \Delta x/2)$$
$$- \hat{u}(x_1 + \sqrt{3}\Delta x/2, x_2 - \Delta x/2) - \quad \hat{u}(x_1 - \sqrt{3}\Delta x/2, x_2 - \Delta x/2),$$

$$(7.46)$$

and $\delta_\perp^2$ as in (7.34). Figure 7.10 shows their graphical symbolizations. Due to the rotational symmetry of the leading order term, the same denominator as for the Laplace operator can be used. Using a Taylor series expansion of $\hat{u}$ about (x_1, x_2), δ_1 and δ_2 are found as

$$\delta_\nu = \left\{6\Delta x + \tfrac{3}{4}(\Delta x)^2 \partial_\kappa \partial_\kappa + \mathcal{O}[(\Delta x)^4]\right\} \partial_\nu. \qquad (7.47)$$

The discretized derivative $\langle\partial_\nu\rangle$ equals

$$\langle\partial_\nu\rangle = 6a_3 \left\{1 + \tfrac{3}{2}a_4(\Delta x)^2 \partial_\kappa \partial_\kappa + \mathcal{O}[(\Delta x)^4]\right\}^{-1}$$
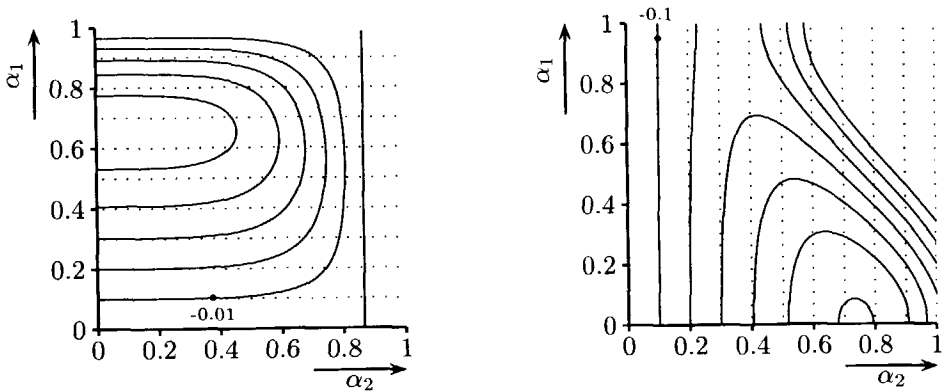$$\left\{1 + \tfrac{1}{8}(\Delta x)^2 \partial_\rho \partial_\rho + \mathcal{O}[(\Delta x)^4]\right\} \partial_\nu. \quad (7.48)$$

Figure 7.11: *The imaginary part of the spectrum or symbol of the approximate (solid) and exact (dotted) derivatives ∂_1 (left) and ∂_2 (right) with $a_4 = 1/12$. Here $\omega = 1$ s^{-1} and $\Delta x_1 = \pi$ m.*

Taking the following values of a_3 and a_4

$$a_3 = 1/6, \qquad a_4 = 1/12, \tag{7.49}$$

an error of order $\mathcal{O}[(\Delta x)^4]$ is obtained. Note that the leading order error term is rotationally symmetric. Instead, however, a_3 and a_4 are used as fitting parameters. Requiring that, in the limit $\Delta x \downarrow 0$, the spectrum of $\langle \partial_\nu \rangle$ tends to the spectrum of the derivative up to the lowest order, leads necessarily to (using a Taylor series) $a_3 = 1/6$. The parameter a_4 is determined by minimizing nonlinearly the difference between the spectra of the approximate and the exact derivatives with respect to the L_2 norm over the Nyquist-interval. Thus, a more accurate spectrum over the spatial bandwidth as a whole is obtained. Instead of using an optimization routine based on the simplex method (E04CCF - NAG Fortran Library Routine), as we have done for determining a_2, we choose

$$a_4 = a_2. \tag{7.50}$$

The main advantage of this choice is that the approximate Laplace operator and the approximate first-order derivatives have a common denominator. Therefore, the final scheme will contain sparser matrices. Figure 7.11 illustrates the spectrum of the exact and approximated derivatives ∂_1 and ∂_2 with a_3 and a_4 as in Equation (7.49). The deviation between the exact and numerical derivatives is reasonable large near the boundaries of the grid, because these numerical molecules were not optimized.

The difference operators δ_1 and δ_2 can be split into the elementary difference

operators,

$$\delta_1 = \sqrt{3}\left(\overline{\overline{\delta}}_1 - \overline{\overline{\delta}}_1^T\right), \tag{7.51}$$

$$\delta_2 = 3\left(\overline{\delta}_2 - \overline{\delta}_2^T\right) + \delta_N, \tag{7.52}$$

where δ_N is the *neutral* difference operator: it is a zero operator up to $\mathcal{O}[(\Delta x)^2]$ (see Figure 7.10). By discretizing the polarization coupling in this way, high degree of accuracy for the molecules is obtained, but corresponding discretization of the original operators, $\hat{A}_{1,2}$ and $\hat{A}_{2,1}$ is lost. This problem is also faced to on a rectangular grid, but it is solved by using a staggered rectangular grid.

7.2.7 Mixed second-order derivative

The discretization of the mixed second-order derivative, $\partial_1\partial_2$, can be accomplished in several ways.

Discretization of $\partial_1\partial_2$

For the operator $\hat{A}_{1,2}$ we need to compute $\partial_1\partial_2$. Note that this operator cannot be defined on a square grid using only the four neighboring grid points, see Rivera[114]. Our recursive filter acting on $\hat{u}$ is defined through the rational equation

$$(1 + a_8\delta_1^2 + a_9\delta_2^2)\langle\partial_1\partial_2\hat{u}\rangle = (\Delta x)^{-2}a_7\delta_{12}\hat{u}, \tag{7.53}$$

where the molecule δ_{12} is

$$\begin{aligned}(\delta_{12}\hat{u})(x_1, x_2) = &\ \hat{u}(x_1 + \sqrt{3}\Delta x/2, x_2 + \Delta x/2) - \hat{u}(x_1 - \sqrt{3}\Delta x/2, x_2 + \Delta x/2) \\ &- \hat{u}(x_1 + \sqrt{3}\Delta x/2, x_2 - \Delta x/2) + \hat{u}(x_1 - \sqrt{3}\Delta x/2, x_2 - \Delta x/2).\end{aligned} \tag{7.54}$$

The pictorial representation of the molecule δ_{12} is shown in Figure 7.12. Using a Taylor series expansion of $\hat{u}$ about (x_1, x_2), δ_{12} is found as

$$\delta_{12} = \sqrt{3}(\Delta x)^2\left[1 + \frac{1}{24}(\Delta x)^2(3\partial_1^2 + \partial_2^2)\right]\partial_1\partial_2. \tag{7.55}$$

It is observed that also on a hexagonal grid, we have to pay a price: the leading order error term is not rotationally symmetric. The discretized operator $\partial_1\partial_2$ equals

$$\langle\partial_1\partial_2\hat{u}\rangle = a_7\sqrt{3}\left\{1 + \frac{3}{2}(\Delta x)^2(a_8\partial_1^2 + a_9\partial_2^2) + \mathcal{O}[(\Delta x)^4]\right\}^{-1}$$
$$\left\{1 + \frac{1}{24}(\Delta x)^2(3\partial_1^2 + \partial_2^2) + \mathcal{O}[(\Delta x)^4]\right\}\partial_1\partial_2\hat{u}. \tag{7.56}$$
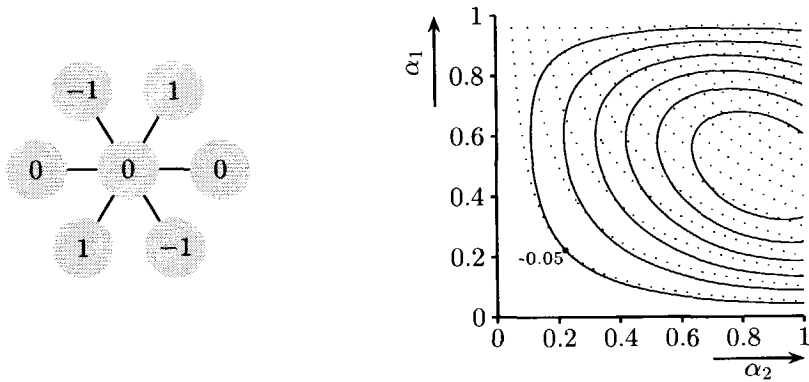
Figure 7.12: Left: pictorial representation of the molecule δ_{12}. Right: the real part of the spectrum or symbol of the approximate (solid) and exact (dotted) second-order derivative $\partial_1 \partial_2$ with $a_2 = 0.0621$. Here $\Delta x_1 = \pi$.

Taking the following values of a_7, a_8 and a_9

$$a_7 = \frac{1}{\sqrt{3}}, \qquad a_8 = \frac{1}{12}, \qquad a_9 = \frac{1}{36}, \qquad (7.57)$$

an error of order $\mathcal{O}[(\Delta x)^4]$ is obtained. Instead, however, a_8 and a_9 are chosen to be

$$a_8 = a_9 = a_2. \qquad (7.58)$$

By doing this, the numerical scheme preserves big sparseness. Figure 7.12 illustrates the spectrum of the discretized $\langle \partial_1 \partial_2 \hat{u} \rangle$.

The molecule δ_{12} can be split into two elementary difference operators

$$\delta_{12} = -\bar{\bar{\delta}}_1 \bar{\delta}_2^1. \qquad (7.59)$$

Discretization of $\partial_1 \partial_2$ based upon the molecules $-\bar{\delta}_1^{\mathrm{T}} \bar{\delta}_2$ and $-\bar{\delta}_2^{\mathrm{T}} \bar{\delta}_1$

Figure 7.13 shows the pictorial representation of the molecules $-\bar{\delta}_1^{\mathrm{T}} \bar{\delta}_2$ and $-\bar{\delta}_2^{\mathrm{T}} \bar{\delta}_1$. Using a Taylor series expansion, $-\bar{\delta}_1^{\mathrm{T}} \bar{\delta}_2$ and $-\bar{\delta}_2^{\mathrm{T}} \bar{\delta}_1$ are found as

$$-\bar{\delta}_1^{\mathrm{T}} \bar{\delta}_2 = \sqrt{3}(\Delta x)^2 \partial_1 \partial_2 + \tfrac{1}{4}(\Delta x)^3 \partial_2 (\partial_1^2 + \partial_2^2) + \mathcal{O}[(\Delta x)^4], \qquad (7.60)$$

$$-\bar{\delta}_2^{\mathrm{T}} \bar{\delta}_1 = \sqrt{3}(\Delta x)^2 \partial_1 \partial_2 - \tfrac{1}{4}(\Delta x)^3 \partial_2 (\partial_1^2 + \partial_2^2) + \mathcal{O}[(\Delta x)^4]. \qquad (7.61)$$

When using the molecule $\bar{\bar{\delta}}_1$, a higher accuracy is obtained ($\mathcal{O}[(\Delta x)^2]$) for $\langle \partial_2 \partial_1 \rangle$, see Equations (7.59) and (7.55), but the accuracy of the corresponding Laplace operator
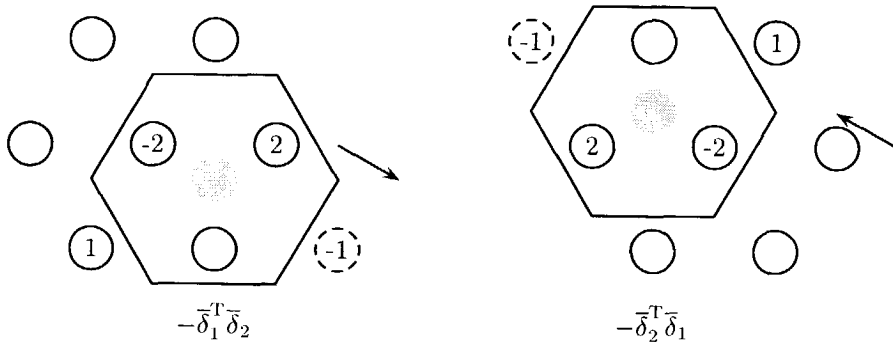
Figure 7.13: *Pictorial representations of the molecules* $-\bar{\delta}_1^{\mathrm{T}}\bar{\delta}_2$ *and* $-\bar{\delta}_2^{\mathrm{T}}\bar{\delta}_1$. *The gray dot indicates where the mixed second-order derivative is approximated.*

$(\bar{\bar{\delta}}_1^{\mathrm{T}}\bar{\bar{\delta}}_1 + \bar{\delta}_2^{\mathrm{T}}\bar{\delta}_2)$ deteriorates, namely to $\mathcal{O}[(\varDelta x)]$. The leading order error term has partly rotational symmetry.

To compute the molecules involving ε, as in $-\bar{\delta}_2^{\mathrm{T}}\varepsilon_{3,3}^{-1}\bar{\delta}_1$, $\varepsilon_{3,3}$ should be determined on the intermediate grid 3.

In view of the order of accuracy, this discretization has a few disadvantages: in order to increase the accuracy of the Laplace operator, a rational approximation of the finite difference operators can be employed. The accuracy of $\langle\partial_1\partial_2\rangle$ is, however, then not increased.

With creating a simple and stable numerical scheme in view, this discretization has the preference.

7.3 Matrix representation of the one-way propagator

Having introduced the transverse discretization, we can discretize the scaled transverse Helmholtz operator. We discuss two strategies. In the first strategy we directly discretize the transverse Helmholtz operator. The second strategy is based upon discretization the building blocks of the transverse Helmholtz operator. These discretizations lead to systems of ordinary differential equations. These equation are integrated over a finite distance, which leads to matrix equation: the propagator can be extracted. The propagator contains two sparse matrix multplications and two sparse matrix inversions. The condition number of these matrices is estimated in order to control the computational speed of the matrix inversions.

Table 7.1:   *The two strategies and the molecules used.*

	$\partial_\nu \partial_\nu$	∂_1^2	∂_2^2	$\partial_1 \partial_2$	∂_1	∂_2
strategy 1	$\delta_\perp^2$	δ_1^2	δ_2^2	δ_{12}	δ_1	δ_2
strategy 2	$-\bar{\delta}_1^T \bar{\delta}_1 - \bar{\delta}_2^T \bar{\delta}_2$	$-\bar{\delta}_1^T \bar{\delta}_1$	$-\bar{\delta}_2^T \bar{\delta}_2$	$-\bar{\delta}_1^T \bar{\delta}_2$	$\bar{\delta}_1, -\bar{\delta}_1^T$	$\bar{\delta}_2, -\bar{\delta}_2^T$

7.3.1   Discretized transverse Helmholtz operator: first strategy

After discretization the scaled transverse Helmholtz operators obtain the following forms,

$$\langle \hat{\Xi}_{\mathrm{EFN}} \rangle = \mathsf{C}^{-1} \hat{\mathsf{M}}, \tag{7.62}$$

$$\langle \hat{\Xi}_{\mathrm{MFN}} \rangle = \hat{\mathsf{M}}^T \mathsf{C}^{-1}. \tag{7.63}$$

Matrix C represents the common denominator and is found to be (see Equation (7.33))

$$\mathsf{C} = (1 + a_2 \delta_\perp^2). \tag{7.64}$$

It is convenient to split matrix $\hat{\mathsf{M}}$ into two parts

$$\hat{\mathsf{M}} = \hat{\mathsf{M}}_1 + r_t^2 \hat{\mathsf{M}}_2, \tag{7.65}$$

where r_t is the reference transverse sampling rate

$$r_t = \frac{c_{\mathrm{ref}}}{\omega \Delta x}. \tag{7.66}$$

In a general anisotropic configuration, the matrices M_1 and M_2 are given by

$$\mathsf{M}_1 = (1 + a_2 \delta_\perp^2)(\varepsilon_{\mathrm{ref}}^{-1} \varepsilon' - 1), \tag{7.67}$$

$$\mathsf{M}_2 = \begin{pmatrix} a_1 \delta_1^2 & a_7 \delta_{12} \\ a_7 \delta_{12} & a_1 \delta_2^2 \end{pmatrix} \varepsilon' \varepsilon_{3,3}^{-1} + \begin{pmatrix} a_1 \delta_2^2 & -a_7 \delta_{12} \\ -a_7 \delta_{12} & a_1 \delta_1^2 \end{pmatrix}$$

$$+ a_3 \Delta x \begin{pmatrix} \delta_1 \\ \delta_2 \end{pmatrix} \left((\partial_1 \varepsilon_{3,3}^{-1}) \quad (\partial_2 \varepsilon_{3,3}^{-1}) \right) \varepsilon'. \tag{7.68}$$

However, by discretizing the transverse Helmholtz operator in this way the equality between the transverse Helmholtz operator $\hat{A}_{EFN}$ and the composition of operators $\hat{A}_{1,2}$ and $\hat{A}_{2,1}$ is lost:

$$\langle\hat{A}_{EFN}\rangle \simeq \langle\hat{A}_{1,2}\rangle\langle\hat{A}_{2,1}\rangle, \qquad \langle\hat{A}_{MFN}\rangle \simeq \langle\hat{A}_{2,1}\rangle\langle\hat{A}_{1,2}\rangle. \qquad (7.69)$$

In addition, the operators $\langle\hat{A}_{1,2}\rangle$ and $\langle\hat{A}_{2,1}\rangle$ themselves must preserve their symmetry. Therefore, the symmetry relation in Equation (6.88) and also stability might have been lost in the above discretization procedure. In order to force numeric stability, the whole scheme has to be eveluated in both the electric-field and magnetic-field strength normalization analogs. See also the detailed discussion in Subsection 6.6.2.

7.3.2 Discretized transverse Helmholtz operator: second strategy

An alternative approach "ensuring stability" yields discretizing the operators $\hat{A}_{1,2}$ and $\hat{A}_{2,1}$ first, as given in Equations (6.36) and (6.37). In order to obtain a scheme on the smallest molecule of a hexagonal grid we substitute $\overline{\delta}_1$ ($\overline{\delta}_2$) for the derivative ∂_1 (∂_2) on the right-hand side, and their transpose for the derivatives on the left-hand side. By doing this, we find the symmetric operators

$$\langle\hat{A}_{1,2}\rangle = \mu_0 + \omega^{-2}(\Delta x)^{-2} \begin{pmatrix} -\overline{\delta}_1^{T}/\sqrt{3} \\ -\overline{\delta}_2^{T} \end{pmatrix} \varepsilon_{3,3}^{-1} \left(\overline{\delta}_1/\sqrt{3} \quad \overline{\delta}_2\right), \qquad (7.70)$$

$$\langle\hat{A}_{2,1}\rangle = \varepsilon' + \mu_0^{-1}\omega^{-2}(\Delta x)^{-2} \begin{pmatrix} \overline{\delta}_2 \\ -\overline{\delta}_1/\sqrt{3} \end{pmatrix} \left(-\overline{\delta}_2^{T} \quad \overline{\delta}_1^{T}/\sqrt{3}\right). \qquad (7.71)$$

The corresponding discretized transverse Helmholtz operator equals

$$\langle\hat{A}_{EFN}\rangle = \langle\hat{A}_{1,2}\rangle\langle\hat{A}_{2,1}\rangle, \qquad \langle\hat{A}_{MFN}\rangle = \langle\hat{A}_{2,1}\rangle\langle\hat{A}_{1,2}\rangle. \qquad (7.72)$$

Note that the terms of order ω^{-4} vanish (compare with Equation (6.82)). This term also vanishes by taking $\overline{\overline{\delta}}_1$ instead of $\overline{\delta}_1$. It is, however, not clear how to introduce the common denominator $(1 + a_2\delta_\perp^2)$ in Equation (7.70) without disturbing the symmetry. The scaled transverse Helmholtz operator equals

$$\langle\hat{\Xi}_{EFN}\rangle = \langle\hat{\Xi}_{MFN}\rangle^T = \mathsf{C}\hat{\mathsf{M}}', \qquad (7.73)$$

with

$$\hat{\mathsf{M}}' = \mathsf{M}_1 + r_t^2\mathsf{M}_2'. \qquad (7.74)$$

In a general anisotropic configuration, the matrix M_2' equals

$$\mathsf{M}_2' = \mathsf{C} \begin{pmatrix} -\overline{\delta}_1^{T}/\sqrt{3} \\ -\overline{\delta}_2^{T} \end{pmatrix} \varepsilon_{3,3}^{-1} \left(\overline{\delta}_1/\sqrt{3} \quad \overline{\delta}_2\right) \varepsilon' + \mu_0^{-1} \begin{pmatrix} \overline{\delta}_2 \\ -\overline{\delta}_1 \end{pmatrix} \left(-\overline{\delta}_2^{T} \quad \overline{\delta}_1^{T}/\sqrt{3}\right) \varepsilon'. \qquad (7.75)$$

It is observed that this scheme has denser matrices than the scheme in the previous subsection. This is due to the presence of C in M_2'.

7.3.3   System of ordinary differential equations

Substituting the discretized transverse Helmholtz operator into the one-way wave equation (7.1) with longitudinal slowness (7.5), we obtain a system of ordinary differential equations of the form

$$(1 + \beta_3 \langle \hat{\Xi} \rangle) \partial_3 \hat{h} + j \omega c_{\text{ref}}^{-1} (\beta_1 \langle \hat{\Xi} \rangle + \beta_2 \langle \hat{\Xi} \rangle^2 + c_{\text{ref}} (1 + \beta_3 \langle \hat{\Xi} \rangle) \langle \hat{A}_{1,1} \rangle) \hat{h}. \tag{7.76}$$

7.3.4   Integration of the longitudinal derivative

The solution of (7.76) can formally be written as a product integral. This product integral has to be evaluated, recursively, for every propagation step with size Δx_3. The product integral is given by

$$\hat{h}(x_\nu, x_3 + \Delta x_3) = \prod_{\zeta = x_3}^{x_3 + \Delta x_3}$$

$$\exp \left\{ -j \omega \left[c_{\text{ref}}^{-1} (1 + \beta_3 \langle \hat{\Xi} \rangle)^{-1} (\beta_1 \langle \hat{\Xi} \rangle + \beta_2 \langle \hat{\Xi} \rangle^2) + \langle \hat{A}_{1,1} \rangle \right] (x_\nu, \zeta) \, d\zeta \right\}$$

$$\hat{h}(x_\nu, x_3). \tag{7.77}$$

It is approximated by

$$\hat{h}(x_\nu, x_3 + \Delta x_3) \simeq$$

$$\exp \left\{ -j \omega \Delta x_3 \left[c_{\text{ref}}^{-1} (1 + \beta_3 \langle \hat{\Xi} \rangle)^{-1} (\beta_1 \langle \hat{\Xi} \rangle + \beta_2 \langle \hat{\Xi} \rangle^2) + \langle \hat{A}_{1,1} \rangle \right] (x_\nu, x_3 + \tfrac{1}{2} \Delta x_3) \right\}$$

$$\hat{h}(x_\nu, x_3). \tag{7.78}$$

To speed up the computations, the exponent is approximated by a (n, n)-Padé approximant. The $(1,1)$-Padé approximant is given by

$$\exp(Z) \simeq \frac{1 + \beta_0 Z}{1 - \beta_9 Z}, \tag{7.79}$$

where

$$Z \equiv \Delta x_3 \partial_3 \Big|_{x_3 + \Delta x_3 / 2}, \tag{7.80}$$

is the derivative that appears in Equation (7.76). According to Padé's formula, we have

$$\beta_9 = 1/2. \tag{7.81}$$

Instead of taking this exact value, we let β_9 be a free parameter for an optimization procedure. If $\hat{A}_{1,1} = 0$, the numerical scheme can be written as a two-step scheme:

the (1,1)-Padé approximation of the exponent yields

$$(1 - \beta_{11}\langle\hat{\Xi}\rangle)\,(1 - \beta_{12}\langle\hat{\Xi}\rangle)\,\hat{h}(x_3 + \Delta x_3) = (1 + \beta_{13}\langle\hat{\Xi}\rangle)\,(1 + \beta_{14}\langle\hat{\Xi}\rangle)\,\hat{h}(x_3),$$
(7.82)

with

$$\beta_{11} = -\tfrac{1}{2}\beta_3 - \tfrac{1}{2}j\beta_9 r_1^{-1}\beta_1 - \tfrac{1}{2}\left[\left(\beta_3 + \tfrac{1}{2}j\beta_9 r_1^{-1}\beta_1\right)^2 - 4j\beta_9 r_1^{-1}\beta_2\right]^{1/2},$$
(7.83)

$$\beta_{12} = -\tfrac{1}{2}\beta_3 - \tfrac{1}{2}j\beta_9 r_1^{-1}\beta_1 + \tfrac{1}{2}\left[\left(\beta_3 + \tfrac{1}{2}j\beta_9 r_1^{-1}\beta_1\right)^2 - 4j\beta_9 r_1^{-1}\beta_2\right]^{1/2},$$
(7.84)

$$\beta_{13} = \tfrac{1}{2}\beta_3 - \tfrac{1}{2}j\beta_9 r_1^{-1}\beta_1 - \tfrac{1}{2}\left[\left(\beta_3 - \tfrac{1}{2}j\beta_9 r_1^{-1}\beta_1\right)^2 + 4j\beta_9 r_1^{-1}\beta_2\right]^{1/2},$$
(7.85)

$$\beta_{14} = \tfrac{1}{2}\beta_3 - \tfrac{1}{2}j\beta_9 r_1^{-1}\beta_1 + \tfrac{1}{2}\left[\left(\beta_3 - \tfrac{1}{2}j\beta_9 r_1^{-1}\beta_1\right)^2 + 4j\beta_9 r_1^{-1}\beta_2\right]^{1/2},$$
(7.86)

and the reference longitudinal sampling rate

$$r_1 = \frac{c_{\text{ref}}}{\omega \Delta x_3}.$$
(7.87)

Note that $\beta_{11} = -(\beta_{13})^*$ and $\beta_{12} = -(\beta_{14})^*$ if c_{ref} is real.

If $\hat{A}_{1,1} \neq 0$, the scheme is written as a denser one-step scheme

$$\left[(1 + \beta_3\langle\hat{\Xi}\rangle) - \beta_9 c_{\text{ref}}(\beta_1\langle\hat{\Xi}\rangle + \beta_2\langle\hat{\Xi}\rangle^2) - \beta_9(1 + \beta_3\langle\hat{\Xi}\rangle)\langle\hat{A}_{1,1}\rangle\right]\hat{h}(x_3 + \Delta x_3)$$

$$= \left[(1 + \beta_3\langle\hat{\Xi}\rangle) + \beta_9 c_{\text{ref}}(\beta_1\langle\hat{\Xi}\rangle + \beta_2\langle\hat{\Xi}\rangle^2) + \beta_9(1 + \beta_3\langle\hat{\Xi}\rangle)\langle\hat{A}_{1,1}\rangle\right]\hat{h}(x_3).$$
(7.88)

7.3.5 Propagator matrix

Equation (7.82) is decomposed into a two-step algorithm. The resulting scheme is

$$\hat{h}(x_3 + \Delta x_3) = \mathsf{Q}_{11}^{-1}\mathsf{P}_{13}\mathsf{Q}_{12}^{-1}\mathsf{P}_{14}\hat{h}(x_3),$$
(7.89)

in the electric-field strength normalization analog, and

$$\hat{h}(x_3 + \Delta x_3) = \mathsf{P}_{14}^{\mathrm{T}}(\mathsf{Q}_{12}^{-1})^{\mathrm{T}}\mathsf{P}_{13}^{\mathrm{T}}(\mathsf{Q}_{11}^{-1})^{\mathrm{T}}\hat{h}(x_3),$$
(7.90)

in the magnetic-field strength normalization analog, with

$$\mathsf{P}_j = \mathsf{C} + \beta_j\hat{\mathsf{M}},$$
(7.91)

$$\mathsf{Q}_j = \mathsf{C} - \beta_j\hat{\mathsf{M}},$$
(7.92)

for $j = 11, 12, 13, 14$. Introduce the diagonal matrix $\hat{\mathsf{T}}$, representing the change of reference frame, with diagonal elements (see Equation (7.16)) (no subscript summation)

$$\hat{\mathsf{T}}_{i,i} = \exp\left[j\omega\tau_{\text{ref}}(x_{1;i}, x_{2;i}, x_3)\right].$$
(7.93)

The propagator matrix equals

$$\langle P_{i,n}\rangle(m+1) = \hat{\mathsf{T}}_{i,j}(\mathsf{Q}_{11}^{-1})_{j,k}(\mathsf{P}_{13})_{k,l}(\mathsf{Q}_{12}^{-1})_{l,m}(\mathsf{P}_{14})_{m,n}. \tag{7.94}$$

The extension to a higher-order Thiele approximation for the square root in (7.4) and higher-order Padé approximations for the exponent in (7.79) is straightforward.

7.3.6   Condition number

The matrix inversions are performed using the Biconjugate Gradient method, see Gutknecht[200] and Rivera[114]. A preconditioner and initial guess can improve the speed of matrix inversion. In addition, good numerical performance (accurate and fast) is obtained if the spectrum of Q_j stays away from the origin. The location of the spectrum can partly be controlled in the optimization procedure.

We have made a lot of numerical experiments in order to investigate the condition number.

We observed that, in general, the matrices are better conditioned for a coarser grids. Consequently, we do not recommand to use a total rational-approximation scheme for dense discretizations (> 10 points per wavelength).

7.4   Transverse boundaries

At the boundaries of the computational window, linear boundary conditions are employed. These boundary conditions are also known as *Robin's boundary conditions* or *impedance conditions*. These boundary conditions do not influence the symmetry relations which are satisfied by the transverse Helmholtz operator $\hat{A}$ and the longitudinal slowness operator $\hat{\Gamma}$.

In Section 5.4, we discussed the boundary condition implementation in the 2-D scheme. Here, we extend the method to the 3-D scheme. It is noted that the implementation is slightly different (and simpler) due to the use of a co-moving reference frame with respect to an x_1- and x_2-independent reference frame (see Subsection 7.1.4): the numerical scheme now contains two sparse matrix equations instead of one with denser matrices.

We now make a distinction between the left/right and lower/upper boundaries. At the left/right boundary

$$\partial_2 \hat{h} + j\omega\eta^{(\pm,2)}(x_1)\hat{h} = 0, \qquad \text{at } x_2 = 0 \text{ and } x_2 = (N_{x_2}+1)\Delta x. \tag{7.95}$$

while at the lower/upper boundary

$$\partial_1 \hat{h} + j\omega\eta^{(\pm,1)}(x_2)\hat{h} = 0, \qquad \text{at } x_1 = 0 \text{ and } x_1 = (N_{x_1}+1)\Delta x_1. \tag{7.96}$$

By choosing $\eta^{(\pm,1)}$ and $\eta^{(\pm,2)}$ adapatively, the boundary conditions can be made highly transparent. As an example, at the left boundary the derivative ∂_2 is replaced by $\overline{\delta}_2$

$$\overline{\delta}_2 \hat{h} + \mathrm{j}\omega \Delta x \eta^{(\pm,2)}(x_1)\hat{h} = 0. \tag{7.97}$$

A similar boundary condition is applied at the other boundaries.

7.5 Longitudinal group and phase slowness

In this section, we derive the slowness surfaces associated with the numerical scheme. An optimization procedure is introduced to match the numerical and exact slowness surfaces. For simplicity, we restrict ourselves to isotropic media. The extension to anisotropic media is straightforward.

7.5.1 Slownesses after discretization

Substitute a plane-wave constituent in Equation (7.89)

$$\hat{h}(i_1\Delta x, i_2\Delta x_2, i_3\Delta x_3, \omega) = \exp[\mathrm{j}\omega\tau_{\mathrm{ref}}(i_3\Delta x_3)] \exp(-\mathrm{j}\omega\hat{\gamma}^{\mathrm{ph}}\Delta x_3)$$
$$\exp[-\mathrm{j}\omega(\alpha_1 i_1\Delta x + \alpha_2 i_2\Delta x_2)]. \tag{7.98}$$

We then obtain the *amplification* factor of the finite-difference scheme

$$\mathsf{p}_{13}\mathsf{q}_{11}^{-1}\mathsf{p}_{14}\mathsf{q}_{12}^{-1} = \exp(-\mathrm{j}\omega\hat{\gamma}^{\mathrm{ph}}\Delta x_3) \exp(\mathrm{j}\omega c_{\mathrm{ref}}^{-1}\Delta x_3), \tag{7.99}$$

in which $\hat{\gamma}^{\mathrm{ph}}$, p_j and q_j are the left symbols of the numerical representation for $\hat{\Gamma}$, P_j and Q_j, respectively. Note that in a homogeneous isotropic medium (constant $c = 1/\sqrt{\varepsilon\mu_0}$), the polarization interaction vanishes and the operator of interest $\hat{\Gamma}$ equals

$$\hat{\Gamma} = (\mu_0\varepsilon + \omega^{-2}\partial_\nu\partial_\nu)\begin{pmatrix} 1 & 0 \\ 0 & 1 \end{pmatrix}. \tag{7.100}$$

Its left symbol equals

$$\hat{\gamma}^{\mathrm{ph}} = (\mu_0\varepsilon - \omega^{-2}\alpha_\nu\alpha_\nu)\begin{pmatrix} 1 & 0 \\ 0 & 1 \end{pmatrix}. \tag{7.101}$$

For a homogeneous isotropic medium, we find (we only consider the nonzero elements: the diagonal elements, which are equal)

$$\mathsf{p}_j = \mathsf{P}_1^{(j)} + \mathsf{P}_2^{(j)}\left[4\cos(\omega\alpha_2\Delta x/2)\cos(\sqrt{3}\,\omega\alpha_1\Delta x/2) + 2\cos(\omega\alpha_2\Delta x)\right], \tag{7.102}$$

and

$$\mathsf{q}_j = \mathsf{Q}_1^{(j)} + \mathsf{Q}_2^{(j)} \left[4 \cos(\omega \alpha_2 \Delta x/2) \cos(\sqrt{3}\, \omega \alpha_1 \Delta x/2) + 2 \cos(\omega \alpha_2 \Delta x) \right],$$
(7.103)

with

$$\mathsf{P}_1^{(j)} = 1 - 6a_2 + \beta_j [(1 - 6a_2)\chi - 6a_1 r_t^2],$$
(7.104)

$$\mathsf{P}_2^{(j)} = \qquad a_2 + \beta_j (\qquad a_2 \chi + a_1 r_t^2),$$
(7.105)

$$\mathsf{Q}_1^{(j)} = 1 - 6a_2 - \beta_j [(1 - 6a_2)\chi - 6a_1 r_t^2],$$
(7.106)

$$\mathsf{Q}_2^{(j)} = \qquad a_2 - \beta_j (\qquad a_2 \chi + a_1 r_t^2).$$
(7.107)

The symbol of the finite difference scheme is the longitudinal phase slowness $\hat{\gamma}^{\mathrm{ph}}$ given by

$$\hat{\gamma}^{\mathrm{ph}}(\alpha_\nu, \omega) = c_{\mathrm{ref}}^{-1} - \frac{\ln(\mathsf{p}_{13}\mathsf{q}_{11}^{-1}\mathsf{p}_{14}\mathsf{q}_{12}^{-1})}{\mathrm{j}\omega \Delta x_3},$$
$$= c_{\mathrm{ref}}^{-1} - (\mathrm{j}\omega \Delta x_3)^{-1} \left[\ln(\mathsf{p}_{13}) + \ln(\mathsf{p}_{14}) - \ln(\mathsf{q}_{11}) - \ln(\mathsf{q}_{12}) \right], (7.108)$$

which reduces, if ω is real valued, to

$$\hat{\gamma}^{\mathrm{ph}}(\alpha_\nu, \omega) = c_{\mathrm{ref}}^{-1} + \frac{2}{\omega \Delta x_3} \left[\arg(\mathsf{p}_{13}) + \arg(\mathsf{p}_{14}) - \arg(\mathsf{q}_{11}) - \arg(\mathsf{q}_{12}) \right].$$
(7.109)

Note that $\hat{\gamma}^{\mathrm{ph}}(0, \omega) = c^{-1}$ is only ensured if $c = c_{\mathrm{ref}}$. The spectrum of $\hat{\varGamma}$ is periodic. The period is determined by the cosines in (7.102) and (7.103). The longitudinal group slowness can be derived from the longitudinal phase slowness, see Section 5.5

$$\hat{\gamma}^{\mathrm{gr}} = \hat{\gamma}^{\mathrm{ph}} + \omega(\partial_\omega \hat{\gamma}^{\mathrm{ph}})$$
$$= c_{\mathrm{ref}}^{-1} + \mathrm{j}(\Delta x_3)^{-1} \left(\mathsf{q}_{11}^{-1} \partial_\omega \mathsf{q}_{11} + \mathsf{q}_{12}^{-1} \partial_\omega \mathsf{q}_{12} - \mathsf{p}_{13}^{-1} \partial_\omega \mathsf{q}_{13} - \mathsf{p}_{14}^{-1} \partial_\omega \mathsf{q}_{14} \right).$$
(7.110)

Note that $\hat{\gamma}^{\mathrm{gr}} - \hat{\gamma}$ is indicative of the numerical anisotropy, whereas $\hat{\gamma}^{\mathrm{ph}} - \hat{\gamma}^{\mathrm{gr}}$ is indicative of the numerical dissipation.

7.5.2   Optimization

The longitudinal phase and group slownesses are functions of our parameters $\{\beta_1, \beta_2, \beta_3, a_2, \beta_9, \varOmega, c_{\mathrm{ref}}\}$, arising from the various approximations made to arrive at a sparse matrix representation for the propagator. The optimization procedure is analogeous to the optimization procedure described in Subsection 5.1.2. However,

Table 7.2: *The parameter sets for propagation ($c_{\mathrm{ref}} = c$).*

parameter set	1	2	3	4
$\Delta x/\lambda_0$	-	0.2	0.2	0.2
$\Delta x_3/\lambda_0$	-	0.2	0.2	0.2
$\mathrm{Re}(\beta_1)$	1/2	0.635	0.405	0.357
$\mathrm{Im}(\beta_1)$	0	0	0	-0.112
$\mathrm{Re}(\beta_2)$	1/8	0.215	0.139	0.142
$\mathrm{Im}(\beta_2)$	0	0	0	-0.015
$\mathrm{Re}(\beta_3)$	1/2	0.706	0.699	0.728
$\mathrm{Im}(\beta_3)$	0	0	0	-0.031
$\mathrm{Re}(a_2)$	1/24	0.038	0.039	0.036
$\mathrm{Im}(a_2)$	0	0	0	0.011
$\mathrm{Re}(\beta_9)$	1/2	0.353	0.564	0.572
$\mathrm{Im}(\beta_9)$	0	0	0	0.166
Ω	0	0	0	≥ 0.031

it is noted that the optimization here also depends on the chosen reference speed c_{ref}.

As motivated in Subsection 5.1.2, we choose an overall optimization procedure to determine the parameter set. The overall optimization procedure is carried out by minimizing an objective function, which might be subject to some constraints. These constraints arise, e.g., from forcing artificial poles out of the pre-critical region or from introducing attenuation in the artificial post-critical region. The optimization procedure is used as a tool to design an accurate pre-critical one-way propagation algorithm. The final optimization procedure depends on, e.g., the configuration or the taste of the user. If a higher accuracy is required, the fifth-order Thiele approximation can be considered. Then, the computation time increases by roughly 50%. Here, we discuss our choices for designing the parameters. The corresponding parameter sets are listed in Table 7.2.

Without optimization

First, we consider parameter set 1. The values arise from the consistent rational expansions; thus without any optimization procedure. Figure 7.14 shows the corresponding phase and group slownesses. The sampling rate is 5 points per wavelength. The longitudinal slowness for isotropic media is still highly isotropic after discretization; this is due to the nearly isotropic discretization of the Laplace operator on a hexagonal grid. Only outside the pre-critical region, thus in the post-critical region, is weak anisotropy present. Significant deviations are observed for larger propagation angles.
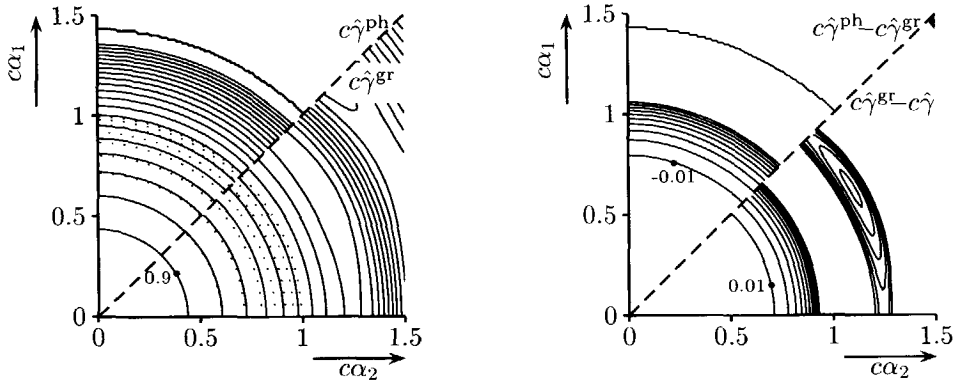
Figure 7.14: *The group slowness (left $0°$-$45°$) and the phase slowness (left $45°$-$90°$) associated with the discretized, one-way wave equation with $\beta_1 = 1/2$, $\beta_2 = 1/8$, $\beta_3 = 1/2$, $a_2 = 1/24$ and $\beta_9 = 1/2$, and a sampling rate of 5 points per wavelength. The exact slowness is dotted. The corresponding differences ($c\hat{\gamma}^{\mathrm{gr}} - c\hat{\gamma}$ and $c\hat{\gamma}^{\mathrm{ph}} - c\hat{\gamma}^{\mathrm{gr}}$) are drawn on the right-hand side.*

Pre-critical optimization

In the optimization procedure, we introduce the objective function as

$$f_{\mathrm{obj}}(\alpha_1, \alpha_2) = |\hat{\gamma}^{\mathrm{gr}} - \hat{\gamma}|^2 + |\hat{\gamma}^{\mathrm{ph}} - \hat{\gamma}^{\mathrm{gr}}|^2. \tag{7.111}$$

As a second approach, we optimize this function in the pre-critical region. In this approach, we introduce polar coordinates in the transverse spatial frequency domain

$$\alpha_1 = R\cos(\phi), \qquad \alpha_2 = R\sin(\phi). \tag{7.112}$$

The pre-critical region is then described by $0 \leq R < 1$ and $0 \leq \phi < 2\pi$. The optimization is performed by integrating over the pre-critical region; i.e., by minimizing the integral

$$\int_{\phi=0}^{\pi/6} \int_{R=0}^{1} f_{\mathrm{obj}}(R, \phi) R \; dR d\phi. \tag{7.113}$$

The obtained parameter set — number 2 — benefits wave propagation at higher angles, because the wide-angle wave propagation covers a larger area in the pre-critical region (which is a circle in the $\alpha_1\alpha_2$ plane) than the small-angle wave propagation.

As a third aproach, we introduce a weighting function $f_{\mathrm{w}}(R, \phi)$ in the integral (7.113). The weighting function $f_{\mathrm{w}}(R, \phi) = 1/R$ is used to equally treat wave propagation at different angles. Executing the optimization procedure results in parameter set 3. We now compare the above, introduced parameter sets, see Figure
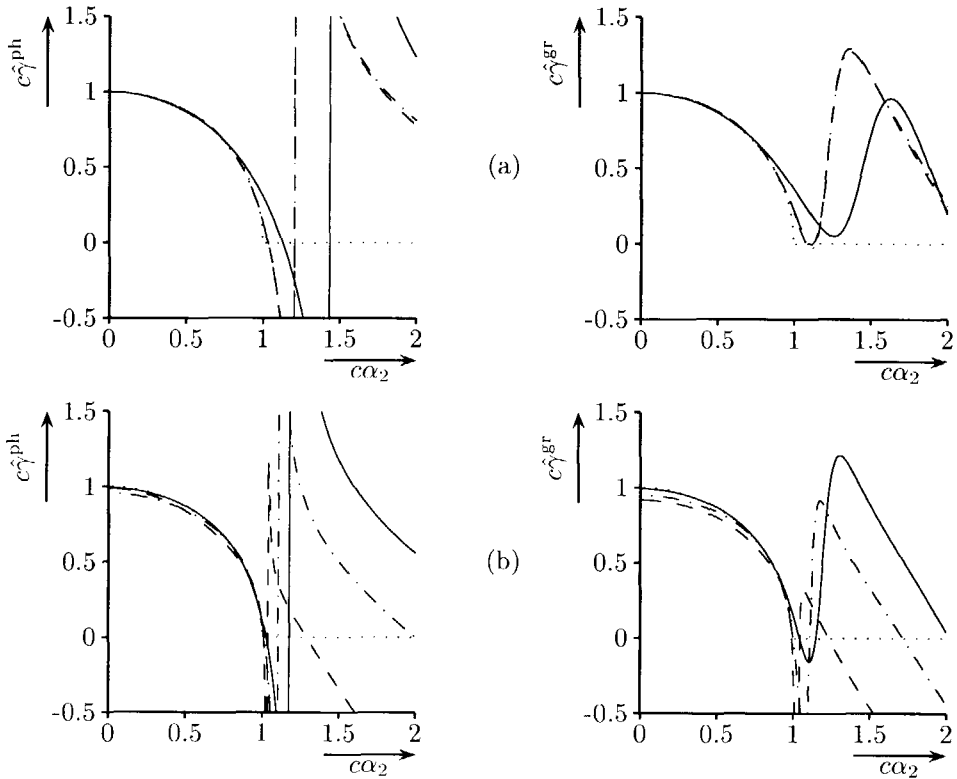
Figure 7.15: *The phase slownesses (left) and the group slownesses (right) at $\alpha_1 = 0$ associated with the discretized, approximate, one-way wave equation. The real part of the exact slowness is dotted. (a) Parameter set 1 (solid), 2 (dashed-dotted), 3 (dashed). The dashed-dotted and dashed curves optically coincide for $c\alpha_2 < 1.5$. (b) Parameter set 3. Different values for the reference speed are used: $c_{ref}/c = 1.1$ (solid), $c_{ref}/c = 1.5$ (dashed-dotted) and $c_{ref}/c = 3$ (dashed).*

7.15a: surprisingly, the difference between the second and the third parameter sets is small and even neglectable in the pre-critical region.

Since, for the 3-D numerical implementation, we have chosen to approximate the slowness with respect to the inverse of a reference speed instead of the local speed, the dependence on the reference speed has to be investigated, too. Figure 7.15b illustrates the phase and group slownesses for different contrasts using parameter set 3. Clearly, the slownesses differ from the exact slowness. It is observed that $\hat{\gamma}(\alpha_1 = 0) = c^{-1}$ is only ensured if $c = c_{ref}$.

Complex optimization

Thus far, the optimization procedure has been focussed on the real slowness surface. However, as we have seen in the preceeding sections, the approximations lead to artifacts in the post-critical regime. In fact, the post-critical constituents have been mapped on propagating constituents (slow waves). We have designed the dissipation trick to attenuate these constituents. In addition to this trick, some artificial constituents are forced to leave the computational domain through the transparent boundary conditions. This dissipation trick introduces a "complexification" of the parameters used in the optimization, and hence it seems to be natural to complexify the procedure accordingly (see also Collins[186]). Pursuing this complexification, the optimization procedure is extended with the constraint that the post-critical power is attenuated strongly while the attenuation/amplification in the pre-critical region is kept minimal (less than 5%). In more detail, we used the object function

$$f_{\mathrm{obj}}(R, \phi) = |c\hat{\gamma}^{\mathrm{gr}} - c\hat{\gamma}^{\mathrm{ex}}|^2 + |c\hat{\gamma}^{\mathrm{ph}} - c\hat{\gamma}^{\mathrm{gr}}|^2 + 10 \, |\mathrm{Im}(c\hat{\gamma}^{\mathrm{ph}})|^2 + |\mathrm{Im}(c\hat{\gamma}^{\mathrm{gr}})|^2, \tag{7.114}$$

for the precritical region $(0 < R < 1)$, and

$$f_{\mathrm{obj}}(R, \phi) = 10^3 \, H[\mathrm{Im}(c\hat{\gamma}^{\mathrm{ph}}) + 0.15] \, [\mathrm{Im}(c\hat{\gamma}^{\mathrm{ph}}) + 0.15]^2, \tag{7.115}$$

for the main part of the post-critical region $(1.25 < R < R_{\mathrm{Nyq}} = 5)$. The imaginary part of the corresponding phase slowness for other spatial sampling rates can be positive: an amplificative nature. By increasing the imaginary frequency Ω to 0.041, the phase slownesses have a negative imaginary part in a range from 12 to 2 sampling points per wavelength. This parameter set is used for most numerical results. The resulting parameter set is shown in the fourth column of Table 7.2. The accuracy of the complex parameter set is illustrated in Figure 7.16.

Comparing the 3-D optimization procedure with the 2-D version in Chapter 5, we observe that two extra contraints are included

① the dependence on c_{ref}, and

② the numerical speed to invert the matrices.

This pushes the third-order Thiele approximation to its limits, and accuracy at higher angles is lost.

7.5.3   Numerical examples

Three configurations are selected to demonstrate the forward propagation scheme. The configurations are: free space, an optical fiber and a rib waveguide.

It is noted that, in the present numerical implementation, the construction of the matrices requires much time. Therefore, we compute the relevant matrices in advance, and save them on a disk. A special and "smart" procedure must be developed for this task.
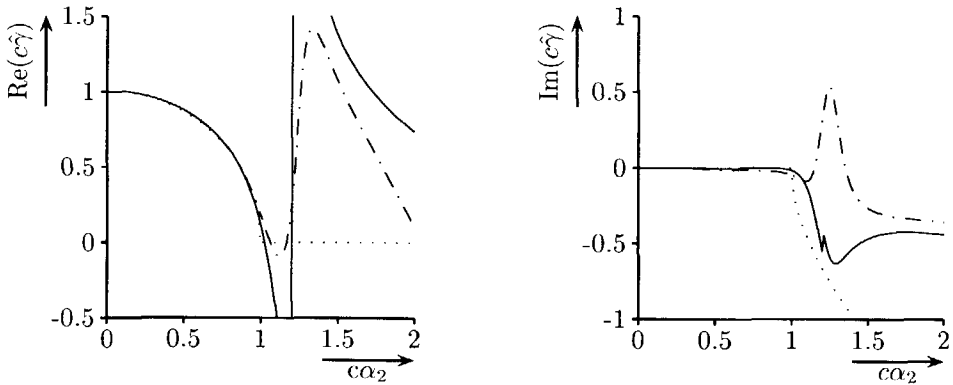
Figure 7.16: *The group slownesses (solid) and the phase slownesses (dashed-dotted) at $\alpha_1 = 0$ associated with the discretized, approximate, one-way wave equation with parameter set 4. The real part is plotted in the left figure, while the imaginary part is plotted in the right figure. The exact slowness is dotted.*

Free space

In order to demonstrate the wide-angle behavior of our numerical scheme, we show the electric field of the time response of a pulsed magnetic current point-source $\hat{K}_2^e$ in free space ($n = 1$). We choose this point-source because, for this type of point-source, we do not have to implement any additional operator. For instance, for an electric point source $\hat{J}_1^e$ we also have to implement the decomposition operator. This is discussed in Subsection 7.6.7.

The numerical grid consists of 114, 99, 60 points along the x_1, x_2 and x_3 directions, respectively. The discretization step is 0.25 μm in the transverse plane and in the longitudinal direction. Given a source signature with a trapezoidal spectrum with corner frequencies 100, 200, 250, and 400 THz (see Figure 2.12), we encounter sampling rates of 3 to 12 points per wavelength. The point source is located at the origin, which is chosen to be the center of the transverse input plane. We have taken an inverse Fourier transform with 128 points and $\Delta T = 0.4$ fs. We show snapshots of the electric field at 30 fs. The point source is an magnetic current with a component only in the x_1 direction: $\hat{N}_1^T = \begin{pmatrix} \hat{K}_2^e & 0 \end{pmatrix}$. The wave propagation problem is reduced in dimension since only one polarization is excited ($\hat{E}_1 \neq 0$, $\hat{E}_2 = 0$). In Figure 7.17, the snapshot is shown using the fourth parameter set and an analytical expression (on the left-hand side and right-hand side, respectively). The snapshot is taken in a plane at 60 degrees with respect to the x_1 direction. This configuration is equivalent to the 2-D acoustic example in Figure 5.15.

The size of the matrices is 22572-by-22572 elements. The computation time was 24800 s ($34\frac{2}{3}$ hours) on a Hewlett Packet 735/125 workstation using Matlab for the
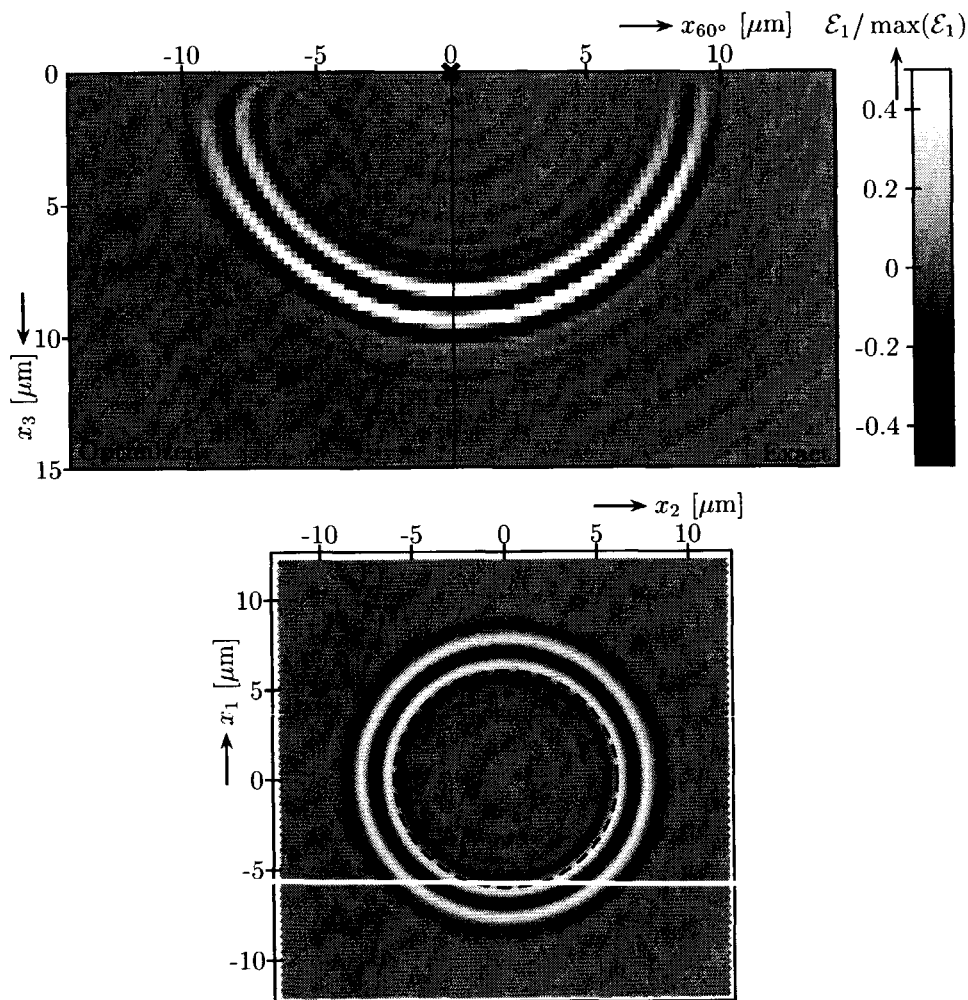
Figure 7.17: Snapshot at $t = 30$ fs of a magnetic current point-source response in free space. The right-hand side is obtained analytically, while the left-hand side is obtained with our numerical scheme. The lower figure shows the snapshot in the transverse plane at $x_3 = 5$ μm. Here, we used parameter set 4 of Table 7.2.

full vectorial scheme. Most matrices were constructed in advance. The computation of the matrix inverses costs most time. We used BiCGStab without preconditioning with tolerance 10^{-5}. One propagation steps consistes of two matrix inversion. The first matrix inversion takes about 20 iterations for lower frequencies and 3 iteretions for higher frequencies, while the second matrix inversion takes about 400 iterations for lower frequencies and 12 iteretions for higher frequencies. Near the source, more iterations are needed (1.5 to 5 times more, for lower and higher frequencies, respectively).

Optical fiber

As a second numerical example, we consider wave progation through an optical fiber, see Figure 7.18. The refractive index of the fiber's core is $n_{co} = 1.469$, while the refractive index of the cladding is $n_{cl} = 1.46$. The even and odd HE_{11} modes are the fundamental modes, since they are not cut off when reducing the frequency or radius. Choosing the radius r to be 3 μm and the wavelength to be 1.3 μm, the optical fiber is single moded. The normalized frequency[a] V equals 2.35417, see Snyder and Love[143]. This fiber has also been analyzed by Huang et al.[109] and Rivera[114]. The latter modeled a glas fiber with radius $r = 2$ μm.

We now perform the following BPM experiment. A Gaussian beam is launched into this fiber, by which only the even modes are excited. At single-mode operation, there is only one guided (even) mode, namely the even HE_{11} mode. After a certain propagation distance along the fiber, this mode will not die out, while all other modes are radiated away. Now, we can compare the exact mode with our above-given numerical test.

There are several ways to extract the modal propagation constants from this BPM experiment. We used Feit and Fleck's spectral method[35]. Recently, this method was also described by Li[194] and Rivera[114] in their dissertations. Although the spectral method is not accurate, it gives some indications of the forward propagation.

The input Gaussian beam has a width of 0.3 μm in both transverse directions and is polarized along the x_2 direction: $\hat{E}_1^{in} = 0$, $\hat{E}_2^{in} \neq 0$. The numerical grid consists of 78, 68, 3450 points along the x_1, x_2 and x_3 directions, respectively. The discretization step is approximately 1.77 μm in the transverse plane and in the longitudinal direction. This corresponds to exactly 5 points per wavelength in the core of the glass fiber. The reference refrative index is chosen to be equal to the core's refractive index: $n_{ref} = 1.469$. We have chosen the complex parameter set 4 for the forward propagation. The tolerance of the biconjugate gradient method was set at 10^{-5}. In each propagation step, about 3 and 30 iterations for the biconjugate

---

[a]The normalized frequency[144] V is defined as (see also Equation (4.132))

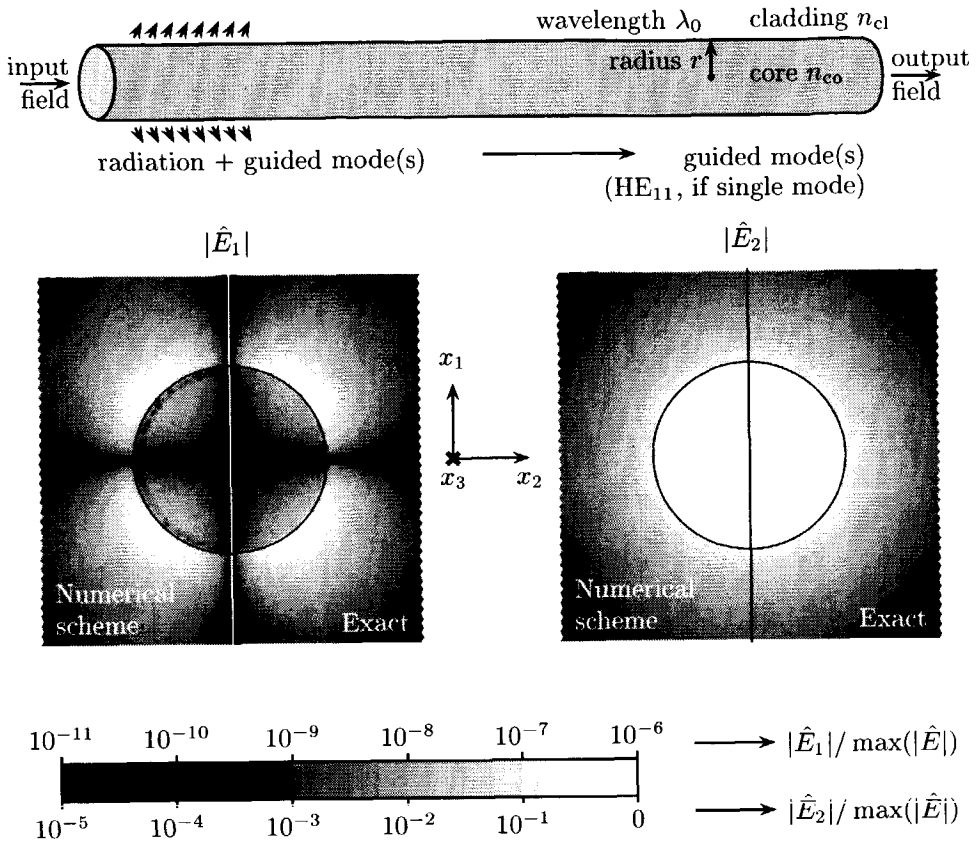$$V = k_0 r \sqrt{n_{co}^2 - n_{cl}^2}.$$

Figure 7.18: *Illustration of the evaluation of a Gaussian beam through an optical glass fiber. The absolute value of the electric field strength after a propagation distance of 611 μm is shown. The solid line represents the dielectric interface. Here: $r = 3$ μm, $\lambda = 1.3$ μm, $n_{co} = 1.469$, $n_{cl} = 1.46$, $N_{x_1} = 78$, $N_{x_2} = 68$, $N_{x_3} = 3450$ and 5 discretization points per wavelength inside the core.*

gradient method were needed for the two matrix inversions, respectively. This corresponds to less than 16 seconds per propagation step on a Hewlett Packett 735/125 workstation using Matlab! The computation of the matrices is excluded, which costs relatively much time. There are several ways to reduce the time to create the matrices. One way is to store frequently used matrices on disc.

The numerical propagation constant, the effective refractive index n_{eff}, of the fundamental mode is found to be 1.46559 ± 0.00106. Using the spectral method of Feit and Fleck[35], the effective refractive index is corrected to 1.46495. This

value is very close to the exact value of 1.46466. The error $(n_{\text{eff}}^{\text{ex}}/n_{\text{eff}}^{\text{num}} - 1)$ is 0.02%. It can be compared to the errors found by Huang et al.[109]: approximately 0.01% for a sligly smaller sampling rate and 0.08% for slightly larger sampling rate. They used a rectangular grid without the equivalent medium theory. They also found irregularities near the dielectric boundary. For better comparison with other methods and configurations, we also computed the core parameter[b] U. It equals 1.581 or 1.636, respectively. The corresponding error $(U^{\text{ex}}/U^{\text{num}} - 1)$ is 3.5%. This definition of the error is more indicative of the accuracy of our method, or any other method.

As discussed above, the field after propagating through the 611 μm long optical fiber contains mainly the fundamental HE$_{11}$ mode. Parts of the propagating radiation modes still remain in the field and an interference pattern is still observed after 611 μm. The ratio between the amplitudes of $\hat{E}_1$ and $\hat{E}_2$ at the end of this fiber is found to be about 636, thereby the modal field is primary x_2 polarized. The ratio of the exact fundamental HE$_{11}$ mode is about 499.

Rib waveguide

As a third numerical example, we consider a BPM-benchmark test for wave propagation through a rib waveguide, see i.e., Li[194]. Both laterally ($\hat{E}_1 = 0$, $\hat{E}_2 \neq 0$) and transversely polarized ($\hat{E}_1 \neq 0$, $\hat{E}_2 = 0$) Gaussian beams with a beam width of 0.3 μm are launched into a rib waveguide at $x_3 = 0$ μm. Our results for the parabolic approximation are very similar to the results obtained by Li[194], but then for a coarser grid.

7.6   Sparse matrix representation of the (de)composition operators

The computation of the generalized Bremmer coupling series starts with the decomposition of the field into forward and backward propagating constituents; e.g. in the electric field normalization analog (see Equation (6.67))

$$\begin{pmatrix} \hat{W}_{\text{EFN}}^{(+)} \\ \hat{W}_{\text{EFN}}^{(-)} \end{pmatrix} = \frac{1}{2} \begin{pmatrix} 1 & \hat{Z} \\ 1 & -\hat{Z} \end{pmatrix} \begin{pmatrix} \hat{F}_1 \\ \hat{F}_2 \end{pmatrix}. \tag{7.116}$$

Upon completing the calculation of a sufficiently large number of terms of the Bremmer coupling series, the constituents are recomposed into observables (see Equation

---

[b]The core parameter[143] U is defined as (see also Equation (4.133))

$$U = k_0 r \sqrt{n_{\text{co}}^2 - n_{\text{eff}}^2}.$$

(6.66))

$$\begin{pmatrix} \hat{F}_1 \\ \hat{F}_2 \end{pmatrix} = \begin{pmatrix} 1 & 1 \\ \hat{Y} & -\hat{Y} \end{pmatrix} \begin{pmatrix} \hat{W}_{\text{EFN}}^{(+)} \\ \hat{W}_{\text{EFN}}^{(-)} \end{pmatrix}. \tag{7.117}$$

In these procedures, the admittance operator $\hat{Y}$ and impedance operator $\hat{Z}$ must be computed. Here, using the results of Section 7.3, we will derive sparse matrix representations for these operators. These operators contain the longitudinal slowness operators $\hat{\Gamma}_{\text{EFN}}$ and $\hat{\Gamma}_{\text{MFN}}$, and operators $\hat{A}_{1,2}$ and/or $\hat{A}_{2,1}$ (see Equations (6.78) and (6.78)). Since $\hat{A}_{2,1}$ does not contain any derivative of the medium properties — this is in contrast to $\hat{A}_{1,2}$ —, higher numerical accuracy is reached if an expression containing $\hat{A}_{2,1}$ is used, e.g., $\hat{Y} = \hat{A}_{2,1}\hat{\Gamma}_{\text{EFN}}^{-1} = \hat{Z}^{-1}$.

7.6.1   Inverse slowness operator

The decomposition operator essentially contains the inverse of the longitudinal slowness operator. To find a sparse matrix representation of $\hat{\Gamma}_{\text{MFN}}^{-1}$ and its transposed $\hat{\Gamma}_{\text{EFN}}^{-1}$, we use the same Thiele approximation as in Equation (7.5). We write, however, the fraction in a slightly different way

$$\hat{\Gamma}^{\text{III}} = c_{\text{ref}}^{-1} (1 + \beta_3 \hat{\Xi})^{-1} [1 + (\beta_1 + \beta_3)\hat{\Xi} + \beta_2 \hat{\Xi}^2]. \tag{7.118}$$

Factoring the operator between brackets, yields (compare with Equation (5.81))

$$1 + (\beta_1 + \beta_3)\hat{\Xi} + \beta_2 \hat{\Xi}^2 = (1 - \beta_6 \hat{\Xi})(1 - \beta_7 \hat{\Xi}), \tag{7.119}$$

with

$$\beta_6 = -\tfrac{1}{2} \left\{ \beta_1 + \beta_3 + \left[(\beta_1 + \beta_3)^2 - 4\beta_2 \right]^{1/2} \right\}, \tag{7.120}$$

$$\beta_7 = -\tfrac{1}{2} \left\{ \beta_1 + \beta_3 - \left[(\beta_1 + \beta_3)^2 - 4\beta_2 \right]^{1/2} \right\}. \tag{7.121}$$

Then it is straightforward to invert the longitudinal slowness operator, viz.,

$$\left(\hat{\Gamma}^{\text{III}} \right)^{-1} = c_{\text{ref}}^{-1} (1 + \beta_3 \langle \hat{\Xi} \rangle)(1 - \beta_6 \langle \hat{\Xi} \rangle)^{-1} (1 - \beta_7 \langle \hat{\Xi} \rangle)^{-1}. \tag{7.122}$$

Observe that the symbol of this operator has two poles on either side of the origin (the zero crossings of $\hat{\gamma}^{\text{III}}$). The discretized inverse slowness operator becomes

$$\langle (\hat{\Gamma}_{\text{EFN}}^{\text{III}})^{-1} \rangle = c_{\text{ref}}^{-1} Q_6^{-1} P_3 Q_7^{-1} C. \tag{7.123}$$

7.6.2 Slowness operator

Note that the composition operator, and thus also the slowness operator, are not computed in the combined Bremmer approach.

Using the results for the slowness operator in Equation (7.123), we find

$$\langle \hat{\Gamma}^{\mathrm{III}}_{\mathrm{EFN}} \rangle = c_{\mathrm{ref}} \mathsf{C}^{-1} \mathsf{Q}_7 \mathsf{P}_3^{-1} \mathsf{Q}_6. \tag{7.124}$$

Observe that the symbol of this operator has one pole on both sides of the origin.

7.6.3 Operator $\hat{A}_{2,1}$

The operator $\hat{A}_{2,1}$ equals (see Equation (6.36))

$$\hat{A}_{2,1} = \begin{pmatrix} \varepsilon_{\mathrm{a}} & \varepsilon_{\mathrm{b}} \\ \varepsilon_{\mathrm{b}} & \varepsilon_{\mathrm{c}} \end{pmatrix} + \omega^{-2} \mu_0^{-1} \begin{pmatrix} \partial_2 \\ -\partial_1 \end{pmatrix} \begin{pmatrix} \partial_2 & -\partial_1 \end{pmatrix}. \tag{7.125}$$

The discretization yields

$$\langle \hat{A}_{2,1} \hat{h} \rangle = \varepsilon_{\mathrm{ref}} \mathsf{C}^{-1} \hat{\mathsf{N}} \hat{h}, \tag{7.126}$$

with

$$\hat{\mathsf{N}} = \mathsf{N}_1 + r_{\mathrm{t}}^2 \mathsf{N}_2, \tag{7.127}$$

and

$$\mathsf{N}_1 = (1 + a_2 \delta_1^2) \varepsilon_{\mathrm{ref}}^{-1} \mathcal{E} = \mathsf{C} \varepsilon_{\mathrm{ref}}^{-1} \mathcal{E}, \tag{7.128}$$

$$\mathsf{N}_2 = \begin{pmatrix} a_1 \delta_2^2 & -a_7 \delta_{12} \\ -a_7 \delta_{12} & a_1 \delta_1^2 \end{pmatrix}. \tag{7.129}$$

From numerical tests follows that this matrix is badly conditioned for inversion.

7.6.4 Operator $\hat{A}_{1,2}$

The operator $\hat{A}_{1,2}$ equals (see Equation (6.37))

$$\hat{A}_{1,2} = \mu_0 \begin{pmatrix} 1 & 0 \\ 0 & 1 \end{pmatrix} + \omega^{-2} \varepsilon_{3,3}^{-1} \begin{pmatrix} \partial_1 \\ \partial_2 \end{pmatrix} \begin{pmatrix} \partial_1 & \partial_2 \end{pmatrix} - \omega^{-2} \begin{pmatrix} (\partial_1 \varepsilon_{3,3}^{-1}) \\ (\partial_2 \varepsilon_{3,3}^{-1}) \end{pmatrix} \begin{pmatrix} \partial_1 & \partial_2 \end{pmatrix}. \tag{7.130}$$

The discretization of $\hat{A}_{1,2}$ yields

$$\langle \hat{A}_{1,2} \hat{h} \rangle = \mu_0 \hat{\mathsf{N}}' \mathsf{C}^{-1} \hat{h}, \tag{7.131}$$

with

$$\hat{\mathsf{N}}' = \mathsf{N}_1' + r_{\mathrm{t}}^2 \mathsf{N}_2', \tag{7.132}$$

and

$$N_1' = (1 + a_2 \delta_\perp^2) \begin{pmatrix} 1 & 0 \\ 0 & 1 \end{pmatrix} = C, \tag{7.133}$$

$$N_2' = \frac{\varepsilon_{\text{ref}}}{\varepsilon_{3,3}} \begin{pmatrix} a_1 \delta_1^2 & a_7 \delta_{12} \\ a_7 \delta_{12} & a_1 \delta_2^2 \end{pmatrix} - \varepsilon_{\text{ref}} \begin{pmatrix} \Delta x(\partial_1 \varepsilon_{3,3}^{-1}) \\ \Delta x(\partial_2 \varepsilon_{3,3}^{-1}) \end{pmatrix} \begin{pmatrix} a_3 \delta_1 & a_3 \delta_2 \end{pmatrix}. \tag{7.134}$$

The corresponding transverse Helmholtz operator $\hat{A}_{\text{EFN}}$ equals

$$\langle \hat{A}_{\text{EFN}} \rangle = \langle \hat{A}_{1,2} \hat{A}_{2,1} \rangle = c_{\text{ref}}^{-2} \hat{N}' \hat{N}. \tag{7.135}$$

7.6.5   Admittance operator

The admittance operator can numerically be computed by

$$\hat{Y} = \hat{A}_{2,1} \hat{\Gamma}_{\text{EFN}}^{-1} = c_{\text{ref}}^{-1} \varepsilon_{\text{ref}} C^{-1} \hat{N} Q_6^{-1} P_3 Q_7^{-1} C. \tag{7.136}$$

Note that $\hat{Y} = \hat{Y}^{\mathrm{T}}$ is no longer guaranteed. A small discretization error has been made: $\mathcal{O}[(\Delta x)^4]$.

7.6.6   Impedance operator

The impedance operator is numerical computed by

$$\hat{Z} = \hat{\Gamma}_{\text{EFN}}^{-1} \hat{A}_{1,2} = c_{\text{ref}}^{-1} \mu_0 Q_6^{-1} P_3 Q_7^{-1} C \hat{N}' C^{-1}. \tag{7.137}$$

The matrices Q_6 and Q_7 are hard to invert with the preconditioned BiCGStab-routine due to the poles.

7.6.7   Numerical example

At the computational boundaries we apply, as before, the Robin boundary conditions (Section 7.4). We also apply an optimization procedure for the (de)composition operators, considering the parameter subset $\{\beta_1, \beta_2, \beta_3, a_2, \Omega\}$. To avoid instabilities, we have to move the poles arising in the symbols of the approximate operators into the complex transverse slowness plane. The outcome of the pre-critical optimization for a sampling rate of 5 points per wavelength is

$$\beta_1 = 0.508, \tag{7.138}$$
$$\beta_2 = 0.332, \tag{7.139}$$
$$\beta_3 = 0.707, \tag{7.140}$$
$$a_2 = 0.122, \tag{7.141}$$
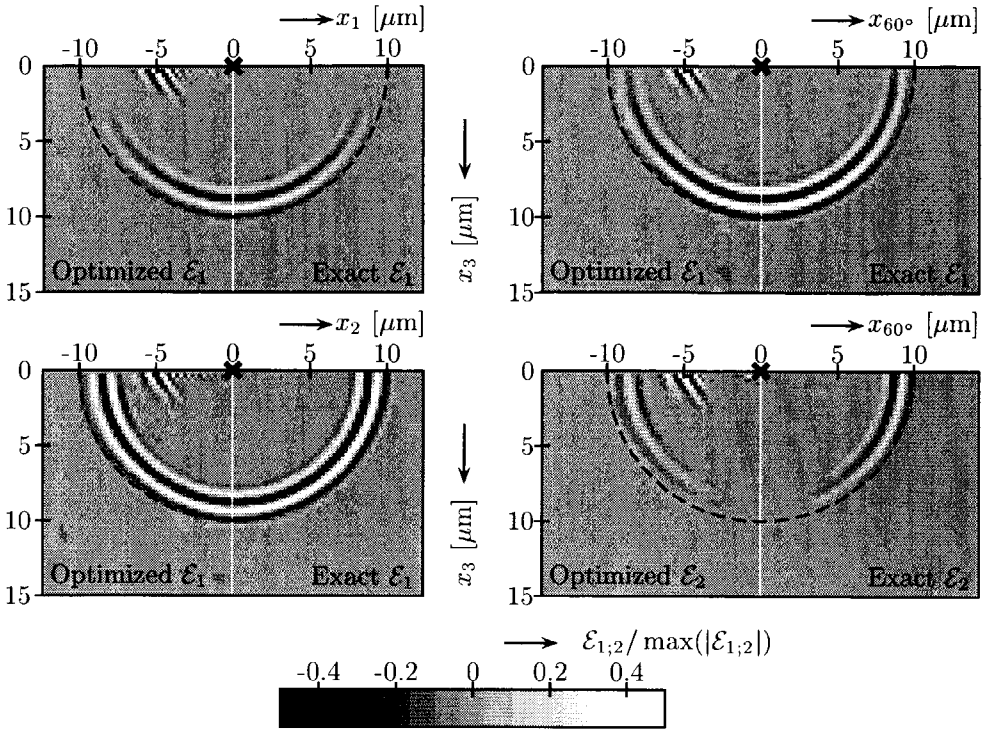$$\Omega = -0.01. \tag{7.142}$$

Figure 7.19: Snapshot at $t = 30$ fs of an electric current point-source response in free space. The right-hand side is obtained analytically, while the left-hand side is obtained with our numerical scheme. Here, we used parameter set 4 of Table 7.2.

When optimizing for several sampling rates (3, 5, 10 and 50 points per wavelength), the outcome is

$$\beta_1 = 0.522, \tag{7.143}$$

$$\beta_2 = 0.359, \tag{7.144}$$

$$\beta_3 = 0.820, \tag{7.145}$$

$$a_2 = 0.048. \tag{7.146}$$

Subsequently, the poles are moved into the complex plane by setting

$$\Omega = -0.01. \tag{7.147}$$

This is equivalent with deforming the integration contour into the complex plane.

We illustrate the final optimized, one-way propagation and decomposition by computing the electric wave-field excited by a electric point source in free space

($n = 1$). The point source under consideration is an electric current with only one component in the x_2 direction: $\hat{N}_2^T = \left(-\hat{j}_1^{(e)} \quad 0 \right)$. Two electric field components are excited: $\hat{E}_1$ and $\hat{E}_2$. This is due the presence of operator $\hat{A}_{1,2}$ (or $\hat{A}_{2,1}$) in the admittance operator. From the expression $\hat{Y} = \hat{\Gamma}_{MFN}^{-1} \hat{A}_{1,2}$, it is clear that the coupling terms in free space are small far away from the source, because they contain the derivatives $\partial_1 \partial_2$ only: these derivatives are zero where the source is absent. The radiation pattern of the point-source under consideration is a dipole: its field is zero along the x_1 and x_2 direction. We expect an isoptropic radiation pattern in the $x_1 x_3$ plane.

We used the same discretization as in Subsection 7.5.3. In Figure 7.19, the snapshot is shown, using the the fourth parameter set.

Note that similar radiation patterns are obtained for the magnetic field with a magnetic point source. In the electric field strength normalization analog, the composition operator has to be computed at every x_3 position, while in the magnetic field strength normalization analog the decomposition operator has only to be computed at the x_3 position of the source.

7.7   Sparse matrix representation of the reflection and transmission operators

The coupling matrix equals

$$-\hat{L}^{-1}(\partial_3 \hat{L}) = \begin{pmatrix} \hat{T} & \hat{R} \\ \hat{R} & \hat{T} \end{pmatrix}, \tag{7.148}$$

with the reflection and transmission operators in both EFN and MFN analog

$$\hat{T}_{EFN} = -\hat{R}_{EFN} = \hat{Y}^{-1}(\partial_3 \hat{Y}), \tag{7.149}$$

$$\hat{T}_{MFN} = -\hat{R}_{MFN} = \hat{Z}^{-1}(\partial_3 \hat{Z}). \tag{7.150}$$

There are two numerical implementations under investigation. The first one is the straightforward extension of the 2-D implemention in Section 5.7. The second implementation is based upon the boundary conditions and employs the admittance matrix operator and its derivative.

For the second approach, the results of the previous section are used.

7.8   Discusion of the results

We employed a total rational-approximation approach to find, upon discretization, sparse matrix representations of the relevant pseudo-differential operators. This discretization is based upon the third-order Thiele approximation of the longitudinal

slowness. Similarly, the transverse and longitudinal derivatives are replaced by their rational approximations. We introduced a hexagonal numerical grid. The advantages above the usual rectangular grids are: (1) less numerical anisotropy, (2) possibility to construct a rational approximation in order to increase the accuracy and (3) fewer numerical grid points to model the desired Nyquist region. The longitudinal phase and group slownesses of this numerical scheme are derived and used to analyze the numerical scheme. The difference between the phase and group slowness is identified with the numerical dissipation, while the difference between the group slowness and exact slowness is a measure for the numerical anisotropy.

In the optimization procedure, the numerical anisotropy and dissipation are simultaneously minimized in the pre-critical region. Numerical artifacts in the post-critical regions can be suppressed by using a complex optimization procedure. This optimization procedure leads to an improvement of the numerical scheme without increasing the numerical effort. The accuracy is high and nearly constant up to five (or even less) discretization points per wavelength. A transparent boundary condition decreases the size of the relevant matrices.

A 3-D fully vectorial forward numerical scheme for anisotropic media has been derived and implemented. The numerical scheme is accurate up to high propagation angles ($< 80°$) and a few points per wavelength (3-5 points). This is due to a total higher-order rational-approximation approach and the optimization procedure. The (de)composition operator has also been derived and numerically implemented. All operators can now be integrated into a 3-D Bremmer scheme. The construction of the relevant matrices for different configurations is time consuming. A fast and "user-friendly" pre-processing procedure should be developed for this task.

CHAPTER 8

Conclusions and Discussion

In this thesis, we have introduced a directional wave-field decomposition and discussed its implementation. It is a powerful method for modeling electromagnetic and acoustic wave propagation in nonuniform anisotropic waveguiding structures and in heterogeneously layered configurations. It can be seen as an extension of existing parabolic equation methods toward wider propagation angles, and including backscattering. Both electromagnetic and acoustic wave propagation have been discussed. It has been applied to a few typical, simple configurations, in order to elucidate its accuracyand its principles.

The areas of interest are integrated optics, exploration seismics and underwater acoustics. We have given a short overview of the directional wave-field decomposition in general and an extented overview on the Beam Propagation Method (BPM), the name under which the method is known in the field of integrated optics. The acoustic methods which are equivalent to the BPM, are widely known under the name of the "parabolic equation" method.

The directional wave-field decomposition method is applied to model wave propagation in nonuniform waveguides and general layered media. In such structures, the wave propagates dominantly in one direction, the preferred direction, while it is gradually influenced by the transverse inhomogeneities. Accordingly, the directional decomposition method splits the wave-scattering problem into two different parts: (1) the scattering problem along the preferred (or longitudinal) direction, and (2) the scattering problem in the plane perpendicular to it (transverse plane).

In the first part, the field is decomposed into two types of waves: one propagating forward in the preferred direction and one propagating backward in the preferred direction. The longitudinal scattering is analyzed by the Bremmer series. Physically, the Bremmer series can be interpreted as containing multiple reflected and transmitted waves along the preferred direction. This gives us more physical

insight into the wave scattering. As an example, the first term contains the forward directed wave, which is also computed in the BPM, while the second term contains the once-reflected and transmitted waves. In the Bremmer series approach, we encounter pseudo-differential operators in the directional decomposition as well as in the forward and backward propagation, and in the reflections and transmissions due to variations in the medium properties in the preferred direction. We showed the symmetry properties of these operators and the interrelation between different normalization analogs. For the numerical implementation, we derived a novel scheme. Numerical examples show good results for only a few terms.

In the second part, the scattering in the transverse plane is described by a pseudo-differential operator: the well-known square root operator and functions of it. In a transverse homogeneous medium, Fourier techniques are used to transform the square root operator into a symbol: the longitudinal slowness. By studying this symbol, we define the pre-critical region, i.e., wave propagation between $0°$ and $90°$, and the post-critical region, i.e., the region of evanescent waves. In a transverse heterogeneous medium, we have studied two different approaches. The first approach is based upon the eigenvalues and eigenfunctions. This approach is closely related to the modal analysis of waveguides. Together with the Bremmer series, it extends the uniform waveguiding theory to nonuniform waveguides. The second approach is based upon the left symbol from the pseudo-differential operator calculus. It is a plane-wave decomposition. The interaction between the square root operator and a plane-wave is replaced by a multiplication of its left symbol and the same plane-wave. A closer analysis gives us the relation between the two approaches presented above. This relation is used to compute the left symbol in two special cases: the quadratic profile waveguide and the symmetric slab waveguide.

For the numerical implementation, we employ a total rational-approximation approach to find, upon discretization, sparse matrix representations of the relevant pseudo-differential operators. This discretization is based upon the third-order Thiele approximation of the longitudinal slowness. Similarly, the transverse and longitudinal derivatives are replaced by their rational approximations. In 3-D configurations, a hexagonal numerical grid is employed. The advantages above the usual rectangular grids are: (1) less numerical anisotropy, (2) possibility to construct a rational approximation in order to increase the accuracy and (3) fewer numerical grid points to model the desired Nyquist region. The longitudinal phase and group slownesses of this numerical scheme are derived and used to analyze the numerical scheme. The difference between the phase and group slowness is identified with the numerical dissipation, while the difference between the group slowness and exact slowness is a measure for the numerical anisotropy.

In the optimization procedure, the numerical anisotropy and dissipation are simultaneously minimized in the pre-critical region. Numerical artifacts in the post-critical regions can be suppressed by using a complex optimization procedure. This optimization procedure leads to an improvement of the numerical scheme without increasing the numerical effort. The accuracy is high and nearly constant up to five (or even less) discretization points per wavelength. A transparent boundary

condition decreases the size of the relevant matrices. Alternatively, the numerical method can also be seen as an extension of the previously used parabolic methods, like the BPM: the wide-angle behavior is increased by using higher-order rational approximations for the square root operators and derivatives, and by the optimization procedure. The Bremmer series extends the classical one-way BPM to a coupled bidirectional scheme; the interaction between the counter-propagating waves is included.

Summarizing the results that are new in this thesis:

- A bidirectional scheme based upon one-way wave propagation has been derived. The internal reflections are described by a Bremmer series. A novel numerical scheme has been built for 1-D and 2-D configurations. Often only a few terms of the Bremmer series have to be taken into account.

- An analysis based upon the left symbol from the pseudo-differential theory has been introduced. The left symbols in a quadratic profile waveguide and in a symmetric slab waveguide have been computed. This analysis gives a new insight into the one-way wave schemes.

- An 2-D, isotropic TE scalar and a 3-D, anisotropic, fully vectorial forward scheme have been derived and implemented. The numerical scheme is accurate up to high propagation angles ($< 80°$) and a few points per wavelength (3-5 points). This is due to a total higher-order rational-approximation approach and the optimization procedure.

- An equivalent medium averaging has been employed in the numerical code in order to include rapid variation and discontinuities in the medium properties.

- The (de)composition and reflection/transmission operators and the propagator have been derived and numerically implemented. These operators have not been integrated into a 2-D Bremmer scheme, but they have not yet numerically been integrated into a 3-D Bremmer scheme.

- The construction of the relevant matrices for different configurations is time consuming. A fast and "user-friendly" procedure has been developed for the 2-D numerical scheme.

Future work

- Integration of the (de)composition and reflection/transmission operators and the propagator into a 3-D Bremmer scheme.

- The direct construction of the relevant matrices for 3-D configurations is very time consuming. A special and "smart" procedure must be developed for that task.

- Alternative methods must be developed to include post-critical wave propagation. Methods based upon approximate eigenvalue decomposition, such as the Lanczos method, and methods based upon the uniform expansion of the symbols or kernels seem to be good candidates.

- Other boundary conditions can be investigated to decrease the computational window.

- A fifth-order Thiele approximation can be used to increase the accuracy. A seventh-order Thiele approximation is not recommended, because the gain in accuracy is assumed to be low at the cost of increased computing time.

- One should take a closer look at discontinuities of the medium properties at tilted interfaces and study the corresponding propagator and the reflection operator.

Bibliography

[1] S.E. Miller. Integrated optics: an introduction. *The Bell System Technical Journal*, 48(7):2059–2068, 1969.

[2] R.N. Hall, G.E. Fenner, J.D. Kingsley, T.J. Soltys, and R.O. Carlson. Coherent light emission from GaAs junctions. *Physical Review Letters*, 9(9):366–368, 1962.

[3] K.C. Kao and G.H. Hockman. Dielectric-fibre surface waveguides for optical frequencies. *Proceedings IEE*, 113(7):1151–1158, 1966.

[4] M.K. Smit and C. van Dam. PHASAR-based WDM devices: principles, design and applications. *IEEE Journal of Selected Topics in Quantum Electronics*, 2(2):236–250, 1996.

[5] C.G.M. Vreeburg, T. Uitterdijk, Y.S. Oei, M.K. Smit, F.H. Groen, E.G. Metaal, P. Demeester, and H.J. Frankena Frankena. First InP-based reconfigurable integrated add-drop multiplexer. *IEEE Photonics Technology Letters*, 9(2):188–190, 1997.

[6] M.J.N. van Stralen. The design and fabrication of InGaAsP ring lasers with grating and MMI-outcouplers. Master's thesis, Delft University of Technology, Delft, the Netherlands, 1993.

[7] R. van Roijen, E.C.M. Pennings, M.J.N. van Stralen, T. van Dongen, B.H. Verbeek, and J.M.M. van der Heijden. Compact InP-based ring lasers employing multimode interference couplers and combiners. *Applied Physics Letters*, 64(14):1753–1755, 1994.

[8] C.A.M. Steenbergen, C. van Dam, A. Looijen, C.G.P. Herben, M. de Kok, M.K. Smit, J.W. Pedersen, I. Moerman, R.G. Baets, and B.H. Verbeek. Compact low-loss 8x10 GHz polarisation independent WDM receiver. In *ECOC6*, pages 129–132, 1996.

[9] L.F. Tiemeijer, P.J.A. Thijs, T. van Dongen, R.W.M. Slootweg, J.M.M. van der Heijden, J.J.M. Binsma, and P.C.M. Krijn. Polarization insensitive mul-

tiple quantum well laser amplifiers for the 1300 nm window. *Applied Physics Letters*, 62(8):826–828, 1993.

[10] S. Shimada and H. Ishio. *Optical Amplifiers and their Applications*. John Wiley & Sons, Chichester, United Kingdom, 1994.

[11] C. Vassallo. 1993–1995 Optical mode solvers. *Optical and Quantum Electronics*, 29(2):95–114, 1997.

[12] M.J.N. van Stralen, K.F.I. Haak, and H. Blok. On the classification of discrete modes in lossy planar waveguides: the modal analysis revisited. *Optical and Quantum Electronics*, 29(2):243–262, 1997.

[13] H.J.W.M. Hoekstra. On beam propagation methods for modelling in integrated optics. *Optical and Quantum Electronics*, 29(2):157–171, 1997.

[14] X.J.M. Leijtens, P. le Lourec, and M.K. Smit. S-matrix oriented CAD-tool for simulating complex integrated optical circuits. *IEEE Journal of Selected Topics in Quantum Electronics*, 2(2):257–262, 1996.

[15] K. Aki and P.G. Richards. *Quantitive Seismology*. W.H. Freeman and Company, San Francisco, California, USA, 1980.

[16] M. Ewing and J.L. Worzel. Propagation of sound in the ocean. *The Geological Society of America Memoir*, 27, 1948.

[17] W. Munk and A. Baggeroer. The Heard Island papers: a contribution to global acoustics. *Journal of the Acoustical Society of America*, 96(4):2327–2329, 1994. (plus the 17 following papers on page 2330-2484).

[18] L.M. Brekhovskikh and Yu.P. Lysanov. *Fundamentals of Ocean Acoustics*. Springer Verlag, Berlin, Germany, 1991.

[19] I. Tolstoy and C.S. Clay. *Ocean Acoustics: Theory and Experiment in Underwater Sound*. American Institute of Physics, Inc., New York, New York, USA, 1987.

[20] A.T. de Hoop. *Handbook of Radiation and Scattering of Waves*. Academic Press Limited, London, United Kingdom, 1995.

[21] J.F. Nye. *Physical Properties of Crystals*. Clarendon Press, Oxford, United Kingdom, 1972.

[22] J.T. Fokkema and P.M. van den Berg. *Seismic Applications of Acoustic Reciprocity*. Elsevier Science Publishers B.V., Amsterdam, the Netherlands, 1993.

[23] L. Fishman and J.J. McCoy. Derivation and application of extended parabolic wave theories. I. The factorized Helmholtz equation. *Journal of Mathematical Physics*, 25(2):285–296, 1984.

[24] L. Fishman and J.J. McCoy. Derivation and application of extended parabolic wave theories. II. Path integral representations. *Journal of Mathematical Physics*, 25(2):297–308, 1984.

[25] L. Fishman. One-way wave propagation methods in direct and inverse scalar wave propagation modeling. *Radio Science*, 28(5):865–876, 1993.

[26] J.J. McCoy and L.N. Frazer. Pseudodifferential operators, operator orderings, marching algorithms and path integrals for one-way equations. *Wave Motion*, 9:413–427, 1987.

[27] L. Hörmander. *The Analysis of Linear Partial Differential Operators III*. Springer-Verlag, Berlin, Germany, 1985.

[28] M.E. Taylor. *Pseudo-differential operators*. Princeton University Press, Princeton, New Jersey, 1981.

[29] J.J. Duistermaat. Pseudodifferential operators and elliptic boundary problems. Technical report, Rijksuniversiteit Utrecht, Utrecht, the Netherlands, 1995.

[30] M. Leontovich and V. Fock. Solution of the problem of electromagnetic waves along the earths surface by the method of parabolic equation. *Journal of Physics*, 10:13–24, 1946.

[31] Claerbout. Coarse grid calculations of waves in inhomogeneous media with application to delineation of complicated seismic structure. *Geophysics*, 35(3):407–418, 1970.

[32] R.H. Hardin and F.D. Tappert. Applications of the split-step Fourier method to the numerical solution of nonlinear and variable coefficient wave equations. *SIAM Review*, 15:423, 1973.

[33] M.D. Feit and J.A. Fleck, Jr. Light propagation in graded-index optical fibers. *Applied Optics*, 17(24):3990–3998, 1978.

[34] M.D. Feit and J.A. Fleck, Jr. Calculation of dispersion in graded-index multimode fibers by a propagating-beam method. *Applied Optics*, 18(16):2843–2851, 1979.

[35] M.D. Feit and J.A. Fleck, Jr. Computation of mode properties in optical fiber waveguides by a propagating beam method. *Applied Optics*, 19(7):1154–1164, 1980.

[36] J.A. Fleck, Jr., J.R. Morris, and M.D. Feit. Time-dependent propagation of high energy laser beams through the atmosphere. *Applied Physics*, 10:129–160, 1976.

[37] J. van Roey. *Geïntegreerde Optische Roosters en Holografische Optische El-ementen.* PhD thesis, Rijksuniversiteit te Gent, Ghent, Belgium, 1983. (in dutch).

[38] J. van Roey, J. van der Donk, and P.E. Lagasse. Beam-propagation method: analysis and assessment. *Journal of the Optical Society of America,* 71(7):803–810, 1981.

[39] J. van der Donk. *Toepassing van de bundelpropagatiemethode op problemen van de geïntegreerde optika.* PhD thesis, Rijksuniversiteit te Gent, Ghent, Belgium, 1981. (in dutch).

[40] J. van der Donk. Beam propagation method. *Electrical Communication,* 59(4):380–384, 1985.

[41] R. Baets and P.E. Lagasse. Loss calculation and design of arbitrarily curved integrated-optic waveguides. *Journal of the Optical Society of America,* 73:177–182, 1983.

[42] P.E. Lagasse and R. Baets. Appplication of propagating beam methods to electromagnetic and acoustic wave propagation problems: A review. *Radio Science,* 22(7):1225–1233, 1987.

[43] L. Fishman and J.J. McCoy. Factorization, path integral representations and the construction of direct and inverse wave propagation theories. *IEEE Transactions on Geoscience and Remote Sensing,* 22(6):682–692, 1984.

[44] L. Fishman and J.J. McCoy. A new class of propagation models based on a factorization of the Helmholtz equation. *Geophysical Journal of the Royal Astronomical Society,* 80:439–461, 1985.

[45] L. Fishman, J.J. McCoy, and S.C. Wales. Factorization and path integration of the Helmholtz equation: Numerical algorithms. *Journal of the Acoustical Society of America,* 81(5):1355–1376, 1987.

[46] J. McCoy and L. Fishman. Propagation modelling based on wavefield factorization and invariant imbedding. *Geophysical Journal of the Royal Astronomical Society,* 86:703–717, 1986.

[47] J.J. McCoy and L. Fishman. Reflection and transmission at an interface separating transversely inhomogenoeous acoustic half-spaces. *Geophysical Journal of the Royal Astronomical Society,* 85:543–562, 1986.

[48] M.V. de Hoop. *Directional decomposition of transient acoustic wave fields.* PhD thesis, Delft University of Technology, Delft, the Netherlands, 1992.

[49] M.V. de Hoop. Generalization of the Bremmer coupling series. *Journal of Mathematical Physics,* 37(7):3246–3282, 1996.

[50] R.I. Brent and L. Fishman. Derivation of extended parabolic theories for vector and electromagnetic wave propagation. In *SIAM Philadelphia*, pages 90–102, 1992.

[51] L. Fishman, A.K. Gautesen, and Z. Sun. Uniform high-frequency approximations of the square root helmholtz operator symbol. *Wave Motion*. (to appear in 1997).

[52] L. Fishman. Exact and operator rational approximate solutions of the Helmholtz, Weyl composition equation in underwater acoustics - the quadratic profile. *Journal of Mathematical Physics*, 5:1887–1914, 1992.

[53] A.J. Haines and M.V. de Hoop. An invariant imbedding analysis of general wave scattering problems. *Journal of Mathematical Physics*, 37(8):3854–3881, 1996.

[54] H. Kragl. Cases of structural equality between the scalar wave equations of optics and the quantum-mechanical Schrödinger equation. *Journal of the Optical Society of America A*, 9(6):964–973, 1992.

[55] C. Lämmerzahl. The pseudodifferential operator square root of the Klein-Gordon equation. *Journal of Mathematical Physics*, 34(9):3918–3932, 1993.

[56] Y.V. Kopylov, A.V. Popov, and A.V. Vinogradov. Application of the parabolic wave equation to X-ray diffraction optics. *Optics Communications*, 118:619–636, 1995.

[57] A. Bamberger, F. Coron, and J.-M. Ghidaglia. An analysis of the B.P.M. approximation of the Helmholtz equation in an optical fiber. *Mathematical modelling and numerical analysis*, 21(3):405–424, 1987.

[58] L. Thylén. The beam propagation method: an analysis of its applicability. *Optical and Quantum Electronics*, 15:433–439, 1983.

[59] L. Thylen and D. Yevick. Beam propagation method in anisotropic media. *Applied Optics*, 21(15):2751–2754, 1982.

[60] J. Saijonmaa and D. Yevick. Beam-propagation analysis of loss in bent optical waveguides and fibers. *Journal of the Optical Society of America*, 73(12):1785–1791, 1983.

[61] M.D. Feit and J.A. Fleck, Jr. Beam nonparaxiality, filament formation, and beam breakup in the self-focusing of optical beams. *Journal of the Optical Society of America B*, 5(3):633–640, 1988.

[62] B. Hermansson and D. Yevick. Numerical analyses of the modal eigenfunctions of chirped and unchirped multiple-stripe-geometry laser arrays. *Journal of the Optical Society of America A*, 4(2):379–389, 1987.

[63] D. Yevick and B. Hermansson. New fast Fourier transform and finite-element approaches to the calculation of multiple-stripe-geometry laser modes. *Journal of Applied Physics*, 59(5):1769–1771, 1986.

[64] D. Yevick and B. Hermansson. Split-step finite difference analysis of rib waveguides. *Electronics Letters*, 25:461–462, 1989.

[65] M. Glasner, D. Yevick, and B. Hermansson. Generalized propagation formulas of arbitrarily high order. *Journal of Chemical Physics*, 95(11):8266–8272, 1991.

[66] M. Glasner, D. Yevick, and B. Hermansson. High-order generalized propagation techniques. *Journal of the Optical Society of America B*, 8(2):413–415, 1991.

[67] R. Accornero, M. Artiglia, G. Coppa, P. di Vita, G. Lapenta, M. Potenza, and P. Ravetto. Finite difference methods for the analysis of integrated optical waveguides. *Electronics Letters*, 26(23):1959–1960, 1990.

[68] Y. Chung and N. Dagli. An assessment of finite difference beam propagation method. *IEEE Journal of Quantum Electronics*, 26(8):1335–1339, 1990.

[69] R. Scarmozzino and R.M. Osgood, Jr. Comparison of finite-difference and Fourier-transform solutions of the parabolic wave equation with emphasis on integrated-optics applications. *Journal of the Optical Society of America A*, 8(5):724–731, 1991.

[70] C.M. Kim and R.V. Ramaswamy. Modeling of graded-index channel waveguides using nonuniform finite difference method. *Journal of Lightwave Technology*, 7(10):1581–1589, 1989.

[71] R. Clauberg and P. von Allmen. Vectorial beam-propagation method for integrated optics. *Electronics Letters*, 27(8):654–655, 1991.

[72] G.R. Hadley. Transparent boundary condition for beam propagation. *Optics Letters*, 16(9):624–626, 1991.

[73] G.R. Hadley. Transparent boundary condition for the beam propagation method. *IEEE Journal of Quantum Electronics*, 28(1):363–370, 1992.

[74] J. Willems, J. Haes, and R. Baets. The bidirectional mode expansion method for two-dimensional waveguides: the TM-case. *Optical and Quantum Electronics*, 27:995–1007, 1995.

[75] R. Baets, J. Willems, and J. Haes. Diversity in beam propagation methods. In *European Conference on Integrated Optics*, pages 13.1–13.3, 1993.

[76] J. Haes. *Studie van Bundeleigenschappen van Laserdiodes en Ontwerp van Geïntegreerde Bundelexpansiestrukturen*. PhD thesis, Universiteit te Gent, Ghent, Belgium, 1996. (in dutch).

[77] G. Sztefka and H.P. Nolting. Bidirectional eigenmode propagation for large refractive index steps. *IEEE Photonics Technology Letters*, 5(5):554–557, 1993.

[78] S. Banerjee and A. Sharma. Propagation characteristics of optical waveguiding structures by direct solution of the Helmholtz equation for total fields. *Journal of the Optical Society of America A*, 6(12):1884–1894, 1989. (Errata in 7(11):2156, 1990).

[79] A. Sharma and S. Banerjee. Method for propagation of total fields or beams through optical waveguides. *Optics Letters*, 14(1):96–98, 1989.

[80] A. Sharma and A. Taneja. Unconditionally stable procedure to propagate beams through optical waveguides using the collocation method. *Optics Letters*, 16(15):1162–1164, 1991.

[81] A. Sharma and A. Taneja. Variable-transformed collocation method for field propagation through waveguiding structures. *Optics Letters*, 17(11):804–806, 1992.

[82] A. Tanaje and A. Sharma. Propagation of beams through optical waveguiding structures: comparison of the beam-propagation method and the collocation method. *Journal of the Optical Society of America A*, 10(8):1739–1745, 1993.

[83] L. Thylén and C.M. Lee. Beam-propagation method based on matrix diagonalization. *Journal of the Optical Society of America A*, 9(1):142–145, 1992.

[84] L. Sun and G.L. Yip. Modified finite-difference beam-propagation method based on the Douglas scheme. *Optics Letters*, 18(15):1229–1231, 1993.

[85] J. Gerdes, B. Lunitz, D. Benish, and R. Pregla. Analysis of slab waveguide discontinuities including radiation and absorption effects. *Electronics Letters*, 28(11):1013–1015, 1992.

[86] J. Gerdes and R. Pregla. Beam-propagation algorithm based on the methods of lines. *Journal of the Optical Society of America B*, 8:389–394, 1991.

[87] A. Kornatz and R. Pregla. Increase of the order of approximation and improvement of the interface condition for the Method of Lines. *Journal of Lightwave Technology*, 11(2):249–251, 1993.

[88] R. Pregla and E. Ahlers. Method of Lines for the analysis of discontinuities in optical waveguides. *Electronics Letters*, 29(21):1845–1847, 1993.

[89] U. Rogge and R. Pregla. Method of Lines for the analysis of strip-loaded optical waveguides. *Journal of the Optical Society of America B*, 8(2):459–463, 1991.

[90] R.P. Ratowsky, J.A. Fleck, Jr., and M.D. Feit. Accurate solution of the Helmholtz equation by Lanczos orthogonalization for media with loss or gain. *Optics Letters*, 17(1):10–12, 1992.

[91] R.P. Ratowsky and J.A. Fleck. Accurate numerical solution of the Helmholtz equation by iterative Lanczos reduction. *Optics Letters*, 16(11):787–789, 1991.

[92] R.P. Ratowsky, J.A. Fleck, Jr., and M.D. Feit. Helmholtz beam propagation in rib waveguides and couplers by iterative Lanczos reduction. *Journal of the Optical Society of America A*, 9(2):265–273, 1992.

[93] B. Hermansson, D. Yevick, W. Bardyszewski, and M. Glasner. A comparison of Lanczos electric field propagation methods. *Journal of Lightwave Technology*, 10(6):772–776, 1992.

[94] D. Yevick, W. Bardyszewski, B. Hermansson, and M. Glasner. Lanczos reduction techniques for electric field reflection. *Journal of Lightwave Technology*, 10:1234–1237, 1992.

[95] P.-L. Liu and B.-J. Li. Full vectorial mode analysis of rib waveguides by iterative Lanczos reduction. In *European Conference on Integrated Optics*, pages 13.13–13.14, 1993.

[96] P.-L. Liu and B.-J. Li. Semivectorial Helmholtz beam propagation by Lanczos reduction. *IEEE Journal of Quantum Electronics*, 29(8):2385–2389, 1993.

[97] G.R. Hadley. Multistep method for wide-angle beam propagation. *Optics Letters*, 17(24):1743–1745, 1992.

[98] G.R. Hadley. Wide-angle beam propagation using Padé approximant operator. *Optics Letters*, 17(20):1426–1428, 1992.

[99] H.J.W.M. Hoekstra, G.J.M. Krijnen, and P.V. Lambeck. Efficient interface conditions for the finite difference beam propagation method. *Journal of Lightwave Technology*, 10(10):1352–1355, 1992.

[100] H.J.W.M. Hoekstra, G.J.M. Krijnen, and P.V. Lambeck. On the accuracy of the finite difference method for applications in beam propagating techniques. *Optics Communications*, 94:506–508, 1992.

[101] H.J.W.M. Hoekstra, G.J.M. Krijnen, and P.V. Lambeck. New formulation of the beam propagation method based on the slowly varying envelope approximation. *Optics Communications*, 97:301–303, 1993.

[102] P.C. Lee, D. Schulz, and E. Voges. Three-dimensional finite difference beam propagation algorithms for photonic devices. *Journal of Lightwave Technology*, 10(12):1832–1838, 1992.

[103] D. Schulz, C. Glingener, and E. Voges. Novel generalized finite difference beam propagation method. *IEEE Journal of Quantum Electronics*, 30(4):1132–1140, 1994.

[104] D. Schulz, W. Nöker, and E. Voges. Novel propagation algorithm for the analysis of optical waveguides in the time domain. In *IPR'94*, pages 93–95, 1994.

[105] A. Splett, M. Majd, and K. Petermann. A novel beam propagation method for large refractive index steps and large propagation distances. *IEEE Photonics Technology Letters*, 3(5):466–468, 1991.

[106] F. Gonthier, A. Hénault, S. Lacroix, R.J. Black, and J. Bures. Mode coupling in nonuniform fibers: comparison between coupled-mode theory and finite-difference beam-propagation method simulations. *Journal of the Optical Society of America B*, 8(2):416–421, 1991.

[107] M.D. Feit and J.A. Fleck, Jr. Simple spectral method for solving propagation problems in cylindrical geometry with fast Fourier transforms. *Optics Letters*, 14(13):662–664, 1989.

[108] W. Huang, C. Xu, S.-T. Chu, and S.K. Chaudhuri. The finite-difference vector beam propagation method: analysis and assessment. *Journal of Lightwave Technology*, 10(3):295–305, 1992.

[109] W.P. Huang, C.L. Xu, and S.K. Chaudhuri. A finite-difference vector beam propagation method for three-dimensional waveguide structures. *IEEE Photonics Technology Letters*, 4(2):148–151, 1992.

[110] C.L. Xu, W.P. Huang, and S.K. Chaudhuri. Efficient and accurate vector mode calculation by beam propagation method. *Journal of Lightwave Technology*, 11(7):1209–1215, 1993.

[111] J.M. Liu and L. Gomelsky. Vectorial beam propagation method. *Journal of the Optical Society of America A*, 9(9):1574–1585, 1992.

[112] G.L. Yip and P.C. Noutsios. An improved finite-difference vector beam propagation formulation for graded-index waveguides. *IEEE Photonics Technology Letters*, 6(4):543–545, 1994.

[113] D. Li, H. van Brug, and H.J. Frankena. Vectorial FD-BPM for 3-D waveguide structures. In *Linear and Nonlinear Integrated Optics*, pages 36–46, 1994.

[114] M. Rivera. *Bent waveguide analysis with a modified version of the beam propagation method*. PhD thesis, University of Arizona, Tucson, Arizona, USA, 1996.

[115] F. Schmidt. An adaptive approach to the numerical solution of Fresnel's wave equation. *Journal of Lightwave Technology*, 11(9):1425–1434, 1993.

[116] A. Kunz, F. Zimulinda, and W.E. Heinlein. Fast three-dimensional split-step algorithm for vectorial wave propagation in integrated optics. *IEEE Photonics Technology Letters*, 5:1073–1076, 1993.

[117] E.C.M. Pennings, R. van Roijen, M.J.N. van Stralen, P.J. de Waard, R.G.M.P. Koumans, and B.H. Verbeek. Reflection properties of multimode interference devices. *IEEE Photonics Technology Letters*, 6(6):715–718, 1994.

[118] P. Kaczmarski and P.E. Lagasse. Bidirectional beam propagation method. *Electronics Letters*, 24(11):675–676, 1988.

[119] H.-H. Lin and A. Korpel. Heuristic scalar paraxial beam propagation method taking into account continuous reflections. *Journal of the Optical Society of America B*, 8(4):849–857, 1991.

[120] D. Yevick, W. Bardyszewski, B. Hermansson, and M. Glasner. Split-operator electric field reflection techniques. *IEEE Photonics Technology Letters*, 3:527–529, 1991.

[121] C.J. Smartt, T.M. Benson, and P.C. Kendall. Exact analysis of waveguide discontinuities: junctions and laser facets. *Electronics Letters*, 29:1352–1353, 1993.

[122] O.J.F. Martin, A. Dereux, and C. Girard. Iterative scheme for computing exactly the total field propagating in dielectric structures of arbitrary shape. *Journal of the Optical Society of America A*, 11(3):1073–1080, 1994.

[123] G.R. Hadley. Numerical simulation of reflecting structures by solution of the two-dimensional Helmholtz equation. *Optics Letters*, 19(2):84–86, 1994.

[124] F. Wijnands, H.J.W.M. Hoekstra, G.J.M. Krijnen, and R.M. de Ridder. Modal fields calculations using a finite difference beam propagation method. *Journal of Lightwave Technology*, 12(12):2066–2072, 1994.

[125] F. Wijnands, H.J.W.M. Hoekstra, G.J.M. Krijnen, and R.M. de Ridder. Means to find modal fields for nonlinear structures using a finite difference Beam Propagation Method. In *Linear and Nonlinear Integrated Optics*, pages 85–94, 1994.

[126] F. Wijnands, H.J.W.M. Hoekstra, G.J.M. Krijnen, and R.M. de Ridder. Numerical solution method of nonlinear guided modes with a finite difference complex axis beam propagation method. *IEEE Journal of Quantum Electronics*, 31(5):782–790, 1995.

[127] D. Schulz, C. Glingener, W. Nöker, and E. Voges. Beam propagation algorithms for the analysis of optical waveguides in the frequency and time domain. In *ECOC'93*, pages 445–448, 1993.

[128] W.P. Huang, C.L. Xu, and J. Chrostowski. A time-domain propagating scheme for simulation of dynamics of optical guided-wave devices. *IEEE Photonics Technology Letters*, 5(9):1071–1073, 1993.

[129] L. Gomelsky and J.M. Liu. Extension of beam propagation method to time-dependent optical waveforms. *IEEE Photonics Technology Letters*, 6(4):546–548, 1994.

[130] G. Krijnen. *All-optical switching in nonlinear integrated optic devices*. PhD thesis, University of Twente, Enschede, the Netherlands, 1992.

[131] H. Bremmer. The W.K.B. approximation as the first term of a geometric-optical series. *Communications on Pure and Applied Mathematics*, 4:105–115, 1951.

[132] F.V. Atkinson. Wave propagation and the Bremmer series. *Journal of Mathematical Analysis and Applications*, 1:255–276, 1960.

[133] R. März. *Integrated Optics: Design and Modeling*. Artech House, Norwood, Massachusetts, USA, 1995.

[134] C.P.A. Wapenaar and J.L.T. Grimbergen. Reciprocity theorems for one-way wave fields. *Geophysical Journal International*, 127:169–177, 1996.

[135] C. DeWitt-Morette, A. Maheshwari, and B. Nelson. Path integration in non-relativistic quantum mechanics. *Physics Reports*, 50(5):255–372, 1979.

[136] M.V. de Hoop, M.J.N. van Stralen, and H. Blok. Construction of exact left symbols of the vertical slowness operator. *Journal of the Acoustical Society of America*, 100(4):2834, 1996.

[137] L. Fishman, 1996-1997. Personal communications.

[138] J.F. Claerbout. Coarse grid calculations of waves in inhomogeneous media with application to delineation of complicated seismic structure. *Geophysics*, 35:407–418, 1970.

[139] R. Baets and P.E. Lagasse. Calculation of radiation loss in integrated-optic tapers and y-junctions. *Applied Optics*, 21(11):1972–1978, 1982.

[140] A.R. Mitchell and D.F. Griffiths. *The finite difference method in partial differential equations*. John Wiley & Sons, New York, New York, USA, 1980.

[141] H. Blok. Theory of electromagnetic waveguides, Part 1. Lecture notes, Delft University of Technology, Delft, the Netherlands, 1995.

[142] D. Marcuse. *Light Transmission Optics*. Van Nostrand Reinhold Company, New York, New York, USA, 1972.

[143] A.W. Snyder and J.D. Love. *Optical Waveguide Theory*. Chapman and Hall Ltd., New York, New York, USA, 1983.

[144] C. Vassallo. *Optical waveguide concepts*. Elsevier Science Publishers B.V., Amsterdam, the Netherlands, 1991.

[145] M. Abromowitz and I.A. Stegun. *Handbook of mathematical functions with formulas, graphs, and mathematical tables*. Dover Publications, Inc., New York, New York, USA, 1972.

[146] I.S. Gradshteyn and I.M. Ryzhik. *Table of integrals, series, and products*. Academic Press, Inc., New York, New York, USA, 1980.

[147] W. Magnus, F. Oberhettinger, and R.P. Soni. *Formulas and Theorems for the Special Functions of Mathematical Physics*. Springer-Verlag, Berlin, Germany, 1966.

[148] C. Lanczos. *Applied Analysis*. Prentice Hall, Inc., 1956.

[149] B.K.P. Scaife. *Studies in Numerical Analysis*. Academic Press, 1974.

[150] The MATH WORKS Inc. *MATLAB High-Performance Numerical Computation and Visualization Software*. The MATH WORKS Inc., 1992.

[151] F.D. Tappert. The parabolic approximation method. In J.B. Keller and J.S. Papadakis, editors, *Wave Propagation and Underwater Acoustics*, pages 224–287. Springer-Verlag, New York, New York, USA, 1977.

[152] Z. Ma. Finite-difference migration with higher order approximation. *Oil Geophys. Prosp. China*, 1:6–15, 1982.

[153] R.R. Greene. The rational approximation to the acoustic wave equation with bottom interaction. *Journal of the Acoustical Society of America*, 76(6):1764–1773, 1984.

[154] L. Halpern and L.N. Trefethen. Wide-angle one-way wave equations. *Journal of the Acoustical Society of America*, 84(4):1397–1404, 1988.

[155] M.D. Collins. Applications and time-domain solution of higher-order parabolic equations in underwater acoustics. *Journal of the Acoustical Society of America*, 86(3):1097–1102, 1989.

[156] M.D. Collins and E.K. Westwood. A higher-order energy-conserving parabolic equation parabolic equation for range-dependent ocean depth, sound speed, and density. *Journal of the Acoustical Society of America*, 89(3):1068–1075, 1991.

[157] M.D. Collins. Minimax rational approximations for the parabolic equation method. *Journal of the Acoustical Society of America*, 94(3):1884, 1993.

[158] R.J. Cederberg, M.D. Collins, and W.L. Siegmann. Applications of optimized rational approximations to parabolic equation modeling. *Journal of the Acoustical Society of America*, 98(3):2971, 1995.

[159] L.N. Trefethen. Group velocity in finite difference schemes. *SIAM Review*, 24(2):113–136, 1982.

[160] C.M. Beaumont, J.F. Boyce, and R. Silva. Phase errors of finite-difference migration. *Geophysical Prospecting*, 35:267–280, 1987.

[161] O. Holberg. Computational aspects of the choice of operator and sampling interval for numerical differentiation in large-scale simulation of wave phenomena. *Geophysical Prospecting*, 35:629–655, 1987.

[162] O. Holberg. Towards optimum one-way wave propagation. *Geophysical Prospecting*, 36:99–114, 1988.

[163] R.W. Graves and R.W. Clayton. Modeling acoustic waves with paraxial extrapolators. *Geophysics*, 55(3):306–319, 1990.

[164] T. Rühl, C. Kopp, and D. Ristow. Fourier finite-difference migration for steeply dipping reflectors with complex overburden. *Geophysical Prospecting*, 43:919 938, 1995.

[165] M.J.N. van Stralen, M.V. de Hoop, and H. Blok. Design of sparse matrix representations for the propagator used in the BPM and directional wave-field decomposition. *Optical and Quantum Electronics*, 29(2):179–197, 1997.

[166] M.J.N. van Stralen, M.V. de Hoop, and H. Blok. Generalized Bremmer series with rational approximation for the scattering of waves in inhomogeneous media. *Journal of the Acoustical Society of America*, 1996. (submitted to the Journal of the Acoustical Society of America (1996)).

[167] M.J.N. van Stralen, M.V. de Hoop, and H. Blok. Directional decomposition of the electromagnetic field in integrated optics. In *Zeitschrift für Angewandte Mathematik und Mechanik*, volume 76, pages 569–570. Akademie Verlag, 1996. ICIAM/GAMM 95, Hamburg, Germany, 3-7 July 1995.

[168] M.J.N. van Stralen, M.V. de Hoop, and H. Blok. Numerical implementation of the Bremmer coupling series. In *Integrated Photonics Research*, volume 6, pages 20–23, 1996.

[169] H.C. Serafini and M.V. de Hoop. Even-versus-odd order Thiele approximations of the one-way operator in the space-time domain. In *61st Annual Meeting of the Society of Exploration Geophysicists*, volume 61, pages 1580–1583, 1991.

[170] M.V. de Hoop and A.T. de Hoop. Scalar space-time waves in their spectral-domain first- and second-order thiele approximations. *Wave Motion*, 15:229–265, 1992.

[171] We employed the routine E04CCF of the NAG FORTRAN Library Manual Mark 15 (1991).

[172] M.W. Lee and S.Y. Suh. Optimization of one-way wave equations. *Geophysics*, 50(10):1634–1637, 1985.

[173] C. Bunks. Optimization of paraxial wave equation operator coefficients. In *62nd Annual Meeting of the Society of Exploration Geophysicists*, volume 62, pages 897–900, 1992.

[174] R.T. Coates and M. Schoenberg. Finite-difference modeling of faults and fractures. *Geophysics*, 60(5):1514–1526, 1995.

[175] M. Schoenberg and F. Muir. A calculus for finely layered anisotropic media. *Geophysics*, 54(5):581–589, 1989.

[176] F. Muir, J. Dellinger, J. Etgen, and D. Nichols. Modeling elastic fields across irregular boundaries. *Geophysics*, 57(9):1189–1193, 1992.

[177] W.H. Press, B.P. Flannery, S.A Teukolsky, and W.T. Vetterling. *Numerical Recipes*. Cambridge University Press, Cambridge, United Kingdom, 1986.

[178] O.B. Widlund. On the stability of parabolic difference schemes. *Mathematics of Computation*, 19:1–13, 1965.

[179] R.D. Richtmyer and K.W. Morton. *Difference methods for intial-value problems*. Interscience Publishers, John Wiley & Sons, New York, New York, USA, 1967.

[180] We employed the routines F07BRF and F07BSF of the NAG FORTRAN Library Manual Mark 15 (1991).

[181] R.W. Clayton and B. Engquist. Absorbing boundary conditions for wave-equation migration. *Geophysics*, 45(5):895–904, 1980.

[182] J.-P. Berenger. A perfectly matched layer for the absorption of electromagnetic waves. *Journal of Computational Physics*, 114:185–200, 1994.

[183] C. Vassallo and J.M. van der Keur. Highly efficient transparent boundary conditions for finite difference beam propagation method at order 4. *Journal of Lightwave Technology*, 1996. (accepted for publication).

[184] Y. Arai, A. Maruta, and M. Matsuhara. Transparent boundary for the finite-element beam-propagating method. *Optics Letters*, 18(10):765–766, 1993.

[185] R.G. Keys. Absorbing boundary conditions for acoustic media. *Geophysics*, 50(6):892–902, 1985.

[186] M.D. Collins. Higher-order Padé approximations for accurate and stable elastic parabolic equations with application to interface wave propagation. *Journal of the Acoustical Society of America*, 89(3):1050–1057, 1991.

[187] M.V. de Hoop and A.T. de Hoop. Interface reflections of spherical acoustic waves in the first-and second-order rational parabolic approximations and their artifacts. *Journal of the Acoustical Society of America*, 93(1):22–35, 1993.

[188] H.-P. Nolting and R. März. Results of benchmark tests for different numerical BPM algorithms. *Journal of Lightwave Technology*, 13(2):216–224, 1995.

[189] P.M. van den Berg. Iterative computational techniques in scattering based upon the integrated square error criterion. *IEEE Transactions on antennas and propagation*, 32(10):1063–1071, 1984.

[190] M.V. de Hoop and A.T. de Hoop. Elastic wave up/down decomposition in inhomogeneous and anisotropic media: an operator approach and its approximations. *Wave Motion*, 20:57–82, 1994.

[191] M. Shamonin. *Nonreciprocal mode propagation in magnetooptic waveguides.* PhD thesis, Universität Osnabrück, Germany, 1995.

[192] Y. Tsuji and M. Koshiba. A finite element beam propagation method for strongly guiding and longitudinally varying optical waveguides. *Journal of Lightwave Technology*, 14(2):217–222, 1996.

[193] M.S. Stern. Semivectorial polarised finite difference method for optical waveguides with arbitrary index profiles. *IEE Proceedings-J*, 135(1):56–63, 1988.

[194] D. Li. *Analysis, design and fabrication of tapered integrated optical structures; Implementation of the fully vectorial 3-D beam propagation method.* PhD thesis, Delft University of Technology, Delft, the Netherlands, 1995.

[195] W.P. Huang and C.L. Xu. Simulation of three-dimensional optical waveguides by a full-vector beam propagation method. *IEEE Journal of Quantum Electronics*, 29:2639–2649, 1993.

[196] P. Lüsse, K. Ramm, and H.-G. Unger. Vectorial eigenmode calculation for anisotropic planar optical waveguides. *Electronics Letters*, 32:38–39, 1996.

[197] M.J.N. van Stralen, M.V. de Hoop, and H. Blok. Numerical implementation of the 3D one-way wave propagator using the third-order Thiele approximation on a hexagonal grid. *Journal of the Acoustical Society of America*, 100(4):2834, 1996.

[198] R.M. Mersereau. The processing of hexagonally sampled two-dimensional signals. *Proceedings of the IEEE*, 67(6):930–949, 1979.

[199] D.P. Petersen and D. Middleton. Sampling and reconstruction of wavenumber-limited functions in N-dimensional euclidean spaces. *Information and Control*, 5:279–323, 1962.

[200] M.H. Gutknecht. Variants of BiCGStab for matrices with complex spectrum. *SIAM Journal on Scientific Computing*, 14(5):1020–1033, 1993.

Samenvatting

Het numeriek modelleren van golfvoortplanting in willekeurige, grote structuren is rekenintensief en vereist zeer snelle computers met grote geheugens. Daarom zoekt men naar alternatieve rekenmethoden op maat gemaakt voor een groep van configuraties met gemeenschappelijke eigenschappen, die nauwkeurig en toch snel zijn.

In golfgeleidende structuren kan men een voorkeursrichting van de golfvoortplanting aanwijzen. Hierin variëren de eigenschappen van de structuur langzamer in de voorkeursrichting dan in de richting loodrecht daarop. Een richtingsafhankelijke decompositie van elektromagnetische of akoestische golven is een methode om dit veldprobleem te beschrijven. Daarbij valt de beschrijving uiteen in twee deelproblemen: (a) de golfvoortplanting in de voorkeursrichting en (b) de verstrooiing ten gevolge van variaties in het vlak loodrecht daarop. Daarvoor wordt gebruik gemaakt van Bremmer's reeks ontwikkeling en de theorie van de pseudo-differentiaal operatoren.

Eén van de toepassingsgebieden is de geïntegreerde optica. De grote drijfveer hierachter is de glasvezeltelecommunicatie. Met de huidige techniek kan men complexe ontvangers en zenders op een optische chip maken waarin naast lichtgeneratie en detectie ook ingewikkelde signaalbewerkingen optisch worden uitgevoerd. Voor het ontwerpen van zulke chips is er behoefte aan numerieke methoden om de elektromagnetische velden in de voorkomende golfgeleidende structuren te berekenen. In de jaren 70 is de ontwikkeling van de Bundel Propagatie Methode (BPM) begonnen. Sindsdien is deze methode sterk verbeterd. In feite is de BPM een primitief voorbeeld van de richtingsafhankelijke golfvelddecompositie.

Andere toepassingen komen uit de exploratiegeofysica en onderwaterakoestiek. Naast de akoestische golfgeleiding in de aardlagen tussen twee boorgaten, kan men ook golfvoortplanting loodrecht op de aardlagen met een directionele golfvelddecompositie beschrijven en modelleren. In de literatuur behandelt men vaak methoden die gebaseerd zijn op de zogenaamde parabolische benadering. Deze methoden zijn het akoestische equivalent van de BPM.

De in dit proefschrift beschreven methode wordt in frequentie-domein uitgevoerd. Een inverse Fourier transformatie vertaalt het resultaat eventueel naar het tijddomein. Na de keuze van de voorkeursrichting wordt het elektromagnetische veld in

een willekeurige dwarsdoorsnede in twee verschillende golfconstituenten ontrafeld: één in de voorkeursrichting en één in de tegengestelde richting. De reeks van Bremmer is een wiskundige methode om de interactie tussen deze twee golven te beschrijven. Sommatie van die golven levert uiteindelijk het te berekenen veld.

De afzonderlijke termen in de reeks van Bremmer kunnen fysisch geïnterpreteerd worden als de golven die een aantal keren heen en weer hebben gelopen door de configuratie. Zo komt de eerste term overeen met de golf in voorwaartse richting, die ook in de BPM berekend wordt, terwijl de tweede term de één keer gereflecteerde golf beschrijft. De numerieke implementatie van Bremmer's reeks is relatief eenvoudig en leidt tot een nieuw efficiënt rekenschema. Numerieke voorbeelden tonen aan dat vaak een beperkt aantal termen van deze reeks al nauwkeurige resultaten geeft.

Het verstrooiingsprobleem in het dwarsvlak is wiskundig een stuk lastiger. Pseudo-differentiaaloperatoren (of worteloperatoren) beschrijven namelijk dit verstrooiingsprobleem. Een grondige analyse geeft ons twee wiskundige gereedschappen: (a) een eigenwaardenontbinding en (b) een vlakkegolfontbinding. De eigenwaardenanalyse is nauw verwant met de modale analyse van golfgeleiders. Het geeft ons samen met de reeks van Bremmer de mogelijkheid om het modelleren van uniforme (rechte) golfgeleiders uit de breiden naar niet-uniforme golfgeleiders. Daartegenover staat de vlakkegolfontbinding. De interactie van de worteloperator met een vlakke golf wordt daarbij vervangen door een vermenigvuldiging van een linker symbool met dezelfde vlakke golf. In feite breidt de theorie voor golfvoortplanting in een homogeen gelaagde structuur zich zo uit naar een heterogeen gelaagde structuur. Een nadere analyse van het linker symbool verduidelijkt het verband tussen dit symbool en de modale analyse. Voor twee specifieke configuraties wordt dit symbool berekend en gebruikt voor de analyse van het rekenschema: een golfgeleider met kwadratisch profiel en een symmetrische drie-lagen golfgeleider.

Doel bij de numerieke implementatie is een snel en nauwkeurigheid rekenschema. Hiervoor dient men kleine ijle matrixrepresentaties van de relevante operatoren te ontwerpen. Als eerste krijgt de twee dimensionale configuratie alle aandacht. De in dit proefschrift gevolgde numerieke strategie is gebaseerd op de derde-orde-benadering van Thiele's ontwikkeling van de worteloperator. Daarnaast worden alle ruimtelijke afgeleiden ook vervangen door hun rationale eindige-differenties benaderingen. Om de uiteindelijke nauwkeurigheid op een grof rooster op te voeren, wordt met behulp van de linker symbolen een zodanige optimalisatie geïntroduceerd dat de golfvoortplanting in het rekenschema tot bijna 90 graden nauwkeurig beschreven wordt, terwijl de numerieke optredende artefacten minimaal zijn. Een soortgelijke analyse wordt uitgevoerd voor de reflectie- en (de)compositie-operatoren. Dit alles leidt tot een snel en nauwkeurig rekenschema. Een aantal numerieke voorbeelden verduidelijken de reeks van Bremmer.

Als proef op de som wordt de methode ook toegepast op elektromagnetische velden in drie dimensionale configuraties met anisotrope materialen. Bij het ontrafelen van het veld in tegen elkaar inlopende golven, dient men de symmetrieën van de relevante operatoren nauwlettend in de gaten te houden. Daarnaast verdient ook de elektromagnetische polarisatiewisselwerking extra aandacht. Aan de

basis van de numerieke implementatie liggen wederom de derde-orde-benadering van Thiele's ontwikkeling van de worteloperator en de rationale benaderingen van spatiële afgeleiden. Om een snel rekenschema op een grof rooster te ontwikkelen worden hexagonale roosters gebruikt. De optredende fout is dan rotatie-symmetrisch, wat niet tot noemenswaardige numerieke anisotropie leidt. Een aantal numerieke voorbeelden verduidelijken de methode.

Dit proefschrift geeft een uitvoerige beschrijving van een algemene wiskundige methode voor golfveldverstrooiing in structuren met een richtingsafhankelijkheid. Men kan de methode ook zien als een uitbreiding van de standaard parabolische methoden, zoals de bundelpropagatiemethode. Er zijn twee belangrijke numerieke aspecten: (1) de reeks van Bremmer neemt ook de interactie tussen de tegen elkaar inlopende golven mee en (2) de numerieke voortplantingshoek wordt vergroot door het gebruik van rationele benaderingen van de relevante operatoren en een optimalisatieprocedure.

Curriculum Vitae

Mathé van Stralen was born in Haarlem, the Netherlands, on March 5, 1970. From 1982, his secondary school education was at the Gymnasium Felisenum in Velsen, where he graduated in 1988. He enrolled as a student in Electrical Engineering at the Delft University of Technology, the Netherlands, from where he graduated in 1993. During his studies, he carried out a research project on the propagation properties of strongly absorbing, multilayer planar waveguides under the supervision of Professor Dr. ir. H. Blok. The research for his master's thesis was carried out at the Philips Optoelectronics Centre in Eindhoven under the supervision of Professor Dr. B.H. Verbeek (Laboratory of Telecommunications and Remote Sensing Technology). He designed and fabricated InGaAsP ring lasers with grating and MMI outcouplers. Delft Instruments Nederland BV presents the Bouwers-Van Leer prize for the best master's thesis at any Dutch university in the field of optics, optronics and fine mechanics every year. The second prize of 1993 was awarded to Mathé.
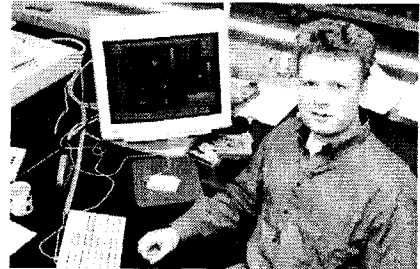
In March 1993, he started to work on this Ph.D. thesis under the supervision of Professor Dr. ir. H. Blok at the Laboratory of Electromagnetic Research, Department of Electrical Engineering, Delft University of Technology, The Netherlands. His first explorations in the field of the directional wave-field decomposition were carried out together with Professor Dr. Gy. Veszely from the Department of Electromagnetic Theory, Technical University of Budapest, Hungary, who visited the laboratory for three months in the spring of 1993 and in May 1995. In the summer of 1994 and April 1995, Mathé stayed four months at Schlumberger Cambridge Research, Cambridge, United Kingdom, where he conducted research for his Ph.D. thesis under the supervision of Dr. M.V. de Hoop. He was a member of the organizing comittee of the international workshop on optical waveguide theory and numerical modeling in Roosendaal, september 1995. In May 1996, he visited the Center of Wave Phenomena, Colorado School of Mines, Golden, USA.

The research for his master's thesis and Ph.D. thesis led to several scientific publications in international journals, presentations at international conferences in Europe and USA and scientific talks in Germany and England.